UNIVERSITÉ DE GRENOBLE

THÈSE

pour obtenir le grade de

DOCTEUR DE L'UNIVERSITÉ DE GRENOBLE

Spécialité : **Signal Image parole Télécoms (SIPT)**

Arrêté ministériel : 7 août 2006

Présentée par
Bo WU

Thèse dirigée par **Annemie Van Hirtum**
préparée au sein du
laboratoire Grenoble Image Signal parole Automatique (GIPSA-lab)
dans **l'école doctorale Electronique Electrotechnique Automatique Traitement du Signal (EEATS)**

The influence of the cross section shape on channel flow: modeling, simulation and experiment

Thèse soutenue publiquement le **23 Janvier 2014**,
devant le jury composé de:

Pierre-Yves Lagrée
Institut Jean le Rond d'Alembert, Rapporteur
Christian Lacor
Vrije Universiteit Brussel, Rapporteur
Benoît Fabre
Institut Jean le Rond d'Alembert, Examinateur
Thomas Hélie
IRCAM, Examinateur
Thomas Podgorski
Université de Grenoble, Président et Examinateur
Annemie Van Hirtum
Université de Grenoble, Directrice de thèse

UNIVERSITÉ DE GRENOBLE

ÉCOLE DOCTORALE SIGLE ED

Electronique Electrotechnique Automatique Traitement du Signal (EEATS)

T H È S E

pour obtenir le titre de

docteur en sciences

de l'Université de GRENOBLE

Mention : Signal Image parole Télécoms (SIPT)

Présentée et soutenue par

Bo WU

The influence of the cross section shape on channel flow: modeling, simulation and experiment

Thèse dirigée par Annemie Van Hirtum

préparée au laboratoire Grenoble Image Signal Parole Automatique (GIPSA-Lab)

soutenue le 23 Janvier 2014

Jury :

Rapporteurs :	Pierre-Yves Lagrée	-	Institut Jean le Rond d'Alembert
	Christian Lacor	-	Vrije Universiteit Brussel
Examinateurs :	Benoît Fabre	-	Institut Jean le Rond d'Alembert
	Thomas Hélie	-	IRCAM
	Thomas Podgorski	-	Université de Grenoble
Directrice :	Annemie Van Hirtum	-	Université de Grenoble

Acknowledgments

I thank the members of the jury Pierre-Yves Lagrée, Christian Lacor, Benoît Fabre, Thomas Hélie and Thomas Podgorski for their patience to read and correct this manuscript.

I want to thank my supervisor Annemie Van Hirtum who gave tremendous help during my thesis in the past three years, without her I probably have not succeed.

Thanks to Xiaoyu Luo who greeted me during my long stay in Glasgow and the people of her term: Hao Gao, Xinshuang Ma, Beibei Li, Nan Qi, Weiwei Chen and Lei Wang who gave me much help during my stay.

I thank all members of the department and in particular: Yo, Nicolas, Xavier, Louis, Noel, Audrey, Olha, Kelem, Amelie, Benjamin, Laurent and Nathalie for all these great moments spent with you.

But also I would like to thank the people of administration: Lucia, Akila, Isabell, Nadine, Christian, Patricia, Gelu, Cecilia and Jean-Claude. Thanks to you.

I sincerely thank all my friends: Yan Lu, Zuheng Ming, Haiyang Ding, Nan Yu, Xiangwei Zhang, Kai Wang, Xiyan He, Tinghong Wang, Hai Yu, Yi Gang, Junshi Xia, Ying Tang and all the other people for their selfless help during my living in Grenoble.

Thanks to Gang Feng, without his help I may not be Grenoble to have a wonderful experience.

Thanks to my best friend and my private teacher of French, Michelle who treat me as a member of her family. Thanks to you.

Thanks to the student Matthias and Daniel who did a favor in my experiments.

I gratefully acknowledge financial support from the French Ministry of Education, the Explora'Doc program from the Rhône Alpes Region (France), Centre national de la recherche scientifique (CNRS, France) and the Royal Society (UK).

Finally, I want to thank my family who accompanied and supported me through my study.

Résumé — abstract
La modélisation des phénomènes physiologiques induits par un écoulement, tels que l'écoulement sanguin au travers d'une sténose ou l'écoulement d'air lors de la production de parole, repose souvent sur des théories quasi-unidimensionnelles ou bi-dimensionnelles. Cependant, il est établi que le développement des couches limites dépend de la section transversale. Le but de cette thèse est de modéliser, simuler et caractériser l'importance potentielle de la section transversale sur les écoulements laminaires, contrôlés en pression, en l'absence ou en présence d'une constriction. Des coordonnées de translation sont utilisées pour obtenir des solutions pour des écoulement visqueux au travers d'une section de forme arbitraire. Cette paramétrisation est appliquée à la résolution des équations physiques pour des formes à deux et à trois dimensions. Un modèle d'écoulement simplifié quasi-tridimensionnel, qui prend en compte les pertes dissipatives par convection, la viscosité et la forme de la section est présenté et appliqué à la description de l'écoulement le long d'une sténose. Des données expérimentales et issues de simulations numériques sont collectées afin de caractériser l'influence de la forme de la section transversale dans le cas d'une constriction. simulation numérique sont comparées.
Mots clés: écoulement; modèle analytique; simulation numérique; sténose; parole

Abstract — abstract
Physical models of physiological flow-induced phenomena, such as blood flow through a stenosis or air flow during human speech production, often rely on a quasi-one-dimensional or two-dimensional flow model, so that details of the cross section shape are neglected. Nevertheless, boundary layer development is known to depend on the cross section shape. The aim of this thesis is to model, simulate and characterize the potential impact of the cross section shape for pressure-driven laminar channel flow without and with constriction. Stretched coordinates are introduced to obtain viscous flow solutions for channels with an arbitrary cross section. The proposed cross section shape parametrization is applied to solve physical equations for two-dimensional and three-dimensional shapes. A simplified quasi-three-dimensional flow model, which accounts for kinetic losses, viscosity and the cross section shape, is presented and applied to describe the flow through a stenosis. Finally, flow data are gathered experimentally and numerically in order to characterize the influence of the cross section shape in the case of a constricted channel. Modeled, experimental and numerical data are compared.
Keywords: laminar viscous flow; pressure-driven channel flow; analytical flow model; immersed boundary method; stenosis; speech production

GIPSA Lab, BP 46, 11 rue des Mathematiques,
38402, Grenoble, France

Contents

List of Figures

List of Tables

Chapter 1

Introduction

1.1 Formulation of the problem

Pressure–driven channel flow is associated with physiological flows for which constricted channel portions occur either naturally or are due to a pathology or an abnormality. Well known examples are for instance airflow through the human lower (asthma) or upper airways (human speech production, obstructive sleep apnea) and blood flow through a stenosis.

Consequently, efforts are made to model pressure–driven flow through constricted channels in order to understand the mechanisms involved and to develop aiding tools for health care workers such as surgeons, medical doctors, speech therapists, prosthesis designers (dental or glottal), aerosol spray designers, *etc.* Due to the complexity of the human respiratory (Fig. 1.1) and cardiovascular system, most studies severely simplify the physiological reality in order to come up with a configuration depending on a limited number of meaningful physiological and physical parameters [56, 117, 5, 98, 72, 112, 71, 8, 104, 74]. Such a simplification enhances understanding of the ongoing physical phenomena and facilitates experimental validation of the models accuracy [107, 15, 97, 70, 76, 25, 111].

In general, simplifications of the flow model through portions of the respiratory or cardiovascular system are based on a non dimensional analysis of the governing Navier-Stokes equations [9] while accounting for typical values of physiological, geometrical and flow characteristics. From these observations relevant non-dimensional numbers (Mach number Ma, Reynolds number Re, Strouhal number Sr and mean channel width-to-height ratio Ar) allow one simplify the flow model. For instance, glottal flow during phonation can be assumed to be incompressible ($Ma^2 \ll 0.7$), laminar inviscid ($Re \approx O(10^3)$), quasi-steady ($Sr \ll 1$) and two-dimensional ($Ar \geqslant 4$) [28, 51, 98, 110, 63, 120, 23]. The assumption of a two-dimensional glottal flow implies a rectangular glottal cross section shape for which height $h(x)$ varies along main flow direction x, whereas glottal width w is fixed [56, 117, 5, 98, 72, 112, 71, 8, 64, 104, 74]. Theoretical flow models based on these assumptions result in a quasi-one-dimensional flow description when accounting for kinetic losses as well as viscous losses [30, 25, 23]. Therefore, quasi-one-dimensional (1D) or two-dimensional (2D) flow models have proven to be extremely useful to grasp the underlying physics and are applied to mimic and predict ongoing phenomena using few computational resources while allowing experimental validation on replicas with different degrees of complexity [120, 23, 20]. Naturally, the assumption of a 1D or 2D geometry implies that details of the cross section shape perpendicular to main flow direction

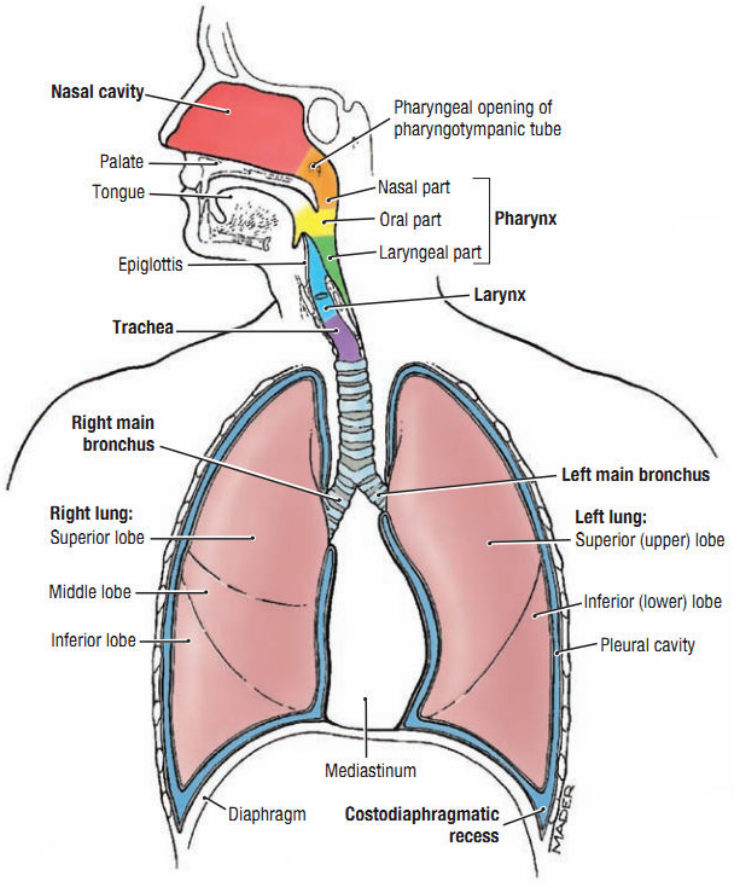

Figure 1.1: The human airway system [1].

x are neglected.

Nevertheless, visualization of the auto-oscillation of deformable mechanical glottal replicas [121] as well as observations of the glottal geometry during human speech production [37, 28, 91, 131, 31] revealed that the cross section shape defers from a rectangular shape. For example, a "neutral" vowel (‘e’ as in taken or ‘i’ as in pencil) is defined as a vowel produced by a vocal tract configuration that has uniform cross section area along its entire length in which the vocal tract can be treated mathematically as a single uniform tube closed at one end (the glottis). While in reality the configuration of the vocal tract during speech production is much more complex. Fig 1.2a shows the derived medial section of a vocal tract during the production of a high central spread-lipped vowel. The red line approximately represents the mid line of the vocal tract during this gesture. Fig. 1.2b displays seven cross section shapes along the vocal tract taken from the equivalently numbered locations in Fig. 1.2a. It can be seen that the actual cross section shape of the vocal tract varies greatly along its length and this is the case even during the production of a neutral vowel. Fig. 1.3 shows that the assumption of a rectangular shape can be questioned even for non-pathological conditions. The same way a large diversity of cross section shapes is observed for the cardiovascular system as illustrated in Fig. 1.4.

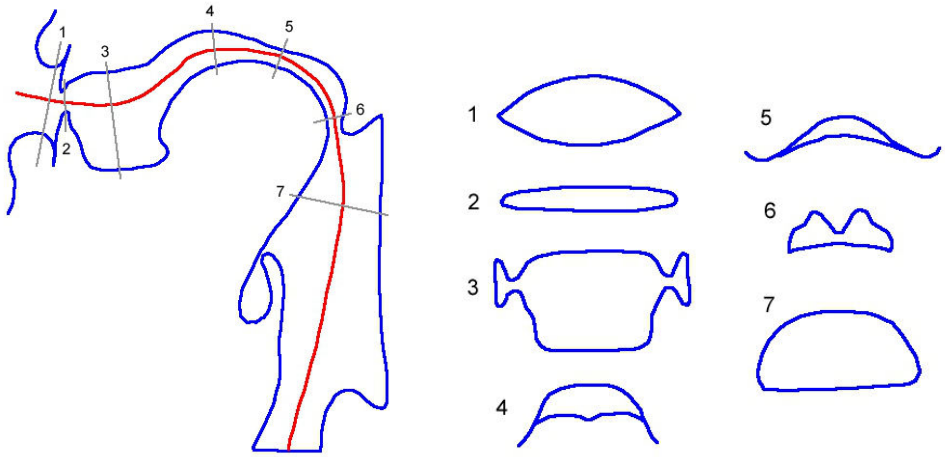

(a) (b)

Figure 1.2: a) X-ray derived vocal tract medial section during the articulation of a high central spread-lipped vowel (/i/) spoken by an adult male. b) cross section shapes were determined along the vocal tract at the cross section lines numbered 1 to 7 (see Fig. 1.2b) [37].

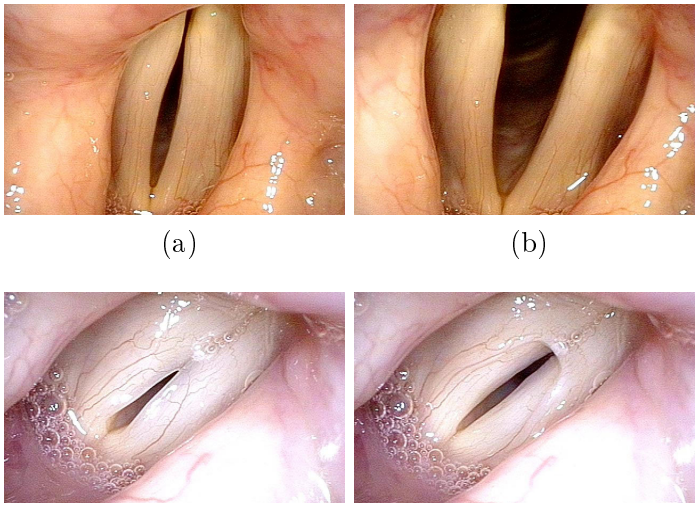

(a) (b)

(c) (d)

Figure 1.3: Still images of vibrating vocal folds (`http://bastianmedicalmedia.com/photos/vocal-fold-bowing/`).

Since the cross section shape is known to affect boundary layer development [9], varying the cross section shape might alter the viscous contribution to the pressure drop, the theoretical flow models using the above mentioned simplifications can thus be questioned for normal as well as pathological geometrical conditions.

Recently, Computational Fluid Dynamics (CFD) has been utilized to characterize the fluid flow in human biological circulation models. Efforts have been made to understand the

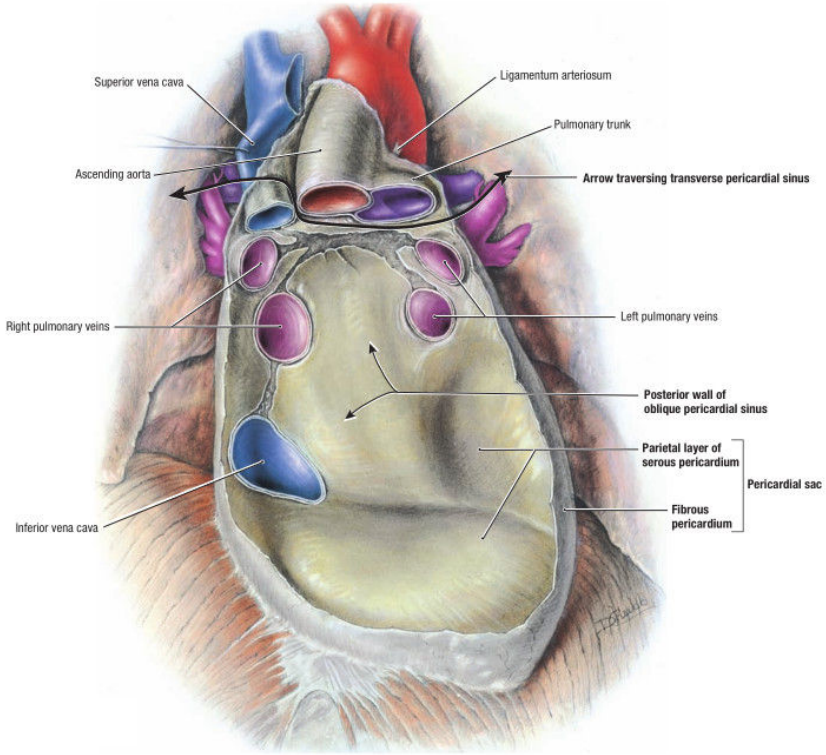

Figure 1.4: The anterior view of heart and pericardium [1].

blood flow and related problems in cardiovascular system [116, 14, 60, 69, 17, 89, 115, 118, 123] using patience-specific computational model. Several authors [130, 103, 68, 79, 114, 128, 13, 57, 58, 93, 84, 92, 124, 67, 36] give important contributions to three-dimensional steady and unsteady modeling of flow through bifurcating lung branches and realistic oropharynx geometries with respect to quiet respiration. Experimental validation of flow simulations through human upper airways is presented in [50, 90]. In order to assess systematic variation of the constricted passage and flow conditions instead of quiet respiration three-dimensional models of the impact of the geometry and flow circulation on the flow development with finite element modeling are assessed in [19, 3, 132, 16]. In particular, automatic mesh adaptation, as proposed in [19], is of interest considering modeling of the total fluid-structure interaction involving varying geometrical configurations in space and time. Other studies propose large eddy simulation (LES) of flow in simplified human airways [78, 59, 122, 22, 21]. Nevertheless, the computational load of accurate three-dimensional modeling, requiring a large amount of mesh points, should not be underestimated and seems at current date out of reach for clinical applications [69].

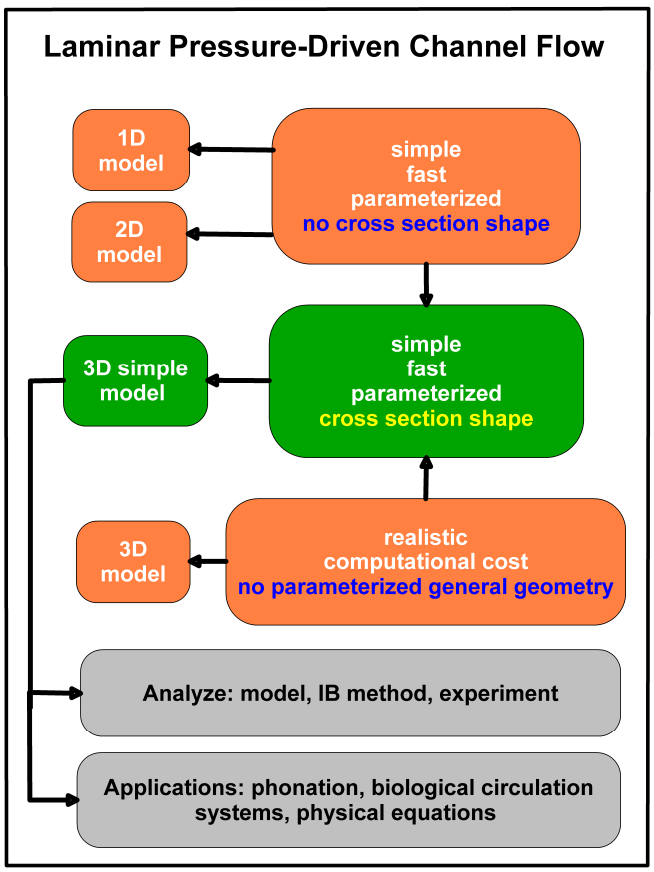

Figure 1.5: Overview of the thesis objectives.

1.2 Objectives and outline of the thesis

The aim of the current work is to assess the potential impact of a simple 'quasi-three-dimensional' flow model – with low computational cost and which takes into account kinetic losses, viscosity as well as the cross section shape – on the flow outcome. The flow model outcome is analyzed with respect to the outcome of quasi-one-dimensional and two-dimensional flow model, a three-dimensional flow model as well as experimental flow data. The proposed model with low computational cost, is applied to phonation, biological circulation systems and physical equations. An overview of the thesis objectives is presented in Fig. 1.5.

In the following chapter, Chap. 2, we consider pressure-driven viscous flow through uniform channels with different, but constant cross section shape. We extend results for classical cross section shapes to an arbitrary cross section shape for which the solution is obtained either numerically using a pseudo-spectral approach or quasi-analytically.

Next, in Chap. 3, we exploit the proposed parametrization of an arbitrary cross section

shape following the 'superformula' to physical equations such as the wave equation for two-dimensional and three-dimensional geometries.

In Chap. 4, we integrate the cross section shape in a flow model which can be applied to pressure-driven flow through a constricted channel with different cross section shape. The flow model is used to estimate the influence of the cross section shape on a major phonation parameter, *i.e.* the minimum phonation threshold pressure required to sustain vocal folds auto-oscillation.

In order to assess the influence of the cross section shape of a constriction on the flow, experimental and numerical data are gathered as reported in Chap. 5 and 6, respectively. Besides the effect of the cross section shape on the flow, the influence of flow conditions upstream from the constriction are experimentally assessed. Numerical data are simulated using the Immersed Boundary (IB) method. In the current work the structure is fixed to match the experimental and model geometry so that the accuracy of the flow model can be evaluated. Notice that the Immersed Boundary method is suitable to capture the fluid-structure interaction, which is of particular interest for the aimed biological applications. A comparison is made between modeled, experimental and numerical data.

Finally, conclusions with respect to the influence of the cross section shape on the flow and the ability of the different model approaches to capture its effect are presented in Chap. 7.

Chapter 2

Developed laminar viscous flow through uniform channels

Contents

In the current chapter we present quasi-analytical solutions for developed pressure-driven laminar viscous flow through uniform channels of different, but constant cross section shape. Fig. 2.1 illustrates the main geometrical characteristics for a channel of length L oriented in the streamwise x direction with its entry at $x = x_0$ and a constant arbitrary cross section with area A, perimeter P_m and hydraulic diameter D defined as $D = 4A/P_m$. At first, a quasi-analytical solution for a limited number of cross section shapes is presented. Next, a general quasi-analytical solution for an arbitrary cross section shape is proposed and the solution is compared to a numerical solution obtained using a pseudo-spectral approach.

2.1 Poisson equation in polar and Cartesian coordinates

We consider the Navier-Stokes equation

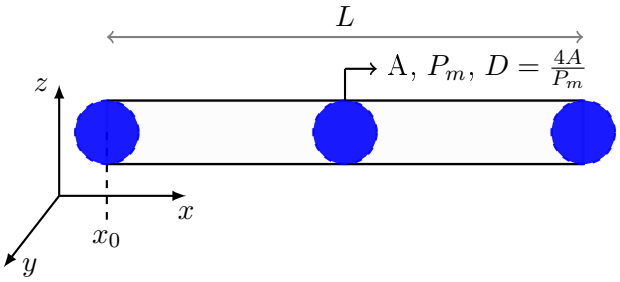

Figure 2.1: Illustration of a uniform channel geometry of length L with arbitrary but constant cross section shape of area A, perimeter P_m and hydraulic diameter D. The channel is oriented along the streamwise direction x and the streamwise channel onset coordinate is denoted x_0. The spanwise direction y and transverse direction z are indicated.

$$\rho\left(\frac{\partial \mathbf{u}}{\partial t} + (\mathbf{u}\cdot\nabla)\mathbf{u}\right) = -\nabla P + \nabla\cdot\mathbf{T} + \mathbf{f}, \tag{2.1}$$

where $\mathbf{u} = (u, v, w)$ is the flow velocity, ρ is the fluid density, P is the pressure, $\mathbf{T}$ is the (deviatoric) component of the total stress tensor, and $\mathbf{f}$ represents body forces (per unit volume) acting on the fluid and ∇ is the *del* operator.

Next, we consider conservation of mass expressed by the continuity equation

$$\frac{\partial \rho}{\partial t} + \nabla\cdot\rho\mathbf{u} = 0. \tag{2.2}$$

If the flow is assumed to be incompressible with constant density ρ, then the continuity equation simplifies to $\nabla\cdot\mathbf{u} = 0$. Taking the incompressible flow assumption into account and assuming constant dynamic viscosity μ, the Navier-Stokes equation (2.1) will read, in vector form:

$$\rho\left(\frac{\partial \mathbf{u}}{\partial t} + (\mathbf{u}\cdot\nabla)\mathbf{u}\right) = -\nabla P + \mu\Delta\mathbf{u} + \mathbf{f}. \tag{2.3}$$

Now let us consider a straight duct of arbitrary but constant cross section shape of sufficient length to obtain fully developed laminar channel flow. Ref. ([126]) shows that, regardless of the cross section shape, the minimum channel length, entry length L_f, for laminar flow is given as,

$$L_f \approx (0.05Re + 0.5)D, \tag{2.4}$$

where D denotes the hydraulic diameter and Re denotes the flow's Reynolds number based on D[1]. Fig. 2.2 illustrates the relationship between entry length L_f and hydraulic diameter D for typical range Reynolds number, $Re \leq 0(10^3)$, mentioned in the introduction.

[1] so $Re = \frac{QD}{A\nu}$ with volume flow rate Q, hydraulic diameter D, area A and kinematic viscosity of the fluid

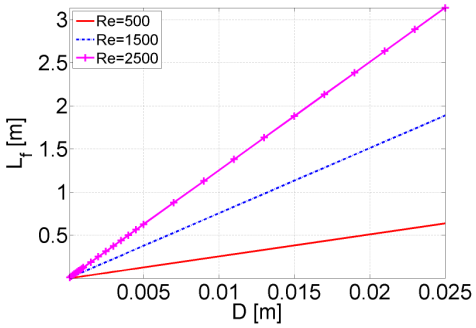

Figure 2.2: Illustration of the relationship between entry length L_f and hydraulic diameter D for different Reynolds numbers. The hydraulic diameter range and the Reynolds number range is relevant for the aimed biological flow applications mentioned in Fig. 1.5.

When the streamwise coordinate $x > L_f$ (or $L > L_f$ with $x_0 = 0$), the velocity becomes purely axial and varies only with the lateral coordinate, thus $v = w = 0$ and $u = u(y, z)$. The flow is then called fully developed. For fully developed pressure-driven flow through a uniform channel with arbitrary but constant cross section shape, and under the assumptions of laminar, incompressible, parallel and steady viscous flow, the streamwise component of the momentum equation expressed in Cartesian coordinates (x, y, z) reduces to the following Poisson equation [9, 126][2]

$$\frac{1}{\mu}\frac{dP}{dx} = \frac{\partial^2 u}{\partial y^2} + \frac{\partial^2 u}{\partial z^2}, \tag{2.5}$$

with driving pressure gradient dP/dx, velocity $u(y, z)$ and dynamic viscosity μ. The spanwise and transverse components of the momentum equation become,

$$\frac{\partial P}{\partial y} = 0, \quad \frac{\partial P}{\partial z} = 0, \tag{2.6}$$

and the continuity equation yields,

$$\frac{\partial u}{\partial x} = 0. \tag{2.7}$$

In cylindrical coordinates (r, θ, x), and under the same assumptions, the Poisson equation (2.5) becomes

ν. Unless mentioned differently, we present results using air as a fluid with density $\rho = 1.2\text{kg/m}^3$, dynamic viscosity $\mu = 1.8 \times 10^{-5}$ Pa·s and kinematic viscosity $\nu = 1.5 \times 10^{-5}\text{m}^2/\text{s}$.

[2]The gravitational force is neglected.

$$\frac{1}{\mu}\frac{dP}{dx} = \frac{1}{r}\frac{\partial}{\partial r}\left(r\frac{\partial u}{\partial r}\right) + \frac{1}{r^2}\frac{\partial^2 u}{\partial \theta^2}, \tag{2.8}$$

while the spanwise and transverse components of the momentum equation become,

$$\frac{\partial P}{\partial r} = 0, \quad \frac{\partial P}{\partial \theta} = 0, \tag{2.9}$$

and the continuity equation is still the one given in (2.7).

For uniform geometries and applying the no slip boundary condition $u = 0$ on the channel walls, (2.5) can be rewritten as a classical Dirichlet problem which can be solved analytically for simple geometries using *e.g.* separation of variables or conformal mapping [86, 11, 106, 48, 66]. Therefore exact solutions can be obtained for: local velocity $u(y, z)$, local pressure $P(x)$, wall shear stress $\tau(x)$ and derived quantities such as volume flow rate Q and bulk Reynolds number $Re = \frac{QD}{\nu A}$ again based on hydraulic diameter D. The local pressure $P(x)$ can be obtained by integrating (2.5) or (2.8). The wall shear stress is defined as $\tau = \pm\mu\frac{\partial u}{\partial y}|_w$ or $\pm\mu\frac{\partial u}{\partial z}|_w$ in plane coordinates and $\tau = \pm\mu\frac{\partial u}{\partial r}|_w$ in cylindrical coordinates, in which the symbol depend on the positive normal direction of the boundary.

In the following quasi-analytical solutions are given for some cross section shapes defined by geometrical parameters, denoted (a, b), of which some are validated on expressions reported in literature [95, 126, 81, 101, 49, 11]. Analytical solutions of the volume flow rate can be described in general by an expression of the form,

$$Q = \beta_q(a, b)\frac{1}{\mu}\left(-\frac{dp}{dx}\right), \tag{2.10}$$

for which β_q depends on the cross section shape parameters (a, b). Consequently, the resulting volume flow rate is proportional to the ratio of the driving pressure gradient dP/dx to the dynamic viscosity μ. Expression (2.10) also holds in the case of a quasi-one dimensional flow model approach [25] for which the viscous contribution to the pressure drop is accounted for by a Poiseuille term under the assumption of a rectangular cross section with fixed width w and height h.

It is seen that besides the volume flow rate Q also the velocity distribution $u(y, z)$ is proportional to the ratio of the driving pressure gradient dP/dx and the dynamic viscosity μ so that the following holds using (2.10),

$$u = \beta_u(a, b)\frac{1}{\mu}\left(-\frac{dp}{dx}\right) \quad \text{or} \quad u = Q\frac{\beta_u(a, b)}{\beta_q(a, b)}, \tag{2.11}$$

in which $\beta_u(a, b)$ expresses the influence of the cross section shape on the velocity distribution.

The wall shear stress

$$\tau = \beta_t(a,b)\left(\frac{dp}{dx}\right), \tag{2.12}$$

depends on the driving pressure gradient dP/dx and the cross section shape $\beta_t(a,b)$.

From expression (2.10), it follows that the viscous contribution to the pressure drop is

$$\Delta P_{visc}(x) = -\mu Q \int_{x_0}^{x} \frac{dx}{\beta_q(a,b)},, \tag{2.13}$$

with x_0 denotes the channel onset and $x > x_0$. Consequently, ΔP_{visc} varies linearly with volume flow rate Q and dynamic viscosity μ and is reversed proportional to the cross section shape factor β_q. In the following section, expressions for β_q, β_u and β_t are derived quasi-analytically for some particular cross section shapes.

2.1.1 Quasi-analytical solutions for particular cross section shapes

The uniform channel geometry is fully defined by the cross section shape. In order to use the cross section shape in quasi-analytical models only shapes for which the geometry can be expressed analytically using one or two geometrical parameters (a,b) are assessed: circle (cl), rectangle (re), ellipse (el), eccentric annulus (ea), concentric annulus (ca), half moon (hm), circular sector (cs), equilateral triangle (tr) and limacon (lm). Different cross section shapes and associated geometrical parameters are illustrated in Fig. 2.3.

The chosen shapes have, although a severe idealization, some relevance to describe the channel cross section shape in the case of normal as well as pathological geometrical conditions of the human respiratory and cardiovascular systems. The circular, rectangular and elliptical cross section shapes are idealized shapes assuming a perfect symmetry of the channel or the constricted portion with respect to the spanwise y and transverse z directions. The eccentric annulus, half moon and limacon are crude approximations to an asymmetrical shape due to *e.g.* the presence of a polyp, a tumor, an asymmetrical stenosis or a vocal tract during articulation. The circular sector and the equilateral triangle are approximations of asymmetrical cross section shapes occurring *e.g.* at the glottis during normal respiration. Comparison between different shapes is done by imposing either area A or hydraulic diameter D. Cross section shapes which are defined using two instead of one geometrical parameter require an addition condition for a geometrical quantity. Expressions for area A, hydraulic diameter D, total width y_{tot} and perimeter P_m as a function of geometrical parameters (a,b) for the shapes shown in Fig. 2.3 are given in Table 2.1.

Quasi-analytical solutions for the cross section shapes shown in Fig. 2.3 are obtained as

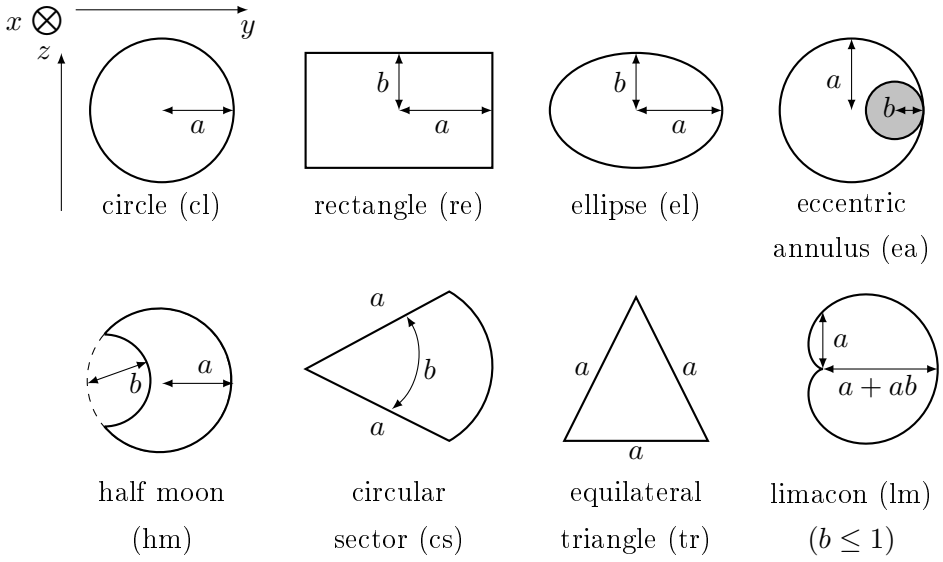

Figure 2.3: cross section shapes with parameters (a, b) in the (y, z) plane. Note that for a circular sector, b indicates an angle. As in Fig. 2.1, x denotes the streamwise, y the spanwise and z the transverse direction.

detailed in Appendix A. From the obtained solutions for the volume flow rate Q, velocity profile u and wall shear stress τ the terms depending on the cross section shapes are defined. The term $\beta_q(a, b)$ needed to quantify the volume flow rate (2.10) is provided in Table 2.2. The term $\beta_u(a, b)$ of (2.11) describing velocity distribution $u(y, z)$ for different cross section shapes is given in Table 2.3. Table 2.4 lists the corresponding term $\beta_t(a, b)$ needed to quantify the wall shear stress.

In the following the influence of the cross section shape on the model outcome is assessed for developed laminar viscous flow through a uniform channel. The comparison between different cross section shapes is assessed by imposing either area A or hydraulic diameter D. As mentioned the circle and equilateral triangle cross section shapes are fully described by one parameter, a_{cl} and a_{tr}, whose value follows immediately from the imposed A or D. For the remaining cross section shapes, an additional condition is necessary in order to obtain the geometrical parameter set $\{a, b\}$ illustrated in Fig. 2.3. Two different types of additional conditions are considered. Firstly, an explicit condition requiring a parameter α_{shape} is introduced scaling the cross section shape as: $a_{re} = \alpha_{re} a_{cl}$, $a_{el} = \alpha_{el} a_{cl}$, $b_{ea} = \alpha_{ea} a_{ea}$, $b_{cs} = \alpha_{cs}$, $b_{hm} = \alpha_{hm} a_{hm}$ and $b_{lm} = \alpha_{lm}$. Secondly, the required additional condition is obtained by imposing, besides area A or hydraulic diameter D, a fixed width w in the spanwise direction, *i.e.* $y_{tot} = w$. The relationship between the geometrical parameters and quantities was given in Table 2.1. The influence of the cross section shape on the quasi-analytical velocity distribution is considered by quantifying the velocity distribution as presented in the next section 2.1.2.

Table 2.1: Geometrical quantities for different shapes as a function of the cross section parameters (a, b) defined in Fig. 2.3 [12].

shape	A	D	y_{tot}	P_m
circle	πa^2	$2a$	$2a$	$2\pi a$
ellipse(1,3)	πab	$\frac{4ab}{(a+b)\left(1+\frac{h}{4}+\frac{h^2}{64}+\frac{h^3}{256}\right)}$	$2a$	$4aE\left(\sqrt{1-(\frac{b}{a})^2}\right)$
rectangle	$4ab$	$\frac{4ab}{a+b}$	$2a$	$4(a+b)$
equilateral triangle	$\frac{\sqrt{3}}{4}a^2$	$\frac{\sqrt{3}}{3}a$	$\frac{\sqrt{3}}{2}a$	$3a$
circular sector	$\frac{a^2}{2}b$	$\frac{2ab}{2+b}$	a	$a\,(2+b)$
eccentric annulus	$\pi(a^2-b^2)$	$2(a-b)$	$2(a-b)$	$2\pi\,(a+b)$
concentric annulus				
half moon(2)	$a^2\left(\pi-\theta_2+\frac{1}{2}\sin(2\theta_2)\right)$ $-\frac{b^2}{2}(\pi-\theta_2-\sin\theta_2)$	$\frac{4A}{(\pi-\theta_2)(2a+b)}$	$a+a\cos(\theta_2)$	$(\pi-\theta_2)\,(2a+b)$
limacon	$\pi a^2\left(1+\frac{b^2}{2}\right)$	$4a\frac{b^2+2}{b^2+4}$	$a(1+b)$ $+\left(\frac{1}{4b^2}-\frac{a}{2b}\right)$	$\frac{a\pi}{2}\left(b^2+4\right)$

(1) $h=\frac{(a-b)^2}{(a+b)^2}$.

(2) $\theta_2=2\arcsin\left(\frac{b}{2a}\right)$.

(3) $E(x)=\int_0^{\frac{\pi}{2}}\sqrt{1-x^2sin^2t}dt$ is the complete elliptic integral of the second kind.

2.1.2 Quasi-analytical velocity distribution

The ratio of maximum velocity u_{max} and maximum velocity for a circular cross section shape u^{cl}_{max} is assessed for an imposed area[3] $A = 79$ mm^2 in order to estimate the influence of the cross section shape. The ratio u_{max}/u^{cl}_{max} is constant for a circle (=1) and equilateral triangle (=0.8) since these shapes are fully determined by the imposed area and hence do not

[3]The imposed area $A = 79$ mm^2 corresponds to a circle with radius 5mm, *i.e.* $a_{cl} = 5$mm, which is relevant to human airways and other biological circulation systems.

Table 2.2: $\beta_q(a,b)$ of (2.10) for volume flow rate Q [95, 126, 101, 11].

Shape	$\beta_q(a,b)$
circle	$\frac{\pi a^4}{8}$
ellipse	$\frac{\pi}{4}\frac{a^3b^3}{a^2+b^2}$
rectangle[1]	$\frac{4a^3}{3}\left[b-\frac{192a}{\pi^5}\sum_{n=1,3,\ldots}^{\infty}\frac{\tanh(n\pi b/2a)}{n^5}\right]$
equilateral triangle	$\frac{\sqrt{3}a^4}{320}$
circular sector[1]	$\frac{a^4}{4}\left[\frac{\tan b-b}{4}-\frac{32b^4}{\pi^5}\sum_{n=1,3\ldots}^{\infty}\frac{1}{n^2(n+2b/\pi)^2(n-2b/\pi)}\right]$
eccentric annulus[1,2]	$\frac{\pi}{8}\left[a^4-b^4-\frac{4c^2M^2}{\beta-\gamma}-8c^2M^2\sum_{n=1}^{\infty}\frac{ne^{-n(\beta+\gamma)}}{\sinh(n\beta-n\gamma)}\right]$ $0<c\le a-b,\ F=\frac{a^2-b^2+c^2}{2c}$ $M=\sqrt{F^2-a^2}$ $\gamma=\frac{1}{2}\ln\frac{F+M}{F-M},\ \beta=\frac{1}{2}\ln\frac{F-c+M}{F-c-M}$
concentric annulus	$\frac{\pi}{8}\left[a^4-b^4-\frac{(a^2-b^2)^2}{ln\frac{a}{b}}\right]$
half moon	$\frac{1}{4}\left[(2a^3b+\frac{21}{12}ab^3)\sin(\theta_1)+(a^4-\frac{b^4}{2}-2a^2b^2)\theta_1\right]$ $\theta_1=\arccos(b/2a)$
limacon	$\frac{\pi}{8}a^4\left(1+4b^2-2b^4\right)$
Poiseuille[3]	$\frac{wh^3}{12}$

[1] infinite sum is limited to $n \le 60$.

[2] c yields the distance between inner and outer circle centers.

[3] quasi-one-dimensional approach: height h and fixed width w.

depend on the parameter α. For all other cross section shapes, the choice of the parameter α does influence to some extent the velocity distribution as shown in Fig. 2.4 by considering u_{max}/u^{cl}_{max} as a function of α.

It is seen from Fig. 2.4a that varying the cross section shape by increasing α from 0 (corresponding to a circle) to 0.95 reduces the maximum velocity with 40% for a half moon

Table 2.3: $\beta_u(a,b)$ of (2.11) for velocity distribution u [95, 126, 101, 81, 11] .

Shape	$\beta_u(a,b)$
circle	$\frac{1}{4}(a^2-r^2)$
ellipse	$\frac{1}{2}\frac{a^2b^2}{a^2+b^2}(1-\frac{y^2}{a^2}-\frac{z^2}{b^2})$
rectangle[1]	$\frac{1}{2}\left[b^2-z^2-\frac{32b^2}{\pi^3}\sum_{n=1,3,\ldots}^{\infty}(-1)^{\frac{n-1}{2}}\frac{\cosh(\frac{n\pi y}{2b})}{\cosh(\frac{n\pi a}{2b})}\frac{\cos(\frac{n\pi z}{2b})}{n^3}\right]$
equilateral triangle	$\frac{1}{4\sqrt{3}}\frac{1}{a}(3y^2-z^2)(2z-\sqrt{3}a)$
circular sector[1]	$-\frac{1}{4}[r^2\left(1-\frac{\cos 2\theta}{\cos b}\right)-\frac{16a^2b^2}{\pi^3}\sum_{n=1,3\ldots}^{\infty}(-1)^{\frac{n+1}{2}}\left(\frac{r}{a}\right)^{\frac{n\pi}{b}}\frac{\cos(n\pi\theta/b)}{n(n+2b/\pi)(n-2b/\pi)}]$
eccentric annulus (1,2,3)	$M^2\left[\sum_{n=1}^{\infty}(-1)^n\frac{e^{-n\beta}\coth\beta\sinh(n(\eta-\gamma))-e^{-n\gamma}\coth\gamma\sinh(n(\eta-\beta))}{\sinh(n(\beta-\gamma))}\right.$ $\left.\cdot\cos(n\xi)+\frac{\coth\gamma-\coth\beta}{2(\gamma-\beta)}\eta+\frac{\beta(1-2\coth\gamma)-\gamma(1-2\coth\beta)}{4(\gamma-\beta)}-\frac{\cosh\eta-\cos\xi}{4(\cosh\eta+\cos\xi)}\right]$ $0<c\le a-b,\ F=\frac{a^2-b^2+c^2}{2c},\ M=\sqrt{F^2-a^2}$ $\gamma=\frac{1}{2}\ln\frac{F+M}{F-M},\ \beta=\frac{1}{2}\ln\frac{F-c+M}{F-c-M}$
concentric annulus	$\frac{1}{4}\left[a^2-r^2+(a^2-b^2)\frac{\ln(a/r)}{\ln(b/a)}\right]$
half moon	$\frac{1}{4}\left(r^2-b^2\right)\left(\frac{2a\cos\theta}{r}-1\right)$
limacon[4]	$\frac{a^2}{4}\left[1+2b\xi+b^2-(\xi+b(\xi^2-\eta^2))^2-(\eta+2b\xi\eta)^2\right]$
Poiseuille[5]	$-\frac{1}{2}(y^2-hy)$

[1] infinite sum is limited to $n\le 60$.

[2] c yields the distance between inner and outer circle centers.

[3] the mapping is $y+iz=M\tanh\frac{1}{2}(\xi+i\eta)$ with $0\le\xi\le 2\pi$, $\gamma\le\eta\le\beta$.

[4] the mapping is $(y,z)=(a(\xi+b(\xi^2-\eta^2)),\ a(\eta+2b\xi\eta))$ on the circle $(\xi^2+\eta^2)\le 1$.

[5] quasi-one-dimensional approach: height h, $0\le y\le h$.

and with 5% for a limacon cross section shape. Fig. 2.4b shows that varying the cross section shape by increasing α from $\sqrt{\pi/4}$ (corresponding to a square) for a rectangular and from 1 (corresponding to a circle) for an ellipse to 12 reduces the maximum velocity with 99%. Fig. 2.4c illustatrates that for a circular sector increasing the angle b decreases the influence of

Table 2.4: $\beta_t(a,b)$ of (2.12) for wall shear stress τ [49, 11].

Shape	$\beta_t(a,b)$
circle	$\frac{a}{2}, (r=a)$
ellipse	$-\frac{a^2b^2}{a^2+b^2}\sqrt{\frac{y^2}{a^4}+\frac{z^2}{b^4}}, (\frac{y^2}{a^2}+\frac{z^2}{b^2}=1)$
rectangle[1]	$\frac{8a}{\pi^2}\sum_{n=1,3,\ldots}^{\infty}\frac{(-1)^{\frac{n-1}{2}}}{i^2}\left[1-\frac{\cosh(\frac{n\pi z}{2a})}{\cosh(\frac{n\pi b}{2a})}\right], (y=\pm a)$ $\frac{8a}{\pi^2}\sum_{i=1,3,\ldots}^{\infty}(-1)^{\frac{n-1}{2}}\tanh(\frac{n\pi b}{2a})\frac{\cos(\frac{n\pi y}{2a})}{n^2}, (z=\pm b)$
equilateral triangle	$-\frac{1}{a}z(z-\frac{\sqrt{3}}{2}a), (y=\pm\frac{\sqrt{3}}{3}z)$ $\frac{\sqrt{3}}{2a}(y^2-\frac{a^2}{4}), (z=\frac{\sqrt{3}a}{2})$
circular sector[1]	$-\left[\frac{r^2}{4}(1+2\tan\alpha)+\frac{4a^2\alpha}{\pi^2}\sum_{n=1,3\ldots}^{\infty}\frac{(\frac{r}{a})^{\frac{n\pi}{\alpha}}}{(n+\frac{2\alpha}{\pi})(n-\frac{2\alpha}{\pi})}\right], (\theta=\pm\frac{\alpha}{2})$ $-\frac{a}{2}\left[(1-\frac{\cos 2\theta}{\cos\alpha})-\frac{8\alpha}{\pi^2}\sum_{n=1,3\ldots}^{\infty}(-1)^{\frac{n+1}{2}}\frac{\cos(n\pi\theta/\alpha)}{(n+\frac{2\alpha}{\pi})(n-\frac{2\alpha}{\pi})}\right], (r=a)$
eccentric annulus [1,2,3]	$-M^2\left[\sum_{n=1}^{\infty}(-1)^n\frac{e^{-n\beta}\coth\beta\cosh(n(\eta-\gamma))-e^{-n\gamma}\coth\gamma\cosh(n(\eta-\beta))}{\sinh(n(\beta-\gamma))}\right.$ $\left.\cdot n\cos(n\xi)+\frac{\coth\gamma-\coth\beta}{2(\gamma-\beta)}-\frac{\sinh\eta\cos\xi}{2(\cosh\eta+\cos\xi)^2}\right], (\eta=\gamma,\beta)$ $0<c\le a-b,\ F=\frac{a^2-b^2+c^2}{2c}, M=\sqrt{F^2-a^2}$ $\gamma=\frac{1}{2}\ln\frac{F+M}{F-M},\ \beta=\frac{1}{2}\ln\frac{F-c+M}{F-c-M}$
concentric annulus	$\frac{1}{4}\left[2b+\frac{a^2-b^2}{b\ln(b/a)}\right], (r=b)$ $-\frac{1}{4}\left[2a+\frac{a^2-b^2}{a\ln(b/a)}\right], (r=a)$
half moon	$\frac{1}{4}(4a\cos\theta-2b), (r=b)$ $-\frac{1}{4}(\frac{b^2}{2a\cos\theta}-2a\cos\theta), (r=2a\cos\theta)$
limacon	$-\frac{a^2}{2}(1+2b\cos\theta+2b^2)\cos\theta, (0\le\theta\le 2\pi)$
Poiseuille[4]	$y-\frac{h}{2}, (y=0,h)$

[1] infinite sum is limited to $n \le 60$.

[2] c yields the distance between inner and outer circle centers.

[3] the mapping is $y+iz = M\tanh\frac{1}{2}(\xi+i\eta)$ with $0\le\xi\le 2\pi$, $\gamma\le\eta\le\beta$.

[4] quasi-one-dimensional approach: height h, $0\le y\le h$.

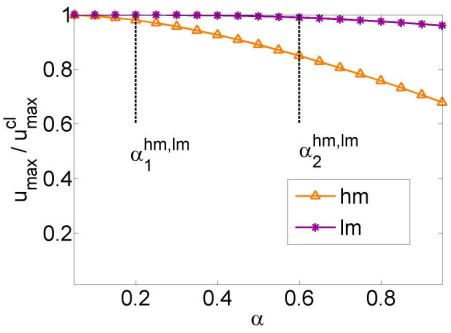

(a) half moon 'hm' and limacon 'lm'

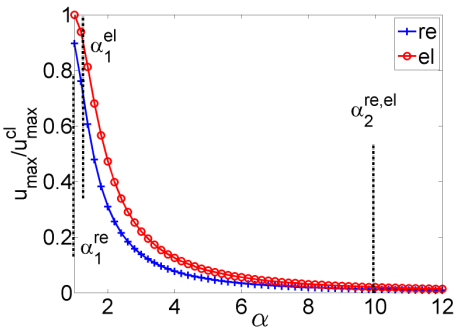

(b) rectangle 're' and ellipse 'el'

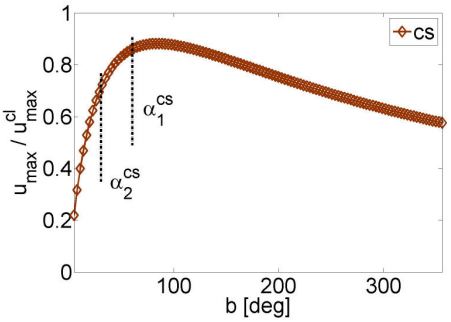

(c) circular sector 'cs'

Figure 2.4: Illustration of the influence of geometrical parameter α on normalized maximum velocity, u_{max}/u^{cl}_{max}, for different cross section shapes and imposed area $A = 79\,\mathrm{mm}^2$. Vertical lines indicate values corresponding to default parameter set (α_1) and non-default parameter set (α_2) for which $u_{max}/u^{cl}_{max} \approx 1$ and $u_{max}/u^{cl}_{max} \ll 1$, respectively.

viscosity at first until $b \simeq 85^o$. Further increasing the angle enforces the influence of viscosity, so that the ratio U_{max}/U^{cl}_{max} decreases. Actually, this general tendency reflects the variation of the hydraulic diameter D as a function of angle b. Since the minimum effect of viscosity near $b \simeq 85^o$ corresponds to a minimum perimeter P_m and hence a maximum hydraulic diameter D (since the area A is fixed and $D = \frac{4A}{P_m}$) which is illustrated in Fig. 2.5. Consequently, Fig. 2.4 shows that for a constant area A and cross section shape, the scaling parameter α influences the effect of viscosity on the flow development since the variation of the ratio u_{max}/u^{cl}_{max} with α is significant for all assessed cross section shapes.

In order to evaluate the impact of the cross section shape in more detail, two sets of parameters α are selected, default parameter set (α_1) and non-default parameter set (α_2), resulting in $u_{max}/u^{cl}_{max} \approx 1$ and $u_{max}/u^{cl}_{max} \ll 1$, respectively. Default parameter set (α_1) is defined as: $a_{re} = 1a_{cl}$, $a_{el} = 1.2a_{cl}$, $b_{ea} = 0.2a_{ea}$, $b_{cs} = \pi/3$, $b_{hm} = 0.2a_{hm}$ and $b_{lm} = 0.2$. Non-default parameter set (α_2) yields: $a_{re} = 10a_{cl}$, $a_{el} = 10a_{cl}$, $b_{ea} = 0.6a_{ea}$, $b_{cs} = \pi/6$, $b_{hm} = 0.6a_{hm}$ and $b_{lm} = 0.6$. Both parameter sets are indicated in Fig. 2.4.

Three different cross section shapes are obtained by imposing area A=79mm^2 together

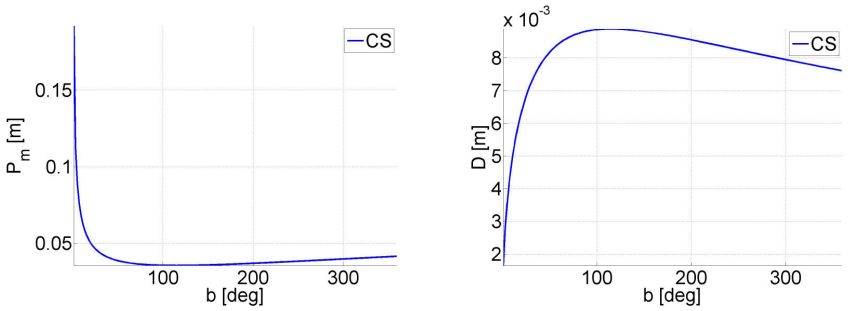

(a) perimeter, $P_m(b)$ (b) hydraulic diameter, $D(b)$

Figure 2.5: Circular sector (cs) of fixed area and varying angle b: a) perimeter $P_m(b)$ and b) hydraulic diameter $D(b)$.

with one of the following conditions:

- default parameter set (α_1),
- non-default parameter set (α_2),
- fixed spanwise width w, *i.e.* $y_{tot} = w$.

The resulting velocity distribution $u(y/a_{cl}, z/a_{cl})$ for a uniform channel with imposed area $A = 79$ mm^2 and pressure gradient $dP/dx = 75$ Pa is further illustrated in Fig. 2.6 for default parameter set (α_1) and in Fig. 2.7 for non-default parameter set (α_2) and fixed spanwise width ($y_{tot} = w$).

From Fig. 2.6, obtained using default parameter set (α_1), it is seen that in accordance with Fig. 2.4 the maximum velocity for all cross section shapes varies between values observed for a circular and an equilateral triangle cross section shape so that the maximum velocity reduction compared to a circular cross section yields 20%. From Fig. 2.7 is seen that using non-default parameter set (α_2) or imposing a fixed width (w) reduces the velocity more (20% up to 98%).

The influence of the cross section shape on the maximum velocity is further quantified in Fig. 2.8 by imposing either area $A = 79$ mm^2 or the corresponding hydraulic diameter $D = 10$ mm in combination with default parameter set (α_1), non-default parameter set (α_2) or fixed width ($w = 20$mm).

Fig. 2.8a shows the maximum velocity normalized with respect to the maximum velocity of a rectangular cross section shape [4]. As before, the variation from u^{re}_{max} for default parameter set (α_1) is small yielding less than 5% when imposing A and less than 15% when imposing D.

[4]The rectangular cross section shape is taken as a reference since the shape is related to the quasi-one-

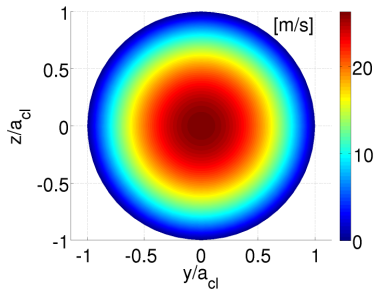

(a) circle

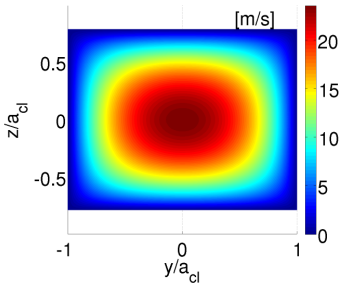

(b) rectangle

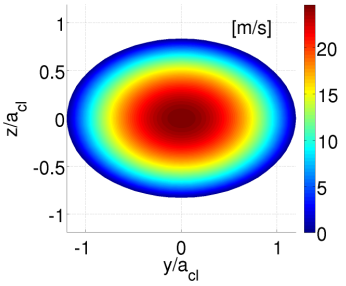

(c) ellipse

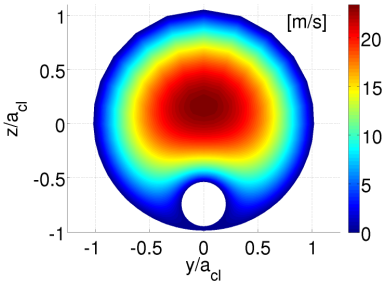

(d) eccentric annulus

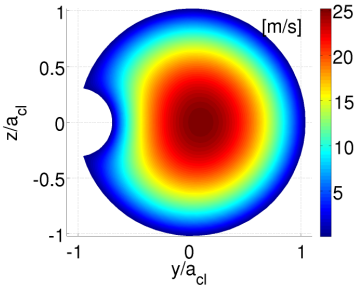

(e) half moon

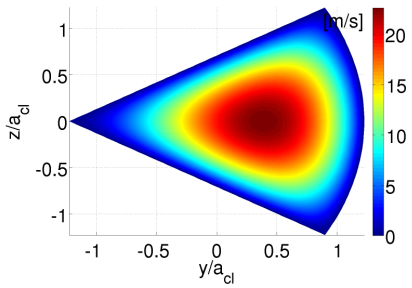

(f) circular sector

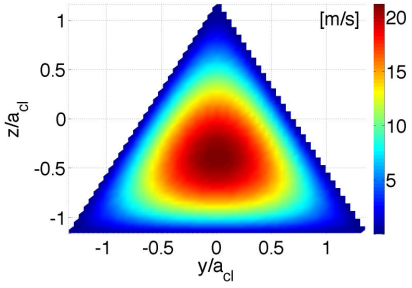

(g) equilateral triangle

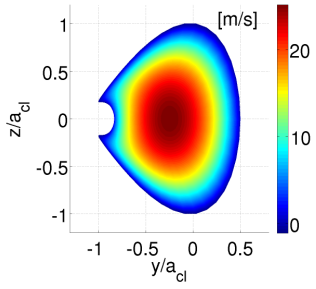

(h) limacon

Figure 2.6: Velocity distribution $u(y/a_{cl}, z/a_{cl})$ for $A = 79$ mm^2 and $dP/dx = 75$ Pa/m for airflow and geometrical default parameter set (α_1) while $a_{cl} = 5$mm.

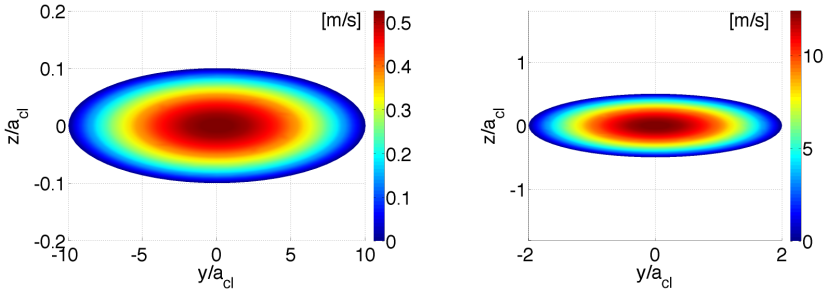

(a) ellipse

(b) ellipse

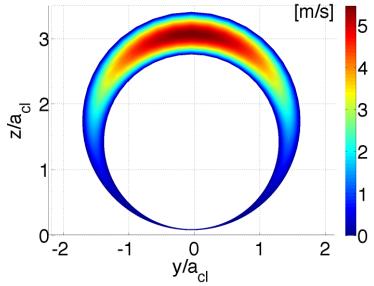

(c) eccentric annulus

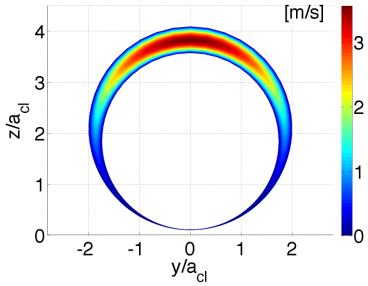

(d) eccentric annulus

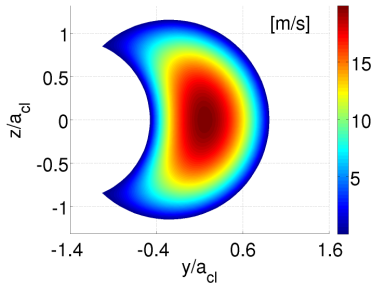

(e) half moon

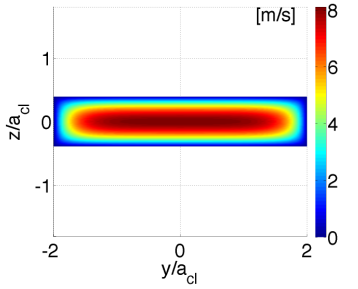

(f) rectangle

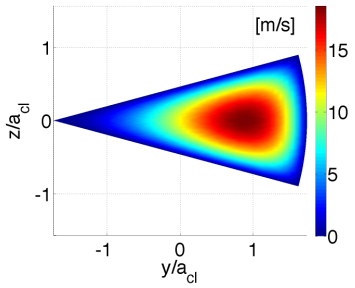

(g) circular sector

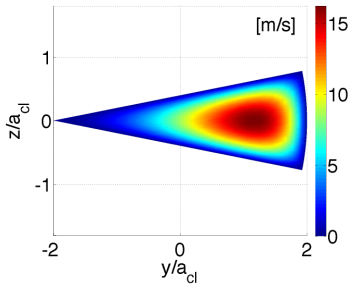

(h) circular sector

Figure 2.7: Velocity distribution $u(y/a_{cl}, z/a_{cl})$ for $A = 79$ mm^2 and $dP/dx = 75$ Pa/m for airflow: left) geometrical non-default parameter set (α_2) and right) fixed width (w) with $w = 4 \times a_{cl}$ while $a_{cl} = 5$mm.

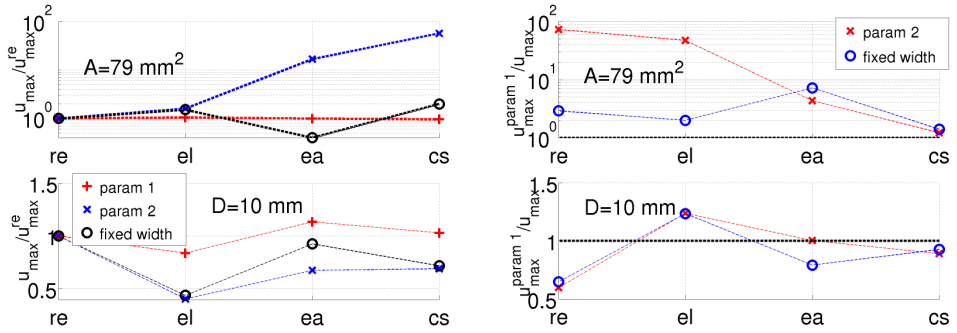

(a) cfr. rectangular cross section (b) cfr. set α_1

Figure 2.8: Illustration of influence of cross section shapes (re: rectangle, el: ellipse, ea: eccentric annulus, cs: circular sector) obtained from imposing different conditions (default parameter set (α_1), non-default parameter set (α_2) and fixed width ($w = 20$mm)) for imposed area $A = 79\text{mm}^2$ or hydraulic diameter $D = 10$mm on the maximum velocity: a) with respect to maximum velocities associated with a rectangular cross section and b) with respect to maximum velocities associated with default parameter set. The dashed line corresponds to $u_{max}^{param1}/u_{max} = 1$.

For fixed area A the variation from u_{max}^{re} increases to 60% in the case of a fixed width w and to more than 300% when non-default parameter set (α_2) is used. Imposing the hydraulic diameter D instead of area A limits the velocity variation to 60% for both non-default parameter set (α_2) and fixed width (w).

Fig. 2.8b illustrates for each cross section shape the ratio of the maximum velocity of default parameter set (α_1) to the maximum velocity obtained using non-default parameter set (α_2) or a fixed width (w). The relative difference between different parameter sets is limited to 40% when the hydraulic diameter D is imposed. In the case where area A is imposed, the velocity ratio varies from 40% up to >100%.

The mean wall shear stress on the boundary of the cross section shape as a function of driving pressure gradient dP/dx is illustrated in Fig. 2.9. The normalized wall shear stress increases as driving pressure gradient dP/dx decreases or as area A decreases.

dimensional model assumption of fixed width w (two-dimensional flow is assumed to take into account the viscous contribution to the pressure drop) and is a case which occurs frequently when flow models are experimentally validated. Note that in case a fixed width w is imposed its value is set to $w = 20$mm in accordance with a common value in experimental studies.

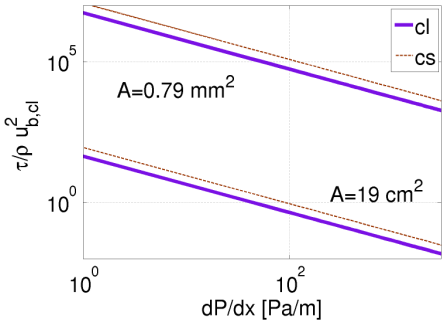

Figure 2.9: Normalized wall shear stress τ as a function of dP/dx, area A and cross section shape (circular sector with $b = 60^o$) with $u_{b,cl}$ indicating the bulk velocity in the case of a circular cross section shape.

2.2 Poisson equation in stretched coordinates

2.2.1 Arbitrary cross section shape

In[5] the previous section 2.1.1 solutions are discussed for particular cross section shapes. Nevertheless, given the variation and irregularity of cross section shapes observed for biological circulation systems, it is important to introduce a general quasi-analytical solution for a channel with an arbitrary cross section shape. In the following, we introduce a general polar equation, the so called "superformula" [39], in order to describe the boundary $\partial\Omega$ of an arbitrary shape with $0 \leq \theta \leq 2\pi$:

$$r(\theta) = g(\theta)\left[\left|\frac{\cos(\frac{m\theta}{4})}{a}\right|^{n_2} + \left|\frac{\sin(\frac{m\theta}{4})}{b}\right|^{n_3}\right]^{-1/n_1} = g(\theta)\cdot f(\theta), \quad m > 0. \tag{2.14}$$

This equation describes almost any closed curve based on the deformed circle, $f(\theta)$ with parameter set $\{m, n_1, n_2, n_3, a, b\}$[6]. The function $g(\theta)$ can be considered as a modifier factor of the function $f(\theta)$ for which parameters depend on the used function, for example, the modifier with limacon shape $g(\theta) = n_4 + n_5 cos\theta$. Fig. 2.10 illustrates some of the particular cross section shapes introduced previously in Fig 2.3. The shapes are generated using the general polar equation (2.14) with the parameters listed in Table 2.5.

Now let us consider the (x, y) plane expressed in polar coordinates (ρ, θ)

$$x = \rho\cos\theta, \quad y = \rho\sin\theta, \tag{2.15}$$

and assuming that the radius equation ρ on boundary $\partial\Omega$

[5] In this section, the symbol ρ denotes the polar radius and not the fluid density.

[6] The method to estimate these parameters from empirical data is presented in Appendix B.

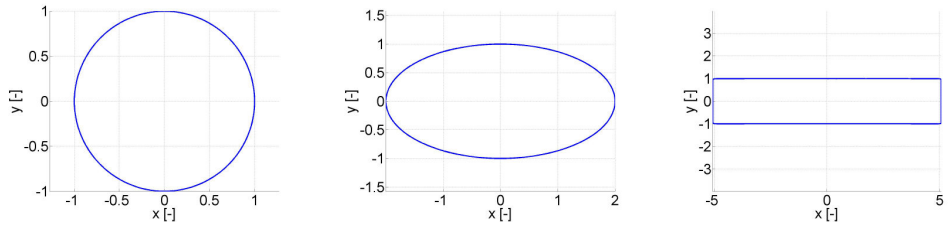

(a) circle (b) ellipse (c) rectangle

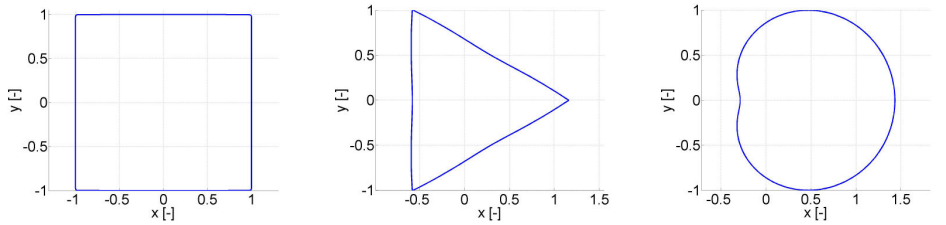

(d) square (e) equilateral triangle (f) limacon

Figure 2.10: Illustration of some cross section shapes generated using the general polar equation (2.14) with the parameters listed in Table 2.5.

Table 2.5: Overview of parameter values used in (2.14) to generate the shapes show in Fig. 2.10.

shape	m	n_1	n_2	n_3	$g(\theta)$	a, b
circle[(1)]	1	2	2	2	c	a=b
ellipse[(1)]	4	2	2	2	c	-
rectangle[(1)]	4	100	100	100	c	-
equilateral triangle[(1)]	3	0.5	1	1	c	a=b
limacon[(2)]	4	2	2	-2	$n_4 + n_5 \cos\theta$	a=b

[(1)] c is an arbitrary constant scaling the channel cross section.

[(2)] n_4, n_5 are arbitrary constants.

$$\rho = r(\theta), \quad 0 \leq \theta \leq 2\pi, \tag{2.16}$$

where $r(\theta) \in C^2[0, 2\pi]$ and suppose the radius $\rho > 0$ so that $r(\theta) > 0$ in the domain Ω.

We introduce the stretched radius ρ^* such that

$$\rho = \rho^* r(\theta), \tag{2.17}$$

and in stretched coordinates (ρ^*, θ) the plane (x, y) is given as

$$x = \rho^* r(\theta)\cos\theta, \quad y = \rho^* r(\theta)\sin\theta. \tag{2.18}$$

Therefore, using the stretched coordinates, the domain Ω is transformed to the domain $0 \leq \theta \leq 2\pi$, $0 \leq \rho^* \leq 1$.

2.2.2 The Laplace equation in stretched coordinates

Now consider a $\mathcal{C}^2$ function $u(x, y) = u(\rho\cos(\theta), \rho\sin(\theta)) = u(\rho, \theta)$ in the domain Ω and the Laplace equation in cylindrical coordinate

$$\Delta u = \frac{\partial^2 u}{\partial x^2} + \frac{\partial^2 u}{\partial y^2} = \frac{\partial^2 u}{\partial \rho^2} + \frac{1}{\rho}\frac{\partial u}{\partial \rho} + \frac{1}{\rho^2}\frac{\partial^2 u}{\partial \theta^2}. \tag{2.19}$$

Now we want to represent the general polar equation (2.8) in the new stretched coordinates system (ρ^*, θ) using

$$U(\rho^*, \theta) = u(\rho^* r(\theta)\cos(\theta), \rho^* r(\theta)\sin(\theta)) = u(\rho, \theta). \tag{2.20}$$

Substituting this transformation into the Laplace equation (2.19) one finds that

$$\begin{aligned}\Delta u = {} & \frac{1}{r^2(\theta)}\left(1 + \frac{r'^2(\theta)}{r^2(\theta)}\right)\frac{\partial^2 U}{\partial \rho^{*2}} + \frac{1}{\rho^* r^2(\theta)}\left(1 + \frac{2r'^2(\theta) - r(\theta)r''(\theta)}{r^2(\theta)}\right)\frac{\partial U}{\partial \rho^*} \\ & - \frac{2r'(\theta)}{\rho^* r^3(\theta)}\frac{\partial^2 U}{\partial \rho^* \partial \theta} + \frac{1}{\rho^{*2} r^2(\theta)}\frac{\partial^2 U}{\partial \theta^2},\end{aligned} \tag{2.21}$$

with the boundary $r(\theta) = \rho$ when $\rho^* = 1$.

For convenience, the Laplace equation (2.21) on the boundary $\partial\Omega$ is rewritten using the transformation

$$\rho = r(\theta) = \frac{1}{R(\theta)}, \ 0 \leq \theta \leq 2\pi. \tag{2.22}$$

With this transformation, the function U in stretched coordinates corresponding to u is given as

$$U(\rho^*, \theta) = u\left(\rho^* \cos(\theta)/R(\theta), \rho^* \sin(\theta)/R(\theta)\right).$$

So that the Laplace equation (2.21) becomes

$$\begin{aligned}\Delta u = &\left(R^2(\theta) + R'^2(\theta)\right)\frac{\partial^2 U}{\partial \rho^{*2}} + \frac{1}{\rho^*}\left(R^2(\theta) + R(\theta)R''(\theta)\right)\frac{\partial U}{\partial \rho^*} \\ &+ \frac{2}{\rho^*}R(\theta)R'(\theta)\frac{\partial^2 U}{\partial \rho^* \partial \theta} + \frac{R^2(\theta)}{\rho^{*2}}\frac{\partial^2 U}{\partial \theta^2}.\end{aligned} \tag{2.23}$$

Thus in stretched coordinates the Poisson equation (2.8) describing laminar viscous pressure-driven flow through a uniform channel with an arbitrary cross section shape is given as

$$\begin{aligned}\frac{1}{\mu}\frac{dP}{dx} = &\left(R^2(\theta) + R'^2(\theta)\right)\frac{\partial^2 U}{\partial \rho^{*2}} + \frac{1}{\rho^*}\left(R^2(\theta) + R(\theta)R''(\theta)\right)\frac{\partial U}{\partial \rho^*} \\ &+ \frac{2}{\rho^*}R(\theta)R'(\theta)\frac{\partial^2 U}{\partial \rho^* \partial \theta} + \frac{R^2(\theta)}{\rho^{*2}}\frac{\partial^2 U}{\partial \theta^2}.\end{aligned} \tag{2.24}$$

2.3 Numerical solution for Poisson equation

In order to solve the Poisson equation (2.5) for arbitrary cross section shapes firstly a numerical solution is considered. In the following the pseudo-spectral approach on the unit disc in polar coordinate [18, 34, 55, 62, 82, 108, 113] is outlined and numerical results are presented.

Consider the classical Poisson equation (2.5)

$$\frac{1}{\mu}\frac{dP}{dx} = \frac{\partial^2 u}{\partial y^2} + \frac{\partial^2 u}{\partial z^2}. \tag{2.25}$$

This equation can be rewritten as a classical Dirichlet problem by introducing the following dimensionless variables:

$$y^* = \frac{y}{h}, \quad z^* = \frac{z}{h}, \quad u^* = \frac{\mu u}{h^2(-dp/dx)},$$

where h denotes some characteristic duct width.

Note that the pressure gradient $\frac{dP}{dx} < 0$ is needed to hold in order to make u^* a positive quantity, $u^* > 0$. So when substituting these variables and introducing the Laplace operator Δ, the Poisson equation (2.25) becomes,

$$\Delta u^* = -1, \tag{2.26}$$

subjected to $u^* = 0$ for all points on the boundary $\partial\Omega$ of the duct cross section Ω.

Recall the Laplace equation in stretched coordinates

$$\begin{aligned}\Delta u = &\left(R^2(\theta) + R'^2(\theta)\right)\frac{\partial^2 U}{\partial \rho^{*2}} + \frac{1}{\rho^*}\left(R^2(\theta) + R(\theta)R''(\theta)\right)\frac{\partial U}{\partial \rho^*} \\ &+ \frac{2}{\rho^*}R(\theta)R'(\theta)\frac{\partial^2 U}{\partial \rho^* \partial \theta} + \frac{R^2(\theta)}{\rho^{*2}}\frac{\partial^2 U}{\partial \theta^2},\end{aligned} \tag{2.27}$$

Using (2.27) the transformed Laplace equation (2.26) can be rewritten as

$$\begin{aligned}\Delta u^* = &\left(R^2(\theta) + R'^2(\theta)\right)\frac{\partial^2 U^*}{\partial \rho^{*2}} + \frac{1}{\rho^*}\left(R^2(\theta) + R(\theta)R''(\theta)\right)\frac{\partial U^*}{\partial \rho^*} \\ &+ \frac{2}{\rho^*}R(\theta)R'(\theta)\frac{\partial^2 U^*}{\partial \rho^* \partial \theta} + \frac{R^2(\theta)}{\rho^{*2}}\frac{\partial^2 U^*}{\partial \theta^2} = -1,\end{aligned} \tag{2.28}$$

For simplicity this is rewritten in the form

$$LU^* = -1, \tag{2.29}$$

with the operator L:

$$\begin{aligned}L = &\left(R^2(\theta) + R'^2(\theta)\right)\frac{\partial^2}{\partial \rho^{*2}} + \frac{1}{\rho^*}\left(R^2(\theta) + R(\theta)R''(\theta)\right)\frac{\partial}{\partial \rho^*} \\ &+ \frac{2}{\rho^*}R(\theta)R'(\theta)\frac{\partial^2}{\partial \rho^* \partial \theta} + \frac{R^2(\theta)}{\rho^{*2}}\frac{\partial^2}{\partial \theta^2}.\end{aligned} \tag{2.30}$$

2.3.1 Pseudo-spectral method

Instead of the domain Ω used in section 2.2 with $\rho^* \in [0, 1]$ we employ the Chebyshev discretization for radius ρ^* and Fourier discretization for angle $\theta \in [0, 2\pi]$. The domain Ω is then discretized as

$$(\rho_i^*, \theta_j) = \left(\cos\left(\frac{i\pi}{N}\right), \frac{2j\pi}{M}\right), \; i = 0, ..., N, \; j = 1, ..., M, \tag{2.31}$$

with $\rho^* \in [-1, 1]$. The nodes are only dense near the boundary of the unit disc but not in the center. By choosing an odd number N for radial nodes the center of $r = 0$ is not a node

and no condition is needed to avoid a singularity at $r = 0$. The angle is chosen $\theta > 0$ with a shift of $2\pi/M$ so that overlap of nodes is avoided. The number M must be even in order to capture the angle 2π. So, we need to solve the Poisson equation on the domain $\theta \in [0, 2\pi]$ and $\rho^* \in [-1, 1]$. In the following, the spectral derivatives are given in matrix notation. First since we employ a Chebyshev expansion we obtain the following matrix

$$T = \cos\left(k\frac{i\pi}{N}\right), \ i, k = 0, ..., N. \tag{2.32}$$

Further the differentiation matrix in the Chebyshev coefficient space is explicitly given by $\widehat{D} = (d_{i,j}) \in R^{N+1,N+1}$ with

$$d_{i,j} = \begin{cases} \frac{2j}{c_i} & j = i+1, i+3, ..., N \\ 0 & others \end{cases}$$

and

$$c_i = \begin{cases} 2 & i = 0 \\ 1 & others \end{cases}$$

Now we are able to write the first and second spectral derivative matrices D_1 and D_2 which are explicitly given by

$$\begin{aligned} \widetilde{D_1} &= T\widehat{D}T^{-1} = \begin{bmatrix} E_1 & E_2 \\ 0 & 0 \end{bmatrix}, \\ \widetilde{D_2} &= T\widehat{D}^2T^{-1} = \begin{bmatrix} D_1 & D_2 \\ 0 & 0 \end{bmatrix}, \end{aligned} \tag{2.33}$$

Where

$$\begin{aligned} E_1 &= \widetilde{D_1}_{(2,...,\frac{N+1}{2}),(2,...,\frac{N+1}{2})}, \ E_2 = \widetilde{D_1}_{(2,...,\frac{N+1}{2}),(N,...,\frac{N+3}{2})}, \\ D_1 &= \widetilde{D_2}_{(2,...,\frac{N+1}{2}),(2,...,\frac{N+1}{2})}, \ D_2 = \widetilde{D_2}_{(2,...,\frac{N+1}{2}),(N,...,\frac{N+3}{2})}, \end{aligned}$$

and

$$0 = [0]_{\frac{N+1}{2},\frac{N+1}{2}}.$$

The first and second spectral derivatives $\widetilde{D_\theta^1}$, $\widetilde{D_\theta^2}$ can be written in matrix form as respec-

tively

$$\widetilde{D^1_\theta} = \begin{bmatrix} 0 & \frac{(-1)^{M-1}}{2}\cot\left(\frac{(M-1)d}{2}\right) & & -\frac{1}{2}\cot(\frac{d}{2}) \\ -\frac{1}{2}\cot(\frac{d}{2}) & 0 & \ddots & \frac{1}{2}\cot(\frac{2d}{2}) \\ \frac{1}{2}\cot(\frac{2d}{2}) & -\frac{1}{2}\cot(\frac{d}{2}) & \ddots & -\frac{1}{2}\cot(\frac{3d}{2}) \\ -\frac{1}{2}\cot(\frac{3d}{2}) & \frac{1}{2}\cot(\frac{2d}{2}) & \ddots & \vdots \\ \vdots & \vdots & \ddots \quad \ddots & \frac{(-1)^{M-1}}{2}\cot\left(\frac{(M-1)d}{2}\right) \\ \frac{(-1)^{M-1}}{2}\cot\left(\frac{(M-1)d}{2}\right) & & & 0 \end{bmatrix}, \tag{2.34}$$

and

$$\widetilde{D^2_\theta} = \begin{bmatrix} -\frac{\pi^2}{3d^2}-\frac{1}{6} & \frac{1}{2}\csc^2(\frac{d}{2}) & & \frac{(-1)^{M}}{2}\csc^2\left(\frac{(M-1)d}{2}\right) \\ \frac{1}{2}\csc^2(\frac{d}{2}) & -\frac{\pi^2}{3d^2}-\frac{1}{6} & \ddots & \\ -\frac{1}{2}\csc^2(\frac{2d}{2}) & \frac{1}{2}\csc^2(\frac{d}{2}) & \ddots & \vdots \\ \vdots & -\frac{1}{2}\csc^2(\frac{2d}{2}) & \ddots & -\frac{1}{2}\csc^2(\frac{2d}{2}) \\ & \vdots \quad \ddots & \ddots & \frac{1}{2}\csc^2(\frac{d}{2}) \\ \frac{(-1)^{M}}{2}\csc^2\left(\frac{(M-1)d}{2}\right) & & & -\frac{\pi^2}{3d^2}-\frac{1}{6} \end{bmatrix}, \tag{2.35}$$

where d denotes the shift of angle $d = 2\pi/M$.

By representing the Kronecker product as

$$A \otimes B = (Ab_{i,j})_{i,j}, \tag{2.36}$$

and introducing identity matrix $I_{\frac{M}{2},\frac{M}{2}}$, we are able to write the spectral derivatives in 2D. The first order partial derivatives are given by

$$\frac{\partial}{\partial \rho^*} = E_1 \otimes \begin{bmatrix} I & 0 \\ 0 & I \end{bmatrix} + E_2 \otimes \begin{bmatrix} 0 & I \\ I & 0 \end{bmatrix}. \tag{2.37}$$

The second order partial derivatives are given by

$$\begin{aligned} \frac{\partial^2}{\partial \rho^{*2}} &= D_1 \otimes \begin{bmatrix} I & 0 \\ 0 & I \end{bmatrix} + D_2 \otimes \begin{bmatrix} 0 & I \\ I & 0 \end{bmatrix}, \\ \frac{\partial^2}{\partial \rho^* \partial \theta} &= E_1 \otimes \widetilde{D^1_\theta} + E_2 \otimes \widetilde{D^1_\theta}, \\ \frac{\partial^2}{\partial \theta^2} &= I \otimes \widetilde{D^2_\theta}. \end{aligned} \tag{2.38}$$

The 2D spectral operators can be efficiently evaluated by fast Fourier transform (FFT). Substituting the first and second order partial derivatives into (2.30) gives

$$\begin{aligned} L = &(\mathcal{R}_0^2 D_1 + R_1^2 D_1) \otimes \begin{bmatrix} I & 0 \\ 0 & I \end{bmatrix} + (\mathcal{R}_0^2 D_2 + \mathcal{R}_1^2 D_2) \otimes \begin{bmatrix} 0 & I \\ I & 0 \end{bmatrix} \\ &(\mathcal{R}\mathcal{R}_0^2 E_1 + \mathcal{R}\mathcal{R}_2 E_1) \otimes \begin{bmatrix} I & 0 \\ 0 & I \end{bmatrix} + (\mathcal{R}\mathcal{R}_0^2 E_2 + \mathcal{R}\mathcal{R}_2 E_2) \otimes \begin{bmatrix} 0 & I \\ I & 0 \end{bmatrix} \\ &2\mathcal{R}\mathcal{R}_0\mathcal{R}_1 E_1 \otimes \widetilde{D_\theta^1} + 2\mathcal{R}\mathcal{R}_0\mathcal{R}_1 E_2 \otimes \widetilde{D_\theta^1} + \mathcal{R}^2\mathcal{R}_0^2 \otimes \widetilde{D_\theta^2}, \end{aligned} \tag{2.39}$$

where $\mathcal{R}$ is the diagonal matrix

$$\mathcal{R} = diag({\rho^*}_j^{-1}), \quad 1 \leq j \leq (N-1)/2,$$

and $\mathcal{R}_0$, $\mathcal{R}_1$, $\mathcal{R}_2$ are the $M \times M$ diagonal matrix of the polar equation $\rho(\theta)$, the first order derivative $\rho'(\theta)$ and the second order derivative $\rho''(\theta)$ respectively.

Therefore, the non-dimensional solution of (2.29) is given as the solution of the linear system of equations [119]

$$U^* = L^{-1} \cdot [-1]_{(M \times \frac{N+1}{2}) \times 1}. \tag{2.40}$$

Finally, the solution with dimensions can be obtained as

$$u(y,z) = \frac{U^* h^2}{\mu} \left(-\frac{dP}{dx} \right). \tag{2.41}$$

2.3.2 Numerical results

The value at $\rho^* = 0$ is not computed in order to avoid the singularity but it is substituted by the averaged value of the surrounding points. In order to assess the accuracy of the method, the numerical solution is validated for shapes for which the analytical solution was described in section 2.1.2. The accuracy is estimated for the maximum velocity using the error measure:

$$E_{max} = \frac{|u_{ana}^{max} - u_N^{max}|}{u_{ana}^{max}}. \tag{2.42}$$

with u_{ana}^{max} denoting the maximum velocity in the quasi-analytical solution and u_N^{max} the maximum velocity of numerical method.

Fig. 2.11 illustrates the estimated maximum error E_{max} as a function of radial discretization number N for shapes for which the stretched parameters are listed in Table 2.6. The estimated error becomes constant when the radial number $N > 40$ and $E_{max} < 10\%$. For shapes with smooth boundaries high accuracy ($E_{max} < 1\%$) can be achieved for a smaller radial number $N < 40$ while $E_{max} < 4\%$ for $N \geq 73$ when shapes are not smooth. Anyway, the decreasing tendency of the estimated error E_{max} as N increases show the convergence of the numerical solution. Moreover, the estimated maximum error E_{max} as a function of angular discretization number M for shapes is illustrated in Fig. 2.12. It is seen that this time the error is stable for symmetric shapes but reaches a quasi-steady values for other shapes so that depends on the cross section shape.

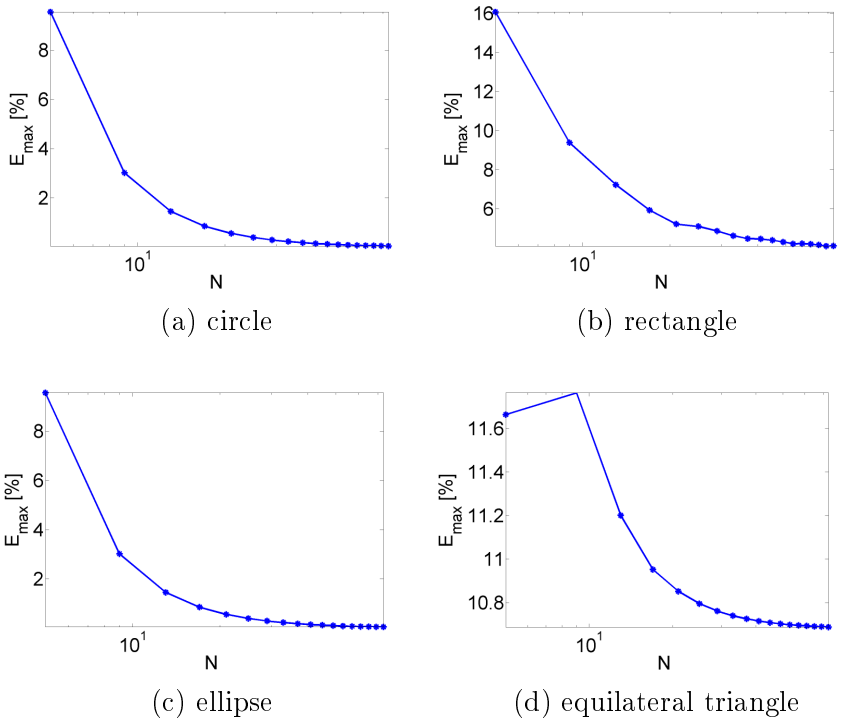

(a) circle (b) rectangle

(c) ellipse (d) equilateral triangle

Figure 2.11: Illustration of the estimated maximum error E_{max} with function of radial number N for shapes shown in Fig. 2.6 when M =72.

2.4 General analytical solution for Poisson equation

In the previous section 2.3 a Pseudo-spectral numerical method is presented. Lower accuracy appears when the shapes are $\mathcal{C}^1$ continuous on the boundary. In the current section, a general analytical solution is proposed to avoid this problem. (2.8) is reduced to the Laplace equation, which is a familiar partial differential equation and can be solved analytically.

In stretched coordinates the radius r is substituted by ρ as before. A reduced velocity u^*

Table 2.6: Overview the stretched parameters of shapes.

shape	m	n_1	n_2	n_3	$g(\theta)$	a	b
circle (Fig. 2.6a)	1	2	2	2	1	5e-3	5e-3
rectangle (Fig. 2.6b)	4	100	100	100	0.002	5.05	1
ellipse (Fig. 2.6c)	4	2	2	2	1	0.006	0.0042
equilateral triangle (Fig. 2.6g)	3	0.5	1	1	0.0038	1.414	1.414

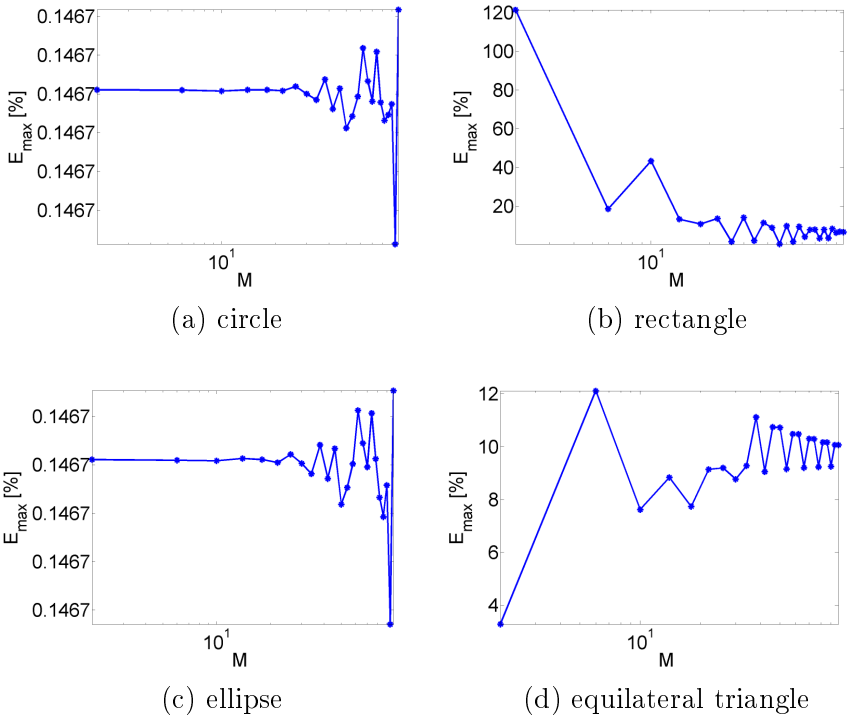

(a) circle (b) rectangle

(c) ellipse (d) equilateral triangle

Figure 2.12: Illustration of the estimated maximum error E_{max} with function of angular number N for shapes shown in Fig. 2.6 when N =41.

is introduced as

$$u = u^* + \frac{\rho^2}{4\mu}\frac{dP}{dx}. \tag{2.43}$$

Applying this transformation to (2.8) shows that the reduced velocity u^* must satisfy the following Laplace equation

$$\nabla^2 u^* = \frac{\partial^2 u^*}{\partial \rho^2} + \frac{1}{\rho}\frac{\partial u^*}{\partial \rho} + \frac{1}{\rho^2}\frac{\partial^2 u^*}{\partial^2 \theta} = 0, \tag{2.44}$$

Then the no slip boundary condition $u = 0$ can be expressed as

$$u^* = -\frac{\rho_i^2}{4\mu}\frac{dP}{dx} = -\frac{r_i^2}{4\mu}\frac{dP}{dx}, \quad on\ \partial\Omega. \tag{2.45}$$

Here, the suffix i denotes the value of a point on the duct boundary $\partial\Omega$. Now the flow problem is transformed to a Dirichlet problem for the Laplace equation with slip condition for reduced velocity u^* and thus has a unique solution.

Using separation of variables, let us look for a solution of the form $P(\rho)\Phi(\theta)$. Substituting this into the (2.23) it follows that the functions $P(\rho)$, $\Phi(\theta)$ must satisfy the following equations

$$\begin{cases} \rho^2 P''(\rho) + \rho P'(\rho) - \lambda^2 P(\rho) = 0, \\ \Phi''(\theta) + \lambda^2 \Phi(\theta) = 0. \end{cases} \tag{2.46}$$

Consider the periodicity of the function $\Phi(\theta)$ one finds that

$$\Phi(\theta) = c_1 \cos(m\theta) + c_2 \sin(m\theta), \tag{2.47}$$

where $\lambda = m$ is an integer number.

Let us now solve the equation for $P(\rho)$. Since the equation is a Cauchy-Euler equation and the solutions of the Cauchy-Euler equation are known to be of the form ρ^m and ρ^{-m}. So the general solution is of the form

$$P(\rho) = d_1 \rho^m + d_2 \rho^{-m}. \tag{2.48}$$

This means that we have found the elementary solutions for the Laplace equation (2.44)

$$\begin{aligned} u^*(\rho, \theta) &= (c_1 \cos(m\theta) + c_2 \sin(m\theta))(d_1 \rho^m + d_2 \rho^{-m}), \\ & m = 0, 1, 2... \end{aligned} \tag{2.49}$$

For the interior problem one needs to require $d_2 = 0$ to make sure that $u^* < \infty$, then

$$u^*(\rho, \theta) = \sum_{m=0}^{\infty} (a_m \cos(m\theta) + b_m \sin(m\theta))\rho^m. \tag{2.50}$$

Actually as coefficient $b_0 \equiv 0$, (2.50) then can be rewritten as follows

$$u^*(\rho,\theta) = a_0 + \sum_{m=1}^{\infty} (a_m \cos(m\theta) + b_m \sin(m\theta))\rho^m, \tag{2.51}$$

where the coefficients a_0, a_m and b_m are arbitrary constants that can be determined by imposing the boundary condition.

In order to get the unknown coefficients the general solution (2.51) can be represented by the partial sum of N polynomials

$$u_N^*(\rho,\theta) = a_0 + \sum_{m=1}^{N} \rho^m \left(a_m \cos(m\theta) + b_m \sin(m\theta)\right). \tag{2.52}$$

Applying the boundary condition (2.45), thus

$$a_0 + \sum_{m=1}^{N} r_i^m \left(a_m \cos(m\theta_i) + b_m \sin(m\theta_i)\right) = -\frac{r_i^2}{4\mu}\frac{dP}{dx}, \tag{2.53}$$

This equation includes the total $L = 2N + 1$ unknown coefficients a_m and b_m. The values r_i and θ_i are provided with L points on the boundary $\partial\Omega$ so that L equations are available to get the unknown coefficients. Finally combining (2.43) and (2.52) the solution for the velocity distribution is obtained as

$$u_N(\rho,\theta) = a_0 + \sum_{m=1}^{N} \rho^m \left(a_m \cos(m\theta) + b_m \sin(m\theta)\right) + \frac{\rho^2}{4\mu}\frac{dP}{dx}, \tag{2.54}$$

To assess the performance of the proposed method in terms of numerical accuracy, as the maximum error will occur at the boundary points, the root mean square error (E_{RMS}) on the boundary values has been thus evaluated as follows

$$E_{RMS} = \sqrt{\frac{1}{n}\sum_{i=1}^{n}\left[a_0 + \sum_{m=1}^{N} r_i^m \left(a_m \cos(m\theta_i) + b_m \sin(m\theta_i)\right) + \frac{r_i^2}{4\mu}\frac{dP}{dx}\right]^2}, \tag{2.55}$$

E_{max} is computed to determine the degree of precision for the velocity profile and in addition, the accuracy is assessed as before with respect to the analytical solutions in case the no slip condition is applied as in (2.42) with:

$$E_{max} = \frac{|u_{ana}^{max} - u^{max}|}{u_{ana}^{max}}, \tag{2.56}$$

where u_{ana}^{max} denotes as before the maximum velocity on the quasi-analytical solution given in section 2.42.

2.4.1 Numerical results

Firstly, the solution for the cross section shapes shown in Fig. 2.6 and Fig. 2.7 with no slip condition is investigated. Fig. 2.13 illustrates the velocity distribution for the same shapes with parameters listed in Table 2.6.

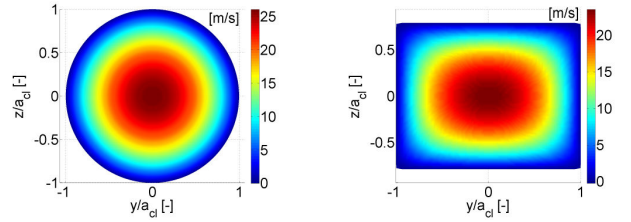

(a) circle (N=2) (b) rectangle (N=10)

(c) ellipse (N=2) (d) equilateral triangle (N=10)

Figure 2.13: Illustration of the velocity distribution for the cross section shapes shown in Fig. 2.6a, Fig. 2.6b, Fig. 2.6c and Fig. 2.6g.

Fig. 2.14 and Fig. 2.15 illustrate the estimated root mean square error and the maximum error as a function of the sum truncation number N. It is seen that the solution for a circular shape matches the one analytical described in section 2.1 for $N = 2$. For all assessed shapes good accuracies are achieved ($E_{RMS} < 0.5\%$ and $E_{max} < 0.03\%$) for $N > 6$. In particular, for shapes without a sharp corner results with high accuracy can be obtained using a very small sum truncation number N. Table 2.7 illustrates the comparison errors E_{max}. High accuracy of the presented solution is found for all assessed cross section shapes so that the accuracy of the approach is validated.

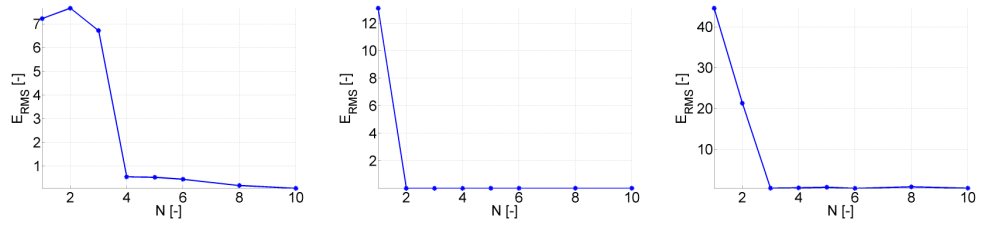

(a) rectangle (b) ellipse (c) equilateral triangle

Figure 2.14: Illustration of the estimated root mean square error E_{RMS} with function of sum truncation number N for shapes shown in Fig. 2.6b, Fig. 2.6c and Fig. 2.6g.

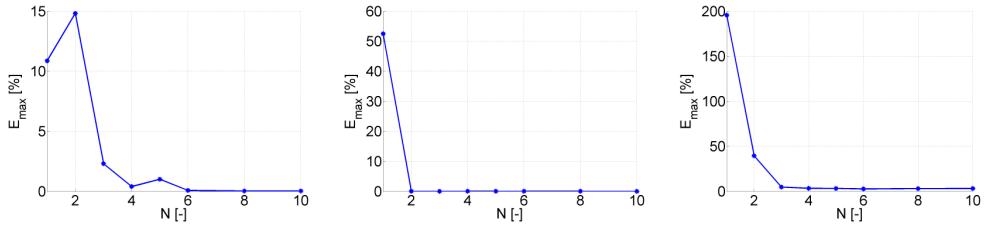

(a) rectangle (b) ellipse (c) equilateral triangle

Figure 2.15: Illustration of the estimated maximum error E_{max} as a function of sum truncation number$N$ for shapes shown in Fig. 2.6b, Fig. 2.6c and Fig. 2.6g.

Table 2.7: Comparison of error E_{max} for the general analytical and numerical pseudo-spectral approach. Examples of Fig. 2.6a, Fig. 2.6b, Fig. 2.6c and Fig. 2.6g are assessed.

Approach	circle	rectangle	ellipse	equilateral triangle
present [%] ($N > 6$)	0	0.393	1.44e-14	0.479
numerical [%] ($N > 40$)	0.046	0.046	4.09	10.69

2.5 Summary

In the current chapter, analytical solutions for laminar viscous pressure-driven flow through a uniform channel of an arbitrary cross section shape are presented so that the influence of cross section shape on the viscous flow is accounted for. A wide range of cross section shapes is considered. The transformed Poisson equation with stretched coordinates provides an analytical solution for an arbitrary cross section shape, avoiding the use of conformal

mapping.

Next, a pseudo-spectral approach is assessed to solve the Poisson problem for an arbitrary cross section shape based on stretched coordinates. The presented numerical results show good performance of the approach but lower accuracy when shapes have no continuous boundary. Finally, the proposed general analytical method avoid this problem and improves the accuracy for all assessed cross section shapes at a low computational cost.

Chapter 3

Application to physical equations

Contents

In this chapter, we exploit the proposed parametrization of an arbitrary cross section shape using stretched coordinates following the "superformula" (2.14) described in chapter 2. Previously, solutions of the Poisson equation for two-dimensional shapes were presented. In this chapter, we focus on solutions in terms of stretched coordinates for physical equations in case of two-dimensional (2D) as well as three-dimensional (3D) parametrized shapes. In the following, solutions of the Laplace, Helmholtz and wave equation are formulated and numerical results are presented.

3.1 Two-dimensional shapes

3.1.1 Laplace equation

Firstly, consider the interior Dirichlet problem for the Laplace equation with a domain Ω, whose boundary is described by the polar equation $\rho = r(\theta)$

$$\begin{cases} \frac{\partial^2 u}{\partial x^2} + \frac{\partial^2 u}{\partial y^2} = 0 & \text{in} \quad \Omega \\ u = f(x, y) & \text{on} \quad \partial\Omega \end{cases} \tag{3.1}$$

Recall the coordinate transform from plane (x, y) to stretched (ρ^*, θ) coordinates and the derivation process described in section 2.4 of the previous chapter 2. The same way, we get

$$U(\rho^*, \theta) = \sum_{m=0}^{\infty} \left(a_m \cos(m\theta) + b_m \sin(m\theta)\right) \left[\rho^* r(\theta)\right]^m , \tag{3.2}$$

with $u(x, y) = u(\rho\cos\theta, \rho\sin\theta) = U(\rho^*, \theta)$ and the domain Ω is transformed to $0 \leq \theta \leq 2\pi$, $0 \leq \rho^* \leq 1$.

In order to determine the coefficients a_m, b_m the boundary condition ($\rho^* = 1$, thus $\rho = r(\theta)$) can be rewritten as

$$F(\theta) = f(r(\theta)\cos(\theta), r(\theta)\sin(\theta)) = \sum_{m=0}^{\infty} \left(a_m \cos(m\theta) + b_m \sin(m\theta)\right) r(\theta)^m. \tag{3.3}$$

Now consider the Fourier method and the solution to be of the form

$$F(\theta) = \sum_{m=0}^{\infty} \left(\alpha_m \cos(m\theta) + \beta_m \sin(m\theta)\right), \tag{3.4}$$

where the Fourier coefficients α_m and β_m are constants.

Clearly $F(\theta)$ is a periodic function with period 2π since the right hand side of (3.4) has this property. By considering the orthogonality of the functions $\cos(m\theta)$ and $\sin(m\theta)$ we deduce that

$$\left\{ \begin{array}{c} \alpha_m \\ \beta_m \end{array} \right\} = \frac{\epsilon_m}{2\pi} \int_0^{2\pi} F(\theta) \left\{ \begin{array}{c} \cos(m\theta) \\ \sin(m\theta) \end{array} \right\} d\theta, \tag{3.5}$$

where ϵ_m denoting the Neumann symbol, so

$$\epsilon_m = \left\{ \begin{array}{ll} 1, & \text{m=0} \\ 2, & \text{m}\neq 0. \end{array} \right.$$

Thus the coefficients a_m and b_m are obtained by solving the following system:

$$\left\{ \begin{array}{l} \sum\limits_{m=0}^{\infty} \frac{\epsilon_k}{2\pi} \left[a_m \int_0^{2\pi} r(\theta)^m \cos(m\theta)\cos(k\theta)d\theta + b_m \int_0^{2\pi} r(\theta)^m \sin(m\theta)\cos(k\theta)d\theta \right] = \alpha_k, \\ \sum\limits_{m=0}^{\infty} \frac{\epsilon_k}{2\pi} \left[a_m \int_0^{2\pi} r(\theta)^m \cos(m\theta)\sin(k\theta)d\theta + b_m \int_0^{2\pi} r(\theta)^m \sin(m\theta)\sin(k\theta)d\theta \right] = \beta_k, \end{array} \right.$$

$$k = 0, 1, 2, ... \tag{3.6}$$

3.1.2 Helmholtz equation

Next, let us consider the interior Dirichlet problem for the Helmholtz equation in a domain Ω

$$\begin{cases} \Delta u + a^2 u = 0 & \text{in} \quad \Omega \\ u = f(x,y) & \text{on} \quad \partial\Omega \end{cases} \tag{3.7}$$

in which the boundary defined by the polar equation $\rho = r(\theta)$ and the propagation coefficient $a > 0$. We use separation of variables to search for a solution of the form $u(\rho,\theta) = U(\rho^*,\theta) = P_1(\rho)P_2(\theta)$. Substituting this form into (3.7) it follows that the functions $P_1(\rho)$, $P_2(\theta)$ must satisfy the following equations

$$\begin{cases} \rho^2 P_1''(\rho) + \rho P_1'(\rho) + (a^2 - \lambda^2)P_1(\rho) = 0, \\ P_2''(\theta) + \lambda^2 P_2(\theta) = 0, \ \lambda = const. \end{cases} \tag{3.8}$$

In order to assure that the function $u(x,y)$ has a single value at any point, the parameter λ is selected to satisfy $\lambda = m \in \mathbb{N}_0$ and we find that

$$P_2(\theta) = c_m \cos(m\theta) + d_m \sin(m\theta), \tag{3.9}$$

where $C_m, d_m \in \mathbb{R}$ are unknown arbitrary constants. Therefore the radial function $P_1(\rho)$ satisfies

$$\rho^2 P_1''(\rho) + \rho P_1'(\rho) + (a^2 - m^2)P_1(\rho) = 0. \tag{3.10}$$

Let $s = a\rho$ and let P_3 be the function of variable s defined by $P_3(s) \equiv P_1(s/a)$. With this transformation of variable (3.10) becomes a Bessel's equation

$$s^2 P_3''(s) + s P_3'(s) + (s^2 - m^2)P_3(s) = 0. \tag{3.11}$$

The general solution of Bessel's equation (3.11) is [2]

$$P_3(s) = a_m J_m(s) + b_m Y_m(s) = a_m J_m(h\rho) + b_m Y_m(h\rho), \tag{3.12}$$

where J_m, Y_m are the Bessel function of the first and second kind with order m respectively. Notice that the Bessel functions of the second kind $Y_m(s)$ has a singularity at $\rho = 0$. To avoid this singularity, we have to assume $b_m = 0$ due to the boundedness of the solution. Thus the solution of (3.10) has the form

$$P_1(\rho) = P_3(s) = a_m J_m(h\rho). \tag{3.13}$$

Finally, the general solution of the problem (3.7) is of the form

$$U(\rho^*, \theta) = \sum_{m=0}^{+\infty} J_m(a\rho^* r(\theta)) \left(C_m \cos(m\theta) + D_m \sin(m\theta)\right). \tag{3.14}$$

The coefficients C_m, D_m are determined by imposing the boundary condition, i.e., assuming $\rho^* = 1$ and therefore putting $\rho = r(\theta)$,

$$F(\theta) = U(1, \theta) = \sum_{m=0}^{+\infty} J_m(ar(\theta)) \left(C_m \cos(m\theta) + D_m \sin(m\theta)\right). \tag{3.15}$$

By using Fourier method, and thus following the same process as described in section 3.1.1, we substitute (3.15) into (3.5) and it follows that the sought coefficients are obtained by solving the following equations

$$\begin{cases} \sum\limits_{m=0}^{+\infty} \frac{\epsilon_k}{2\pi} \left[C_m \int_0^{2\pi} J_m(ar(\theta)) \cos(m\theta) \cos(k\theta) d\theta + D_m \int_0^{2\pi} J_m(ar(\theta)) \sin(m\theta) \cos(k\theta) d\theta\right] = \alpha_k, \\ \sum\limits_{m=0}^{+\infty} \frac{\epsilon_k}{2\pi} \left[C_m \int_0^{2\pi} J_m(ar(\theta)) \cos(m\theta) \sin(k\theta) d\theta + D_m \int_0^{2\pi} J_m(ar(\theta)) \sin(m\theta) \sin(k\theta) d\theta\right] = \beta_k. \end{cases}$$

$$k = 0, 1, 2, ... \tag{3.16}$$

with ϵ_k denoting the Neumann symbol, so

$$\epsilon_k = \begin{cases} 1, & \text{k=0} \\ 2, & \text{k}\neq 0 \end{cases}$$

3.1.3 Wave Equation

Finally, let us consider the interior Dirichlet problem for the wave equation with constant propagation speed a in a domain Ω. Assume the displacement of the boundary is equal to zero at all times t and we define the initial displacement and velocity distribution by continuous functions $f_1(x, y)$ and $f_2(x, y)$ respectively. Thus the system is of the form

$$\begin{cases} \frac{\partial^2}{\partial t^2} u(x, y, t) = a^2 \Delta u(x, y, t), & \text{in} \quad \Omega \\ u(x, y, t) = 0, & \text{on} \quad \partial\Omega \\ u(x, y, 0) = f_1(x, y), \\ \frac{\partial}{\partial t} u(x, y, 0) = f_2(x, y). \end{cases} \tag{3.17}$$

The domain Ω is transformed to a unit circle using stretched coordinates and reconsider separation of variables to assume that the elementary solution of the system has the form

$$u(x,y,t) = u(\rho,\theta,t) = U(\rho^*,\theta,t) = P_1(\rho)P_2(\theta)P_3(t). \tag{3.18}$$

Substituting into the wave equation and considering two separation variables λ and s, one finds that the functions P_1, P_2, P_3 have to satisfy the following equations

$$\begin{cases} \rho^2 P_1''(\rho) + \rho P_1'(\rho) + \left(\lambda^2\rho^2 - s^2\right) P_1(\rho) = 0, \\ P_2''(\theta) + s^2 P_2(\theta) = 0, \\ P_3''(t) + a^2\lambda^2 P_3(t) = 0. \end{cases} \tag{3.19}$$

Due to the reason of periodicity and single-value for θ the constant variable $s = m \in \mathbb{Z}$ so that

$$P_2(\theta) = a_m \cos(m\theta) + b_m \sin(m\theta), \tag{3.20}$$

with undetermined arbitrary constants a_m, b_m. Let $\mu = \lambda\rho$ and let P_4 be the function of μ defined by $P_4(\mu) \equiv P_1(\mu/\lambda)$. With this transformation, the equation of radial function P_1 turns into a Bessel's equation

$$\mu^2 P_4''(\mu) + \mu P_4'(\mu) + \left(\mu^2 - m^2\right) P_4'(\mu) = 0. \tag{3.21}$$

Due to the boundedness, the general solution of this Bessel's equation is of the form

$$P_1(\rho) = c_m J_m(\mu) = c_m J_m(\lambda\rho). \tag{3.22}$$

For the equation of function P_3 one finds that

$$P_3(\theta) = d_\lambda \cos(a\lambda t) + e_\lambda \sin a\lambda t. \tag{3.23}$$

Thus the general solution of (3.17) is of the form

$$\begin{aligned} U(\rho^*,\theta,t) = \sum_{m=0}^{+\infty} \sum_{\lambda} J_m(\lambda\rho^* r(\theta)) \left[A_{m,\lambda}\cos(m\theta)\cos(a\lambda t) + B_{m,\lambda}\cos(m\theta)\sin(a\lambda t)\right. \\ \left. + C_{m,\lambda}\sin(m\theta)\cos(a\lambda t) + D_{m,\lambda}\sin(m\theta)\sin(a\lambda t)\right]. \end{aligned} \tag{3.24}$$

Imposing the boundary condition $u(r(\theta),\theta,t)=0$ results in $J_m(\lambda r(\theta))=0$ so that $\lambda(\theta)=g_m/r(\theta)$ with unknown coefficients g_m. Denote g_k^m is the kth positive root of the Bessel function of the first kind with order m, then $\lambda=g_k^m/r(\theta)$, $k\in\mathbb{N}$. Therefore the general solution of (3.24) becomes

$$\begin{aligned}U(\rho^*,\theta,t)=\sum_{m=0}^{+\infty}\sum_{k=1}^{+\infty}J_m(g_k^m\rho^*)\Big[&[A_{m,k}\cos(m\theta)\cos(\frac{ag_k^mt}{r(\theta)})+B_{m,k}\cos(m\theta)\sin(\frac{ag_k^mt}{r(\theta)})\\&+C_{m,k}\sin(m\theta)\cos(\frac{ag_k^mt}{r(\theta)})+D_{m,k}\sin(m\theta)\sin(\frac{ag_k^mt}{r(\theta)})\Big],\end{aligned}\tag{3.25}$$

and this gives

$$\begin{aligned}U_t(\rho^*,\theta,t)=\frac{a}{r(\theta)}\sum_{m=0}^{+\infty}\sum_{k=1}^{+\infty}&g_k^mJ_m(g_k^m\rho^*)\\&\Big[-A_{m,k}\cos(m\theta)\sin(\frac{ag_k^mt}{r(\theta)})+B_{m,k}\cos(m\theta)\cos(\frac{ag_k^mt}{r(\theta)})\\&-C_{m,k}\sin(m\theta)\sin(\frac{ag_k^mt}{r(\theta)})+D_{m,k}\sin(m\theta)\cos(\frac{ag_k^mt}{r(\theta)})\Big].\end{aligned}\tag{3.26}$$

Using the initial conditions and let them have the forms

$$F_1(\rho^*,\theta)=f_1(\rho\cos(\theta),\rho\sin(\theta))=\sum_{m=0}^{+\infty}\left(\alpha_m\cos(m\theta)+\beta_m\sin(m\theta)\right),\tag{3.27}$$

$$F_2(\rho^*,\theta)=f_2(\rho\cos(\theta),\rho\sin(\theta))=\frac{a}{r(\theta)}\sum_{m=0}^{+\infty}\left(\eta_m\cos(m\theta)+\gamma_m\sin(m\theta)\right),\tag{3.28}$$

where the coefficients α_m, β_m, η_m and γ_m can be found using Fourier method

$$\begin{Bmatrix}\alpha_m\\ \beta_m\end{Bmatrix}=\frac{\epsilon_m}{2\pi}\int_0^{2\pi}\int_0^{\pi}F_1(\rho^*,\theta)\begin{Bmatrix}\cos(m\theta)\\ \sin(m\theta)\end{Bmatrix}d\theta d\phi,\tag{3.29}$$

$$\begin{Bmatrix}\eta_m\\ \gamma_m\end{Bmatrix}=\frac{\epsilon_m}{2\pi a}\int_0^{2\pi}\int_0^{\pi}F_2(\rho^*,\theta)r(\theta)\begin{Bmatrix}\cos(m\theta)\\ \sin(m\theta)\end{Bmatrix}d\theta d\phi,\tag{3.30}$$

with Neumann symbol ϵ_m, so

$$\epsilon_m=\begin{cases}1, & \text{m=0}\\ 2, & \text{m}\neq 0.\end{cases}$$

Consider the orthogonality of the Bessel functions of first kind

$$\int_0^1 J_m(g_k^m\rho^*)J_m(g_n^m\rho^*)\rho^* d\rho^* = \begin{cases} \frac{1}{2}\left[J_{m+1}(g_k^m)\right]^2, & n=k \\ 0, & n\neq k \end{cases} \tag{3.31}$$

and (3.25) $\backsim$ (3.30), the coefficients $A_{m,k}$, $B_{m,k}$, $C_{m,k}$ and $D_{m,k}$ finally can be obtained by solving the following system

$$\begin{Bmatrix} A_{m,k} \\ C_{m,k} \end{Bmatrix} = \frac{2}{\left[J_{m+1}(g_k^m)\right]^2}\int_0^1 J_m(g_k^m\rho^*)\begin{Bmatrix} \alpha_m(\rho^*) \\ \beta_m(\rho^*) \end{Bmatrix}\rho^* d\theta \tag{3.32}$$

$$\begin{Bmatrix} B_{m,k} \\ D_{m,k} \end{Bmatrix} = \frac{2}{g_k^m\left[J_{m+1}(g_k^m)\right]^2}\int_0^1 J_m(g_k^m\rho^*)\begin{Bmatrix} \eta_m(\rho^*) \\ \gamma_m(\rho^*) \end{Bmatrix}\rho^* d\theta. \tag{3.33}$$

$$m = 1,2,3,...,\ k = 1,2,3,...$$

3.1.4 Numerical results

In the following examples the boundary $\partial\Omega$ is described by the called "superformula" [39].

$$r(\theta) = g(\theta)\left[\left|\frac{\cos(\frac{m\theta}{4})}{a}\right|^{n_2} + \left|\frac{\sin(\frac{m\theta}{4})}{b}\right|^{n_3}\right]^{-1/n_1} = g(\theta).f(\theta), \quad m>0. \tag{3.34}$$

In order to assess the numerical accuracy of the applications, the relative boundary errors for Laplace (L), Helmholtz (H) and wave (W)[1] equations have been evaluated as follows

$$err_N^L = \frac{\|U_N^L - F^L(\theta)\|}{\|F^L(\theta)\|}, \tag{3.35}$$

$$err_N^H = \frac{\|U_N^H - F^H(\theta)\|}{\|F^H(\theta)\|}, \tag{3.36}$$

$$err_N^W = \frac{1}{2}\left(\frac{\|U_{M.K}^W - F_1^W(\theta)\|}{\|F_1^W(\theta)\|} + \frac{\|\partial_t U_{M.K}^W - F_2^W(\theta)\|}{\|F_2^W(\theta)\|}\right), \tag{3.37}$$

in which $\|\cdot\|$ denotes the L^2 norm. The solutions of these boundary value problems are represented by the truncated sum with order N in Fourier series expansion, which listed as follows, respectively.

$$U_N^L(\rho^*,\theta) = a_0 + \sum_{m=1}^{N}\left(a_m\cos(m\theta) + b_m\sin(m\theta)\right)(\rho^*\theta)^m, \tag{3.38}$$

[1] Numerical results are in preparation.

$$U_N^H(\rho^*,\theta) = \sum_{m=0}^{N} J_m(a\rho^*\theta)\,(C_m\cos(m\theta) + D_m\sin(m\theta)), \tag{3.39}$$

$$U_{M,K}^W(\rho^*,\theta,t) = \sum_{m=0}^{M}\sum_{k=1}^{K} J_m(g_k^m\rho^*)\left[A_{m,k}\cos(m\theta)\cos(\frac{ag_k^m t}{r(\theta)}) + B_{m,k}\cos(m\theta)\sin(\frac{ag_k^m t}{r(\theta)})\right.$$
$$\left. + C_{m,k}\sin(m\theta)\cos(\frac{ag_k^m t}{r(\theta)}) + D_{m,k}\sin(m\theta)\sin(\frac{ag_k^m t}{r(\theta)})\right]. \tag{3.40}$$

The shape shown in Fig. 3.1 with the stretched parameters listed in Table 3.1 is assessed and the domain Ω is given as $0 \le \theta \le 2\pi$ and $0 \le \rho^* \le 1$.

Table 3.1: Overview of the parameters of (2.14) for the symmetrical shape depicted in Fig. 3.1.

shape	m	n_1	n_2	n_3	$g(\theta)$	a	b
symmetrical shape	5	8	4	4	1	1	1

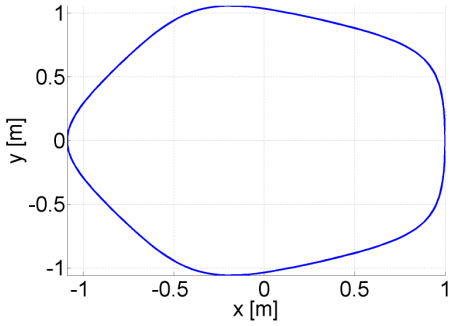

Figure 3.1: Symmetrical shape obtained from (2.14) with the parameters listed in Table 3.1.

For the Laplace equation, we take $f^L(x,y) = \sinh(xy) + \log(x^2+y^2+1)$ as the function to describe the Dirichlet boundary condition. The relative boundary error err_L, plotted in Fig. 3.2a, shows us the convergence of the series expansion function U_N^L (3.38). It is seen that the expansion with order $N = 9$ gives a accurate ($err_L < 2\%$) estimate of the boundary data and modeled and imposed boundary values are shown to match.

Let $f^H(x,y) = x+3y+\cos(x+2y)$ be the boundary condition for the Dirichlet problem of the Helmholtz equation. Fig. 3.3 illustrates the relative boundary error err_H as a function of the truncated sum number N in the series expansion (3.39). From Fig. 3.3 and Fig. 3.4a is seen that a good ($err_H < 2\%$) estimation of the initial condition can be observed for the Fourier expansion solution with order $N = 7$ and modeled and imposed boundary values matches well.

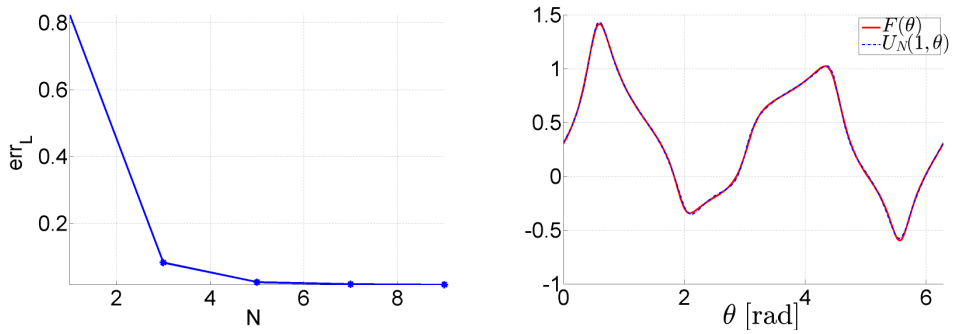

(a) err_N^L (b) $U_{N=9}$

Figure 3.2: (a) The relative boundary error err_N^L as a function of truncated sum number N for Dirichlet problem of Laplace equation. (b) The series expansion function U_N^L with order $N = 9$. The shape with stretched parameters (Table 3.1) is assessed in domain Ω.

In addition, the interior domain solution for $N = 7$ which matches the boundary condition, is shown in Fig. 3.4b.

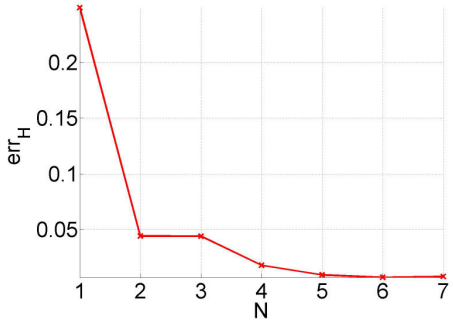

Figure 3.3: Illustration of relative boundary error err_N^H as a function of truncated sum number N for Dirichlet problem of Helmholtz equation. The shape with stretched parameters (Table 3.1) is assessed in domain Ω.

3.2 Three-dimensional shapes

Now, we consider the physical equations for three-dimensional shapes and hence we need a three-dimensional coordinate system. Firstly, we introduce the ordinary spherical coordinates system to describe domain Ω

$$x = \rho\cos\phi\sin\theta,\ y = \rho\cos\phi\cos\theta,\ z = \rho\cos\theta, \tag{3.41}$$

with the boundary condition $\rho = r(\theta, \phi)$, $0 \leq \theta \leq \pi$, $0 \leq \phi \leq 2\pi$. We introduce again a

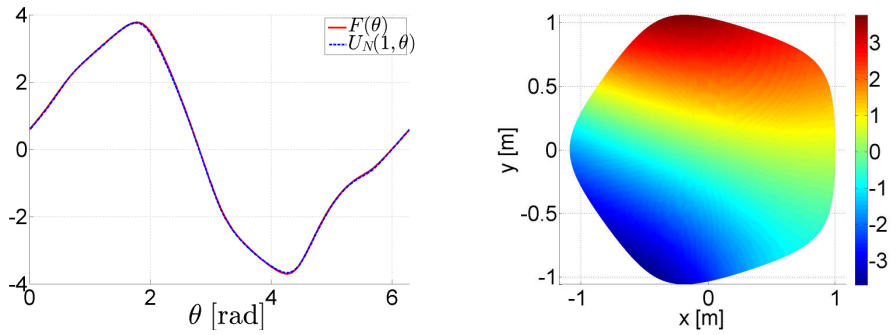

(a) boundary value (b) distribution

Figure 3.4: (a) Comparison of the boundary value between the initial condition and the derived truncated sum U_N^H when the order $N = 7$ for the Helmholtz equation. (b) Distribution of the solution represented by the truncated sum for $N = 7$ (3.39).

stretched radius ρ^* with $\rho = \rho^* r(\theta, \phi)$ and thus the space in stretched coordinates becomes

$$x = \rho^* r(\theta,\phi)\cos\phi\sin\theta,\ \ y = \rho^* r(\theta,\phi)\cos\phi\cos\theta,\ \ z = \rho^* r(\theta,\phi)\cos\theta, \tag{3.42}$$

with domain Ω given as $0 \le \theta \le \pi$, $0 \le \phi \le 2\pi$ and $0 \le \rho^* \le 1$.

Now, we consider the Laplace operator in spherical coordinates [29]

$$\Delta u = \frac{\partial^2 u}{\partial \rho^2} + \frac{2}{\rho}\frac{\partial u}{\partial \rho} + \frac{1}{\rho^2 \sin\theta}\frac{\partial}{\partial \theta}\left(\sin\theta \frac{\partial u}{\partial \theta}\right) + \frac{1}{\rho^2 \sin^2\theta}\frac{\partial^2 u}{\partial \phi^2}. \tag{3.43}$$

By setting $U(\rho^*, \theta, \phi) = u(\rho, \theta, \phi)$ in the new stretched coordinates system (ρ^*, θ, ϕ) and substituting this transform into (3.43), one finds that

$$\begin{aligned}\Delta u = {} & \frac{1}{r^2}\left(1 + \frac{{r_\theta}^2}{r^2} + \frac{{r_\phi}^2}{r^2\sin^2\theta}\right)\frac{\partial^2 U}{\partial \rho^{*2}} \\ & + \frac{1}{\rho^* r^2}\left[2\left(1 + \frac{{r_\theta}^2}{r^2} + \frac{{r_\phi}^2}{r^2\sin^2\theta}\right) - \frac{1}{r}\left(r_{\theta\theta} + r_\theta\cot\theta + \frac{r_{\phi\phi}}{\sin^2\theta}\right)\right]\frac{\partial U}{\partial \rho^*} \\ & - \frac{2r_\theta}{\rho^* r^3}\frac{\partial^2 U}{\partial \rho^* \partial\theta} - \frac{2r_\phi}{\rho^* r^3 \sin^2\theta}\frac{\partial^2 U}{\partial \rho^* \partial\phi} + \frac{1}{\rho^{*2} r^2}\frac{\partial^2 U}{\partial \theta^2} + \frac{\cot\theta}{\rho^* r^2}\frac{\partial U}{\partial \theta} + \frac{1}{\rho^{*2} r^2 \sin^2\theta}\frac{\partial^2 U}{\partial \phi^2},\end{aligned} \tag{3.44}$$

with the boundary $r(\theta, \phi) = \rho$ when $\rho^* = 1$.

For convenience, we rewrite the boundary condition $\partial\Omega$ as

$$\rho = r(\theta, \phi) = \frac{1}{R(\theta, \phi)},\ 0 \leq \theta \leq \pi,\ 0 \leq \pi \leq 2\pi. \tag{3.45}$$

Substituting this equation into the Laplace equation (3.44) results in

$$\begin{aligned}\Delta u = &\left(R^2 + {R_\theta}^2 + \frac{{R_\phi}^2}{\sin^2\theta}\right)\frac{\partial^2 U}{\partial \rho^{*2}} + \frac{R}{\rho^*}\left(2R + R_\theta \cot\theta + {R_\theta}^2 + \frac{R_{\phi\phi}}{\sin^2\theta}\right)\frac{\partial U}{\partial \rho^*} \\ &+ \frac{2RR_\theta}{\rho^*}\frac{\partial^2 U}{\partial \rho^* \partial\theta} + \frac{2RR_\phi}{\rho^* \sin^2\theta}\frac{\partial^2 U}{\partial \rho^* \partial\phi} + \frac{R^2}{\rho^{*2}}\frac{\partial^2 U}{\partial\theta^2} + \frac{R^2\cot\theta}{\rho^{*2}}\frac{\partial U}{\partial\theta} + \frac{R^2}{\rho^{*2}\sin^2\theta}\frac{\partial^2 U}{\partial\phi^2}.\end{aligned} \tag{3.46}$$

3.2.1 Laplace equation

Firstly, consider the interior Dirichlet problem for the Laplace equation with on a domain Ω, whose boundary is described by the polar equation $\rho = r(\theta, \phi)$.

$$\begin{cases} \Delta u(\rho, \theta, \phi) = 0 & \text{in} \quad \Omega \\ u(\rho, \theta, \phi) = f(\theta, \phi) & \text{on} \quad \partial\Omega. \end{cases} \tag{3.47}$$

Consider the method of separation of variables, search for a solution with the form $u(\rho, \theta, \phi) = U(\rho^*, \theta, \phi) = P_1(\rho)P_2(\theta)P_3(\phi)$. Substituting this form into (3.47) gives

$$\rho^2\frac{P_1''}{P_1} + 2\rho\frac{P_1'}{P_1} + \frac{P_2''}{P_2} + \cot\theta\frac{P_2''}{P_2} + \frac{1}{\sin^2\theta}\frac{P_3''}{P_3} = 0. \tag{3.48}$$

Now the first two terms are dependent only on ρ so that it must be constant and we choose $n(n+1)$ as the separation constant which gives

$$\rho^2 P_1'' + 2\rho P_1' - n(n+1)P_1 = 0. \tag{3.49}$$

Setting $t = \ln\rho$, (3.49) becomes

$$P_1''(t) + P_1'(t) - n(n+1)P_1(t) = 0. \tag{3.50}$$

So, the general solution of (3.50) has the form

$$P_1 = A_n e^{nt} + B_n e{-}(n+1)t = A_n\rho^n + B_n\rho^{-(n+1)}. \tag{3.51}$$

Then the remainder of (3.48) is

$$\sin^2\theta\frac{P_2^{''}}{P_2}+\frac{\sin 2\theta}{2}\frac{P_2^{''}}{P_2}+n(n+1)\sin^2\theta+\frac{P_3^{''}}{P_3}=0. \tag{3.52}$$

The first three terms and the last term of (3.52) depend on each other, and we can assume

$$\sin^2\theta\frac{P_2^{''}}{P_2}+\frac{\sin 2\theta}{2}\frac{P_2^{''}}{P_2}+n(n+1)\sin^2\theta=-\frac{P_3^{''}}{P_3}=m^2, \tag{3.53}$$

which gives

$$P_3^{''}+m^2P_3=0, \tag{3.54}$$

$$\sin^2\theta P_2^{''}+\frac{\sin 2\theta}{2}P_2^{''}+\left[n(n+1)\sin^2\theta-m^2\right]P_2=0. \tag{3.55}$$

From (3.54) it is seen that

$$P_3=C_m\cos(m\phi)+D_m\sin(m\phi). \tag{3.56}$$

It follows from periodicity that m is an integer number. For (3.55) and introducing $w=\cos(\theta)$ we have

$$(1-w^2)\frac{d^2P_2(\theta)}{dw^2}-2w\frac{dP_2(\theta)}{dw}+\left[n(n+1)-\frac{m^2}{1-w^2}\right]P_2(\theta)=0, \tag{3.57}$$

which is the associated Legendre equation. The solution of this equation is known as the associated Legendre polynomials, $\mathcal{P}_n^m(w)$ [2]. Therefore, the elementary solution of (3.47) is

$$\begin{aligned}U(\rho^*,\theta,\phi)=&\left(A_n(\rho^*r(\theta,\phi))^n+B_n(\rho^*r(\theta,\phi))^{-(n+1)}\right)\cdot\\&P_n^m(cos\theta)\left(C_m\cos(m\phi)+D_m\sin(m\phi)\right),\\&n=0,1,2,...,\ m=0.1,...,n.\end{aligned} \tag{3.58}$$

For the interior problem one needs to require $U<\infty$ so $B_n=0$. Then, we get

$$\begin{aligned}U(\rho^*,\theta,\phi)=&\left[\rho^*r(\theta,\phi)\right]^nP_n^m(\cos\theta)\left(A_{n,m}\cos(m\phi)+B_{n,m}\sin(m\phi)\right),\\&n=0,1,2,...,\ m=0.1,...,n.\end{aligned} \tag{3.59}$$

So, the general solution is given as,

$$U(\rho^*,\theta,\phi)=\sum_{n=0}^{+\infty}\sum_{m=0}^{n}\left[\rho^* r(\theta,\phi)\right]^n P_n^m(\cos\theta)\left(A_{n,m}\cos(m\phi)+B_{n,m}\sin(m\phi)\right), \tag{3.60}$$

The coefficients A_n^m and B_n^m can be determined by imposing the boundary condition ($\rho^*=1$) and thus

$$f(\theta,\phi)=U(1,\theta,\phi)=\sum_{n=0}^{+\infty}\sum_{m=0}^{n}\left[r(\theta,\phi)\right]^n P_n^m(\cos\theta)\left(A_{n,m}\cos(m\phi)+B_{n,m}\sin(m\phi)\right). \tag{3.61}$$

Consider the solution of (3.61) to be a Fourier series

$$f(\theta,\phi)=\sum_{n=0}^{+\infty}\sum_{m=0}^{n}P_n^m(cos\theta)\left(\alpha_{n,m}\cos(m\phi)+\beta_{n,m}\sin(m\phi)\right). \tag{3.62}$$

Utilize the orthogonality of trigonometric function and Legendre polynomials, multiply (3.62) by $P_h^k(\cos\theta)\cos(k\phi)\sin\theta$ and integral to obtain

$$\alpha_{n,m}=\frac{\epsilon_m(2n+1)}{4\pi}\frac{(n-m)!}{(n+m)!}\int_0^{2\pi}\int_0^{\pi}f(\theta,\phi)P_n^m(\cos\theta)\cos(m\phi)\sin\theta d\theta d\phi, \tag{3.63}$$

with Neumann symbol ϵ_m, so

$$\epsilon_m=\begin{cases}1, & \text{m=0}\\ 2, & \text{m}\neq 0.\end{cases}$$

Similarly, we get

$$\beta_{n,m}=\frac{\epsilon_m(2n+1)}{4\pi}\frac{(n-m)!}{(n+m)!}\int_0^{2\pi}\int_0^{\pi}f(\theta,\phi)P_n^m(\cos\theta)\sin(m\phi)\sin\theta d\theta d\phi. \tag{3.64}$$

Finally the coefficients A_n^m and B_n^m are obtained by solving the following equations

$$\begin{cases}\sum\limits_{n=0}^{+\infty}\sum\limits_{m=0}^{n}\frac{\epsilon_k(2h+1)}{4\pi}\frac{(h-k)!}{(h+k)!}\Big[A_{n,m}\int_0^{2\pi}\int_0^{\pi}\left(r(\theta,\phi)\right)^n P_n^m(\cos\theta)P_h^k(\cos\theta)\cos(m\phi)\cos(k\phi)\sin\theta d\theta d\phi\\ +B_{n,m}\int_0^{2\pi}\int_0^{\pi}\left(r(\theta,\phi)\right)^n P_n^m(\cos\theta)P_h^k(\cos\theta)\sin(m\phi)\cos(k\phi)\sin\theta d\theta d\phi\Big]=\alpha_{h,k},\\ \\ \sum\limits_{n=0}^{+\infty}\sum\limits_{m=0}^{n}\frac{\epsilon_k(2h+1)}{4\pi}\frac{(h-k)!}{(h+k)!}\Big[A_{n,m}\int_0^{2\pi}\int_0^{\pi}\left(r(\theta,\phi)\right)^n P_n^m(\cos\theta)P_h^k(\cos\theta)\cos(m\phi)\sin(k\phi)\sin\theta d\theta d\phi\\ +B_{n,m}\int_0^{2\pi}\int_0^{\pi}\left(r(\theta,\phi)\right)^n P_n^m(\cos\theta)P_h^k(\cos\theta)\sin(m\phi)\sin(k\phi)\sin\theta d\theta d\phi\Big]=\beta_{h,k},\end{cases}$$

$$h = 0, 1, 2..., \ k = 0, 1, ..., h. \tag{3.65}$$

3.2.2 Helmholtz equation

Next, let us consider the interior Dirichlet problem for the Helmholtz equation in a domain Ω

$$\begin{cases} \Delta u(\rho, \theta, \phi) + a^2 u(\rho, \theta, \phi) = 0 & \text{in} \quad \Omega \\ u(\rho, \theta, \phi) = f(\theta, \phi) & \text{on} \quad \partial\Omega \end{cases} \tag{3.66}$$

in which the boundary defined by the polar equation $\rho = r(\theta, \phi)$ and the propagation coefficient $a > 0$.

Similarity, the elementary solution of problem (3.66) can be searched by separation of variables imposing the form $u(\rho, \theta, \phi) = U(\rho^*, \theta, \phi) = P_1(\rho)P_2(\theta)P_3(\phi)$. Substituting this form into (3.66) it is seen that the functions $P_1(\rho)$, $P_2(\theta)$ and $P_3(\phi)$ must satisfy the following equations respectively:

$$\rho^2 \frac{d^2 P_1}{d\rho^2} + 2\rho \frac{dP_1}{d\rho} + (a^2\rho^2 - \lambda^2)P_1 = 0, \tag{3.67}$$

$$\frac{d^2 P_2}{d\theta^2} + \cot\theta \frac{dP_2}{d\theta} + \left(\lambda^2 - \frac{\mu^2}{\sin^2\theta}\right) P_2 = 0, \tag{3.68}$$

$$\frac{d^2 P_3}{d\phi^2} + \mu^2 P_2 = 0, \tag{3.69}$$

The parameters λ and μ are separation constants. From the same derivation as detailed in section 3.2.1, we have $\mu = m \in \mathbb{Z}$, $\lambda^2 = n(n+1)$, $n \in \mathbb{N}_0$ and

$$P_2(\theta) = g_{n,m} P_n^m(cos\theta), \tag{3.70}$$

$$P_3(\phi) = C_m \cos(m\phi) + D_m \sin(m\phi), \tag{3.71}$$

where C_m, D_m, $g_{n,m}$ are unknown constants and $P_n^m(\cdot)$ is the associated Legendre function of the first kind with orders (n, m). In order to solve the radial function $P_1(\rho)$ of (3.67), we set

$$P_4(\rho) = (a\rho)^{\frac{1}{2}} P_1(\rho), \tag{3.72}$$

with this transformation (3.67) becomes

$$\rho^2 \frac{d^2 P_4}{d\rho^2} + \rho \frac{dP_4}{d\rho} + \left[a^2\rho^2 - (n + \frac{1}{2})^2\right] P_4 = 0. \tag{3.73}$$

Let $s = a\rho$ and $P_5(s) \equiv P_4(\frac{s}{a})$, (3.73) turns into a Bessel's equation

$$\frac{d^2P_5}{ds^2} + \frac{dP_5}{ds} + \left[s^2 - (n+\frac{1}{2})^2\right] P_5 = 0. \tag{3.74}$$

Due to the boundedness at $\rho = 0$ the solution of function $P_1(\rho)$ can be expressed as a function of spherical Bessel functions of the first kind [2]

$$P_1(\rho) = A_n j_n(h\rho), \tag{3.75}$$

where $j_n(x) = \sqrt{\frac{\pi}{2x}} J_{n+\frac{1}{2}}(x)$, $J_{n+\frac{1}{2}}$ is the Bessel function of the first kind with order $(n+\frac{1}{2})$. Therefore, the general solution of the Helmholtz problem (3.66) is of the form

$$U(\rho^*, \theta, \phi) = \sum_{n=0}^{+\infty} \sum_{m=0}^{n} j_n(a\rho^* r(\theta,\phi)) P_n^m(\cos\theta)(A_{n,m}\cos(m\phi) + B_{n,m}\sin(m\phi)). \tag{3.76}$$

In order to identify the coefficients $A_{n,m}$, $B_{n,m}$, imposing the boundary condition

$$\begin{aligned} f(\theta,\phi) = U(1,\theta,\phi) = \sum_{n=0}^{+\infty} \sum_{m=0}^{n} & j_n\left(hr(\theta,\phi)\right) P_n^m(\cos\theta) \\ & (A_{n,m}\cos(m\phi) + B_{n,m}\sin(m\phi)). \end{aligned} \tag{3.77}$$

Using the Fourier method we have

$$f(\theta,\phi) = \sum_{n=0}^{+\infty} \sum_{m=0}^{n} P_n^m(cos\theta)\left(\alpha_{n,m}\cos(m\phi) + \beta_{n,m}\sin(m\phi)\right). \tag{3.78}$$

Consider the orthogonality of trigonometric function and Legendre polynomials one can find that

$$\left\{ \begin{array}{c} \alpha_{n,m} \\ \beta_{n,m} \end{array} \right\} = \frac{\epsilon_m(2n+1)}{4\pi} \frac{(n-m)!}{(n+m)!} \int_0^{2\pi} \int_0^{\pi} f(\theta,\phi) P_n^m(\cos\theta) \left\{ \begin{array}{c} \cos(m\phi) \\ \sin(m\phi) \end{array} \right\} \sin\theta d\theta d\phi, \tag{3.79}$$

with Neumann symbol ϵ_m

$$\epsilon_m = \left\{ \begin{array}{ll} 1, & \text{m=0} \\ 2, & \text{m}\neq 0. \end{array} \right.$$

Finally the coefficients $A_{n,m}$, $B_{n,m}$ can be obtained by solving the following equations

$$\sum_{n=0}^{+\infty}\sum_{m=0}^{n}\begin{bmatrix} V^{+}_{n,m,k,l} & W^{+}_{n,m,k,l} \\ V^{-}_{n,m,k,l} & W^{-}_{n,m,k,l} \end{bmatrix}\cdot\begin{bmatrix} A_{n,m} \\ B_{n,m} \end{bmatrix}=\begin{bmatrix} \alpha_{h,k} \\ \beta_{h,k} \end{bmatrix}$$

$$k=0,1,2,...,\ l=0,1,...,k, \tag{3.80}$$

where

$$V^{\pm}_{n,m,k,l}=\frac{\epsilon_l(2k+1)}{4\pi}\frac{(k-l)!}{(k+l)!}\int_0^{2\pi}\int_0^{\pi} j_n\left(ar(\theta,\phi)\right)P_n^m(\cos\theta)P_k^l(\cos\theta)\cos(m\phi)\cdot \left\{\begin{array}{c}\cos(l\phi)\\ \sin(l\phi)\end{array}\right\}\sin\theta d\theta d\phi,$$

$$W^{\pm}_{n,m,k,l}=\frac{\epsilon_l(2k+1)}{4\pi}\frac{(k-l)!}{(k+l)!}\int_0^{2\pi}\int_0^{\pi} j_n\left(ar(\theta,\phi)\right)P_n^m(\cos\theta)P_k^l(\cos\theta)\sin(m\phi)\cdot \left\{\begin{array}{c}\cos(l\phi)\\ \sin(l\phi)\end{array}\right\}\sin\theta d\theta d\phi.$$

3.2.3 Wave equation

Finally, let us consider the interior Dirichlet problem for the wave equation with constant propagation speed a in a domain Ω. Assume the displacement of the boundary is equal to zero at all times t and we define the initial displacement and velocity distribution by continuous functions $f_1(\rho,\theta,\phi)$ and $f_2(\rho,\theta,\phi)$ respectively. Thus the system is of the form

$$\left\{\begin{array}{lll} \frac{\partial^2}{\partial t^2}u(\rho,\theta,\phi,t)=a^2\Delta u(\rho,\theta,\phi,t), & \text{in} & \Omega \\ u(\rho,\theta,\phi,t)=0, & \text{on} & \partial\Omega \\ u(\rho,\theta,\phi,0)=f_1(\rho,\theta,\phi), & & \\ \frac{\partial}{\partial t}u(\rho,\theta,\phi,0)=f_2(\rho,\theta,\phi). & & \end{array}\right. \tag{3.81}$$

Reconsider the method of separation of variables and assume that the elementary solution of the system is of the form

$$u(\rho,\theta,\phi,t)=U(\rho^*,\theta,\phi,t)=P_1(\rho)P_2(\theta)P_3(\phi)P_4(t). \tag{3.82}$$

Substituting into the wave equation and introducing two separation variables λ, s, it is seen that the functions $P_1(\rho)$, $P_2(\theta)$, $P_3(\phi)$ and $P_4(t)$ have to satisfy the following equations

$$\begin{cases} \rho^2 P_1''(\rho) + 2\rho P_1'(\rho) + \left(k^2\rho^2 - \lambda^2\right) P_1(\rho) = 0, \\ P_2''(\theta) + \cot\theta P_2'(\theta) + \left(\lambda^2 - \frac{\mu^2}{\sin^2\theta}\right) P_2(\theta) = 0, \\ P_3''(\phi) + \mu^2 P_3(\phi) = 0, \\ P_4''(t) + a^2 k^2 P_4(t) = 0. \end{cases} \tag{3.83}$$

Due to the periodicity and a single value for θ, the constant variable $\mu = m \in \mathbb{Z}$ so that

$$P_2(\theta) = a_m \cos(m\theta) + b_m \sin(m\theta), \tag{3.84}$$

with unknown arbitrary constants a_m, b_m. For the equation of function P_4 one finds that

$$P_4(t) = c_k \cos(akt) + d_k \sin(akt). \tag{3.85}$$

Using the same process as detailed in section 3.2.2, we have

$$P_1(\rho) = e_n j_n(k\rho), \tag{3.86}$$

$$P_2(\theta) = g_{n,m} P_n^m(\cos\theta), \tag{3.87}$$

where $j_n(\cdot)$ is the spherical Bessel function of the first kind with order n and $P_n^m(\cdot)$ is the associated Legendre function of the first kind with orders (n, m).

Thus the general solution of (3.81) has the form

$$\begin{aligned} U(\rho^*, \theta, \phi, t) = \sum_{n=0}^{+\infty} \sum_{m=0}^{n} P_n^m(\cos\theta) \sum_k j_n(k\rho^* r(\theta)) \cdot \\ [A_{m,k} \cos(m\phi)\cos(akt) + B_{m,k} \cos(m\phi)\sin(akt) \\ + C_{m,k} \sin(m\phi)\cos(akt) + D_{m,k} \sin(m\phi)\sin(akt)]. \end{aligned} \tag{3.88}$$

Imposing the boundary condition $\rho^* = 1$, and thus $u(r(\theta,\phi),\theta,\phi,t) = 0$, results in $j_n(kr(\theta,\phi)) = 0$ so that $k(\theta,\phi) = \xi_n / r(\theta,\phi)$ with unknown coefficients ξ_n. Denote ξ_k^n is the kth positive root of the spherical Bessel function of the first kind with order n so that $k = \xi_k^n / r(\theta,\phi)$, $j \in \mathbb{N}$. Therefore the general solution (3.88) becomes

$$\begin{aligned} U(\rho^*, \theta, \phi, t) = \sum_{n=0}^{+\infty} \sum_{m=0}^{n} \sum_{k=1}^{+\infty} j_n(\xi_k^n \rho^*) P_n^m(\cos\theta) \cdot \\ \left[A_{n,m,k} \cos(m\phi) \cos\left(\frac{a\xi_k^n t}{r(\theta,\phi)}\right) + B_{n,m,k} \cos(m\phi) \sin\left(\frac{a\xi_k^n t}{r(\theta,\phi)}\right) \right. \\ \left. + C_{n,m,k} \sin(m\phi) \cos\left(\frac{a\xi_k^n t}{r(\theta,\phi)}\right) + D_{n,m,k} \sin(m\phi) \sin\left(\frac{a\xi_k^n t}{r(\theta,\phi)}\right) \right], \end{aligned} \tag{3.89}$$

and this gives

$$U_t(\rho^*,\theta,\phi,t) = \frac{a}{r(\theta,\phi)}\sum_{n=0}^{+\infty}\sum_{m=0}^{n}\sum_{k=1}^{+\infty}\xi_k^n j_n(\xi_k^n\rho^*)P_n^m(\cos\theta)\cdot \\ \left[-A_{n,m,k}\cos(m\phi)\sin\left(\frac{a\xi_k^n t}{r(\theta,\phi)}\right) + B_{n,m,k}\cos(m\phi)\cos\left(\frac{a\xi_k^n t}{r(\theta,\phi)}\right)\right. \\ \left. -C_{n,m,k}\sin(m\phi)\sin\left(\frac{a\xi_k^n t}{r(\theta,\phi)}\right) + D_{n,m,k}\sin(m\phi)\cos\left(\frac{a\xi_k^n t}{r(\theta,\phi)}\right)\right]. \tag{3.90}$$

Using the initial displacement and velocity conditions and assuming them to be of the form

$$F_1(\rho^*,\theta,\phi) = f_1(\rho,\theta,\phi) = \sum_{n=0}^{+\infty}\sum_{m=0}^{n} P_n^m(\cos\theta)\cdot(\alpha_{n,m}\cos(m\theta)+\beta_{n,m}\sin(m\theta)), \\ F_2(\rho^*,\theta,\phi) = f_2(\rho,\theta,\phi) = \frac{a}{r(\theta,\phi)}\sum_{n=0}^{+\infty}\sum_{m=0}^{n} P_n^m(\cos\theta)\cdot(\eta_{n,m}\cos(m\theta)+\gamma_{n,m}\sin(m\theta)), \tag{3.91}$$

where the coefficients $\alpha_{n,m}$, $\beta_{n,m}$, $\eta_{n,m}$ and $\gamma_{n,m}$ are obtained using Fourier's method

$$\left\{\begin{array}{c}\alpha_{n,m}\\ \beta_{n,m}\end{array}\right\} = \frac{\epsilon_m(2n+1)}{4\pi}\frac{(n-m)!}{(n+m)!}\int_0^{2\pi}\int_0^{\pi} F_1(\rho^*,\theta,\phi)P_n^m(\cos\theta)\cdot \\ \left\{\begin{array}{c}\cos(m\phi)\\ \sin(m\phi)\end{array}\right\}\sin\theta d\theta d\phi, \tag{3.92}$$

$$\left\{\begin{array}{c}\eta_{n,m}\\ \gamma_{n,m}\end{array}\right\} = \frac{\epsilon_m(2n+1)}{4\pi a}\frac{(n-m)!}{(n+m)!}\int_0^{2\pi}\int_0^{\pi} r(\theta,\phi)F_2(\rho^*,\theta,\phi)P_n^m(\cos\theta)\cdot \\ \left\{\begin{array}{c}\cos(m\phi)\\ \sin(m\phi)\end{array}\right\}\sin\theta d\theta d\phi, \tag{3.93}$$

with

$$\epsilon_m = \left\{\begin{array}{ll}1, & \text{m=0}\\ 2, & \text{m}\neq 0.\end{array}\right.$$

Finally, consider the orthogonality of the Bessel function of the first kind

$$\int_0^1 j_n(\xi_k^n\rho^*)j_n(\xi_k^l\rho^*)\rho^{*2}d\rho^* = \left\{\begin{array}{ll}\frac{1}{2}\left[j_{n+1}(\xi_k^n)\right]^2, & n=l\\ 0, & n\neq l\end{array}\right. \tag{3.94}$$

and (3.89) $\backsim$ (3.93), so that the coefficients $A_{n,m,k}$, $B_{n,m,k}$, $C_{n,m,k}$ and $D_{n,m,k}$ can be obtained by solving the following system

$$\left\{ \begin{array}{c} A_{n,m,k} \\ C_{n,m,k} \end{array} \right\} = \frac{2}{\left[j_{n+1}(\xi_k^n)\right]^2} \int_0^1 j_n(\xi_k^n \rho^*) \left\{ \begin{array}{c} \alpha_{n,m}(\rho^*) \\ \beta_{n,m}(\rho^*) \end{array} \right\} \rho^{*2} d\theta, \tag{3.95}$$

$$\left\{ \begin{array}{c} B_{n,m,k} \\ D_{n,m,k} \end{array} \right\} = \frac{2}{\xi_k^n \left[j_{n+1}(\xi_k^n)\right]^2} \int_0^1 j_n(\xi_k^n \rho^*) \left\{ \begin{array}{c} \eta_{n,m}(\rho^*) \\ \gamma_{n,m}(\rho^*) \end{array} \right\} \rho^{*2} d\theta. \tag{3.96}$$

$$n = 0, 1, 2, ..., \ m = 1, 2, ..., n, \ k = 1, 2, 3, ...$$

3.3 Summary

In this chapter the proposed parametrization of an arbitrary cross section shape following the "superformula" described in previous chapter 2 is exploited to solve quasi-analytically the physical equations for two-dimensional and three-dimensional arbitrary shapes. Concretely, solutions for the interior Dirichlet problem for the Laplace, Helmholtz and wave equation are presented. The numerical solution is presented and the accuracy is validated for the Laplace and Helmholtz equations of two-dimensional shapes.

Chapter 4

Application to biological flows

Contents

In chapter 2, we modeled and discussed the impact of the cross section shape on developed viscous flow through a uniform channel. Since pressure-driven flow in constricted channels is an important issue for physiological flows during normal as well as pathological health conditions (stenosis), in the following section 4.1 a simple quasi-three-dimensional flow model is formulated for steady flow which accounts for kinetic losses, viscosity as well as the cross section shape [127][1]. In the introduction, it was argued that simplified flow models favor model analysis for biological applications due to their interpretation in terms of significant physiological parameters as well as due to their low computational cost which facilitates parameter space analysis. In order to illustrate these points, in section 4.2, we apply the quasi-three-dimensional flow model, proposed in section 4.1, to the stability analysis of a physical model of human phonation, *i.e.* vocal folds auto-oscillation during voiced sound production. We discuss the potential impact of the flow model taking into account the cross section shape on the predicted minimum pressure required to sustain phonation.

4.1 Stenosis

In this section we consider constricted channels due to their relevance for physiological flows during normal as well as pathological health conditions (stenosis). We propose a simple 'quasi-three-dimensional' (quasi-3D) flow model which accounts for kinetic losses, viscosity as well

[1] The quasi-three-dimensional model for unsteady flow is presented in Appendix G.

as the cross section shape [127]. The influence of the cross section shape on the pressure distribution is discussed since the pressure distribution will determine the forces exerted by the flow on the enveloping walls and is therefore a major quantity for biological applications. The outcome of the 'quasi-three-dimensional' flow model is compared to the outcome of a 'quasi-one-dimensional' flow model for which details of the cross section shape are neglected. Biological stenosis occur for different fluids. In the following, we consider blood flow and air flow since these fluids occur in major circulatory systems, *i.e.* the cardiovascular and respiratory system. Characteristic fluid properties are summarized in Table 4.1.

Table 4.1: Overview of major fluid properties.

	dynamic viscosity μ [Pa·s]	density ρ [kg/m^3]
blood	3.5×10^{-3}	1060
air	1.8×10^{-5}	1.2
ratio[1]	194	883

(1) ratio of blood property to air property.

4.1.1 A quasi-three-dimensional flow model

Based on a non-dimensional analysis of the governing Navier-Stokes equations for pressure-driven, steady, laminar and incompressible flow through a channel with varying streamwise area $A(x)$ involving a constricted portion as illustrated in Fig. 4.1. The degree of stenosis is quantified by the ratio $R_c = A_{min}/A_0$, the streamwise extent of the stenosis is given by L_s and the streamwise extent of the constriction with minimum area is denoted L_c. In case of a severe stenosis ($R_c \ll 1$), both flow inertia, *i.e.* kinetic losses (subscript 'ber') , and viscosity (subscript 'visc') need to be accounted for [126, 9].

Therefore, the streamwise momentum equation of the governing Navier-Stokes equation is approximated using volume flow rate conservation $dQ/dx = 0$, as:

$$-\frac{Q^2}{A^3}\frac{dA}{dx} + \frac{1}{\rho}\frac{dP}{dx} = \nu\left(\frac{\partial^2 u}{\partial y^2} + \frac{\partial^2 u}{\partial z^2}\right), \tag{4.1}$$

with driving pressure gradient dP/dx, local velocity $u(x, y, z)$, volume flow rate Q, fluid density ρ and kinematic viscosity $\nu = \mu/\rho$. The spanwise and transverse components of the momentum equation are described by (2.6). The flow model expressed in (4.1) accounts for viscosity (right hand term) as well as flow inertia (first source term at the left hand side) and depends therefore on the area as well as on the shape of the cross section. It is seen that for a uniform channel, so that $dA/dx = 0$ holds, (4.1) reduces to purely viscous flow described by (2.5). The same way, it is seen that when viscosity is neglected, *i.e.* $\nu = 0$ as for an ideal (symbol B) inviscid flow, (4.1) reduces to Euler's equation flow,

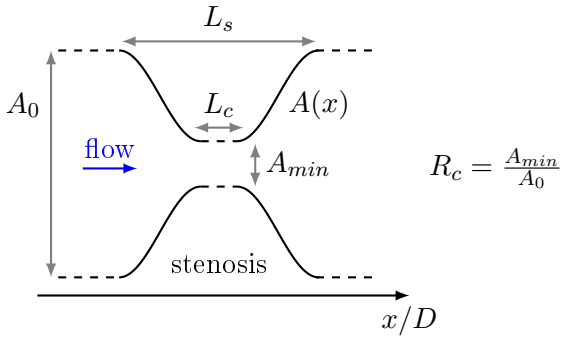

Figure 4.1: Schematic overview of a constricted channel, representing a stenosis, oriented along the streamwise x direction: varying streamwise channel area $A(x)$, unconstricted inlet area A_0 and minimum area A_{min}. The degree of stenosis is expressed by ratio $R_c = A_{min}/A_0$ and its streamwise extent by L_s. The streamwise extent of the minimum constriction is denoted L_c.

$$\bar{u}\frac{d\bar{u}}{dx} = -\frac{1}{\rho}\frac{dP}{dx}, \tag{4.2}$$

with local bulk velocity $\bar{u}(x)$ so that volume flow rate $Q = A(x)\bar{u}(x)$. The contribution of kinetic losses to the pressure drop is then:

$$\Delta P_{ber}(x) = \frac{\rho}{2}Q^2\left[\frac{1}{A(x)^2} - \frac{1}{A_0^2}\right], \tag{4.3}$$

where A_0 denotes the unconstricted channel area at the channel inlet.

Depending on driving pressure, fluid and geometry – in particular the minimum streamwise channel area A_{min} – viscous boundary layer development will affect the flow development and a viscosity needs to be accounted for. When (4.1) is used a three-dimensional aspect is added to the flow model accounting for the viscous term. Classical simplified flow models rely either on a two-dimensional flow assumption by neglecting the spanwise dimension [120, 23, 20] or fully reduce the problem to a one-dimensional model for which the right hand side of (4.1) is reduced to a flow resistance term characterized by a constant [107, 97, 111].

In the following, a constricted channel with a smooth or an abrupt diverging area portion is accounted for, as depicted in Fig. 4.2. For an abrupt expansion characterized by a sharp trailing edge, the streamwise position of flow separation x_s is fixed and coincides with the trailing end of the constriction, so that $x_s = x_3$ as depicted in Fig. 4.2b. In the case of a smooth expansion, the flow separation position depends on the channel geometry as well as on the imposed driving pressure gradient dP/dx, so that $x_3 < x_s \leq x_4$ as illustrated in Fig. 4.2a and the position of flow separation needs to be determined.

The separation position $x = x_s$ corresponds to the position along the diverging portion

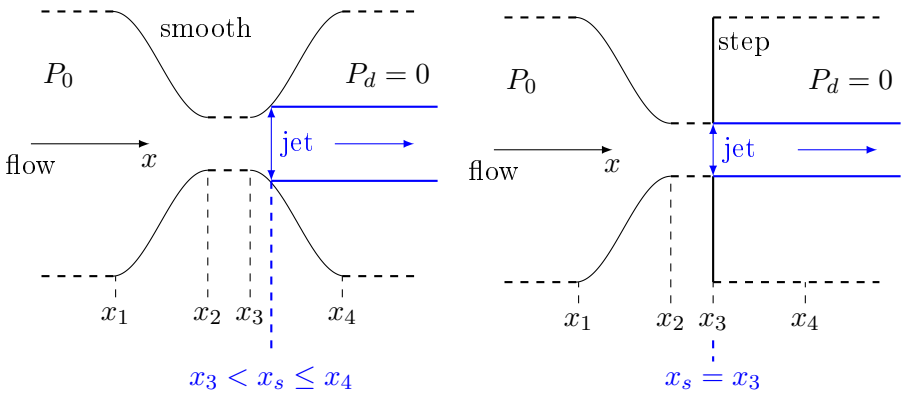

(a) smooth expansion (b) abrupt expansion

Figure 4.2: Schematic overview of flow within a converging-diverging channel geometry ($x_1 \leq x \leq x_4$) with upstream area A_0 and minimum area A_{min} ($x_2 \leq x \leq x_3$) (see Fig. 4.1) for a) a smooth and b) an abrupt expansion. Flow separation and jet formation occurs for $x = x_s$. P_0 denotes the upstream pressure and P_d the downstream pressure.

where the area yields $A(x_s) = c_s \times A_{min}$ with $c_s = 1.2$. This *ad-hoc* criterion is commonly used and validated for a quasi-one-dimensional flow model approach [120, 23, 74]. The pressure downstream from the flow separation point is assumed to be zero so that $P_d = 0$ holds for $x \geq x_s$ and the model outcome remains constant for $x \geq x_s$. Consequently, imposing the upstream pressure P_0 allows to impose the total driving pressure difference.

Therefore, the same way as for a quasi-one-dimensional flow model [25, 120] (symbol BP), firstly the volume flow rate Q can be estimated from the imposed pressure gradient using (4.1). Next, the streamwise distribution of other flow quantities such as the pressure distribution up to flow separation can be derived since from (4.1), it follows that,

$$P_0 - P_d = \Delta P_{visc} + \Delta P_{ber}, \tag{4.4}$$

holds with ΔP_{visc} and ΔP_{ber} as defined in (2.13) and (4.3).

In the following, we model the pressure distribution using the proposed quasi-three-dimensional flow model for a smooth and an abrupt constricted channel with different cross section shapes[2] for air flow (section 4.1.2) and blood flow (section 4.1.3). Different stenosis configurations are considered by varying some of the geometrical parameters depicted in Fig. 4.1: stenosis degree R_c, minimum area A_{min}, and streamwise extent of minimum constriction L_c. The possible impact of cross section details on the pressure distribution is assessed applying default parameter set (α_1), non-default parameter set (α_2) and fixed width ($y_{tot} = w$) to each cross section shape, the same way as was defined previously in section 2.1.2.

[2]The cross section shapes are abbreviated as depicted in Fig. 2.3: circle (cl), rectangle (re), ellipse (el), eccentric annulus (ea), half moon (hm), circular sector (cs), equilateral triangle (tr) and limacon (lm).

4.1.2 Pressure distribution: air flow

Fig. 4.3 and Fig. 4.4 illustrate the pressure distribution for a smooth and an abrupt expansion, as depicted in Fig. 4.2, for the different parameter sets – default parameter set (α_1), non-default parameter set (α_2) and fixed width ($y_{tot} = w$) – applied to each of the cross section shapes. The stenosis parameters are set as minimum area $A_{min} = 79\text{mm}^2$, $R_c = 30\%$ and $L_c/D_{cl} = 6$. The upstream pressure is set to $P_0 = 75\text{Pa}$. For the each of the cross section shapes the pressure distribution is modeled using the quasi-three-dimensional flow model presented in the previous section 4.1.1. For completeness, the pressure distributions associated with a quasi-one-dimensional model (BP)[3] and an ideal flow (B) are indicated as well.

It is seen that, in agreement with the findings outlined in section 2.1.2, the influence of the cross section shape on the model outcome is less pronounced using default parameter set α_1 than using non-default parameter set α_2 or fixed width $y_{tot} = w$. Pressure distributions obtained for all cross section shapes using default parameter set α_1 approximate the distribution of an ideal (B) fluid for which $\Delta P_{visc} = 0$ so that the quasi-one-dimensional (BP) approximation results in a severe underestimation of the pressure drop along the constricted portion. On the other hand, it is seen that for non-default parameter set α_2 and fixed width $y_{tot} = w$ the magnitude of the pressure drop varies significantly so that, depending on the cross section shape, the quasi-one-dimensional (BP) approximation results in an overestimation, an underestimation or an accurate estimation of the pressure drop within the constriction. Note that a rectangular cross section yields the smallest pressure drop using non-default parameter set α_2 and an annulus using fixed width $y_{tot} = w$. Moreover, it is observed that imposing a fixed width $y_{tot} = w$ results in a match between the quasi-one-dimensional (BP) approximation and the pressure distribution obtained using a rectangular cross section (re).

Fig. 4.5 quantifies the normalized pressure P/P_0 at position $x = x_2$, corresponding to the onset of the minimum area as defined in Fig. 4.2, and at position $x = x_m$ corresponding to the position of minimum pressure within the constriction. In the case of an abrupt expansion the minimum pressure equals zero regardless the cross section shape, whereas variations in the cross section shape increases the pressure at $x = x_2$ by up to $\leq 60\%$. In the case of a smooth expansion the impact of the cross section shape is more pronounced. At $x = x_m$, the minimum pressure P/P_0 is negative and varying the cross section shape induces a variation by as much as $\leq 40\%$. At the onset of the constriction $x = x_2$ the influence is even more prominent since the pressure variation increases to 100%. As for an abrupt expansion, the quasi-one-dimensional model accounting for viscosity (BP) results in a significant underestimation or overestimation of the pressure at $x = x_2$ ($\geq 15\%$) as well as at $x = x_m$ ($\leq 25\%$) depending on the cross section shape.

[3] Details are presented in Appendix. C.1

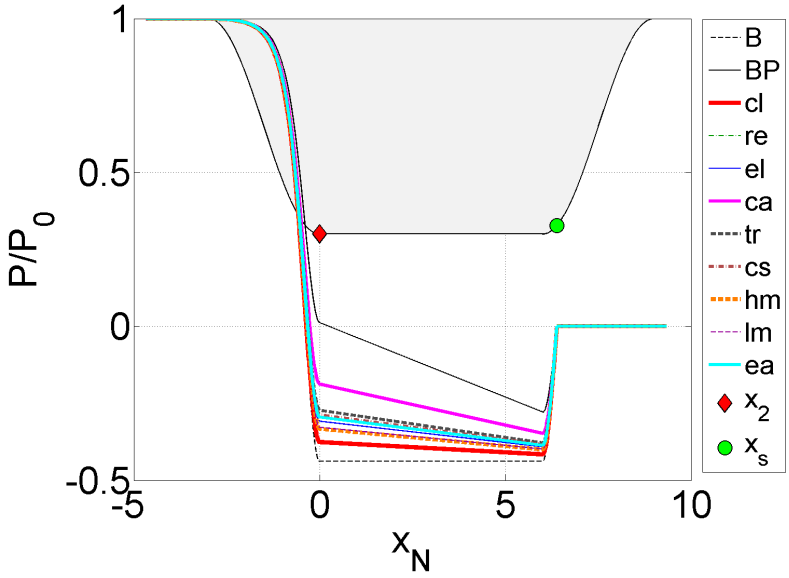

(a) smooth expansion (α_1)

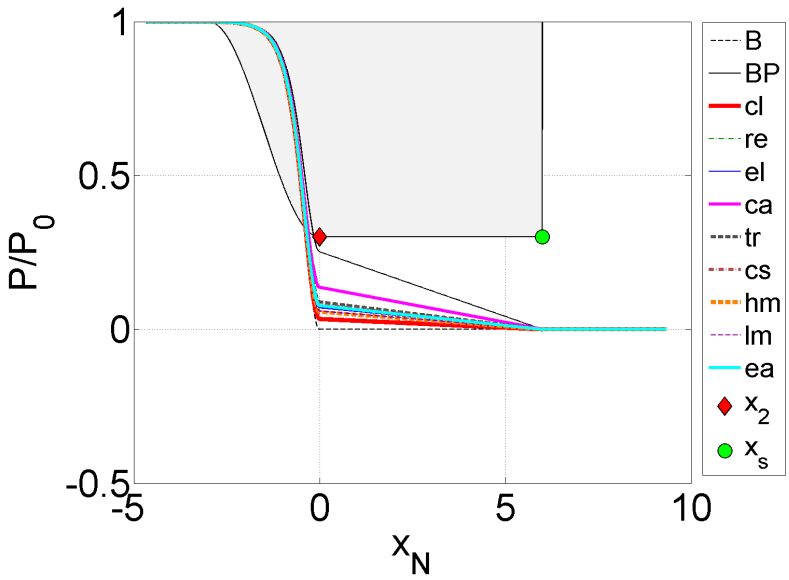

(b) abrupt expansion (α_1)

Figure 4.3: Illustration of normalized pressure distribution $P(x)/P_0$ using the quasi-three-dimensional model for air flow and imposed area $A_{min} = 79\text{mm}^2$, $P_0 = 75\text{Pa}$, $R_c = 30\%$ and $L_c/D_{cl} = 6$ for different cross section shapes obtained for a) smooth expansion and default parameter set (α_1) b) an abrupt expansion and default parameter set (α_1). For completeness also the pressure distribution associated with a quasi-one-dimensional model (BP) and an ideal flow (B) are indicated. The normalized geometry is indicated in gray shade and the streamwise x direction is normalized as $x_N = x/D_{cl}$. As a reference and following the notation in Fig. 4.2, the constriction onset x_2 and flow separation position x_s are indicated.

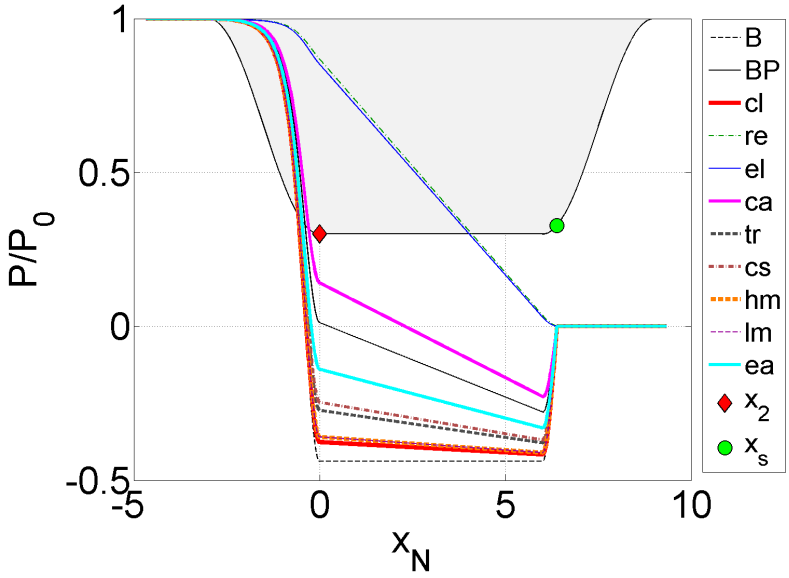

(a) smooth expansion (α_2)

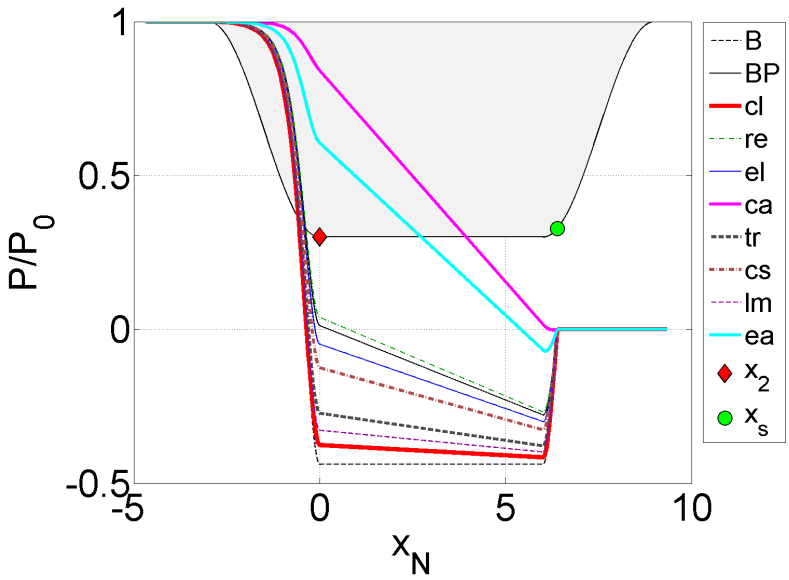

(b) smooth expansion ($y_{tot} = w$)

Figure 4.4: Illustration of normalized pressure distribution $P(x)/P_0$ using the quasi-three-dimensional model for air flow and imposed area $A_{min} = 79\text{mm}^2$, $P_0 = 75\text{Pa}$, $R_c = 30\%$ and $L_c/D_{cl} = 6$ for different cross section shapes obtained for a) non-default parameter set (α_2) and b) fixed width ($y_{tot} = w$). For completeness also the pressure distribution associated with a quasi-one-dimensional model (BP) and an ideal flow (B) are indicated. The normalized geometry is indicated in gray shade and the streamwise x direction is normalized as $x_N = x/D_{cl}$. As a reference and following the notation in Fig. 4.2, the constriction onset x_2 and flow separation position x_s are indicated.

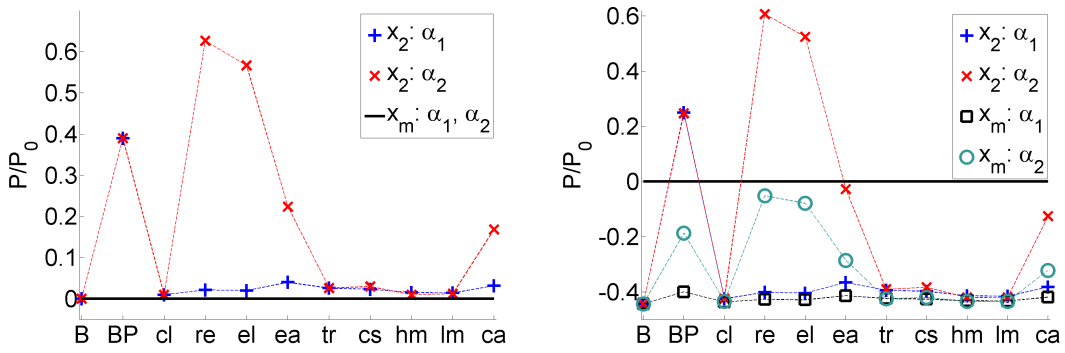

(a) abrupt expansion (b) smooth expansion

Figure 4.5: Normalized pressure values P/P_0 sampled from Fig. 4.3 at the onset of the minimum constriction x_2 and the position of minimum pressure x_m for air flow for an ideal fluid (B), a quasi-one-dimensional model (BP) and a quasi-three-dimensional model for different cross section shapes and parameter sets α_1 and α_2 for a) abrupt expansion and b) smooth expansion. Recall that the stenosis parameters are set to minimum area $A_{min} = 79\text{mm}^2$, $P_0 = 1000\text{Pa}$, $R_c = 30\%$ and $L_c/D_{cl} = 6$.

4.1.3 Pressure distribution: blood flow

In order to illustrate the impact of the fluid on the flow, the velocity distributions of developed flow through a uniform channel of area $A = 79\text{mm}^2$ are illustrated in Fig. 4.6 blood flow and air flow for a circular (cl) cross section shape and for a circular sector (cs) cross section shape. The maximum velocities are summarized in Table 4.2.

Table 4.2: Overview of maximum velocities from the distributions shown in Fig. 4.6 .

	u^{cl}_{max} [m/s]	u^{cs}_{max} [m/s]
blood	0.1339	0.1151
air	26.29	22.59
ratio[1]	5.1×10^{-3}	5.2×10^{-3}

(1) ratio of maximum velocity between blood and air flow.

From Table 4.2, it is seen that the ratio of maximum velocity for blood blow and air flow approximates $\approx 5 \times 10^{-3}$ which yields the inverse of the ratio of their dynamics viscosities listed in Table 4.1. For the circular sector the maximum velocity reduction compared to the circular cross section yields 15%.

Next, we apply the quasi-three-dimensional flow model proposed in section 4.1 to blood fluid through constricted channels of different cross section shape. The pressure distribution for

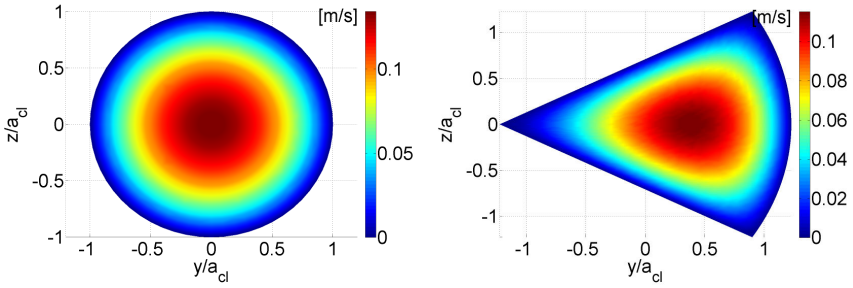

(a) circle + blood (b) circular sector + blood

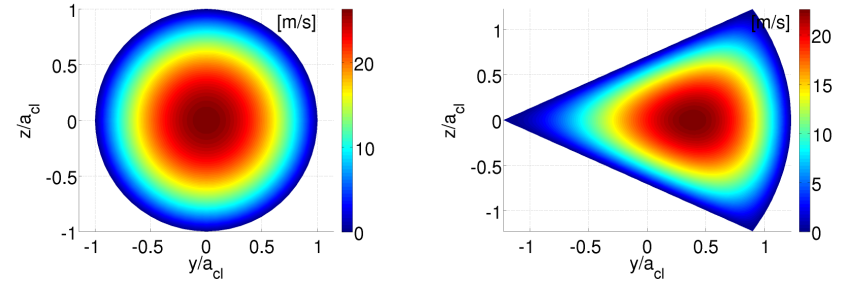

(c) circle + air (d) circular sector + air

Figure 4.6: Velocity distributions $u(y/a_{cl}, z/a_{cl})$ for a uniform channel with area $A = 79\text{mm}^2$ and driving pressure $dP/dx = 75\text{Pa/m}$ for blood flow and air flow. The cross section shapes are defined using geometrical default parameter set α_1.

a smooth and an abrupt expansion with minimum area $A_{min} = 79\text{mm}^2$ and default parameter set α_1 is illustrated in Fig. 4.7 for the same stenosis parameters as used for air flow and the upstream pressure is set to $P_0 = 75\text{Pa}$. It is seen that the same conclusions described for air flow in section 4.1.2 hold in the case of blood flow. The quasi-one-dimensional flow model (BP) severely underestimates the pressure drop compared to the quasi-three-dimensional flow model taking into account the cross section shape. The influence of the cross section shape on the model outcome becomes more prominent using the non-default parameter set (α_2) or imposing a fixed width ($y_{tot} = w$) since the difference between the pressure distributions between cross section shapes increases compared to the use of default parameter set (α_1). The quasi-one-dimensional flow model (BP) either overestimates or underestimates the pressure drop for all the cross section shapes except for the rectangular shape, which is reassuring since obviously the rectangular cross section shape and the two-dimensional flow assumption result in a similar cross section shape.

Comparing results for air flow shown in Fig. 4.3 and for blood flow in Fig. 4.7 and Fig. 4.8, it is observed that the pressure drop at the onset of minimum area x_2 are decreased for blood flow by at least 25% using the default parameter set α_1. This is particular the case for a quasi-one-dimensional (BP) flow model for which a 50% decrease is found. The average between different cross section shapes are increased from 5% to 10%. For non-default parameter set (α_2) and fixed width ($y_{tot} = w$) the same observations can be made as a result of the difference

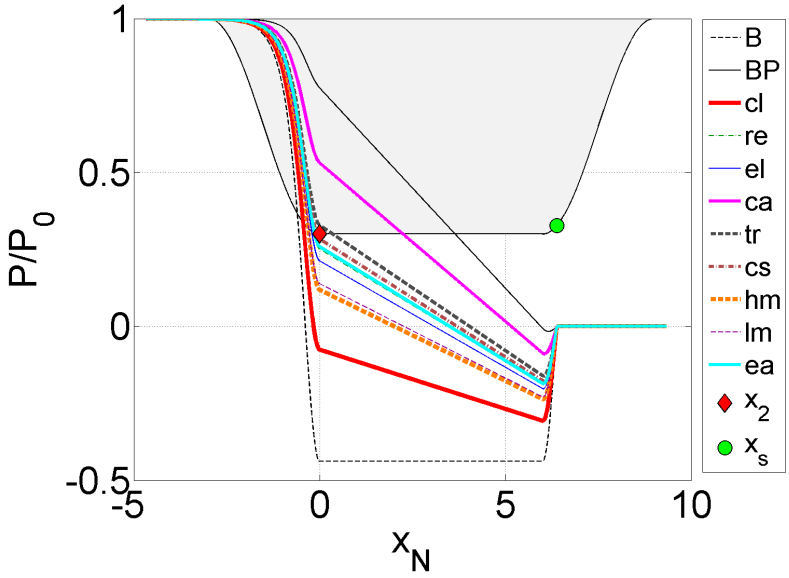

(a) smooth expansion (α_1)

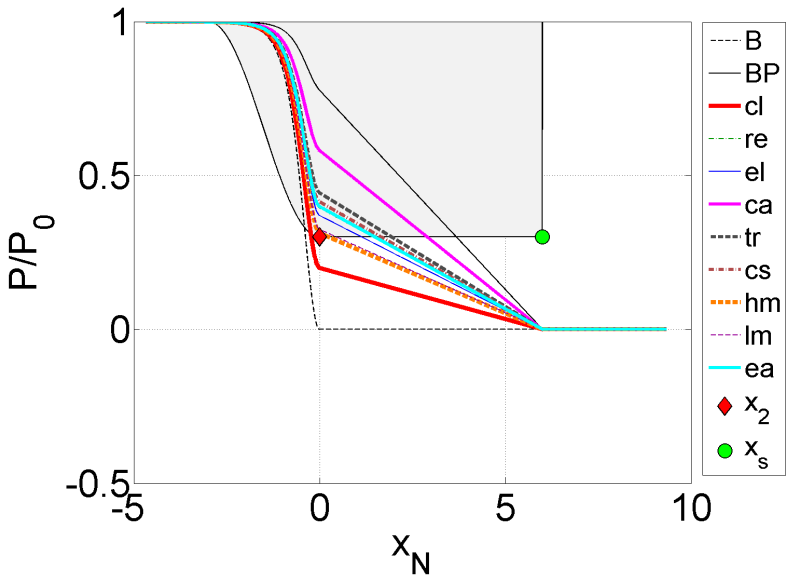

(b) abrupt expansion (α_1)

Figure 4.7: Illustration of normalized pressure distribution $P(x)/P_0$ using the quasi-three-dimensional model for blood flow and imposed area $A_{min} = 79\text{mm}^2$, $P_0 = 75\text{Pa}$, $R_c = 30\%$ and $L_c/D_{cl} = 6$ for different cross section shapes obtained for a) smooth expansion and default parameter set (α_1) b) abrupt expansion and default parameter set (α_1). For completeness also the pressure distribution associated with a quasi-one-dimensional model (BP) and an ideal flow (B) are indicated. The normalized geometry is indicated in gray shade and the streamwise x direction is normalized as $x_N = x/D_{cl}$. As a reference and following the notation in Fig. 4.2, the constriction onset x_2 and flow separation position x_s are indicated.

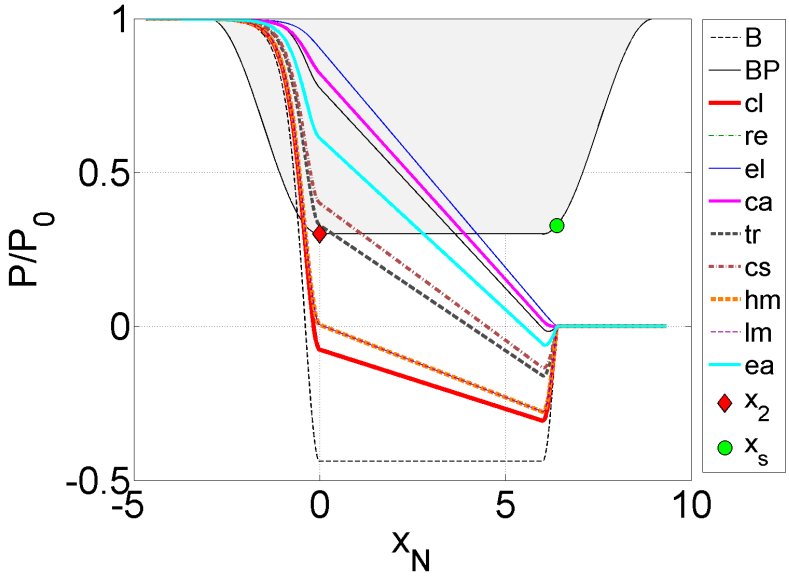

(a) smooth expansion (α_2)

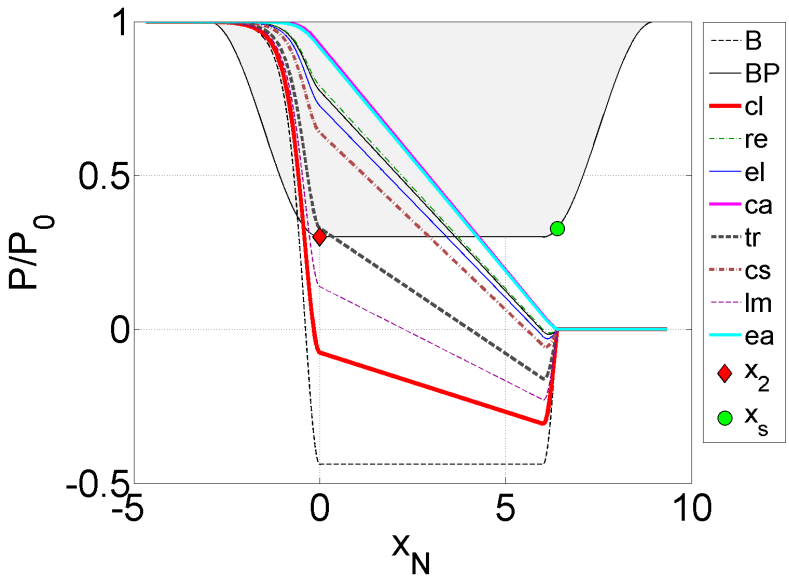

(b) smooth expansion ($y_{tot} = w$)

Figure 4.8: Illustration of normalized pressure distribution $P(x)/P_0$ using the quasi-three-dimensional model for blood flow and imposed area $A_{min} = 79\text{mm}^2$, $P_0 = 75\text{Pa}$, $R_c = 30\%$ and $L_c/D_{cl} = 6$ for different cross section shapes obtained for a) non-default parameter set (α_2) and b) fixed width ($y_{tot} = w$). For completeness also the pressure distribution associated with a quasi-one-dimensional model (BP) and an ideal flow (B) are indicated. The normalized geometry is indicated in gray shade and the streamwise x direction is normalized as $x_N = x/D_{cl}$. As a reference and following the notation in Fig. 4.2, the constriction onset x_2 and flow separation position x_s are indicated.

in dynamic viscosity of the fluids. Indeed since for the same geometries the higher the speed is, the lower the viscosity is. In blood flow the speed is just 0.5% of the one in air flow which will obviously decrease the influence of viscosity. The comparison is further discussed in the next section.

4.1.4 Comparison of modeled results

In the following the influence of flow, fluid and geometrical variables - cross section shape, stenosis parameters, dynamic viscosity, upstream pressure and imposed parameter (A or D) - on the pressure distribution is quantified by considering ζ, defined as the ratio of the slope of the normalized pressure drop within the constriction applying the quasi-three-dimensional flow model and the slope obtained assuming a quasi-one-dimensional (BP) model:

$$\zeta = \frac{|P_{min} - P(x_2)|}{|P_{min} - P(x_2)|_{BP}}, \tag{4.5}$$

where P_{min} denotes the minimum pressure and x_2 as before the onset of the minimum area. The value $\zeta = 1$ indicates that the quasi-one-dimensional (BP) model provides an accurate estimate of viscous effects, $\zeta = 0$ corresponds to an inviscid fluid, $\zeta < 1$ indicates an overestimation of viscous effects and $\zeta > 1$ shows that the quasi-one-dimensional (BP) model results in an underestimation of viscous effects. Values of ζ using default parameter set α_1, non-default parameter set α_2 and fixed width $y_{tot} = w$ are illustrated in Fig. 4.9 and Fig. 4.10.

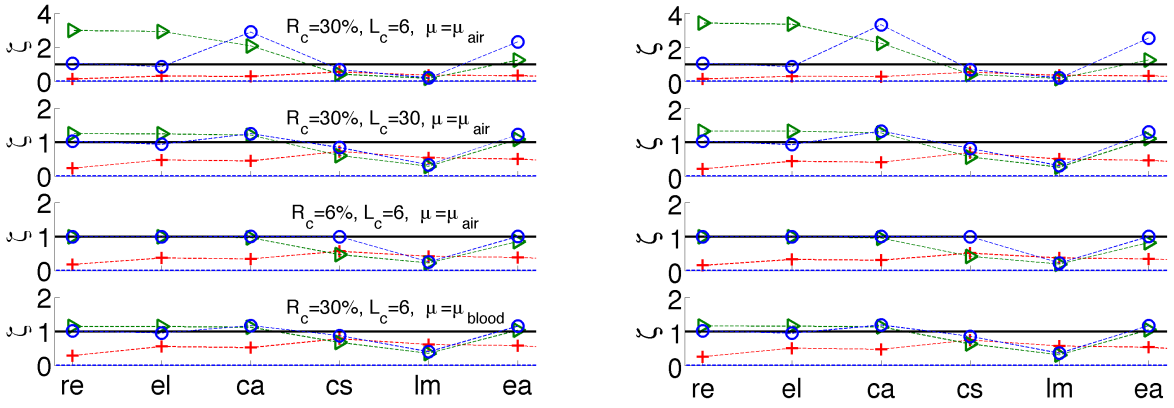

(a) smooth expansion

(b) abrupt expansion

Figure 4.9: Illustration of ζ (4.5) for a stenosis with minimum area $A_{min} = 79$ mm^2 and upstream pressure $P_0 = 75$ Pa. The influence for different cross section shapes is assessed for default parameter set α_1 (+), non-default parameter set α_2 (▷), fixed width $y_{tot} = w$ (o). Different degrees of stenosis and different fluids are assessed as indicated.

Different configurations for stenosis degree R_c (30% or 6%), streamwise constriction extent L_c/D_{cl} (6 or 30), dynamic viscosity μ (air or blood), expansion geometry (smooth or abrupt),

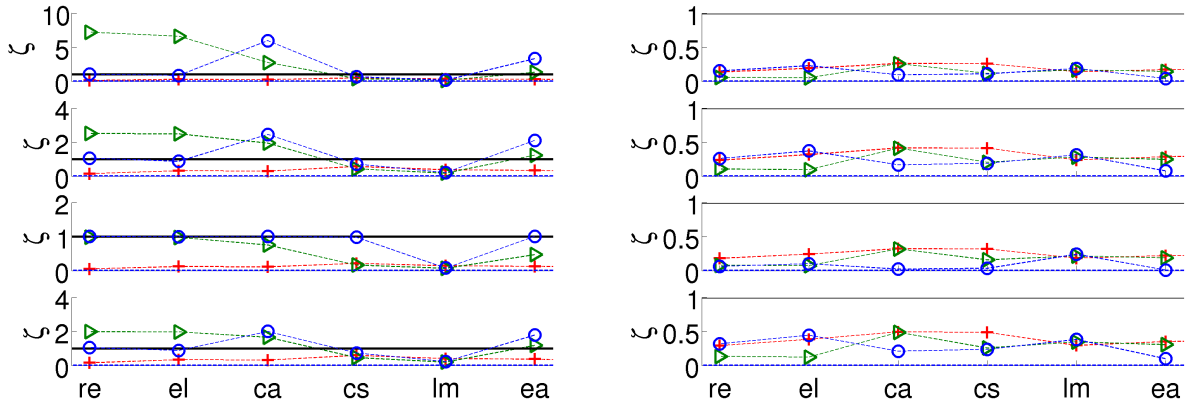

(a) $A = 79\text{mm}^2$, $P_0 = 1000\text{Pa}$ (b) $D = 10\text{mm}$, $P_0 = 75\text{Pa}$

Figure 4.10: Illustration of ζ for a smooth expansion and default parameter set (+), non-default parameter set (▷), fixed width (o) for different geometrical, fluid and flow configurations. For subplots in Fig. 4.10a and Fig. 4.10b values of R_c, L_c/D_{cl} and μ are the same as indicated in Fig. 4.9a.

upstream pressure P_0 (75Pa or 1000Pa) and imposed variable (minimum area $A_{min} = 79$ mm^2 or hydraulic diameter $D = 10$mm) are assessed.

Fig. 4.9a shows that when the minimum area A_{min} of a smooth expansion is imposed, the quasi-one-dimensional (BP) model results in either an overestimation (such as for the default parameter set α_1) or underestimation (such as for non-default parameter set α_2) for a rectangular (re), elliptical (el), concentric annulus (ca) or eccentric annulus (ea) cross section. The magnitude of the over- and in particular the underestimation depends on the configuration. In general, it is observed that the underestimation reduces and even disappears for configurations favoring viscous effects such as increasing stenosis length L_c/D_{cl} ($L_c/D_{cl} = 30$), decreasing stenosis degree R_c ($R_c = 6\%$) or yet increasing dynamic viscosity μ ($\mu = \mu_{blood}$). The overestimation appears to be less sensitive to the exact configuration, including the cross section shape as observed for default parameter set α_1. This is also observed for a circular sector or limacon cross section shape, which is in accordance with previous findings illustrated in Fig. 2.4 or Fig. 4.3. Imposing the minimum area A_{min} for an abrupt instead of a smooth expansion does not alter the observations with respect to the lack of accuracy of the quasi-one-dimensional (BP) model as illustrated in Fig. 4.9b.

Increasing upstream pressure P_0 reduces the impact of viscosity on the flow so that in accordance with the previous findings applying the quasi-one-dimensional (BP) model results in an overestimation or a severe underestimation (600%) of the viscous flow effects. This is illustrated in Fig. 4.10a. Results shown in Fig. 4.9a confirm that the underestimation with the quasi-one-dimensional (BP) model reduces as the geometrical or fluid parameters are altered so that the contribution of viscosity to the pressure distribution within the constriction increases. Moreover, it is seen from Fig. 4.9a, Fig. 4.9b and Fig. 4.10a that the quasi-one-dimensional

(BP) model matches the outcome obtained in the case of a rectangular cross section shape.

In case the hydraulic diameter D is imposed, Fig. 4.10b illustrates that the quasi-one-dimensional (BP) model overestimates viscous effects, for all assessed configurations. Moreover, the variation of the model outcome for different configurations is small compared to the variation obtained when the minimum area A_{min} is imposed.

4.2 Phonation

In section 4.1 a simple quasi-three-dimensional flow model was formulated which accounts for kinetic losses, viscosity as well as the cross section shape [127]. It was shown that varying the cross section shape alters the pressure distribution within a constricted channel significantly, 20% up to 100% when comparing to the quasi-one-dimensional (BP) flow solution [127]. This amounts to the same order of magnitude as well-studied flow events such as the position of flow separation along a convergent-divergent channel constriction [120, 23, 109]. Such a constricted channel is relevant to the glottis during human phonation. Therefore, applying a flow model for which the viscous contribution depends on the cross section shape potentially affects the outcome of physical or mathematical models of human phonation, *i.e.* vocal folds auto-oscillation during voiced sound production. In this section, we focus on the prediction of the phonation onset pressure threshold Pon, *i.e.* the minimum upstream pressure to sustain the auto-oscillation. A schematic overview of the main flow, geometrical and acoustic quantities characterizing human phonation is given in Fig. 4.11.

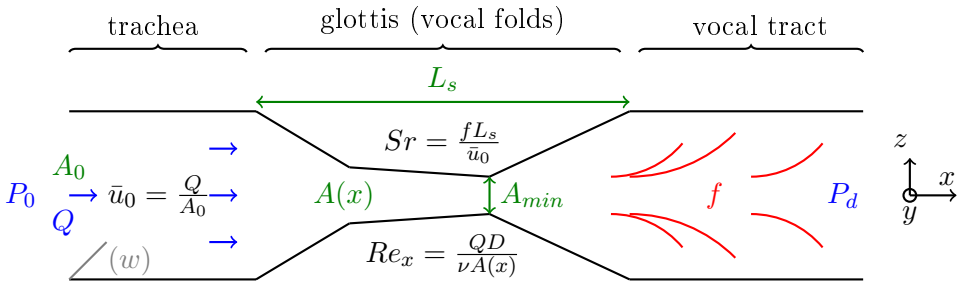

Figure 4.11: Schematic overview of main flow (blue), geometrical (green) and acoustic (red) quantities to determine non-dimensional numbers motivating simplified flow descriptions applied in phonation models. Upstream pressure P_0, downstream pressure P_d, volume flow rate Q, inlet cross section area A_0, minimal glottal area A_{min}, streamwise varying area $A(x)$, glottal streamwise length L_s, acoustic auto-oscillation frequency f, inlet bulk velocity $\bar{u}_0$, Reynolds number Re_x based on hydraulic diameter D and Strouhal number Sr. Note that, the channel has arbitrary cross section shape and hence the width w (in gray shade) is only relevant with respect to the particular case of a rectangular channel with fixed w.

The aim of this section is to assess the potential impact of the quasi-three-dimensional flow model, which takes into account the cross section shape, on the outcome of a physical

phonation model in comparison with a quasi-one-dimensional (BP) flow model. We focus on cross section shapes relevant for the glottal constriction: rectangular (re), elliptical (el) and circular sector (cs) as illustrated in Fig. 4.12.

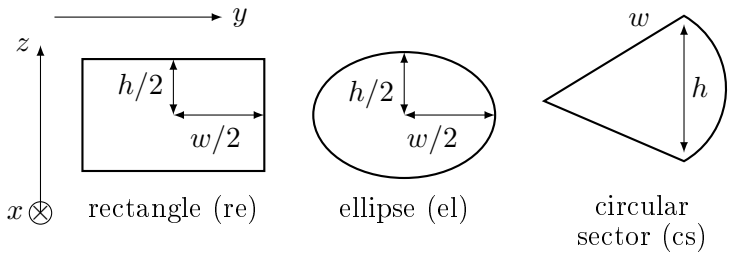

$$A_{re} = h_{re} \cdot w \qquad A_{el} = \tfrac{\pi}{4} h_{el} \cdot w \quad A_{cs} = w^2 \arcsin \tfrac{h_{cs}}{2w}$$

Figure 4.12: cross section shapes in the (y, z) plane (perpendicular to the main flow direction x) defined by two geometrical parameters – width w and height $h.$, with $\cdot = re, el, cs$ – from which geometrical quantities, such as area $A.$, can be derived.

In order to provide a fair comparison with the quasi-one-dimensional (BP) model approach width w is fixed regardless of the cross section shape to $w = 20$mm, which is within the range observed on human speakers (15 up to 25mm [28, 23]) and mechanical glottal replicas (20 up to 25mm [104, 24]). All cross section shapes illustrated in Fig. 4.12 are fully defined by two geometrical parameters, such as width w and height h, from which the area can be derived as shown in Table 2.1.

4.2.1 Stability analysis of a physical phonation model

The symmetrical two-mass model is used to represent the vocal folds during phonation. Each of the vocal folds is modeled as a reduced spring-mass-damper system with two degrees of freedom driven by the pressure difference, $\Delta P = P_0 - P_d$, across the masses as illustrated in Fig. 4.13 [24]. The applied models for glottal airflow, vocal folds mechanics and acoustic interaction with a upstream and downstream pipe, representing the trachea upstream from the glottis and the vocal tract downstream from the glottis, are severe simplifications of the fluid-structure interaction in the larynx during human voiced sound production.

In section 4.1 a three-dimensional aspect is added to the flow model, which is lacking in classically applied flow models for which the anterior-posterior y-dimension is neglected. This results in the common quasi-one-dimensional flow model (labeled BP) assuming a fixed glottal width w and streamwise variable glottal height $h(x,t)$ so that $A_{BP}(x,t) = w \times h(x,t)$. Flow separation along the diverging portion of the glottis is taken into account as $A_s(t) = 1.2 \times \min\big(A(x,t)\big)$ defining the position of flow separation x_s with $x_1 < x_s \leq x_3$. From (2.13) and (4.7) the pressure distribution $P(x,t)$ for $x_0 \leq x \leq x_s$ is written as a quadratic equation

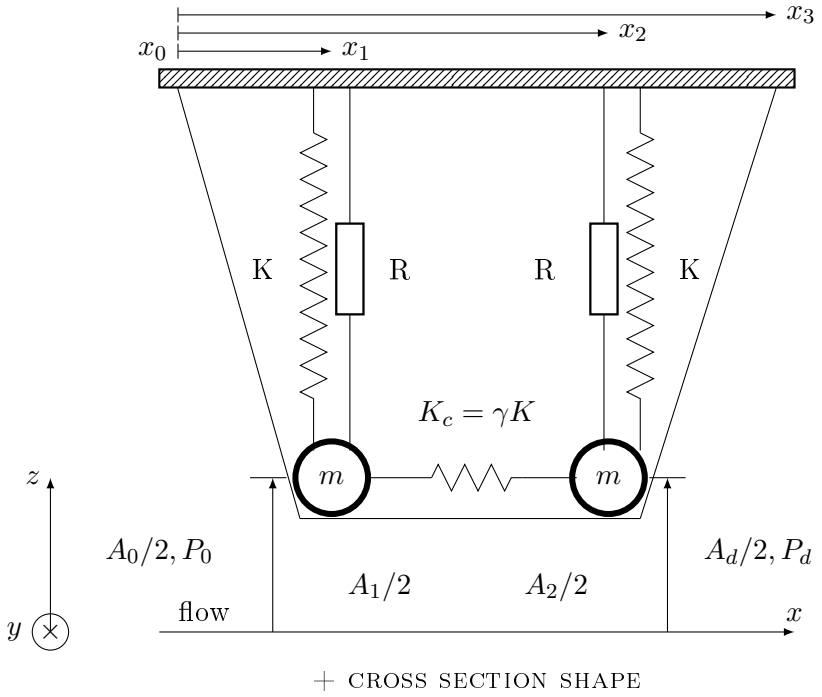

Figure 4.13: Schematic representation of a deformable vocal fold structure modeled as a symmetrical reduced two mass model [24]. The cross section shape is added to the set of input parameters.

of volume flow rate Φ:

$$\begin{aligned} P(x,t) =& P_0 - \frac{1}{2}\rho Q^2 \left(\frac{1}{A^2(x,t)} - \frac{1}{A^2(x_0)} \right) \\ &+ \mu Q \int_{x_0}^{x} \frac{dx}{\beta(x,t)}, \qquad \text{if } x_0 \leq x < x_s, \end{aligned} \tag{4.6}$$

$$P(x,t) = P_d, \qquad \text{if } x \geq x_s, \tag{4.7}$$

with upstream pressure P_0, downstream pressure P_d, dynamic viscosity of air $\mu = 1.8 \times 10^{-5}$Pa·s, β depending on the cross section shape as given in Table 4.3 and volume flow rate Φ estimated as:

$$\begin{aligned} Q = \Bigg[\mu \int_{x_0}^{x} \frac{dx}{\beta(x,t)} + \Bigg\{ \left(\mu \int_{x_0}^{x} \frac{dx}{\beta(x,t)} \right)^2 + \\ 2(P_0 - P_d)\rho \left(1/A_s^2 - 1/A^2(x_0) \right) \Big\}^{1/2} \Bigg] \times \left[\rho \left(1/A_s^2 - 1/A^2(x_0) \right) \right]^{-1}. \end{aligned} \tag{4.8}$$

The vocal folds mechanics is modeled as a symmetrical low order model in which each vocal fold is represented by two identical masses m. The two mass model describes the movement

Table 4.3: β as a function of width w and area A for cross section shapes depicted in Fig. 4.12 [127].

Shape	$\beta(w, A)$
rectangle[(a)]	$\frac{w^3}{6}\left[\frac{A}{2w} - \frac{96w}{\pi^5}\sum_{n=1,3,\ldots}^{\infty}\frac{\tanh(n\pi A/2w^2)}{n^5}\right]$
ellipse	$\frac{w^2A^3}{(\pi^2w^4+16A^2)}$
circular sector[(a)]	$\frac{w^4}{4}\left[\frac{\tan 2A/w^2 - 2A/w^2}{4} - \frac{512A^4}{\pi^5w^8}\sum_{n=1,3\ldots}^{\infty}\frac{1}{n^2(n+4A/\pi w^2)^2(n-4A/\pi w^2)}\right]$
BP[(b)]	$\frac{A^3}{12w^2}$

[(a)] infinite sum is limited to $n \leq 60$.

[(b)] quasi-one-dimensional flow model.

of the two masses perpendicular to the flow direction. The cross section shape is given and assumed not to vary within the glottis. The mechanical model is further expressed as a function of fixed width w and varying area $A(x,t)$ using the relationship $A = f(w, h.)$ given in Fig. 4.12. The main parameters required in the mechanical model are mass m, spring stiffness K, coupling stiffness $K_c = \gamma K$ between the two masses, damping R and critical glottal area threshold A_{crit} triggering vocal folds collision when $A_c < A_{crit}$, with minimum glottal area $A_c = \min(A_1, A_2)$. Whenever collision is detected the values of K and R are increased to $K = 4K$ and $R = R + 2\sqrt{Km}$. The two masses have the same mechanical parameters K, R and m as depicted in Fig. 4.13. With these notations the mechanical model is written as two coupled equations:

$$\frac{m}{2}\frac{d^2A_1}{dt^2} + \frac{R}{2}\frac{dA_1}{dt} + \frac{K(1+\gamma)}{2}A_1 - \frac{\gamma K}{2}A_2 = F_1(A_1, A_2, P_0, P_d), \tag{4.9}$$

$$\frac{m}{2}\frac{d^2A_2}{dt^2} + \frac{R}{2}\frac{dA_2}{dt} + \frac{K(1+\gamma)}{2}A_2 - \frac{\gamma K}{2}A_1 = F_2(A_1, A_2, P_0, P_d), \tag{4.10}$$

with $F_{1,2}$ the force exerted by the fluid on the first and second mass respectively. The mechanical equations at equilibrium reduces to:

$$\frac{K(1+\gamma)}{2}\bar{A}_1 - \frac{\gamma K}{2}\bar{A}_2 = F_1(\bar{A}_1, \bar{A}_2, \bar{P}_0, \bar{P}_d = 0), \tag{4.11}$$

$$\frac{K(1+\gamma)}{2}\bar{A}_2 - \frac{\gamma K}{2}\bar{A}_1 = F_2(\bar{A}_1, \bar{A}_2, \bar{P}_0, \bar{P}_d = 0), \tag{4.12}$$

from which the equilibrium positions for a given upstream pressure $\bar{P}_0$ are derived by a fixed point method. Assuming a small perturbation (a_1, a_2, p_0, p_d) of the quantities around the equilibrium values $eq = (\bar{A}_1, \bar{A}_2, \bar{P}_0, \bar{P}_d = 0)$ as:

$$A_1 = \bar{A}_1 + a_1, \qquad A_2 = \bar{A}_2 + a_2, \tag{4.13}$$

$$P_0 = \bar{P}_0 + p_0, \qquad P_d = p_d, \tag{4.14}$$

results in the following set of equations:

$$\frac{m}{2}\frac{d^2a_1}{dt^2} + \frac{R}{2}\frac{da_1}{dt} + \frac{K(1+\gamma)}{2}a_1 - \frac{\gamma K}{2}a_2 = \left.\frac{\partial F_1}{\partial A_1}\right|_{eq} a_1 + \left.\frac{\partial F_1}{\partial A_2}\right|_{eq} a_2 + \left.\frac{\partial F_1}{\partial P}\right|_{eq} p_0 + \left.\frac{\partial F_1}{\partial P_d}\right|_{eq} p_d, \tag{4.15}$$

$$\frac{m}{2}\frac{d^2a_2}{dt^2} + \frac{R}{2}\frac{da_2}{dt} + \frac{K(1+\gamma)}{2}a_2 - \frac{\gamma K}{2}a_1 = \left.\frac{\partial F_2}{\partial A_1}\right|_{eq} a_1 + \left.\frac{\partial F_2}{\partial A_2}\right|_{eq} a_2 + \left.\frac{\partial F_2}{\partial P}\right|_{eq} p_0 + \left.\frac{\partial F_2}{\partial P_d}\right|_{eq} p_d. \tag{4.16}$$

Acoustical coupling between the vocal folds and a uniform upstream tube with length L_u representing the trachea and/or a uniform downstream tube with length L_d representing the vocal tract is important when the acoustical resonance frequencies of the pipe and the auto-oscillation frequency are close [24, 73]. The acoustic set of equations is given as

$$\frac{d^2\psi_d}{d^2t} + \frac{\omega_d}{Q_d}\frac{d\psi_d}{dt} + \omega_d^2\psi_d = \frac{Z_d\omega_d}{Q_d}\phi, \tag{4.17}$$

$$\frac{d^2\psi_0}{d^2t} + \frac{\omega_0}{Q_d}\frac{d\psi_0}{dt} + \omega_0^2\psi_u = -\frac{Z_0\omega_0}{Q_0}\phi, \tag{4.18}$$

with $\partial\psi_{0,d}/\partial t = p_{0,d}$ the acoustic pressure and ϕ the unsteady portion of the volume flow velocity, $\omega_{0,d}$ the acoustical pipe resonance pulsations, $Q_{0,d}$ the quality factor and $Z_{0,d}$ the peak value of the acoustical impedance. As for the mechanical equations assuming small variations around equilibrium results in:

$$\frac{d^2\psi_d}{d^2t} + \frac{\omega_d}{Q_d}\frac{d\psi_d}{dt} + \omega_d^2\psi_d = \frac{Z_d\omega_d}{Q_d} \times \left(\left.\frac{\partial Q}{\partial A_1}\right|_{eq} a_1 + \left.\frac{\partial Q}{\partial A_2}\right|_{eq} a_2 + \left.\frac{\partial Q}{\partial P_0}\right|_{eq} p_0 + \left.\frac{\partial Q}{\partial P_d}\right|_{eq} p_d\right), \tag{4.19}$$

$$\frac{d^2\psi_0}{d^2t} + \frac{\omega_0}{Q_d}\frac{d\psi_0}{dt} + \omega_0^2\psi_0 = -\frac{Z_0\omega_0}{Q_0} \times \left(\left.\frac{\partial Q}{\partial A_1}\right|_{eq} a_1 + \left.\frac{\partial Q}{\partial A_2}\right|_{eq} a_2 + \left.\frac{\partial Q}{\partial P_0}\right|_{eq} p_0 + \left.\frac{\partial Q}{\partial P_d}\right|_{eq} p_d \right). \quad (4.20)$$

Consequently, assuming small variations around equilibrium results in a coupled set of equations obtained from (4.15), (4.16), (4.19) and (4.20). The system can be expressed in state-space form as

$$\dot{X} = MX \quad (4.21)$$

with $X = [a_1, a_2, \psi_0, \psi_d, da_1/dt, da_2/dt, d\psi_0/dt, d\psi_d/dt]$ and $M = \left[\begin{array}{c|c} A & B \\ \hline C & D \end{array}\right]$ with null matrix $A = 0_{4,4}$, identity matrix $B = I_4$ and matrices C and D defined as:

$$C = \begin{bmatrix} -\frac{K(1+\gamma)-2\left.\frac{\partial F_1}{dA_1}\right|_{eq}}{m} & \frac{\gamma K+2\left.\frac{\partial F_1}{dA_2}\right|_{eq}}{m} & 0 & 0 \\ \frac{\gamma K+2\left.\frac{\partial F_2}{dA_1}\right|_{eq}}{m} & -\frac{K(1+\gamma)-2\left.\frac{\partial F_2}{dA_2}\right|_{eq}}{m} & 0 & 0 \\ \frac{Z_d\omega_d}{Q_d}\left.\frac{\partial Q}{\partial A_1}\right|_{eq} & \frac{Z_d\omega_d}{Q_d}\left.\frac{\partial Q}{\partial A_2}\right|_{eq} & 0 & -\omega_d^2 \\ -\frac{Z_0\omega_0}{Q_0}\left.\frac{\partial Q}{\partial A_1}\right|_{eq} & -\frac{Z_0\omega_0}{Q_0}\left.\frac{\partial Q}{\partial A_2}\right|_{eq} & -\omega_0^2 & 0 \end{bmatrix} \quad (4.22)$$

and

$$D = \begin{bmatrix} -\frac{R}{m} & 0 & \frac{2}{m}\left.\frac{\partial F_1}{\partial P_0}\right|_{eq} & \frac{2}{m}\left.\frac{\partial F_1}{\partial P_d}\right|_{eq} \\ 0 & -\frac{R}{m} & \frac{2}{m}\left.\frac{\partial F_2}{\partial P_0}\right|_{eq} & \frac{2}{m}\left.\frac{\partial F_2}{\partial P_d}\right|_{eq} \\ 0 & 0 & \frac{Z_d\omega_d}{Q_d}\left.\frac{\partial Q}{\partial P_0}\right|_{eq} & -\frac{\omega_d}{Q_d} + \frac{Z_d\omega_d}{Q_d}\left.\frac{\partial Q}{\partial P_d}\right|_{eq} \\ 0 & 0 & -\frac{\omega_0}{Q_d} - \frac{Z_0\omega_0}{Q_0}\left.\frac{\partial Q}{\partial P_0}\right|_{eq} & -\frac{Z_0\omega_0}{Q_0}\left.\frac{\partial Q}{\partial P_d}\right|_{eq} \end{bmatrix}. \quad (4.23)$$

The system will become in-stable, corresponding to the onset of auto-oscillation, when the real portion of an eigenvalue of M is positive.

4.2.2 Results

We search the influence of the cross section shapes, depicted in Fig. 4.12, on the predicted auto-oscillation onset by assessing the onset pressure threshold Pon. Therefore, a linear stability

analysis is performed by considering the real portion of the eigenvalues of M for increasing upstream pressure P_0 for different cross section shapes and for different initial constriction degrees $1-A_{\cdot}^{10}/A_0$, with A^{10} denotes the initial minimum area in absence of flow. Concretely, the constriction degree is varied from 50% up to 90% whereas the width w is fixed. The resulting aspect ratios yield $1 < w/h_{\cdot}^{10} < 9$ and depend on the cross section shape as illustrated in Fig. 4.14. For fixed width w the aspect ratios of the quasi-one-dimensional geometry and the rectangular cross section shape match since $A^{10} = w \times h_{re}^{10}$ holds in both cases. Besides the constriction degree and the cross section shape the other model parameters are taken constant with values derived from [24] as: geometry $[x_0\ x_1\ x_2\ x_3] = [0\ 1\ 4\ 5]$mm, width $w = 20$mm, upstream area $A_{0,d} = 400\text{mm}^2$, masses $m = 0.2$g, spring stiffness $K = 131\text{N}\cdot\text{m}^{-2}$, coupling spring stiffness $K_c = 65\text{N}\cdot\text{m}^{-2}$, damping $R = 0.006\text{N}\cdot\text{s}\cdot\text{m}^{-2}$ and collision threshold $A_{crit} = 0.4\text{mm}^2$, upstream pipe lengths $L_0 = 0$cm and downstream pipe length $L_d = 17$cm, acoustic pipe resonance pulsations ω_0=0 and $\omega_d = 2965$Hz, quality factors $Q_0 = 0$ and $Q_d = 51$, and acoustic impedance peaks $Z_0 = 0$ and $Z_d = 54\text{MPa}\cdot\text{s}\cdot\text{m}^{-3}$). Simulated results for phonation onset pressure threshold P_{on} are illustrated in Fig. 4.15a as a function of constriction degree $1 - A^{10}/A_0$ which is independent from the cross section shape and in Fig. 4.15b as a function of aspect ratio $Ar_{\cdot}^{10} = w/h_{\cdot}^{10}$, which depends on the cross section shape.

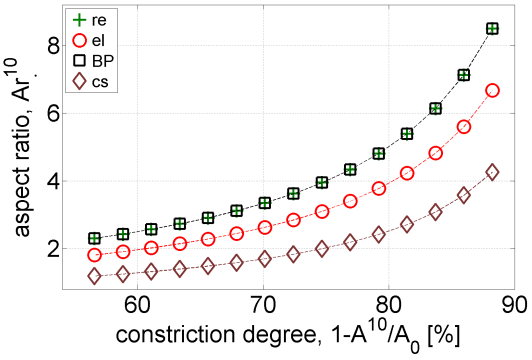

(a) $Ar_{\cdot}^{10}(1 - A^{10}/A_u)$ for $\cdot$ =re,el,BP,cs

Figure 4.14: Aspect ratio $Ar_{\cdot}^{10} = w/h_{\cdot}^{10}$ as a function of initial constriction degree $1 - A^{10}/A_0$ for cross section shapes (rectangle – re, ellipse – el, quasi-one-dimensional – BP and circular sector – cs) with fixed width $w = 20$mm.

For large constriction degrees (greater than 75% in Fig. 4.15a) the cross section shape can be neglected. For medium or small constriction degrees (smaller than 75% in Fig. 4.15a) the predicted phonation onset threshold pressure *Pon* depends on the cross section shape since less pressure is required to sustain oscillation for a circular sector cross section shape than for a rectangular or elliptical cross section shape. The discrepancy between *Pon* estimations belonging to different cross section shapes increases as the constriction degree (Fig. 4.15a) or aspect ratio (Fig. 4.15b) decreases. Moreover, it is observed that for the assessed range of constriction degrees and associated aspect ratios (from 2 up to 9 illustrated in Fig. 4.14), a rectangular geometry can be modeled using a quasi-one-dimensional (BP) flow approximation. The simulated phonation onset threshold pressures *Pon* suggest that for large constriction

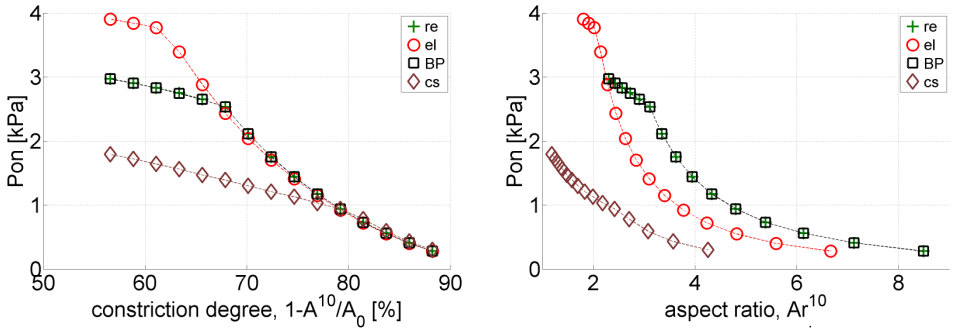

(a) $Pon(1 - A^{10}/A_0)$ for $\cdot$ =re,el,BP,cs (b) $Pon(Ar_{\cdot}^{10})$ for $\cdot$ =re,el,BP,cs

Figure 4.15: (a,b) Modeled onset pressure threshold Pon as a function of constriction degree $1 - A^{10}/A_0$ (a) and as a function of aspect ratio $Ar_{\cdot}^{10}$.

degrees (greater than 75% in Fig. 4.15a) the model outcome depends on an accurate value of the constricted area A^{10} as a model input parameter. This finding is a consequence of the small discrepancy found in the predicted flow quantities when viscosity dominates the flow behavior and flow inertia effects become less pronounced and so the influence of the cross section shape. For medium or smaller constriction degrees (smaller than 75% in Fig. 4.15a) it is necessary to quantify the constricted area A^{10} as well as to obtain information on the cross section shape in order to capture the impact of the cross section shape on the viscous losses in the flow model. When the aspect ratio Ar^{10} is used as model input parameter (Fig. 4.15b) additional information on the cross section shape is required as a model input parameter for all aspect ratios. Experimental studies aiming to validate the modeled influence of the cross section shape on the phonation onset pressure should account for the necessary input parameters. In addition, given the severe influence of the cross section shape on the predicted phonation onset pressure Pon, it is of interest to extent the current model approach to an arbitrary cross section shape. This seems important in order to enlarge the relevance of simplified physical phonation models for applications such as vocal folds pathologies affecting the cross section shape of the glottis during phonation.

4.3 Summary

The current chapter deals with flow through constricted channels with different cross section shape and its application to a stenosis for air flow or blood flow. A simplified quasi-three-dimensional flow model is proposed which accounts for flow inertia, viscosity as well as cross section shape. The model outcome is quantified and compared with respect to a quasi-one-dimensional (BP) model. It is seen that in case the area is imposed the pressure distribution within the constriction varies to a large extent so that the quasi-one-dimensional (BP) model outcome yields either an overestimation or an underestimation of the viscous effects depending on the cross section shape. Nevertheless, it is observed that in general the accuracy of a quasi-

one-dimensional (BP) model improves as the imposed geometrical (stenosis degree, constriction length), fluid (dynamic viscosity) and flow (imposed pressure difference) conditions favor the viscous contribution to the flow development. Note that all those parameters can be altered due to pathologies. In case the hydraulic diameter is imposed the quasi-one-dimensional (BP) model yields an overestimation of viscous effects regardless the configuration.

Next, the proposed quasi-three-dimensional flow model is applied to a theoretical symmetrical two-mass model assuming different cross section shapes as schematically depicted in Fig. 4.13. A stability analysis is performed in order to quantify the impact of the cross section shape on the minimum pressure required to sustain phonation. For large constriction degrees (greater than 75%) the cross section shape can be neglected and the quasi-one-dimensional flow model is capable to describe the flow. For medium and small constriction degrees on the other hand, a discrepancy appears between cross section shapes which increases as the constriction degree decreases.

Consequently, accounting for the cross section shape improves the model accuracy in particular for flow and geometrical configurations which are not completely dominated by viscosity.

Chapter 5

Experiments and model validation

Contents

In chapter 4, the influence of the cross section shape on flow through a constricted channel is shown for the outcome of a quasi-three-dimensional flow model. In the current chapter, it is sought to assess the possible impact of the cross section shape of a constriction on flow properties experimentally. In addition, the quasi-three-dimensional flow model outcome can be validated on experimental data.

The flow field is quantified by temporal and spatial sampling of the pressure and velocity field. In order to fully characterize the flow field, upstream flow conditions are varied. A spatial overview of the flow field is presented using flow visualization.

5.1 Experimental configuration

5.1.1 Constricted channel cross section shapes

Eight constricted channel portions with different cross section shapes[1], previously assessed in chapter 2 and chapter 4, are considered. The constricted channel portions and the different

[1] Circular (cl), square (sq), elliptical (el), rectangular (re), equilateral triangular (tr), isosceles triangular (ntr), small circular sector (scs) and large circular sector (lcs)

cross section shapes are illustrated in Fig. 5.1 and detailed in Appendix D. The geometrical characteristics (hydraulic diameter D, width[2] w along the y-direction and height h along the z-direction) are summarized in Table 5.1. The cross section shapes have constant area $A_c = 79\text{mm}^2$ and constant length $L_c = 25\text{mm}$ along the streamwise x direction. Each constriction can be screwed to an upstream and downstream channel with the screwthread along the outer walls in order to obtain a constricted channel portion. In the current work, unless stated differently, the upstream or downstream channel is a uniform circular channel with inner diameter 25mm, fitting the outer diameter of the constricted portion, so that the constriction inlet and outlet makes a sharp angle with the upstream and downstream unconstricted channel[3]. One or two pressure taps of diameter 0.5mm are positioned at the center of the constriction[4], corresponding to $L_c/2$. Measured pressures at these positions are labeled P_1 for one and $P_{1,2}$ for two pressure taps. The position of the pressure taps and their labels is depicted in Fig. 5.1. It is seen that depending on the symmetry of the cross section shape one or two pressure taps can be used.

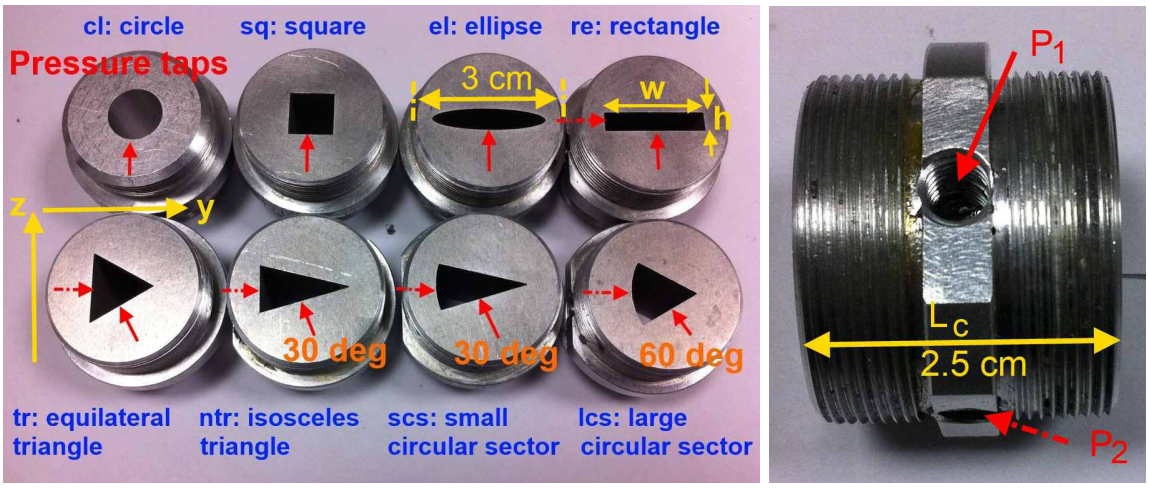

(a) transverse view (b) streamwise view

Figure 5.1: Illustration of experimentally assessed uniform cross section shapes and position of the pressure taps P_1 (full arrow) and P_2 (dashed arrow): a) front view of the cross section shapes along the (y, z) plane. As an example, total width w and height h, summarized in Table 5.1, is indicated for the rectangular cross section shape. b) streamwise view of the constricted portion with length L_c. Screwthread is present at the outer edges of the constricted channel portion. The positions of the pressure taps is pointed out. The geometry is further detailed in Appendix D.

[2]The total width w was denoted y_{tot} in Table 2.1. The geometrical parameters were previously defined in Table 2.1 and illustrated in Fig. 2.3 and Fig. 4.12.

[3]The sharp angle at the outlet of the constriction results in flow separation at the constriction exit, so that its position is known and does not influence the measured or modeled flow outcome. On the other hand, the choice of sharp inlet angle can be criticized since complex flow phenomena might occur at the inlet.

[4]The pressure sensors are screwed in the pressure holes shown in Fig. 5.1b. The pressure tap itself is situated at the bottom of the pressure hole and has a diameter of 0.4mm.

Table 5.1: Overview of geometrical parameters for the constriction cross section shapes illustrated in Fig. 5.1: hydraulic diameter D, width w, height h, cross section area A_c, constriction length L_c and ratios of geometrical parameters.

	cl	sq	lcs	tr	scs	ntr	el	re
D [mm]	10	8.9	8.4	7.8	7.2	7.0	6.7	6.6
w [mm]	10	8.9	12.2	11.7	17.3	17.1	22.4	19.8
h [mm]	10	8.9	12.2	13.5	9.0	9.2	4.5	4.0
w/h [-]	1	1	1	0.9	1.9	1.9	5.0	5.0
w/D [-]	1	0.9	1.5	1.7	2.4	2.5	3.3	3.0
L_c/D [-]	2.5	2.8	3.0	3.2	3.5	3.6	3.7	3.8

$A_c = 79\text{mm}^2$, $L_c = 25\text{mm}$

5.1.2 Experimental setup and flow conditioning

5.1.2.1 Experimental setup

Flow facility and pressure measurements The setup consists of an air compressor (Atlas Copco GA7), followed by a pressure regulator (Norgren type 11-818-987) providing an airflow at constant pressure. A general overview of the experimental setup is depicted in Fig. 5.2. The volume flow rate is controlled by a manual valve placed downstream from the pressure regulator. The volume flow rate is measured by a thermal mass flow meter (Model 4043 TSI) with an accuracy of 2% of its reading. To homogenize the flow, a settling chamber is used, with dimensions 0.25m×0.3m×0.35m, to which a series of 3 perforated plates with holes of diameter 1.5mm are added. The walls of the settling chamber are tapered with acoustic foam (SE50-AL-ML Elastomeres Solutions) in order to avoid acoustic resonances. The influence of the cross section shape on the flow development is assessed experimentally by adding one of the constricted channel portions, illustrated in Fig. 5.1, to a uniform circular tube, with unconstricted internal diameter 25mm. The flow channel is mounted to the settling chamber by means of a converging nozzle. The used nozzle and resulting nozzle flow is detailed in [41]. An acoustic source, pressure driver unit (KU 916T), upstream from the constriction can be used to create unsteady flow[5]. Pressure sensors (Kulite XCS-093) can be positioned in pressure taps of diameter 0.5mm upstream from (P_0), in the middle of (P_1 and P_2) and downstream (P_3) from the constricted portion illustrated in Fig. 5.1. The used pressure taps depend on the value of the length of the channel upstream from the constriction L_u and the length of the channel downstream from the constriction L_d. Two omni directional microphones (B&K 4192) with associated pre-amplifier (B&K 4165) and additional amplifier and power supply (B&K 5935L) are positioned downstream from the flow channel in order to analyze the acoustic signal[6]. Except for the air compressor, the whole setup is placed in a confined room in order to avoid flow disturbances. Electrical signals are amplified and conditioned using a pre-amplifier/conditioning board (National Instruments SXCI-1121) connected to a PC through

[5]Examples of unsteady measurements are presented in Appendix G.

[6]In the current chapter, the acoustic signals are not analyzed since we focus on characterizing the flow field.

a National Instruments BNC-2080 and a National Instruments PCI-MIO-16XE acquisition card. The acquired data are processed using LabView 7 software (National Instruments).

Volume flow rate Q is sampled at 500Hz. Pressure sensors P and microphone M are sampled at 10kHz or 24kHz. Statistical quantities, such as mean values, are derived on 5s of steady signal as shown in Fig. 5.2c for the measured volume flow rate $Q(t)$ and pressure signal $P(t)$. In general, flow experiments are performed for volume rates within the range $0 \leq Q \leq$ 200l/min. The increment is 5l/min for $Q \leq$ 80l/min, 10l/min for 90l/min$\leq Q \leq$ 100l/min and 25l/min for $Q \geq$ 125l/min.

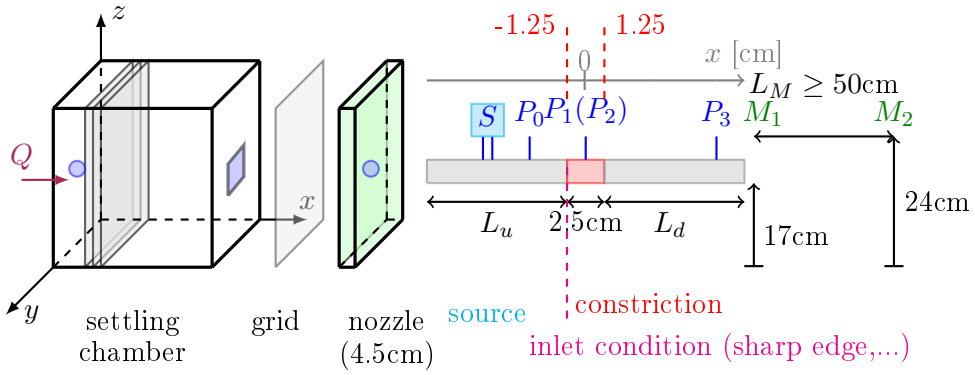

(a) schematic overview

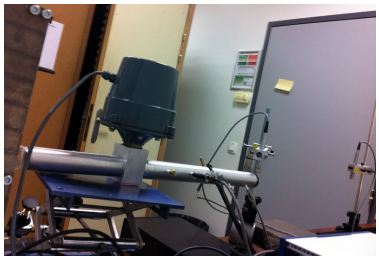

(b) photograph

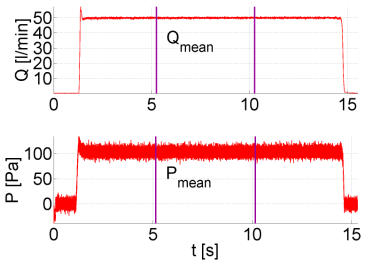

(c) statistics on 5s of signal

Figure 5.2: a) Schematic overview of the experimental setup indicating the position of pressure taps (upstream from the constriction P_0, within the constriction P_1 (P_2) and downstream from the constriction P_3), the position of microphones M_1 and M_2 at a distance $L_M = 50$cm or $L_M = 1$m. The length of the unconstricted upstream L_u and downstream channel L_d is varied as well as the inlet condition immediately upstream from the constriction. b) Photograph and c) Measured volume flow rate $Q(t)$ and pressure $P(t)$ indicating the 5s interval used to determine the steady values.

Velocity measurements The flow velocity downstream of the constriction is measured for different cross section shapes by hot film anemometry for $L_u = 100$cm, a sharp constriction inlet condition and in absence of a downstream channel, *i.e.* $L_d = 0$, as illustrated in Fig. 5.4. Note that the flow facility is the same as described for the pressure measurements. The hot

film (TSI 1201-20), for which the working principle and calibration is detailed in Appendix E.2, is mounted to a home-made positioning system providing a positioning accuracy of 0.1mm. The positioning system is illustrated in Fig. E.7 of Appendix E.2. The probe displacement is controlled by a user-defined matrix implemented in LabView (National Instruments). At each spatial measurement position, the hot-film output voltage is sampled at 10kHz during 40s (the number of samples is sufficient to provide a statistical analysis of the mean and root mean square velocity). The voltage is collected by a constant temperature anemometer system (TSI IFA 300) and corrected for drifts in temperature following the procedure outlined in Appendix E.2.

Transverse velocity profiles are gathered by positioning the hot film at a distance $<$ 1mm downstream from the center of the nozzle exit[7] and displacing the hot film with a transverse step of 0.5mm parallel to the cross section exit plane across the directions shown in Fig. 5.3a. Longitudinal velocity profiles in the near field downstream from the constriction are obtained by positioning the hot film at a distance $<$ 1mm downstream from the center of the nozzle exit and displacing the hot film with streamwise steps of 1mm up to 1cm downstream from its initial position followed by streamwise step of 5mm up to 8cm from its initial position. The streamwise extent of the longitudinal velocity profile is denoted $L_{HF} = 8$cm. The ratio of this extent to hydraulic diameter for the assessed cross section shapes L_{HF}/D is listed in Table. 5.2 in order to characterize the assessed near field region for each cross section shape.

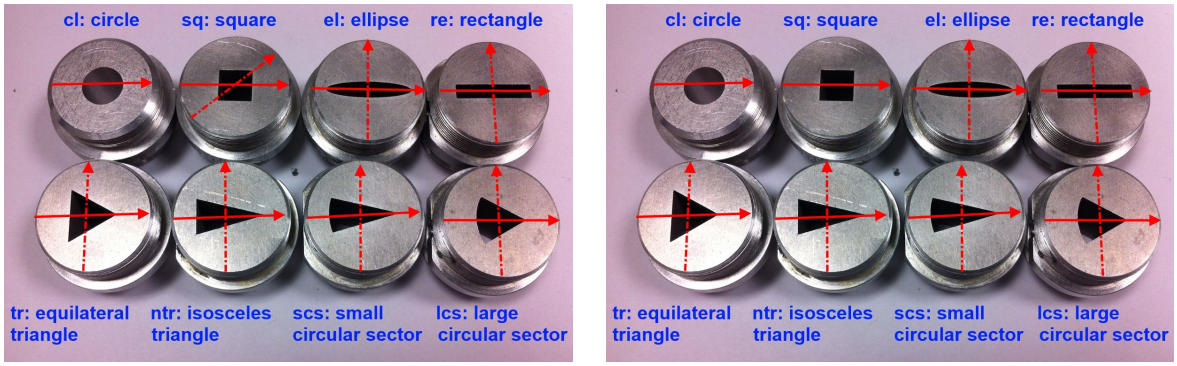

(a) transverse velocity profiles (b) flow visualization sheets

Figure 5.3: Experimentally assessed directions along the major axis (full arrow) and along the minor axis (dashed arrow): a) transverse velocity profiles and b) visualization sheets. Note that except for the squared cross section shape all transverse profiles are taken along the sheets used for flow visualization.

Flow visualization A spatial overview of the impact of the cross section shape on the flow field immediately downstream from the constricted portion is obtained by applying flow visualization. Therefore, the constricted channel is attached to a settling chamber, of dimensions

[7] $<$1mm corresponds to $(x - L_c)/D \leq 0.15$.

Table 5.2: Near field region assessed by the longitudinal velocity profile characterized by the ratio L_{HF}/D with L_{HF} denoting the extent of the longitudinal velocity profile and D the hydraulic diameter for the cross section shapes shown in Fig. 5.1.

	cl	sq	lcs	tr	scs	ntr	el	re
D [mm]	10	8.9	8.4	7.8	7.2	7.0	6.7	6.6
L_{HF}/D	8.0	9.0	9.5	10.3	11.1	11.4	11.9	12.1

$L_{HF} = 80$mm

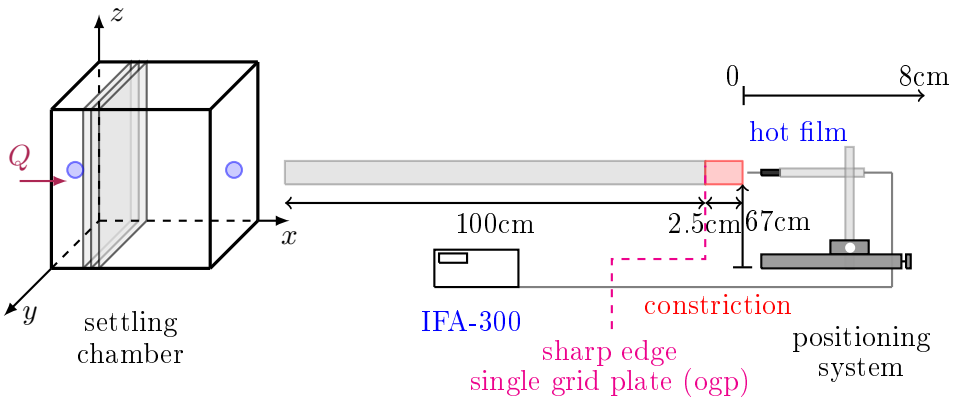

(a) schematic overview

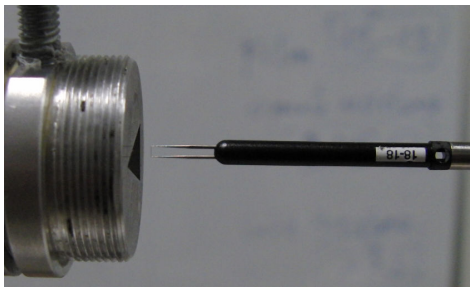

(b) hot film (TSI 1201-20)

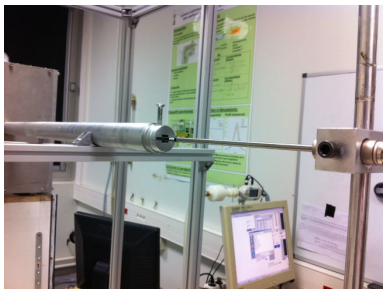

(c) photograph

Figure 5.4: Illustration of hot film anemometry setup. a) Schematic overview of the setup and configuration used to assess the influence of the different cross section shapes of the constricted portion on the velocity field immediately downstream from the constriction. Transverse and longitudinal velocity profiles are assessed. The spatial range of the longitudinal velocity profile is indicated. b) Hot film. c) Photograph of hot film positioning.

0.38m×0.38m×0.48m, to which smoke can be injected. Smoke is generated by a smoke machine (Fog-1200E KOOL). Two-dimensional illumination of the flow field is applied with a two-dimensional laser light beam (class IIIb). The illuminated smoke pattern is recorded at 300fps (Casio EXILIM Pro EX-F1) which ensures good freezing of the flow development. For each flow condition between 600 and 900 images are gathered corresponding to an acquisition time of 2s up to 3s. An overview of the flow visualization setup is given in Fig. 5.5. The digitized two-dimensional images are 512×384 data matrices. Spatial calibration of the images

is performed using the grid illustrated in Fig. E.2 of Appendix E. The streamwise extent of the visualized flow field yields $L_v = 21\text{cm}$. The visualized near field region downstream form the constriction is characterized by its ratio with the hydraulic diameter of the cross section shape L_v/D for which values are listed in Table 5.3. Concretely, two visualization planes are considered: one along the major axis and one along the minor axis of the cross section shapes as illustrated in Fig 5.3b.

Table 5.3: Visualized near field characterized by the ratio L_v/D with L_v denoting the streamwise extent of the visualized area and D the hydraulic diameter of the cross section shapes shown in Fig. 5.1.

	cl	sq	lcs	tr	scs	ntr	el	re
D [mm]	10	8.9	8.4	7.8	7.2	7.0	6.7	6.6
L_v/D [mm]	21	23.6	25	26.9	29.2	30	31.3	31.8

$L_v = 210\text{mm}$.

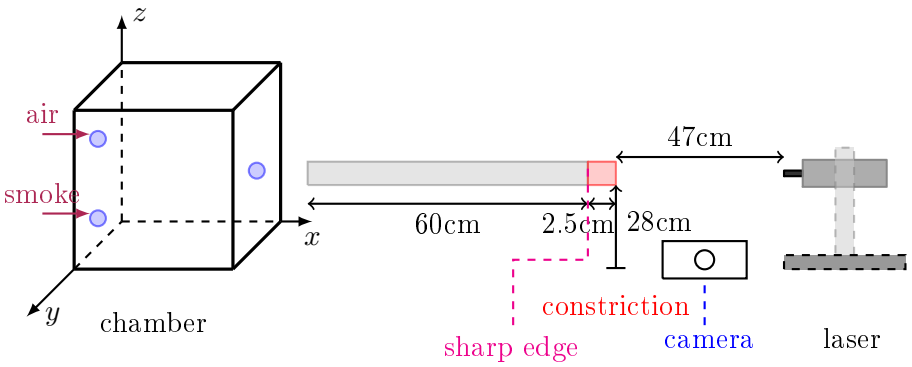

(a) schematic overview

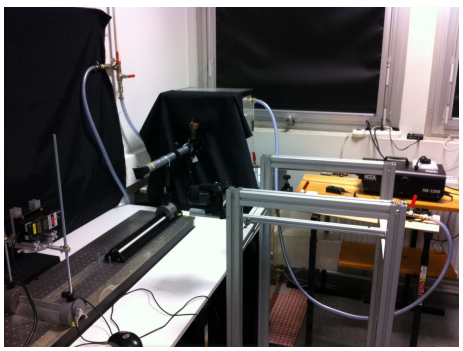

(b) photograph

Figure 5.5: Illustration of the experimental setup used for flow visualization.

5.1.2.2 Flow conditioning

The impact of the constriction cross section shapes illustrated in Fig. 5.1 on the flow field is assessed for different upstream flow conditions. Different upstream conditions are generated by varying the length L_u of the channel upstream from the constriction, by varying the inlet condition immediately upstream from the constriction and by varying the length L_d of the channel downstream from the constriction. In addition, a free and confined jet configuration downstream from the constriction considered for $L_d = 0$cm or $L_d = 15$cm, respectively.

The nozzle flow exiting the settling chamber approximates a top hat profile, characterized by an almost uniform velocity profile [41], so that increasing L_u will result in a more developed flow profile. Concretely, L_u is set to either 2cm, 35cm or 1m. Note that for $L_u = 1$m the length-to-diameter ratio L_u/D_u of the unconstricted upstream channel yields $L_u/D_u = 40$, with $D_u = 25$mm, so that, depending on the applied volume flow rate, the flow is expected to be fully or almost fully developed. For $L_u = 35$cm, the length-to-diameter yields $L_u/D_u = 14$ so that the flow is developing. For $L_u = 2$cm the length-to-diameter ratio $L_u/D_u < 1$ so that velocity profile is imprinted by the almost uniform nozzle profile. Therefore, the upstream profile is either characterized by boundary layer limited to the near wall region for $L_u = 2$cm or by boundary layers occupying almost the entire flow channel.

Since the constriction is uniform regardless of the cross section shape, it follows that the inlet condition a the constriction is defined by sharp edges. Sharp edges might cause a vena contracta to occur at the inlet of the constriction, which will influence the downstream flow field and moreover can not be captured with the simplified quasi-three-dimensional flow model proposed in chapter 4. Therefore, flow mixing at the inlet is altered by putting a flow mixing element immediately upstream from the constriction. Concretely three different mixing elements are introduced, which are illustrated in Fig. 5.6. The transverse dimension fit the diameter D_u of the unconstricted upstream channel and the length of the mixing element is either 3cm in case the mixing element consists of two grid plates containing pipes of diameter 0.65cm (tgph) or steel wool (tgps) or 1mm in case a single grid plate (ogp) is considered. The grid plate is characterized by regular circular holes of diameter 0.15cm equally spaced at 0.08cm. The cross section shapes with the single grid plate at their inlet[8] is illustrated in Fig. 5.7

Two additional upstream flow conditioning conditions are assessed for the constriction with circular cross section shape in order to be able to observe the effect of flow development in absence of shape edges at the constriction inlet. Firstly, a converging cone with angle 26^o is used to provide a smooth transition between the diameter of the unconstricted upstream pipe $D_u = 25$mm and the diameter of the constriction with circular cross section shape $D = 10$mm. The geometry of the converging cone is detailed in Fig. 5.8. Secondly, as a reference, a circular constriction with diameter $D = 10$mm is considered for which the length upstream from the pressure tap P_1 is extended from 12.5mm ($L_c = 25$mm) to 1000mm (or $L_c \approx 1$m so that

[8]The area ratio of the area covered by the holes in the single grid plate to the area of the cross section shape is estimated between 50% to 60%.

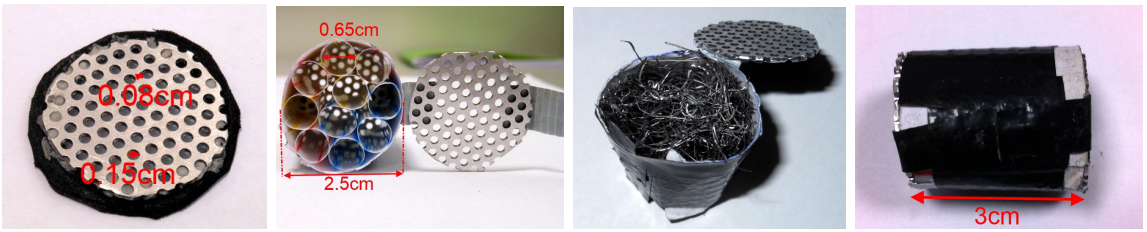

(a) ogp (b) tgph (c) tgps (d) length

Figure 5.6: Illustration of mixing elements. a) one grid plate (ogp), b) two grid plates containing pipes (tgph), c) two grid plates containing steel wool (tgps) and d) length of the mixing element for cases (tgph) and (tgps). Dimensions of the grid plate and pipes are indicated.

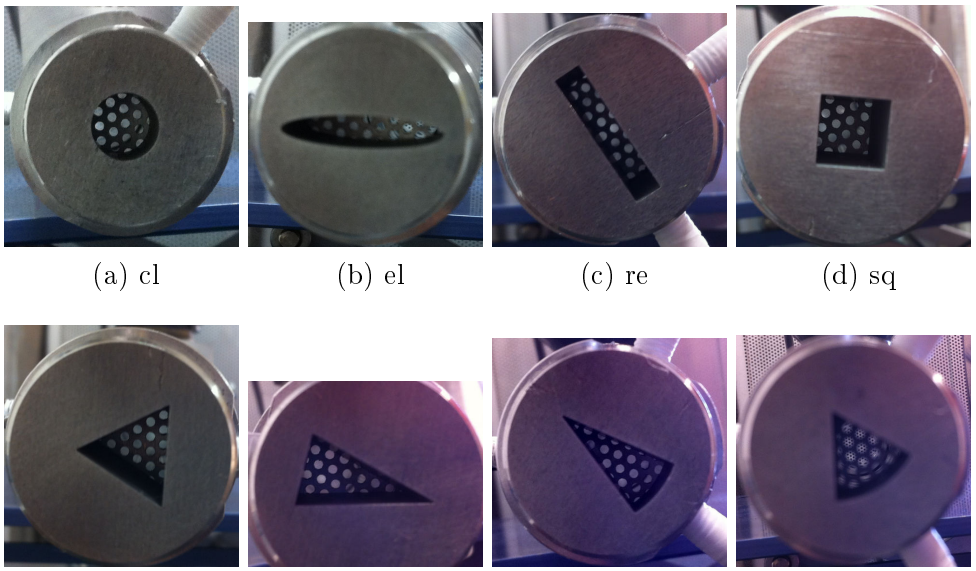

(a) cl (b) el (c) re (d) sq

(e) tr (f) ntr (g) scs (h) lcs

Figure 5.7: Front view of different cross section shapes shown in Fig. 5.1 with one grid plate (ogp) placed at the inlet of the constricted portion.

$L_c/D \approx 100$) in order to compare the flow field resulting from the previous outlined upstream flow conditioning with the flow field observed for fully developed flow.

5.1.2.3 Assessed configurations

The assessed geometrical configurations for each of the constriction shapes shown in Fig. 5.1 result from the described combination of different flow conditioning conditions described in section 5.1.2.2. An overview of the assessed configurations is given in Table 5.4. In this chapter we will focus on steady flow through for $0 < Q \leq 200\text{l/min}$ ($Re \leq 25000$). Measured flow quantities are indicated: used pressure taps along the constricted channel, hot-film anemom-

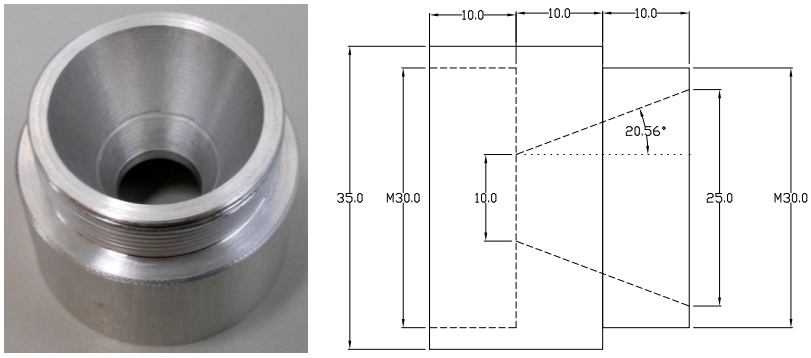

(a) photograph (b) schedule

Figure 5.8: Illustration of the geometry and dimensions [mm] of the cone with converging angle 21^o mounted immediately upstream from the constriction with circular cross section shape in order obtain a smooth inlet condition for the circular constriction with diameter 10mm.

etry and flow visualization. Note that flow visualization is done using the setup shown in Fig. 5.5 so that the upstream channel length yields 60cm instead of 1m.

An overview of the assessed configurations for concrete values of the inlet conditions – upstream channel length L_u and downstream channel length L_d – is given in Fig. 5.9 for the inlet condition corresponding to sharp edges and in Fig. 5.10 in presence of a mixing element. Consequently, the configurations A, B and C depicted in Fig. 5.9 focus on the impact of flow development for the flow through each constriction shape, whereas the configurations D, E and F depicted in Fig. 5.10 focus on the impact of mixing for the flow through each constriction shape.

5.2 Experimental results

5.2.1 Pressure measurements

5.2.1.1 Influence of flow development

The influence of flow development on the measured pressures within the constriction P_1 is assessed for all cross section shapes for constriction with sharp edges at its inlet with and without downstream pipe using the setups depicted in Fig. 5.9 showing the conditions labeled A, B and C in Table 5.4. The measured pressures P_1 and normalized pressures P_1/P_0 are shown in Fig. 5.11. It is seen that the general tendency of the pressure dynamics with increasing upstream pressure is imposed by the presence (or absence) of a downstream pipe (L_d) enveloping the jet downstream from the constriction since its presence ensures negative pressures within the constriction for all cross section shapes. Nevertheless, the impact of the downstream pipe depends on the cross section shape since it is most pronounced for a

Table 5.4: Overview experimental conditions assessed for the constriction shapes shown in Fig. 5.1 indicating the used flow conditioning. In case no flow conditioning is mentioned sharp inlet edges are assessed. The measured flow quantities are indicated: pressure taps defined in Fig. 5.2a, transverse and longitudinal velocity profiles using hot-film anemometry (HF) and flow visualization (FV).

Label	L_u	L_d	**Pressure sensors**(1)	**Flow field**(2,3)	**Comment**	
	Inlet condition: sharp edges (Fig. 5.9) → flow development					
A	2cm	0cm	P_0, $P_1(P_2)$		free jet	all shapes
		15cm	P_0, $P_1(P_2)$, P_3		confined jet	
B	35cm	0cm	P_0, $P_1(P_2)$		free jet	
		15cm	P_0, $P_1(P_2)$, P_3		confined jet	
C	1m	0cm	P_0, $P_1(P_2)$	HF, FV	free jet	
		15cm	P_0, $P_1(P_2)$, P_3		confined jet	
	Inlet condition: use of mixing element (Fig. 5.10) → flow mixing					
D	35cm (ogp)	0cm	P_0, $P_1(P_2)$	HF	free jet	
		15cm	P_0, $P_1(P_2)$, P_3		confined jet	
E	35cm (tgph)	0cm	P_0, $P_1(P_2)$	HF	free jet	circular shape
		15cm	P_0, $P_1(P_2)$, P_3		confined jet	
F	35cm (tgps)	0cm	P_0, $P_1(P_2)$	HF	free jet	
		15cm	P_0, $P_1(P_2)$, P_3		confined jet	
	Inlet condition: no sharp edges (Fig. 5.8) → flow development					
G	35cm (cone)	0cm	P_0, $P_1(P_2)$	HF	free jet	
		15cm	P_0, $P_1(P_2)$, P_3		confined jet	
H	1m (d1cm)			HF	free jet	

(1) Steady flow for $0 < Q \leq 200$l/min or $Re \leq 25000$.
(2) Steady flow for $0 < Q \leq 100$l/min or $Re \leq 15000$.
(3) In hot-film anemometry the upstream channel length yields 1m.

rectangular and circular cross section shape. In addition, it is seen that the effect becomes more prominent as the upstream length increases and hence as flow development increases. When expressing the measured normalized pressure ratio P_1/P_0 as a function of Reynolds number, a minimum value is observed for all cross section shapes for $2000 \leq Re \leq 4000$ immediately followed by a maximum. The exact position of the minimum depends on the Reynolds number. Measured values clearly show the impact of the cross section shape on the flow field for a constriction with sharp inlet edges and incoming flow with different degree of development. Shown results suggest that the main flow dynamics is imposed by sharp edges at the constriction inlet rather than by the degree of flow development.

To gain more insight in the flow development, we briefly consider the root mean square pressure values P_1^{rms} for $L_u = 2$cm presented in Fig. 5.12. It is observed that for Reynolds numbers $Re > 5000$ the root mean square pressure increases quickly, although its growth rate depends on the cross section shape (e.g. values for the isosceles triangle are much larger than values for the circular cross section shape), so that it is an indication that the flows

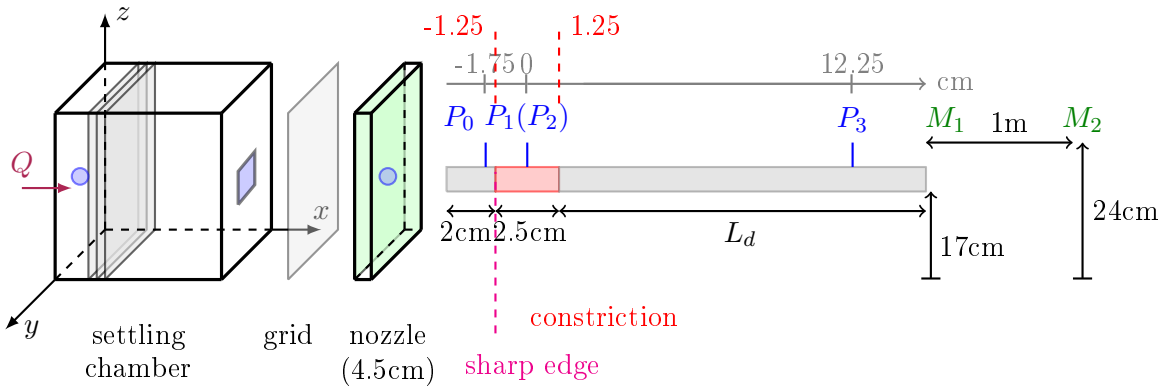

(a) A ($L_u = 2cm$)

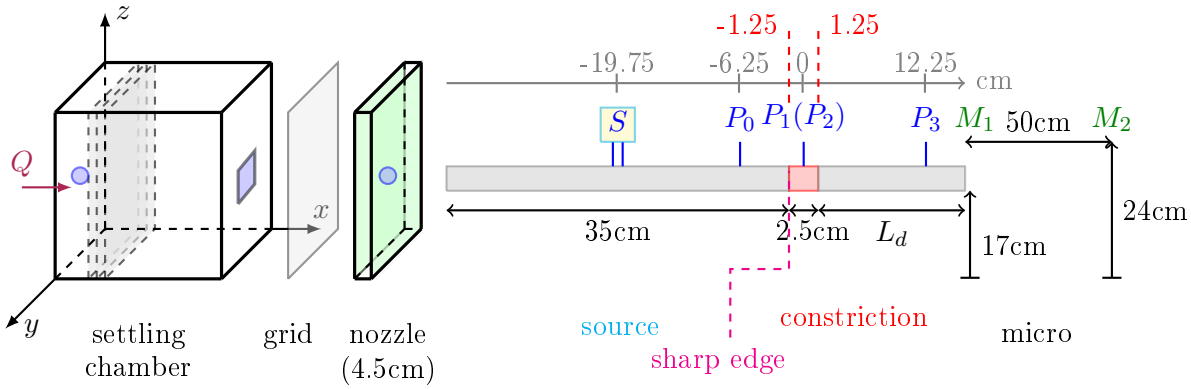

(b) B ($L_u = 35cm$)

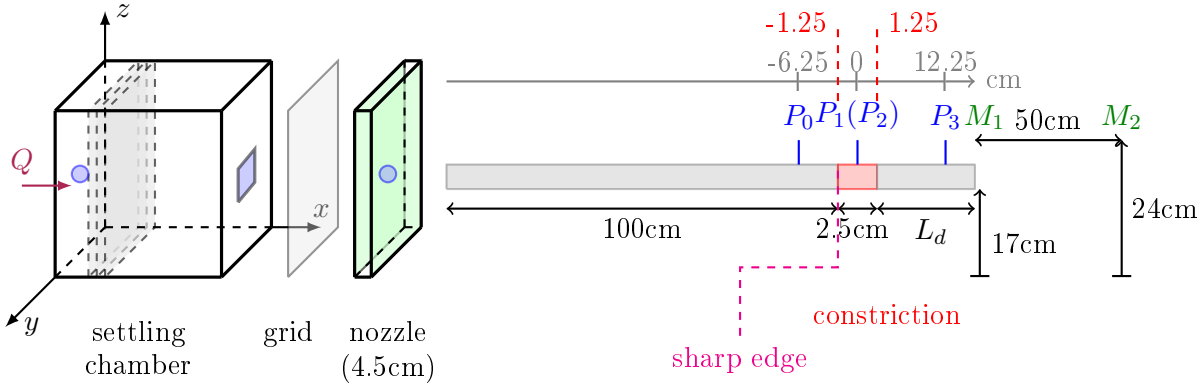

(c) C ($L_u = 1m$)

Figure 5.9: Schematic overview of assessed configurations for all cross section shapes shown in Fig. 5.1 for the values of L_u, L_d and sharp edges at the inlet of constriction (so no use of a mixing element) for the configurations labeled A, B and C listed in Table 5.4: without downstream pipe ($L_d = 0$cm) or with downstream pipe ($L_d = 15$cm).

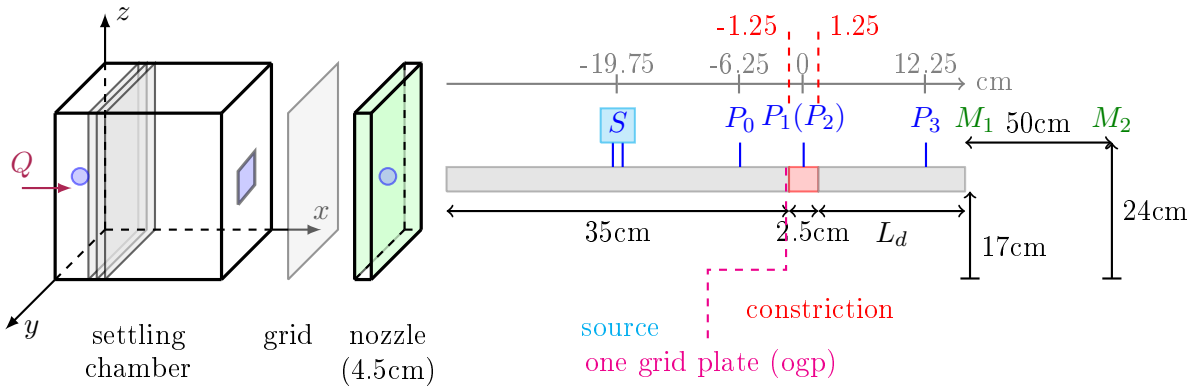

(a) D (ogp)

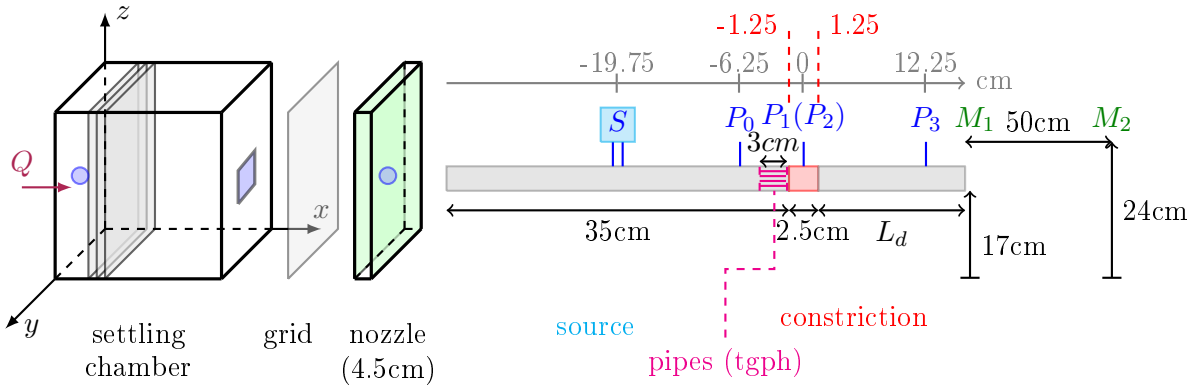

(b) E (tgph)

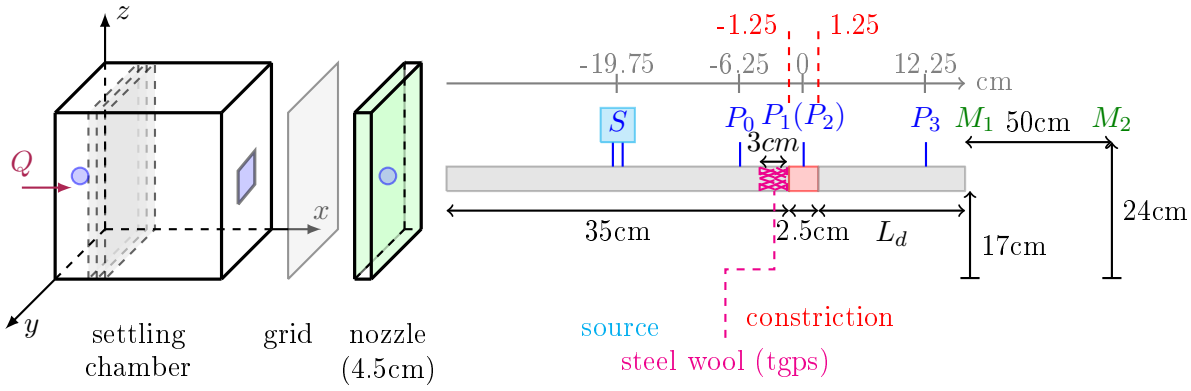

(c) F (tgps)

Figure 5.10: Schematic overview of assessed configurations for all cross section shapes shown in Fig. 5.1 for the values of $L_u = 35$cm, L_d and with the used of a mixing element for the configurations labeled D, E and F listed in Table 5.4: without downstream pipe ($L_d = 0$cm) or with downstream pipe ($L_d = 15$cm).

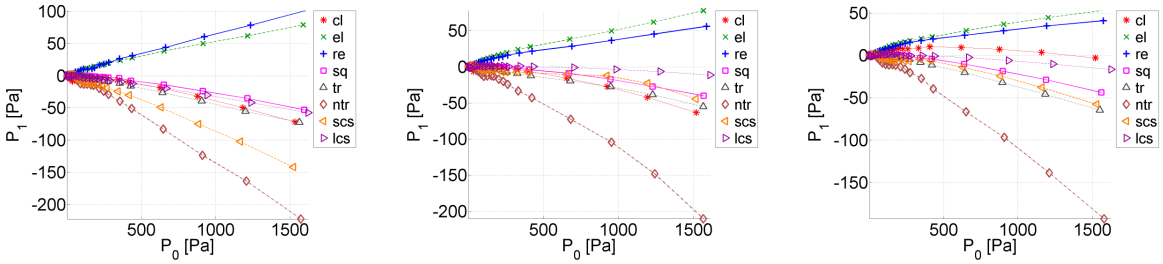

(a) $L_u = 2$cm and $L_d = 0$cm (b) $L_u = 35$cm and $L_d = 0$cm (c) $L_u = 1$m and $L_d = 0$cm

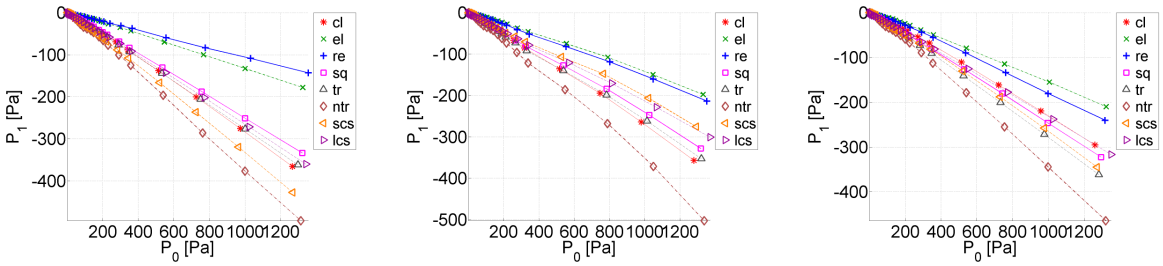

(d) $L_u = 2$cm and $L_d = 15$cm (e) $L_u = 35$cm and $L_d = 15$cm (f) $L_u = 1$m and $L_d = 15$cm

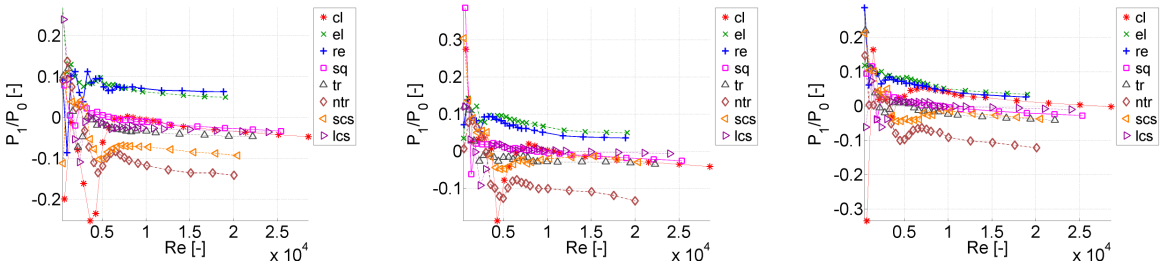

(g) $L_u = 2$cm and $L_d = 0$cm (h) $L_u = 35$cm and $L_d = 0$cm (i) $L_u = 1$m and $L_d = 0$cm

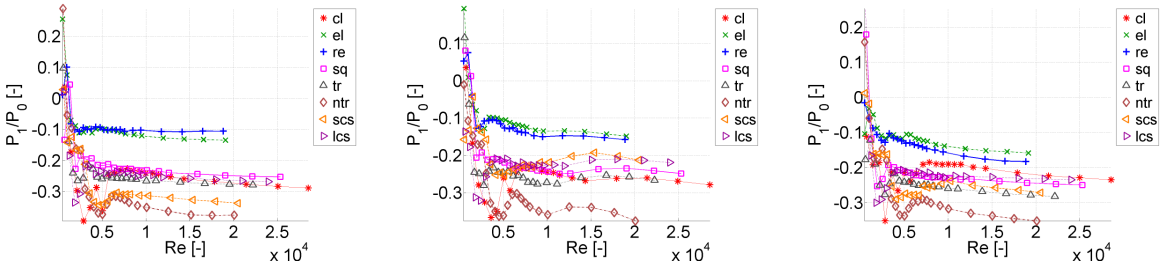

(j) $L_u = 2$cm and $L_d = 15$cm (k) $L_u = 35$cm and $L_d = 15$cm (l) $L_u = 1$m and $L_d = 15$cm

Figure 5.11: Measured mean pressures within the constriction as a function of upstream pressure $P_1(P_0)$ and normalized pressure measured within the constriction as a function of Reynolds number $P_1/P_0(Re)$ for different constriction shapes with sharp inlet edge with ($L_d = 15$cm) and without ($L_d = 0$cm) downstream pipe: $L_u = 2$cm or label A (left) , $L_u = 35$cm or label B (middle) and $L_u = 1$m or label C (right).

becomes turbulent. Consequently, the range of Reynolds numbers for which the minimum and subsequent maximum is found for the pressure ratio $P_1/P_0(Re)$ (Fig. 5.11) is probably associated with the transition regime and passing of vortices triggered somehow by the sharp edged inlet at the constriction inlet. The flow dynamics needs to be sought in more detail in order to inform on the transition mechanism, nevertheless the presence of flow structures might be confirmed (or not) from the flow visualization further in this chapter as well as from an analysis of the measured velocity profiles.

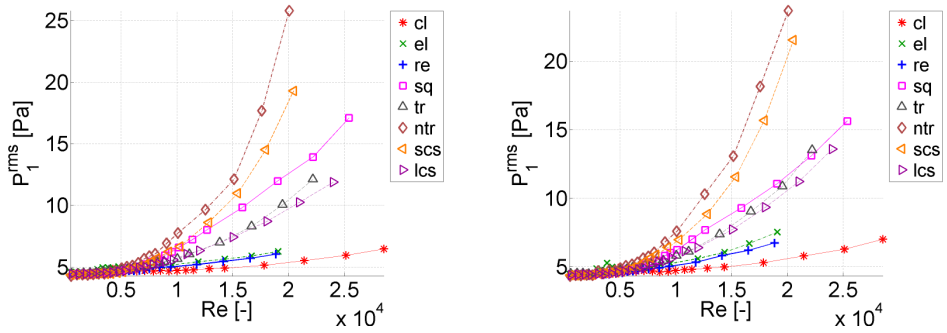

(a) $L_u = 2$cm and $L_d = 0$m (b) $L_u = 2$cm and $L_d = 15$cm

Figure 5.12: Measured root mean pressure values within the constriction P_1^{rms} for $L_u = 2$cm (label A in Table 5.4).

Finally, Fig. 5.13 illustrates the impact of the position of the pressure tap on the measured pressure for cross section shapes for which two pressure taps are present as shown in Fig. 5.1. Obviously, the position of the pressure tap influences the measured values and the position is more relevant for asymmetrical cross section shapes.

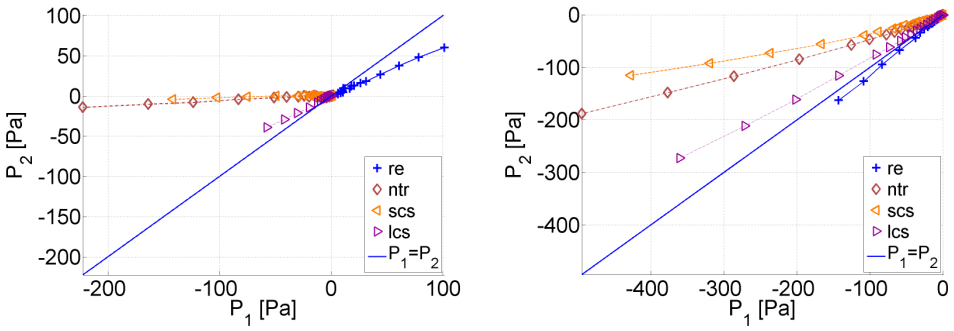

(a) $L_u = 2$cm and $L_d = 0$m (b) $L_u = 2$cm and $L_d = 15$cm

Figure 5.13: Pressure within the constriction measured at positions P_1 and P_2 indicated in Fig. 5.1 for $L_u = 2$cm and a sharp inlet edge to the constriction (label A in Table 5.4).

5.2.1.2 Influence of flow mixing

The influence of flow mixing on the measured pressures within the constriction P_1 is assessed for all cross section shapes by using a mixing element immediately downstream from the constriction with and without downstream pipe using the setups depicted in Fig. 5.10 showing the conditions labeled D, E and F in Table 5.4. The measured pressures P_1 and normalized pressures P_1/P_0 are shown in Fig. 5.14. The same way as for flow development, It is seen that the general tendency of the pressure dynamics with increasing upstream pressure is again imposed by the presence (or absence) of a downstream pipe (L_d) enveloping the jet downstream from the constriction since its presence ensures negative pressures within the constriction for all cross section shapes. Nevertheless – and this was also observed for flow development – the impact of the downstream pipe depends on the cross section shape since it is most pronounced for a rectangular and circular cross section shape. It is noted that the using the mixing element increases the pressure difference between upstream pressure P_0 and the pressure within the constriction P_1.

When expressing the measured normalized pressure ratio P_1/P_0 as a function of Reynolds number, the influence of upstream flow conditioning becomes apparent when comparing the measurements plotted in Fig. 5.11 and in Fig. 5.14. Indeed, the pronounced minimum observed for different degree of upstream flow development in presence of sharp edges, is no longer observed for most cross section shapes when a mixing element is used. Instead, a maximum value is observed in the range $2000 \leq Re \leq 4000$ for which the position depends on the cross section shape. To which extent the presence of the flow dynamics is altered due to flow mixing is partly the aim of the flow visualization further in this chapter as well as from an analysis of the measured velocity profiles.

Measured values show the impact of the cross section shape on the flow field for a constriction using a mixing element at its inlet.

5.2.1.3 Influence of the cross sections shape: flow development and mixing

The previous sections outlined the influence of the cross section shape of the constriction on the measured mean pressures within the constriction for different upstream flow conditions either due to flow development or due to flow mixing[9]. In this section, we compare and quantify the impact of the cross section section shape on the pressure values measured within the constriction. Measured pressures for different flow conditions, labeled from A to G in Table 5.4, are plotted in Fig. 5.15 in the case of a circular constriction. The figure illustrates the severe impact of upstream flow conditioning on the measured pressures within the constriction. Nevertheless, it is interesting to notice that measured values for $L_u = 1$m (label C) and the use of a converging cone (label G) follow the same tendencies. Since besides the cross section shape and upstream flow conditions, the flow dynamics is determined by the applied upstream

[9]For all cases, the flow dynamics merits a more profound analysis.

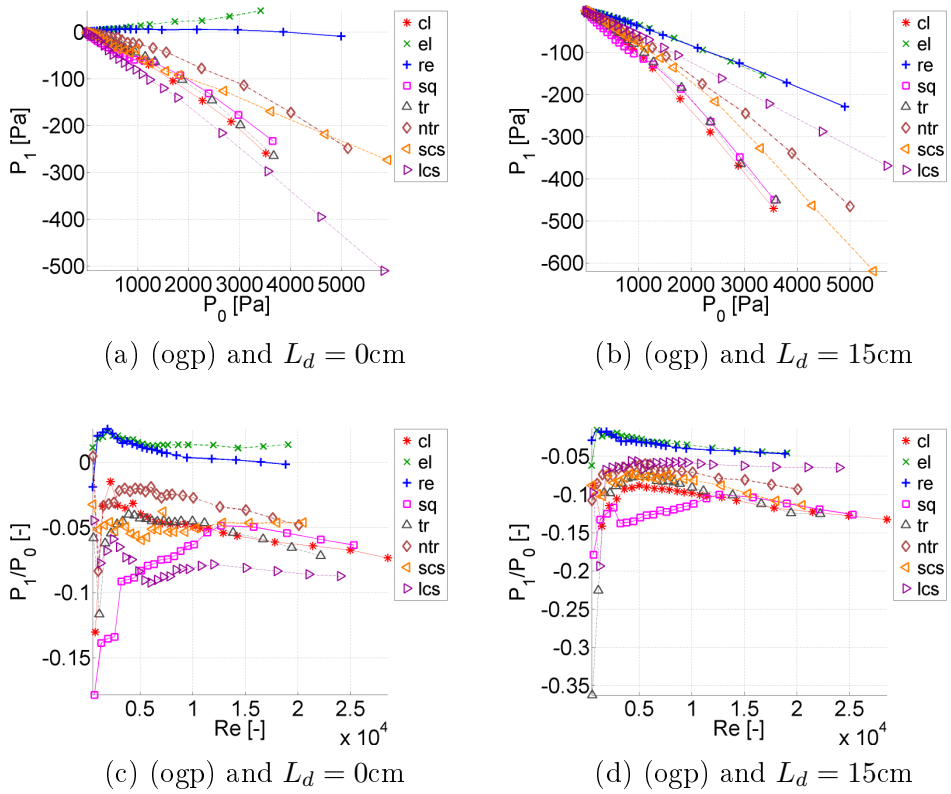

(a) (ogp) and $L_d = 0$cm

(b) (ogp) and $L_d = 15$cm

(c) (ogp) and $L_d = 0$cm

(d) (ogp) and $L_d = 15$cm

Figure 5.14: Measured mean pressures within the constriction as a function of upstream pressure $P_1(P_0)$ and normalized pressure measured within the constriction as a function of Reynolds number $P_1/P_0(Re)$ for different constriction shapes using a mixing element with ($L_d = 15$cm) and without ($L_d = 0$cm) downstream pipe: a single grid is placed immediately upstream from the constriction or label D.

pressure (or Reynolds number) the ranges[10] $\Delta P_1(P_0)$ and $\Delta(P_1/P_0)(Re)$ due to changing the cross section shape will change when their value is taken for different upstream pressures P_0 or associated Reynolds numbers Re. Nevertheless, in order to quantify the influence of the overall impact of the cross section shape on the pressure measured within the constriction the relative value of the range $\Delta P_1/P_0$ and the range of $\Delta(P_1/P_0)$ are quantified for particular values of the upstream pressure P_0 or Reynolds number Re. When the overall impact is sought for multiple cross section shapes (CSS) and a single upstream flow condition, the impact is quantified by evaluating the following expressions at the chosen P_0 value or Re values (Re values are chosen either within ($Re \approx 3600$) or well above ($Re \approx 17500$) the expected laminar-

[10]Note that $\Delta P_1(P_0) = 0$ and $\Delta(P_1/P_0)(Re) = 0$ holds in case the shape of the constriction does not influence the pressure measurements and hence can be neglected.

turbulent transition regime),

$$\frac{\Delta P_1}{P_0} = \frac{\left|\max\left(P_1(\forall \text{ CSS})\right) - \min(P_1(\forall \text{ CSS}))\right|}{P_0}, \tag{5.1}$$

$$\Delta\left(\frac{P_1}{P_0}\right) = \left|\max\left(\frac{P_1}{P_0}(\forall \text{ CSS})\right) - \min\left(\frac{P_1}{P_0}(\forall \text{ CSS})\right)\right|. \tag{5.2}$$

When the overall impact is sought for multiple upstream flow conditions (labeled in Table 5.4) for a single cross section shape (circular), the impact is quantified by evaluating the following expressions at the chosen P_0 value or Re value,

$$\frac{\Delta P_1}{P_0} = \frac{\left|\max\left(P_1(\forall \text{ A to G})\right) - \min(P_1(\forall \text{ A to G}))\right|}{P_0}, \tag{5.3}$$

$$\Delta\left(\frac{P_1}{P_0}\right) = \left|\max\left(\frac{P_1}{P_0}(\forall \text{ A to G})\right) - \min\left(\frac{P_1}{P_0}(\forall \text{ A to G})\right)\right|. \tag{5.4}$$

The resulting overall impact of the cross section shape on the mean pressure within the constriction is summarized in Table 5.5. It is observed that both measures, $\Delta P_1/P_0$ or $\Delta(P_1/P_0)$, of the impact of the cross section shape on the measured pressure within the constriction express the same tendencies from the following observations:

- observations when varying either the cross section shape (impact of the cross section shape) or the flow conditioning (impact of flow conditioning):
  - the order of magnitude of the impact amounts from 10% up to 30% of the upstream pressure. This finding illustrates that, at least for the used P_0 or Re, details of the cross section shape or details of the flow facility are equally important.
  - in general the impact is greater in presence of a channel downstream from the constriction (confined jet at the exit of the constriction) than in absence of such a downstream channel (free jet at the exit of the constriction).
- observations when varying the cross section shape (impact of the cross section shape):
  - the impact of the cross section shapes reduces (from ≈25% to ≈10%) as the upstream flow conditioning favors flow development (L_u increases) or as a mixing element is used (ogp).
  - increasing the upstream pressure or Reynolds number does not significantly increases the impact of the cross section shape. This suggests that due to dissipation and turbulence development, the flow field looses the identity or imprint of the geometry by means of the flow structures characterizing the cross section shape. Flow visualization and flow velocity analysis can possibly offer a confirmation for this point.
- observations when varying the flow conditioning (impact of flow conditioning):
  - the impact of the flow conditioning in presence of an upstream channel (confined jet) is less sensible to an increase of the Reynolds number than in absence of an

upstream channel (free jet for which the impact reduces with more than half its magnitude as Re is increased) so that the upstream channel has a memory effect of the upstream flow conditions even for Reynolds numbers well above the transition regime. Note that no such pronounced memory effect (or flow imprint) is found for the cross section shape[11].

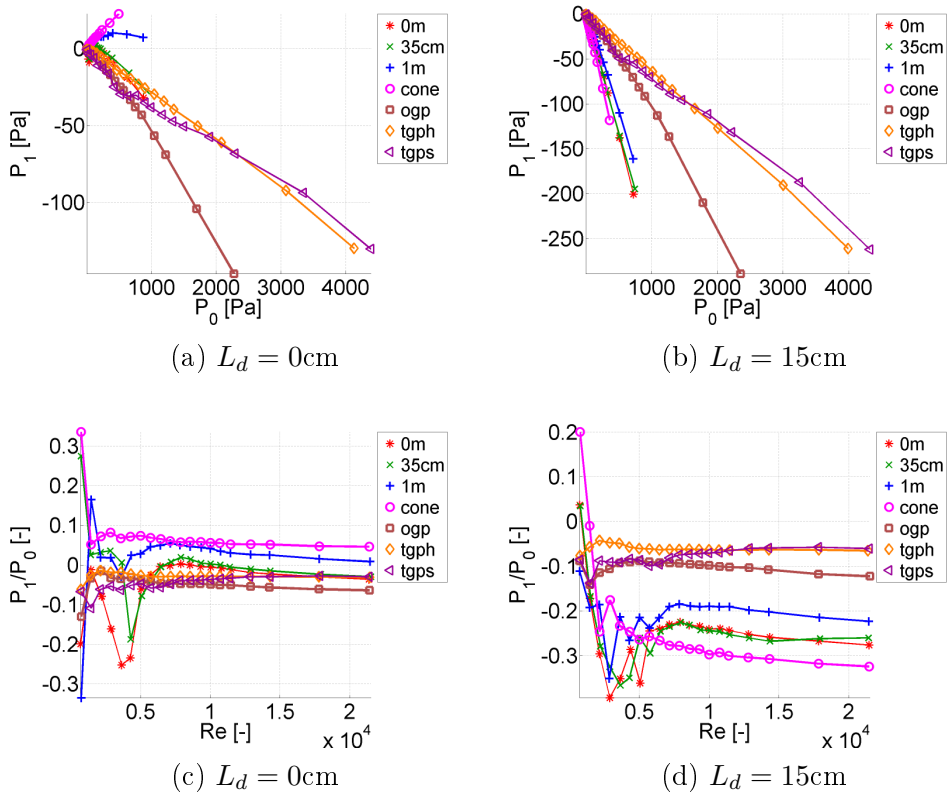

(a) $L_d = 0$cm (b) $L_d = 15$cm

(c) $L_d = 0$cm (d) $L_d = 15$cm

Figure 5.15: Measured mean pressures within the constriction as a function of upstream pressure $P_1(P_0)$ and normalized pressure measured within the constriction as a function of Reynolds number $P_1/P_0(Re)$ for different constriction shapes for different degrees of upstream flow development and sharp inlet edges (label A, B and C in Table 5.4) and for different mixing elements upstream from the constriction (label D, E and F in Table 5.4) with ($L_d = 15$cm) and without ($L_d = 0$cm) downstream pipe: $L_u = 2$cm or label A (0m) , $L_u = 35$cm or label B (35cm) and $L_u = 1$m or label C (1m), one grid plate or label D (ogp), pipes or label E (tgph), steel wool or label F (tgps) and converging cone or label G (cone).

5.2.2 Velocity measurements and flow visualization

In the previous section, the impact of the cross section shape and flow conditioning on the pressure within a constricted channel, with and without a channel downstream from the

[11] It is of interest to further search the spatial extent of the flow memory for steady flow.

Table 5.5: Overall impact of the constriction cross section shape (Fig. 5.1) on the range of ratios $\Delta P_1/P_0$ and $\Delta(P_1/P_0)$ for a particular upstream pressure or Reynolds number for different upstream flow conditions (labeled following Table 5.4). Overall impact of the flow conditioning on the range of ratios $\Delta P_1/P_0$ and $\Delta(P_1/P_0)$ for a particular upstream pressure or Reynolds number for the constriction with circular shape. Results in absence ($L_d = 0$cm) and presence ($L_d = 15$cm) of a channel downstream from the constriction.

	$\Delta P_1/P_0$ [%]		$\Delta(P_1/P_0)$ [%]	
	$L_d = 0$cm	$L_d = 15$cm	$L_d = 0$cm	$L_d = 15$cm
Overall impact of cross section shapes: Eq. (5.1) and Eq. (5.2)				
A (L_u =2cm)	21%[1]	27%[1]	33%[3] 20%[4]	25%[3] 27%[4]
B (L_u =35cm)	18%[1]	23%[1]	18%[3] 17%[4]	27%[3] 21%[4]
C (L_u =1m)	16%[1]	19%[1]	13%[3] 15%[4]	18%[3] 19%[4]
D (ogp)	10%[2]	9%[2]	11%[3] 10%[4]	11%[3] 7%[4]
Overall impact of flow conditioning (circular shape): Eq. (5.3) and Eq. (5.4)				
A to G	9%[5]	26%[5]	32%[3] 11%[4]	32%[3] 26%[4]

[1] $P_0 \approx 1500$Pa for $L_d = 0$cm and $P_0 \approx 1300$Pa for $L_d = 15$cm.

[2] $P_0 \approx 3400$Pa for $L_d = 0$cm and $P_0 \approx 3500$Pa for $L_d = 15$cm.

[3] $Re \approx 3600$ for $L_d = 0$cm and $L_d = 15$cm.

[4] $Re \approx 17500$ for $L_d = 0$cm and $L_d = 15$cm.

[5] $P_0 \approx 360$Pa for $L_d = 0$cm and $L_d = 15$cm.

constriction, was characterized for a large range of Reynolds numbers ($Re \leq 25000$). It was suggested that the flow dynamics is partly governed by flow structures, whose existence is triggered by the sharp edges at the contraction inlet. Therefore, in the current section, a start is made to search the flow dynamics. Hot film anemometry is applied in order to sample the

velocity field in combination with flow visualization in order to obtain an overall view of the flow field.

Concretely, the free jet portion immediately downstream from the constricted channel portion is searched for $Re \leq 15000$. Consequently, as indicated in Table 5.4, we limit ourselves to configurations without downstream channel ($L_d = 0$cm). In addition, we focus on the influence of the cross section shape for two flow conditions: sharp edges at the constriction inlet (label C in Table 5.4) and a single grid placed immediately upstream from the constriction (label D in Table 5.4). As for the pressure measurements outlined in the previous section, additional upstream flow conditions are assessed for a circular constriction.

Measured velocity profiles and visualized flow fields are presented in the following. The analysis focuses on the influence of the cross section shape and flow conditioning. Therefore, the measured profiles are presented as a function of the cross section shape and as a function of the applied flow conditioning rather than as a function of the applied volume flow rate in order to assess their impact on the flow properties. Measured profiles as a function of volume flow rate are shown in Appendix F.

5.2.2.1 Longitudinal velocity profiles

As an example, the measured longitudinal mean velocity profiles downstream from the circular constriction with sharp inlet edges are plotted in Fig. 5.16a for different flow rates[12] illustrating the typical range of velocity magnitudes and the applied spatial increment[13].

Influence of cross section shape The streamwise evolution of the mean velocity shown in Fig. 5.16a, is a fine example of round jet development, which is schematically depicted in Fig. 5.17. Indeed, the centerline velocity immediately downstream from the constriction exit approximates the initial centerline velocity at the exit u_0 characterizing an ideal flow. The extent of the cone of ideal fluid for which $u \approx u_0$ defines the potential cone extent x_{pc}. The potential cone is enveloped by a free shear layer in which the jet flow mixes with the surrounding fluid. Downstream from the potential cone, self similar behavior is expected to occur in the far field, which can be described by a velocity decay equation[14]. In the current chapter, we focus our attention mainly on near field behavior such as the evolution of the potential cone extent as a function of Reynolds number for the cross section shapes shown in Fig. 5.1. Indeed, the longitudinal velocity is assessed in the near field downstream from the

[12] The measured longitudinal normalized velocity profiles for each of the cross section shapes, shown in Fig. 5.1, is plotted as a function of the applied volume flow rate in Appendix F.1: mean (Fig. F.1) and root mean square (Fig. F.2) for sharp inlet edges (flow condition labeled C in Table 5.4) and mean (Fig. F.3) for a single grid placed immediately upstream from the constriction inlet (flow condition labeled D of Table 5.4) and the corresponding root mean square (Fig. F.4).

[13] As a reminder, spatial step Δx applied for the longitudinal velocity profile yields $\Delta x = 1$mm for $x \leq 10$mm and $\Delta x = 5$mm for $x > 10$mm.

[14] The form of the decay equation will depend on the cross section shape and in addition initial conditions of the velocity at the jet emitting nozzle outlet, *i.e.* the constriction outlet.

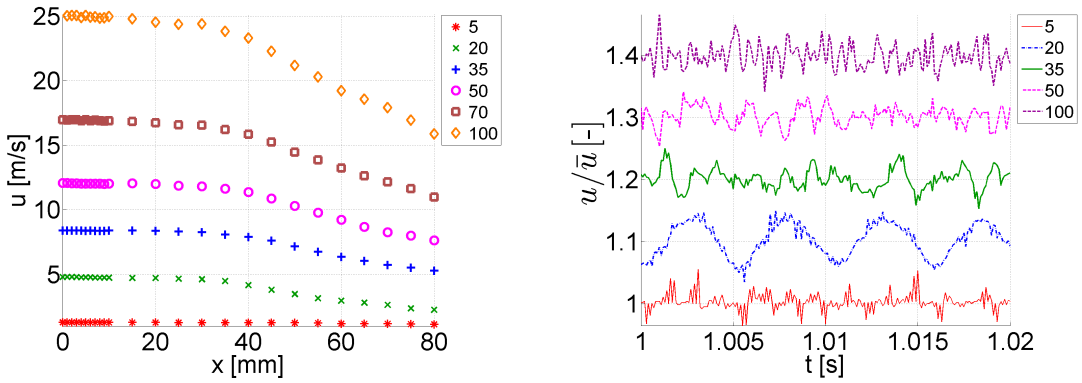

(a) mean longitudinal profile (b) velocity signal

Figure 5.16: Illustration of velocity quantities for the circular constriction with sharp inlet edges (label C in Table 5.4) are plotted in Fig. 5.16a for different flow rates Q (5, 20, 35, 50, 70 and 100l/min): a) near field longitudinal mean velocity profiles along the centerline x downstream from the constriction illustrating typical velocity magnitude and spatial increment (1mm for $x \leq 10$mm and 5mm for $x >$10mm). b) instantaneous velocity signal (0.2s) as a function of time t normalized by its mean value $u/\bar{u}$ at the initial centerline position $x = 0$ for the circa. For clarity, velocity signals are shifted with with 0.1 with respect to the previous one. Quasi-periodicity is observed depending on the flow rate (*e.g.* $Q = 20$l/min).

constriction since variations of the flow structure due to either the cross section shape or the upstream flow conditions will be apparent.

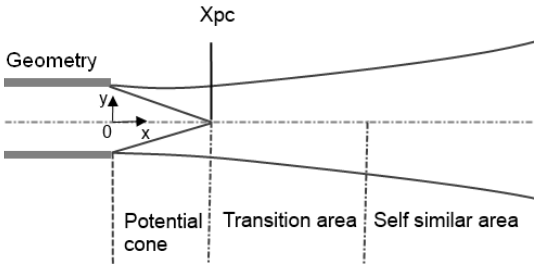

(a) potential cone extent x_{pc}

	cl	sq	lcs	tr	scs	ntr	el	re
D [mm]	10	8.9	8.4	7.8	7.2	7.0	6.7	6.6
α [%]	91	92	90	96	87	93	90	90

(b) threshold criterion $u(x) \geq \alpha u_0$

Figure 5.17: Free jet development: a) schematic overview of potential cone extent x_{pc}. b) Threshold α as a function of the cross section shape applied to determine the potential cone extent x_{pc} presented in Fig. 5.19 [4]. For a round jet, $4 < x_{pc}/D < 8$ [40].

In order to quantify the impact of the cross section shape on the potential cone extent, we consider the measured normalized mean velocity as a function of the cross section shape for sharp edges at the constriction inlet (flow condition labeled C in Table 5.4) plotted in Fig. 5.18.

The impact of the cross section shape on the near field is apparent for all assessed volume flow rates with respect to the initial velocity u_0, the extent of the potential cone as with respect to its initial decay. The initial velocity at the constriction exit for instance is seen to vary up to 20%. As for the pressure measurements, the measured velocity profiles suggest that the flow behavior is shaped by the sharp edges and the presence of flow structures. Indeed, the decreasing tendency of the velocity within the potential cone suggests jet forcing due to the sharp edges at the constriction inlet. In addition, observed humps in the longitudinal velocity profile, such as observed for the rectangular constriction for $Q = 5\text{l/min}$, as well as the quasi-periodicity of the velocity signal illustrated in Fig. 5.16b, suggests the passing of coherent structures. The observed differences in flow dynamics, when varying the cross section shape, motivate the adaptation of the threshold α applied in the threshold criterion to define the potential cone extent. Applied threshold values, listed in Fig. 5.17, are an 'ad-hoc' choice. The resulting estimation of the potential cone extent x_{pc} as a function of Reynolds number for each of the assessed cross section shapes is presented in Fig. 5.19.

Compared to typical values ($4 < x_{pc}/D < 8$ [40] reported for the potential core extent of a round jet emitted by, at least from a flow point of view, well designed nozzles) the constricted channel with sharp inlet edges reduces the potential core extent since in general $x_{pc}/D \leq 4$ holds for $Re > 1000$. For $Re \leq 1000$ a large variation in the potential core extent is observed ranging from 0 (large circular constriction) up to 7 (circular). The general tendency of initially decreasing and consequently increasing of the potential core extent as the Reynolds number increases corresponds to the expected behavior described in literature. The change in tendency is related to the transition region. Note that no such tendency is observed for the large circular sector suggesting that flow mixing and interaction affects the centerline velocity as far upstream as the constriction outlet. Besides, the described general tendency which is likely related to the flow condition, the influence of the cross section shape on the near field downstream from the constriction is clearly illustrated by considering the need of a different threshold for different cross section shapes as well as by the variation of estimated values with as much as 50%. Note that their is no relation between firstly the value of the hydraulic diameter and the applied threshold and secondly between the value of the threshold and the estimated potential cone extent.

Influence of flow conditioning In the previous section it was suggested that the presence of sharp edges at the constriction inlet (flow condition with label C in Table 5.4) results in a reduction of the potential cone extent compared to values obtained for smooth nozzles. In the current section, we further explore the influence of the upstream flow condition based on measured near field longitudinal velocity profiles. Fig.5.20 presents the normalized mean profiles as a function of the cross section shape for a single grid placed immediately upstream from the constriction inlet (flow condition labeled D in Table 5.4). Comparing the velocity

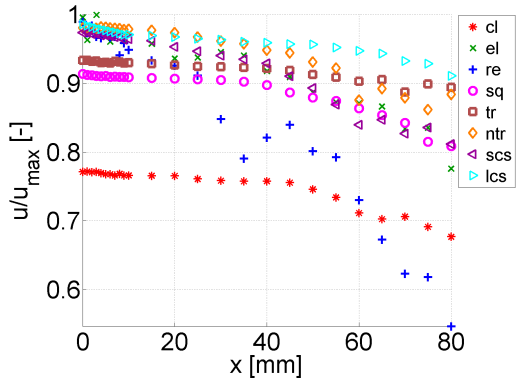

(a) Q=5l/min

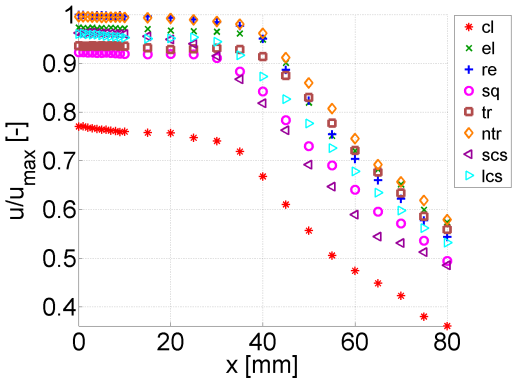

(b) Q=20l/min

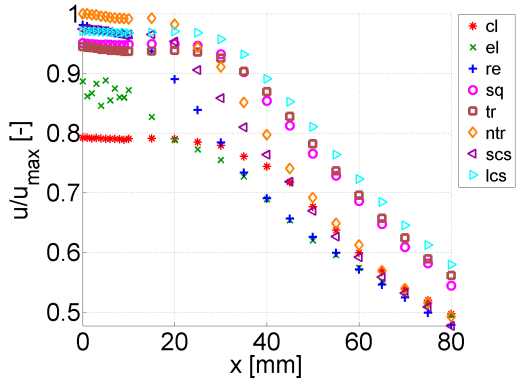

(c) Q=35l/min

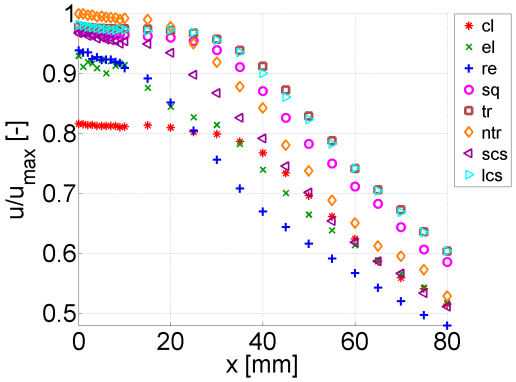

(d) Q=50l/min

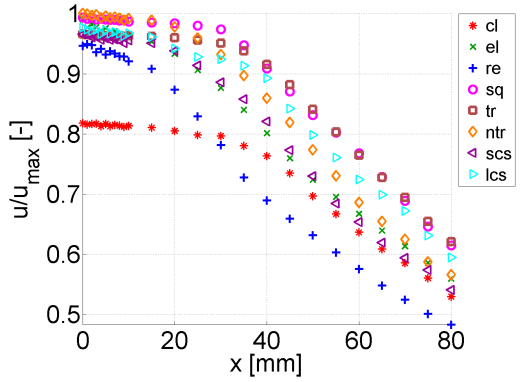

(e) Q=70l/min

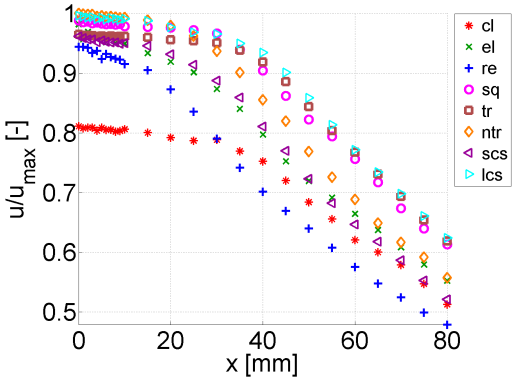

(f) Q=100l/min

Figure 5.18: Measured near field normalized longitudinal mean velocity profiles u/u_{max} along the centerline of the jet for cross section shapes shown in Fig. 5.1 as a function of volume flow rate Q (5, 20, 35, 50, 70 and 100l/min) for sharp edges at the constriction inlet (label C of Table 5.4). u_{max} denotes the maximum mean initial velocity for all cross section shapes for a given volume flow rate.

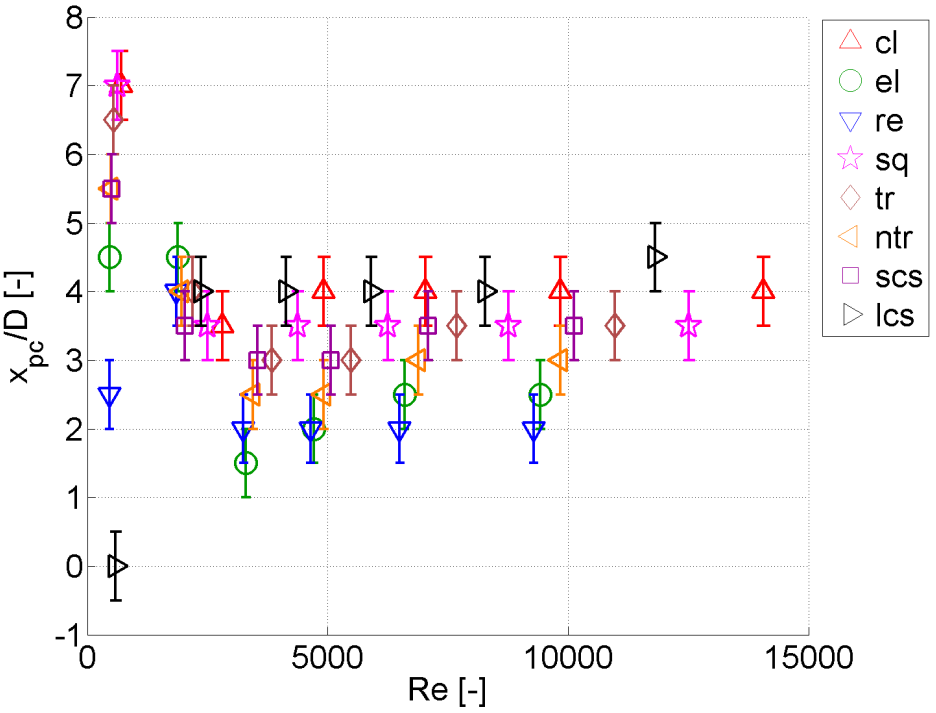

Figure 5.19: Potential cone extent normalized by the hydraulic diameter x_{pc}/D, mean (symbols) and uncertainty due to the spatial step (vertical bars), as a function of Reynolds number Re for all cross section shapes shown in Fig. 5.1 and sharp edges at the constriction inlet (label C in Table 5.4).

profiles in presence of the mixing element (single grid at constriction inlet) presented in Fig.5.20 with the velocity profiles shown in Fig. 5.18 in absence of such a mixing element (sharp edges at constriction inlet) illustrates the severe impact of the mixing element on the near field flow development for all volume flow rates[15].

The presence of the single grid mixing element will decrease the area at the constriction inlet with $\approx$ 50% of the constriction area. Obviously, as a consequence the velocity will increase in presence of the mixing element compared to the velocity obtained in absence of the mixing element for the same volume flow rate. Therefore, besides affecting the near field due to increased flow mixing, the effect of the mixing element is likely to reduce the Reynolds number for which the transition to turbulence occurs. A first confirmation of this effect is provided by the minimum of the potential cone associated with the transition regime extent which reduces from $Q \approx 35$l/min to $Q \approx 20$l/min when a mixing element is used. In addition, increased flow mixing increases the velocity decay observed in the potential cone extent due to the increased interaction of the centerline velocity and the enveloping fluid. This suggests also that the flow pattern is less stable in presence of a mixing element which in turn again justified

[15] and re-illustrates the influence of the cross section shape as well.

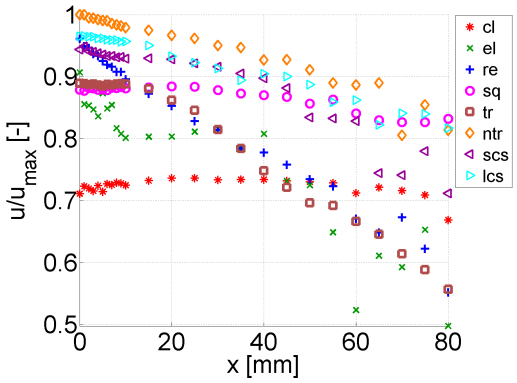

(a) Q=5l/min

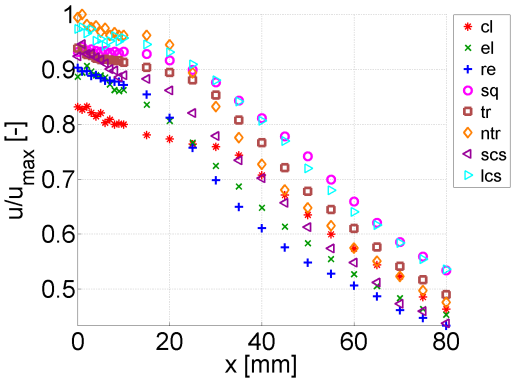

(b) Q=20l/min

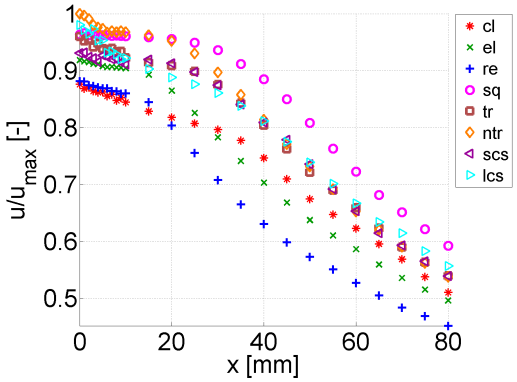

(c) Q=35l/min

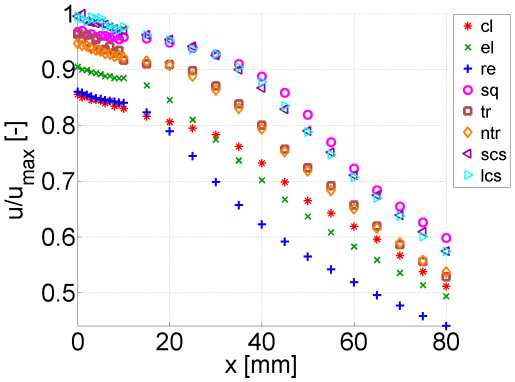

(d) Q=50l/min

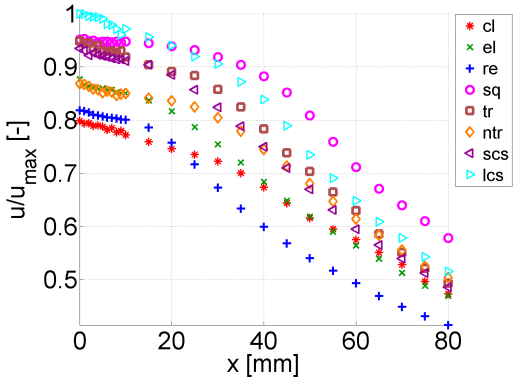

(e) Q=70l/min

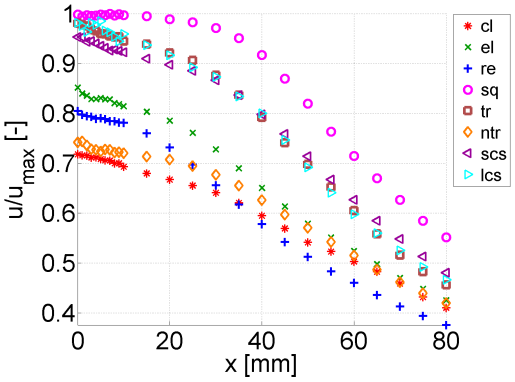

(f) Q=100l/min

Figure 5.20: Measured near field normalized longitudinal mean velocity profiles u/u_{max} along the centerline of the jet for cross section shapes shown in Fig. 5.1 as a function of volume flow rate Q (5, 20, 35, 50, 70 and 100l/min) for a single grid placed immediately upstream from the constriction inlet (label D inTable 5.4). u_{max} denotes the maximum mean initial velocity for all cross section shapes for a given volume flow rate.

the decrease of the Reynolds numbers associated with the transition regime[16]. Nevertheless, although the flow pattern is argued to be less stable, the presence of the mixing element do seems to homogenize the flow behavior[17] so that in particular the velocity profiles measured for the circular and rectangular cross section are more in agreement with tendencies observed for the other cross section shapes .

The influence of the flow condition is further quantified for the circular constriction. The near field flow behavior is assessed in presence of diverse mixing elements and different degrees of flow development using the upstream flow conditions labeled C up to H in Table 5.4. Normalized mean velocity profiles for each of the assessed volume flow rates are presented as a function of the upstream flow condition in Fig. 5.21.

The velocity profiles show the effect of upstream flow development as well as flow mixing on the near field flow development for all assessed volume flow rates (for instance when considering the resulting variation of potential cone extent which *e.g.* for $Q = 5\text{l/min}$ occupies either the entire near field (d1cm) or is absent (tgps)). The following observations are made:

- with respect to upstream flow conditioning using a mixing element (and using the previously discussed single grid (ogp, label D in Table 5.4) as a reference):
  - immediately downstream from constriction outlet[18]
    - Adding pipes to the single grid mixing element (tgph, label E in Table 5.4) straightens the flow and as a result reduces the mixing in the immediate near field.
    - Adding steel wool[19] to the single grid mixing element (tgps, label F in Table 5.4) increases the mixing and hence the initial decay rate immediately downstream from the constriction exit.
  - onset of the decay region
    - Adding pipes to the single grid mixing element (tgph, label E in Table 5.4) does not influences the decay onset region, since the decay rate matches the single grid case at least for higher volume flow rates.
    - Adding steel wool to the single grid mixing element (tgps, label F in Table 5.4) does not influences the decay onset. It is interesting to note that it matches for all volume flow rates the decay observed for pipes, although that the downstream distance needed to 'forget' the details of the mixing element decreases as the Reynolds number (of volume flow rate) increases. This is in accordance with the expected diminishing stability[20] of the flow pattern for higher

[16] More research is motivated for the flow analysis and in particular for the stability of the flow patterns and the transition mechanisms.

[17] A quantitative study of the onset of the decay region is of interest.

[18] Note that in the case of a single grid no potential core is distinguished due to mixing explaining why it is not assessed to obtain the equivalent of Fig. 5.19.

[19] Note that for steel wool the velocity profile consists of an initial decay region, an intermediate region and the onset of a second decay region.

[20] A study aiming flow stability and transition mechanisms is of interest.

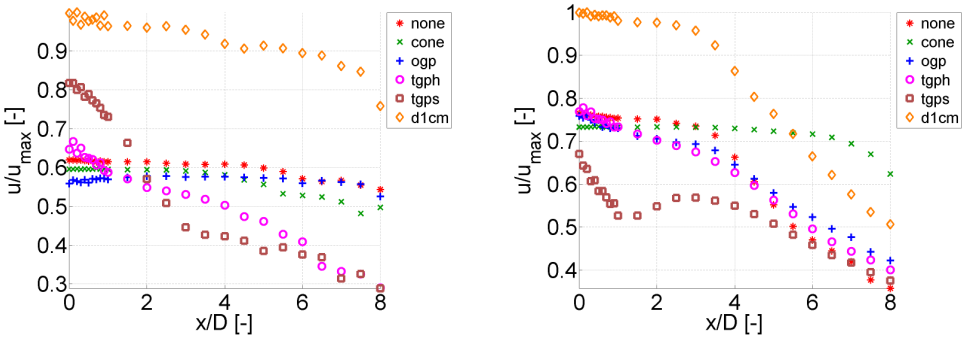

(a) Q=5l/min (b) Q=20l/min

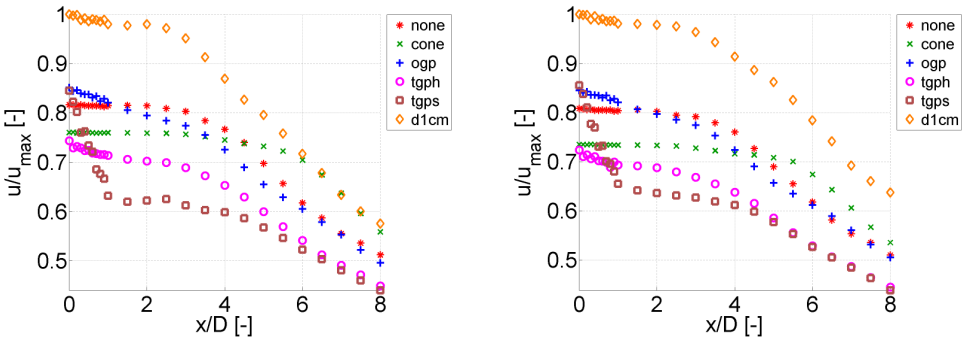

(c) Q=35l/min (d) Q=50l/min

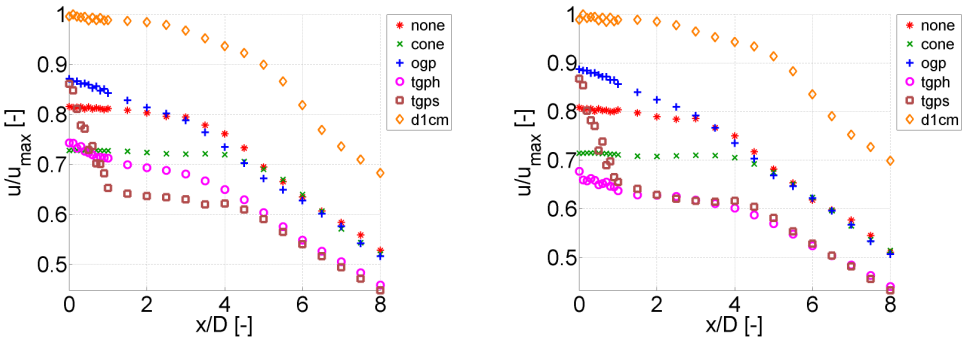

(e) Q=70l/min (f) Q=100l/min

Figure 5.21: Measured near field normalized longitudinal mean velocity profiles u/u_{max} along the centerline of the jet for a circular cross section shape shown in Fig. 5.1 as a function of volume flow rate Q (5, 20, 35, 50, 70 and 100l/min) for different flow conditioning upstream from the constriction: sharp inlet edges (none, label C in Table 5.4), single grid (ogp, label D in Table 5.4), pipes (tgph, label E in Table 5.4), steel wool (tgps, label F in Table 5.4), converging cone (cone, label G in Table 5.4) and $L_u = 1$m with diameter 1cm (d1cm, label H in Table 5.4). u_{max} denotes the maximum mean initial velocity for all cross section shapes for a given volume flow rate.

Reynolds numbers.

- with respect to upstream flow conditioning influencing flow development (and using the previously discussed sharp inlet edges (none, label C in Table 5.4) as a reference):
  - immediately downstream from constriction outlet
    - Using a converging cone to reduce the effect of sharp inlet edges (cone, label G in Table 5.4) enlarges the potential cone extent.
    - Extending the constriction length in order to approximate fully developed flow (d1cm, label H in Table 5.4) increases the initial velocity with 10% or more. This is in agreement with the analytical solution for fully developed flow presented in chapter 2 and in Appendix A, which in case of fully developed flow predict a maximum velocity which yields twice the bulk velocity. Based on the extent of the potential core region, it is interesting to notice that a minima is reached for $Q \approx 35$l/min in case of fully developed flow, whereas in case a cone is used, a minimum is reached for $Q \approx 60$l/min, suggesting that the flow field using a converging cone is more stable than the flow field for the developed flow.
  - onset of the decay region
    - Using a converging cone to reduce the effect of sharp inlet edges (cone, label G in Table 5.4) seems to follow the general tendency that the influence of the used upstream flow condition either based on mixing or based on flow development does not impacts the decay rate for high Q or high Reynolds numbers. Nevertheless, it will impact the Reynolds numbers associated with the transition from laminar to turbulent and hence the flow field stability.
    - Extending the constriction length in order to approximate fully developed flow (d1cm, label H in Table 5.4).

→ summary with respect to both flow development and mixing

  - immediately downstream from constriction outlet
    - upstream flow condition determines the flow behavior as well as its stability and hence the Reynolds numbers associated with the transition.
  - onset of the decay region
    - the decay rate is less influenced by the upstream flow condition and 'forgets' the upstream flow condition. As such it can be noticed that the decay onset observed for the two reference conditions matches (sharp edges or one, label C in Table 5.4 and single grid (ogp, label D in Table 5.4)).

5.2.2.2 Transverse velocity profiles

In the previous section, we showed the influence of the cross section shape and the upstream flow condition on the near field of the jet emitted from the constricted channel. In the current

section, we briefly present transverse velocity flow profiles[21] following the 'major' and 'minor' axes of the cross section shapes indicated in Fig. 5.3a. Transverse profiles for each of the assessed cross section shapes as a function of volume flow rate are presented in Fig. F.5 ('major' axis) and in Fig. F.6 ('minor' axis) of Appendix F.2.1.

We focus again on the influence of the cross section shape on the measured profiles. Normalized transverse profiles for a single volume flow rate ($Q = 5$l/min and $Q = 20$l/min) as a function of the cross section shape are presented in Fig. 5.22. For both the 'major' and 'minor' axis it is seen that the extent of the initial jet at the constriction exit occupied by the boundary layer (compared to the flat center portion) depends on the cross section shape. Obviously, it depends on the volume flow rate as well since increasing the volume flow rate will increase the Reynolds number expressing a reduced viscous contribution to the flow development.

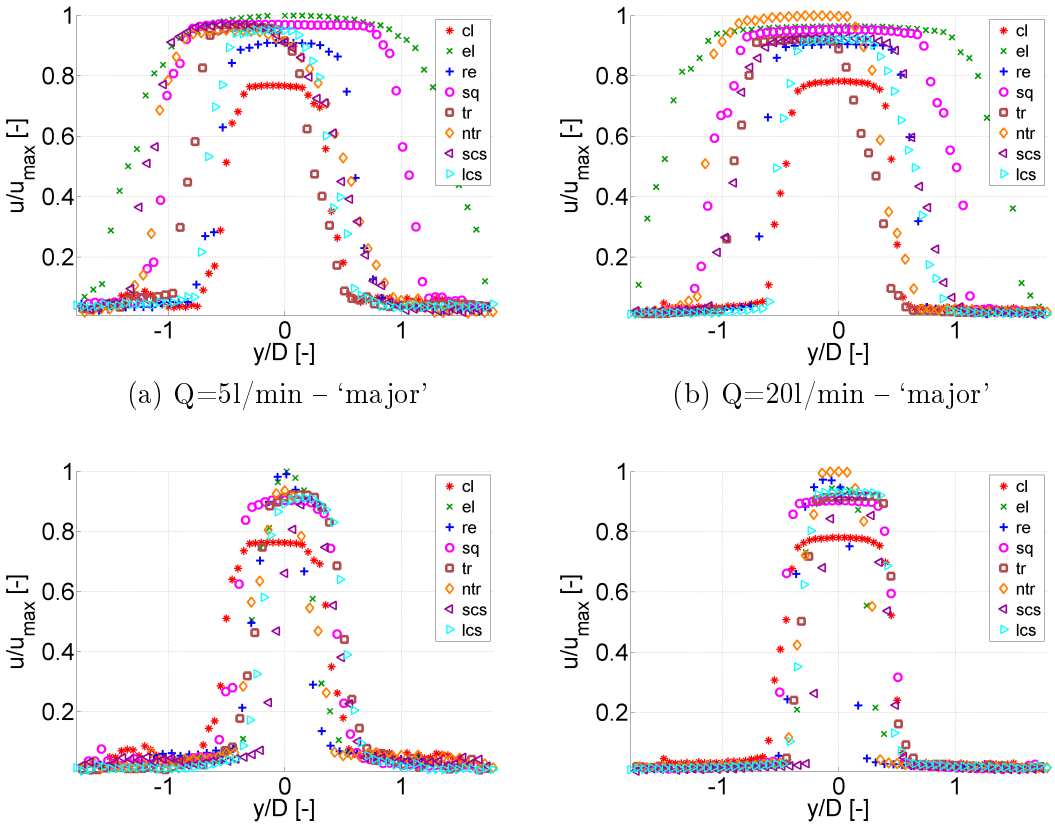

(a) Q=5l/min – 'major' (b) Q=20l/min – 'major'

(c) Q=5l/min – 'minor' (d) Q=20l/min – 'minor'

Figure 5.22: Measured normalized transverse mean velocity profiles u/u_{max} following the 'major' and 'minor' axis defined in Fig. 5.3a as a function of the cross section shape for volume flow rate $Q = 5$l/min and $Q = 20$l/min in the case of sharp edges at the constriction inlet (label C in Table 5.4). u_{max} denotes the maximum mean velocity for all cross section shapes at a given volume flow rate.

[21] As a reminder, spatial step Δy applied for the transverse velocity profile yields $\Delta y = 0.5$mm.

5.2.2.3 Visualization of longitudinal flow development

It was suggested at several occasions that flow structures influences the flow issuing from the constricted channel. In order to provide evidence of the presence of flow structures flow visualization is assessed along the 'major' and 'minor' axis of the cross section shapes as indicated in Fig. 5.3b. Visualization of the flow field for all of the assessed cross section shapes are presented in Fig. 5.23 and Fig. 5.24 for a volume flow rate of $Q = 5\text{l/min}$. More visualization results are shown in Appendix F.3.

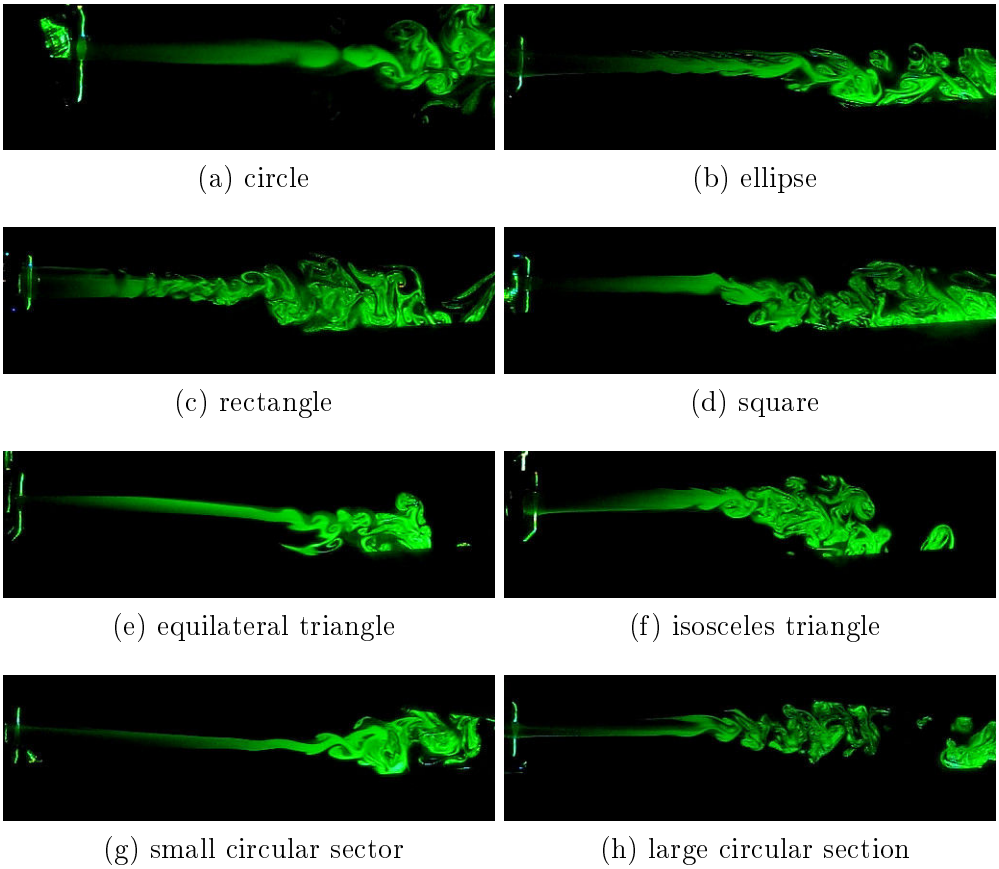

(a) circle (b) ellipse

(c) rectangle (d) square

(e) equilateral triangle (f) isosceles triangle

(g) small circular sector (h) large circular section

Figure 5.23: Flow visualization along the 'major' axis for all cross section shapes for $Q = 5\text{l/min}$. The 'major' axis is indicated in Fig. 5.3b.

Flow structures of a large diversity (including axis switching) are observed when considering all cross section shapes and both visualization sheets.

5.3 Model validation

A comparison of measured and modeled flow quantities is assessed in order to comment on the accuracy and limitations of the simplified quasi-three-dimensional model proposed in chapter 4.

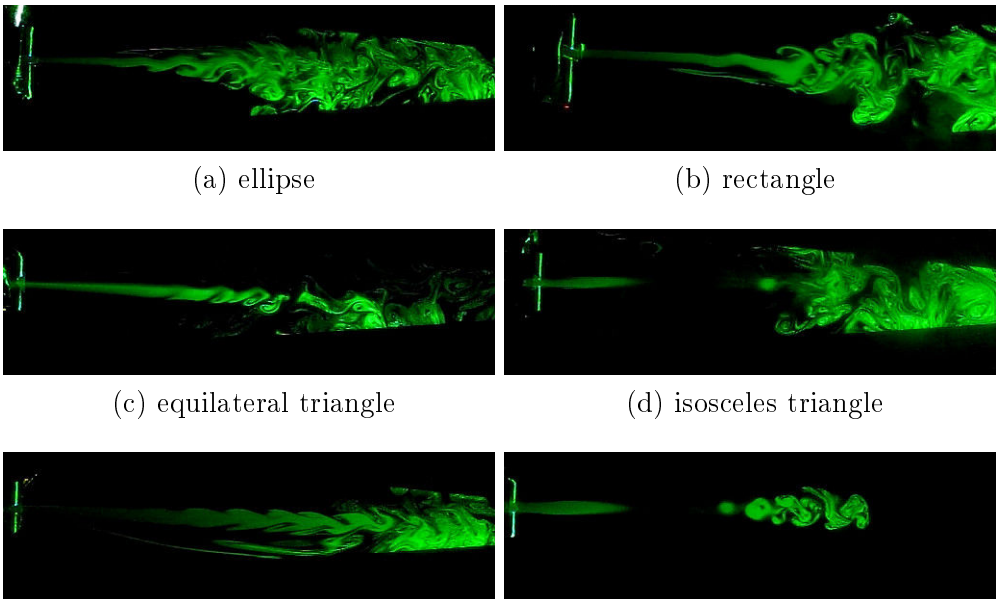

(a) ellipse (b) rectangle

(c) equilateral triangle (d) isosceles triangle

(e) small circular sector (f) large circular section

Figure 5.24: Flow visualization along the 'minor' axis for all cross section shapes for $Q = 5$l/min. The 'minor' axis is indicated in Fig. 5.3b.

Experimental data from the pressure measurements and velocity measurements, described in the previous sections, are used as outlined in the following.

5.3.1 Pressure

The measured pressure values within the constricted channel portion, presented in this chapter, offer a first opportunity to test the pressure distribution predicted with the quasi-three-dimensional flow model proposed in chapter 4. An accurate distribution of he pressure distribution within the constricted channel portion is of particular importance. Indeed, application of the proposed flow model to fluid-structure interaction problems, such as phonation described in section 4.2.1, relies on an accurate prediction of the pressure distribution within the constricted portion in order to provide a good estimation of forces exerted by the flow on the enveloping walls.

In order to evaluate the flow model, we need to decide when the proposed flow model succeeds, and hence results in an accurate prediction, or when on the other hand it fails its prediction. Since the quasi-three-dimensional flow model is presented as an improvement of a quasi-one-dimensional (BP) flow model[22]. It seems fair to decide that a successful prediction is obtained as the quasi-three-dimensional flow model provides a more accurate prediction

[22]Models are denoted the same way as in chapter 4. The quasi-one-dimensional (BP) model is expected to match the quasi-three-dimensional model for the case of an rectangular cross section shape.

compared to the measured data than obtained with the quasi-one-dimensional flow model. In addition, in chapter 4, it was argued that compared to classical boundary layer solutions, the proposed quasi-three-dimensional flow model has the advantage offering a (cruel) way of accounting for the cross section shape. Nevertheless, we are interested in evaluating the outcome of a boundary layer solution against the proposed quasi-three-dimensional flow model. In the following a boundary layer solution is obtained for two-dimensional (2D) flow and axisymmetrical (Axi) flow applying Thwaites (Th) method outlined in Appendix C.2. Consequently, pressure measurements, within the constricted channel portion P_1, for the rectangular and the circular cross section shape are compared to the outcome of the quasi-three-dimensional (mod), quasi-one-dimensional (BP) and boundary layer solution (ThAxi for circular and Th2D for rectangular). For other assessed cross section shapes, the measured pressures within the constriction P_1 are compared to the outcome of the quasi-three-dimensional (mod) and quasi-one-dimensional (BP) model. Concretely, measured pressures obtained for the flow condition labeled B in Table 5.4 (L_u = 35cm) are compared to the modeled values. Measured and modeled normalized pressures P_1/P_0 are plotted in Fig. 5.25 as a function of the pressure upstream from the constriction P_0.

Since the constriction is uniform all modeled values result in a positive prediction of the pressure within the constriction and a continuously decreasing ratio P_1/P_0 for increasing P_0. Consequently, none of the applied flow model is capable to accurately predict the measured negative pressures within the constriction or the extrema observed for the measured pressures within the transition regime $2000 < Re < 4000$. Both phenomena result from more complex flow phenomena then accounted for in the applied flow models and they are likely triggered by the sharp edges at the inlet of the constriction[23].

The following observations are made:

- Modeled pressure ratios P_1/P_0 using the quasi-three-dimensional model are within a close range (5% for $P_0 > 300$Pa and 10% for $P_0 < 300$Pa.) regardless the cross section shape. This range is much less than the variation observed for the measured values of the pressure ratio P_1/P_0.
- For the rectangular cross section shape it is seen that:
  - The quasi-three-dimensional model outcome and the quasi-one-dimensional model outcome are a good match (<2%).

[23] *e.g.* from the measured values shown in Fig. 5.15 it seems likely that a better agreement between modeled and measured values is expected to occur for flow conditioning using the converging cone (label G in Table 5.4) since measured values of P_1 are positive as predicted by models. Nevertheless, in the current section, no such comparison is made since this flow conditioning is only available for the circular cross section shape and not for the other assessed cross section shapes shown in Fig. 5.1. So the flow conditioning used for the comparison between modeled and measured values (label B in Table 5.4) is not in favor of a good quantitative accuracy, but allows to realize the limitations of flow modeling. It further motivates the choice to consider the quality of the quasi-three-dimensional model outcome with respect to the outcome of the other applied simplified model approaches then with respect to whatever quantitative measure of the difference between measured and modeled values.

  - The two-dimensional boundary model (Th2D) provides the most accurate prediction $P_0 < 500$Pa and underestimates the pressure drop for $P_0 > 500$Pa. The quasi-three-dimensional model outcome overestimates the pressure drop and provides the most accurate match for $P_0 > 500$Pa.

- For the circular cross section shape, it is seen that the axisymmetrical boundary layer model (ThAxi) underestimates the pressure drop more than the quasi-three-dimensional model.

- For the elliptical, squared and equilateral triangular cross section shapes, it is seen that using the quasi-three-dimensional model slightly improves the accuracy obtained with the quasi-one-dimensional model. Nevertheless, it is noted that the accuracy gain is small compared to the discrepancy between modeled and measured data.

- The accuracy of the quasi-three-dimensional model compared to the measured data is summarized as $< 5\%$ for $P_0 > 300$ and of $<5\%$ up to $< 20\%$ for $P_0 < 300$ depending on the cross section shape.

Mentioned observations are in general in favor for quasi-three-dimensional flow model, so it is concluded that the proposed quasi-three-dimensional model is evaluated positive, while the poor accuracy when confronted with complex flow phenomena is kept in mind.

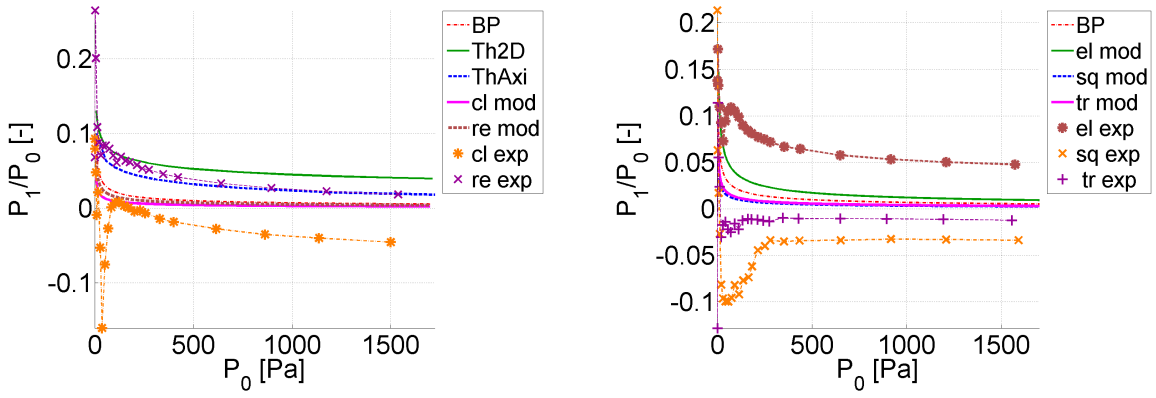

(a) cl and re

(b) sq, tr and el

Figure 5.25: Normalized measured (flow conditioning labeled B in Fig. 5.4 with $L_u = 35$cm) and modeled pressures within the constriction P_1/P_0 as a function of upstream pressure P_0: a) rectangular (re, $D = 6.6$mm) and circular (cl, $D = 10$mm) cross section shape and b) elliptical (el, $D = 6.7$mm), squared (sq, $D = 8.9$mm) and equilateral triangular (tr, $D = 7.8$mm) cross section shape. Modeled values are obtained from the outcome of the quasi-three-dimensional (mod), quasi-one-dimensional (BP) and boundary layer solution (ThAxi for circular and Th2D for rectangular). As a reminder the hydraulic diameter D (Table 5.1) is indicated.

5.3.2 Velocity

Measurements[24] of the mean transverse velocity profile at the exit of the constriction in absence of a downstream pipe, offers (besides the pressure measurements within the constriction) an opportunity to further consider the relevance and limitations of the proposed quasi-three-dimensional model outlined in chapter 4 partly exploiting fully developed flow. Indeed, the measured volume flow rate Q allows to estimate the velocity distribution assuming fully developed viscous flow as outlined in chapter 2. A comparison[25] is made between modeled and measured transverse profiles along the 'major' and 'minor' axis defined in Fig. 5.3a. Examples of measured and modeled profiles for different volume flow rates along the 'major' and 'minor' axis of the constriction with rectangular cross section of presented in Fig. 5.26 and Fig. 5.27, respectively.

In general, for both the 'major' and 'minor' axis, it is observed that the modeled and measured transverse profiles matches well within the boundary layer. However, since the modeled profile is fully developed, it tends to overestimate the velocity for the core flow enveloped by the boundary layers. In addition, it is noticed that simplified flow models can not explain the reduced center velocity such as observed for $Q = 100\text{l/min}$ in Fig. 5.26. Given that the simplified model does not accounts for complex flow dynamics, which based on the presented experimental results suggested to contribute to the flow development – such as vortex generation, vortex interaction or turbulence – at first sight the comparison is surprisingly good.

In order to further quantify the model accuracy with respect to measured transverse profiles shown in Fig. 5.26, Fig. 5.27 and in Appendix F.2.2, the following relative overall error is used:

$$\text{err} = \frac{\sqrt{\frac{1}{n}\sum_{n}\left(u_{exp}(n) - u_{mod}(n)\right)^2}}{\bar{u}} \times 100, \tag{5.5}$$

where u_{mod} and u_{exp} denote the modeled velocity and measured results respectively for n measured velocities and $\bar{u}$ denotes the bulk velocity at the constriction exit.

The resulting overall error (5.5) between modeled and experimental transverse velocity profiles along the 'major' and 'minor' axis is illustrated in Fig. 5.28 for the rectangular constriction shape as a function of the volume flow rate Q. The relative errors for other assessed cross section shapes are presented in Appendix F.2.1. For the rectangular shape, the relative error varies between 25% and 50% of the bulk velocity. The variation of the error with the volume flow rate is more pronounced fore velocity profiles along the 'major' axis than for the 'minor' axis. Note that for the profiles along the 'major' axis a maximum error is retrieved

[24] Measured transverse profiles are presented in Fig. F.5 ('major' axis) and in Fig. F.6 ('minor' axis) of Appendix F.2.2.

[25] In case the spatial discretization used to compute the modeled velocity profile does not matches with the spatial measurement positions, a third order fit is applied to the modeled profile in order to obtain the modeled value for any position independently of the spatial discretization

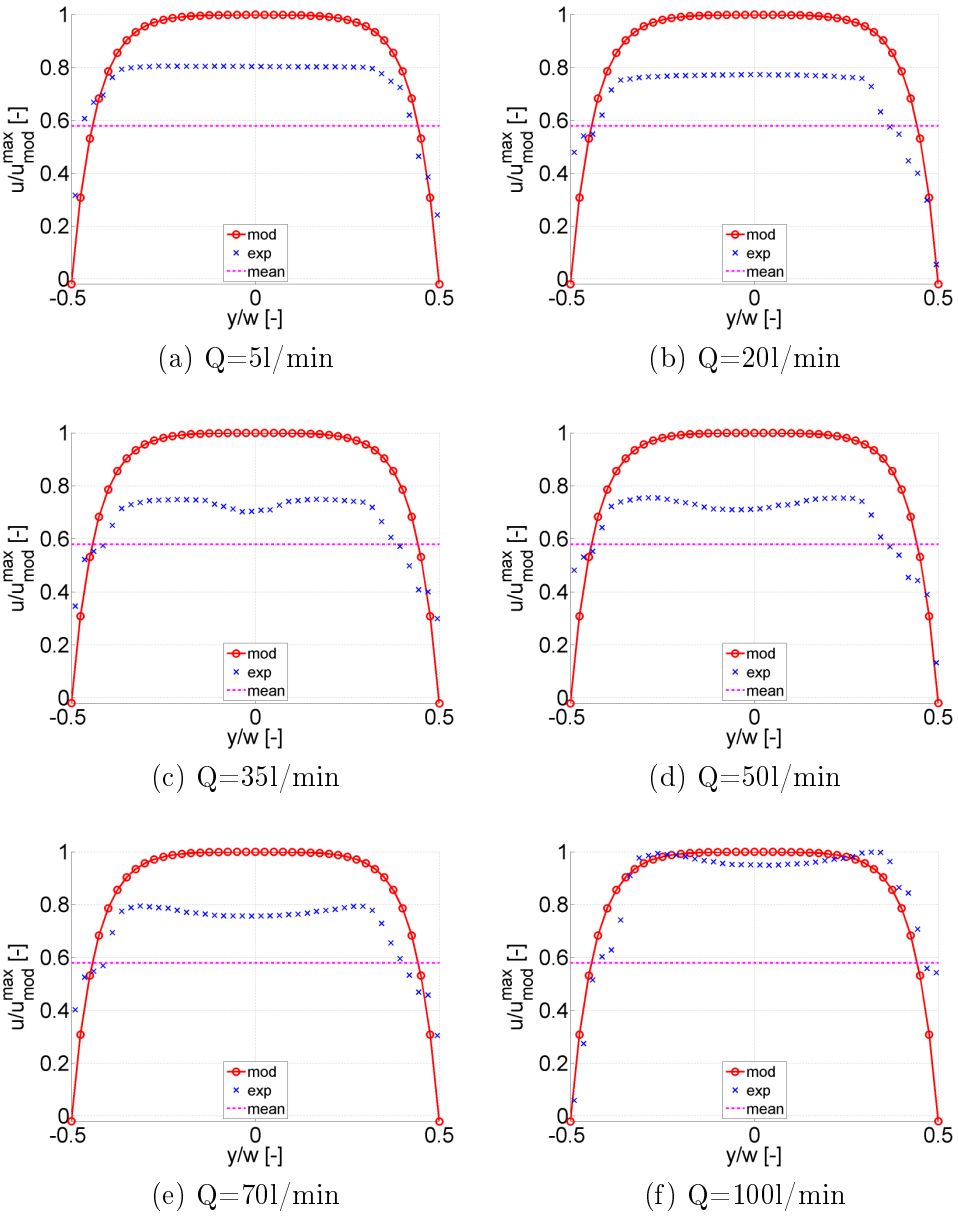

(a) Q=5l/min (b) Q=20l/min

(c) Q=35l/min (d) Q=50l/min

(e) Q=70l/min (f) Q=100l/min

Figure 5.26: Modeled (mod) and measured (exp) transverse velocity profiles along the 'major' axis normalized by the maximum modeled velocity u_{mod}^{max} at the exit of constriction for major axis of a rectangular cross section for different volume flow rates Q. As a reference the bulk velocity $\bar{u}$ is indicated. The transverse coordinate (y or z) is normalized by the total width $y_{tot} = w$ of the constricted portion. Measurements are obtained for sharp edges at the constriction inlet (label C in Table 5.4).

for 50l/min.

In the qualitative description of the flow profiles shown in Fig. 5.26 and Fig. 5.27, it was

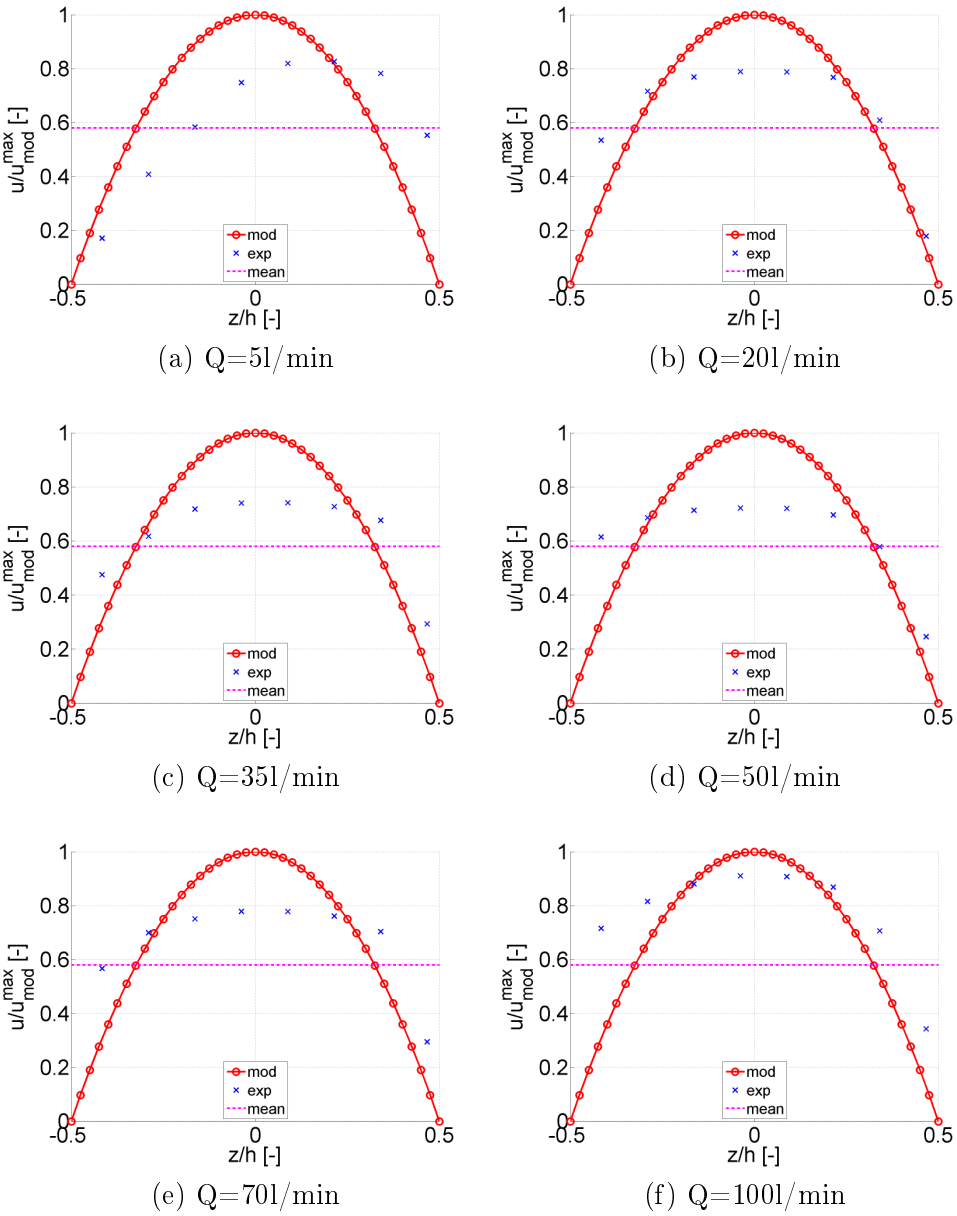

(a) Q=5l/min (b) Q=20l/min

(c) Q=35l/min (d) Q=50l/min

(e) Q=70l/min (f) Q=100l/min

Figure 5.27: Modeled (mod) and measured (exp) transverse velocity profiles along the 'minor' axis normalized by the maximum modeled velocity u_{mod}^{max} at the exit of constriction for major axis of a rectangular cross section for different volume flow rates Q. As a reference the bulk velocity $\bar{u}$ is indicated. The transverse coordinate (y or z) is normalized by the total height h of the constricted portion. Measurements are obtained for sharp edges at the constriction inlet (label C in Table 5.4).

mentioned that the modeled and measured profile matches well in the boundary layer. In the following, we consider the ratio of the modeled and experimental boundary layer $\delta_{exp}/\delta_{mod}$ for transverse profiles along the 'major' and 'minor' axis. The boundary layer thickness of the

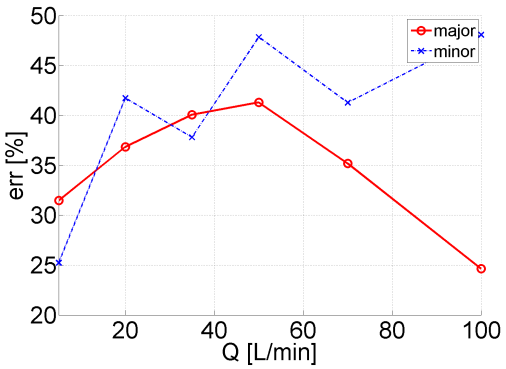

Figure 5.28: Illustration of the overall error (5.5) between modeled and experimental transverse velocity profiles along the 'major' and 'minor' axis of the rectangular cross section for different volume flow rates Q.

measured profiles is determined on the extent of positions for which the velocity is smaller than 90% of the maximum velocity. In order to reduce the error due to spatial sampling to 0.5mm, the spatial position nearest to the threshold is taken into account. The boundary layer thickness of a measured profile is illustrated in Fig. 5.29.

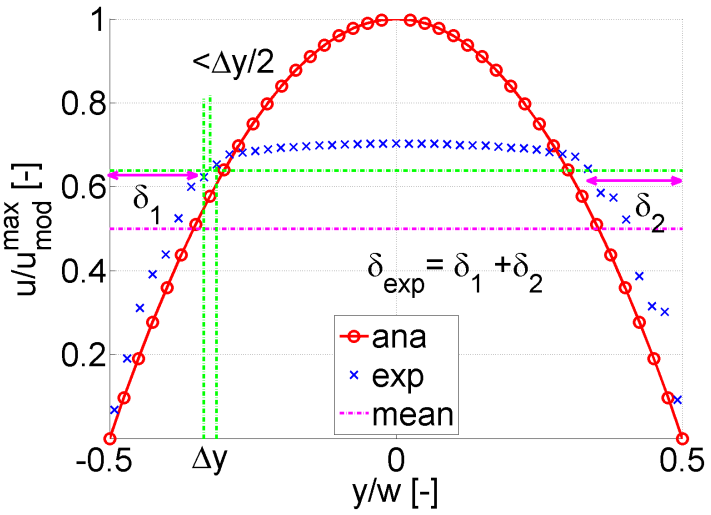

Figure 5.29: Illustration of the procedure to determine the boundary layer thickness δ_{exp} on the measured transverse profile for a spatial step Δy.

Table 5.6 summarizes the resulting ratios of the experimental and modeled boundary layer thicknesses $\delta_{exp}/\delta_{mod}$ along the 'major' and 'minor' axis, respectively. Note that for a square cross section shape the 'minor' follows the diagonal direction. The uncertainty due to the discretization error (spatial step) is indicated. It is observed that the ratio $\delta_{exp}/\delta_{mod}$ varies from 30% to 99% depending on the cross section shape and the volume flow rate. The observed tendency as a function of increasing volume flow rate is indicated.

For the 'major' axis the general tendency for increasing volume flow rate is consecutive decrease and increase of the ratio $\delta_{exp}/\delta_{mod}$ and hence of the accuracy of the boundary layer extent since $\delta_{exp}/\delta_{mod} \ll 100$ is associated with an overestimation of the boundary layer thickness by the model. The volume flow rates for which the tendency changes are associated with Reynolds numbers in the range $2500 < Re < 5000$ associated with the transition regime from laminar to turbulent flow. Nevertheless, the tendency is not confirmed for the profiles along the 'minor' axis. Alternatively, the ratio of the boundary layer thicknesses $\delta_{exp}/\delta_{mod}$ resulting from the threshold criterion illustrated in Fig. 5.29 for a threshold value of 100% or $\delta_{exp}/\delta_{mod} = u_{exp}^{max}/u_{mod}^{max}$ is assessed and results are shown in Table F.1 of Appendix F.2.2. It is shown that both the tendency as volume flow rates associated with a change in tendency depend on the used threshold, so that no definite conclusion can be formulated at present.

Nevertheless, the magnitude of the boundary layer thickness ratio $30\% < \delta_{exp}/\delta_{mod} < 99\%$ confirms the fairly good capturing of boundary layer properties given the simplicity of the model, the complexity of the flow and the relatively short length of the constriction. The last point is illustrated by considering the ratio of the length of the constriction L_c to the entry length L_f required for the flow through a uniform channel to develop fully for different cross section shape. The ratio L_c/L_f is illustrate in Fig. 5.30 for laminar and turbulent flow as function of Reynolds number for a circular (maximum hydraulic diameter of cross section shapes considered in this chapter) and rectangular cross section (minimum hydraulic diameter of cross section shapes considered in this chapter). The entry length L_f for laminar and turbulent flow as function of Reynolds number and hydraulic diameter D is obtained as [125] as:

$$L_f \approx (0.05Re + 0.5)D, \quad \text{laminar}, \tag{5.6}$$

and

$$L_f \approx 4.4Re^{\frac{1}{6}}D, \quad \text{turbulent}. \tag{5.7}$$

Indeed, it is seen that the length of the constriction yields only 1% to 15% for laminar flow and only 10% to 30% for turbulent flow. Therefore, and in case of linear development of the boundary layer one expect $\delta_{exp}/\delta_{mod} \ll 30\%$. Therefore, we have to conclude, that the constriction enhances boundary layer development.

5.4 Summary

The influence of the cross section shape for constricted channel flow is experimentally assessed for a large number of flow and geometrical configurations since besides the cross section shapes, the upstream flow condition is varied as well as the presence or absence of a downstream pipe. The influence of the cross section shape on the flow is analyzed by means of point pressure measurements within the constriction and velocity measurements of the near field of the jet emitted from the constriction in absence of a downstream channel. Moreover

Table 5.6: Ratio $\delta_{exp}/\delta_{mod}$ resulting from the threshold criterion illustrated in Fig. 5.29 for a threshold value of 90% for transverse profiles along the 'major' and 'minor' axis of all assessed cross sections. The uncertainty due to the spatial discretezation (spatial step) is indicated. Bold volume flow rates indicate an overall change of tendency.

	D [mm]	Q [l/min]								discretization error [%]	tendency
		5	10	15	**20**	**35**	50	70	100		
		major axis									
cl	10	43	-	-	36	50	57	57	64	5	↘↗
sq	8.9	50	41	32	32	-	-	-	-	6	↘
lcs	8.4	68	63	57	63	73	-	-	-	4	↘↗
tr	7.8	65	59	59	59	76	-	-	-	4	↘↗
scs	7.2	67	60	56	56	74	-	-	-	3	↘↗
ntr	7.0	70	56	56	63	67	-	-	-	3	↘↗
el	6.7	53	47	50	47	53	50	47	53	2	-
re	6.6	64	-	-	98	89	89	89	89	3	↘↗↘
		minor axis									
sq	8.9	69	64	74	74	-	-	-	-	4	↘↗
lcs	8.4	41	41	28	28	28	-	-	-	4	↘
tr	7.8	58	37	37	47	37	-	-	-	4	↘↗↘
scs	7.2	99	85	68	68	51	-	-	-	6	↘
ntr	7.0	81	81	65	65	50	-	-	-	6	↘
el	6.7	95	63	63	63	63	63	48	48	11	↘
re	6.6	89	-	-	71	53	53	53	71	13	↘↗

flow visualization is assessed in order to provide some evidence for the existence of flow structures. The measured quantities are used to determine the accuracy of the proposed simplified quasi-three-dimensional model approach. It is seen that although the quantitative error is considerable, the performance of the model is surprisingly good given the complexity of the flow dynamics and the simplicity of the model. In the following chapter, numerical data of the flow field are presented in presence of a downstream pipe. In contrast with the current

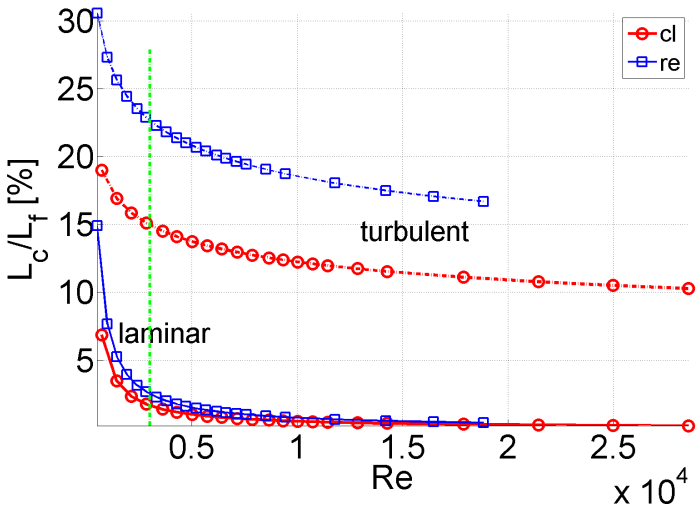

Figure 5.30: Illustration of the ratio of the length of the constriction L_c to the entry length L_f for laminar and turbulent flow as function of Reynolds number for a circular (maximum hydraulic diameter of cross section shapes considered in this chapter) and rectangular cross section (minimum hydraulic diameter of cross section shapes considered in this chapter).

chapter, no attention is given to the upstream flow condition.

Chapter 6

Immersed Boundary method

Contents

Chapter 2 showed the influence of the cross section shape on the velocity distribution for developed viscous flow. In chapter 4, a simple 'quasi-three-dimensional' flow model is proposed for laminar incompressible steady channel flow, which accounts for flow inertia, viscosity and the cross section shape. Flow data are needed in order to test the relevance of this quasi-three-dimensional model and to characterize the influence of the cross section shape on the flow. In chapter 5, experimental data were presented. In the current chapter, we focus on numerical data in order to quantify and analyze modeled, measured and simulated flow quantities.

On one hand, biological flow applications, such as discussed in chapter 4, are the result of a complex fluid-structure(-acoustic) interaction, and on the other hand, the simple 'quasi-three-dimensional' flow model assumes laminar flow. For these two reasons, we prefer a numerical method which is suitable to simulate complex fluid-structure interactions and at same time models laminar incompressible three-dimensional flow. As a result, the immersed boundary (IB) method is used to simulate the flow field [100, 47, 44, 46]. In the current work, the immersed boundary method is applied to a fixed structure matching some of the channel geometries used during the experimental and model study.

Since the IB method is a powerful tool to simulate a fluid-structure interaction, it is commonly used in biological flow dynamics [85, 85, 129, 54, 83, 75, 77, 80]. Nevertheless, most of the applied research reported in the cited references focus on blood flow through the cardiovascular system for which typical Reynolds numbers are smaller than the ones encountered when studying phenomena related to the respiratory system, such as speech production. Therefore, the laminar flow model can be questioned and the aimed validation on experimental data provides a good opportunity to reflect on the accuracy of the flow model.

In the following, the IB method is formulated. Next, numerical results are presented and simulated flow quantities are compared to modeled quantities obtained using the 'quasi-three-dimensional' model and measured flow quantities presented in chapter 5.

6.1 Mathematical formulation

6.1.1 Continuous formulation

The immersed boundary (IB) method for fluid-structure interaction considers an elastic structure immersed in a viscous incompressible fluid. The immersed boundary formulation of such problems uses a Lagrangian description of the immersed structure along with an Eulerian description of the viscous incompressible fluid, which is modeled by the incompressible Navier-Stokes equations. The Lagrangian and Eulerian frames are coupled by interaction equations using Dirac delta function kernels. In the following, the fluid is assumed to have a uniform mass density ρ and dynamic viscosity μ.

First, let $\mathbf{x} = (x, y, z) \in \Omega$ denote Cartesian physical coordinates, with $\Omega \subset \mathbb{R}^3$ denotes the physical region that is occupied by the coupled fluid-structure system. The Lagrangian material coordinates attached to the structure is denoted $\mathbf{s} = (s_1, s_2) \in U \subset \mathbb{R}^2$, with U denoting the Lagrangian coordinate domain. $\chi(\mathbf{s}, t) \in \Omega$ denotes the physical position $\mathbf{s}$ of material points at time t. Throughout the present work, Ω is taken to be a rectangular box with $\Omega = [0,\ L_x] \times [0,\ L_y] \times [0,\ L_z]$. The physical region occupied by the structure at time t is $\chi(U, t) \subseteq \Omega$, and the physical region occupied by the fluid at time t is $\Omega \backslash \chi(U, t)$.

To use an Eulerian description of the fluid and a Lagrangian description of the elasticity of the immersed structure, it is necessary to describe the stress of the fluid-structure system in both Eulerian and Lagrangian forms. If $\sigma = \sigma(\mathbf{x}, t)$ is the Cauchy stress tensor of the coupled fluid-structure system, then

$$\sigma(\mathbf{x}, t) = \begin{cases} \sigma^f(\mathbf{x}, t) + \sigma^e(\mathbf{x}, t) & \text{for } \mathbf{x} \in \chi(U, t) \\ \sigma^f(\mathbf{x}, t) & \text{otherwise,} \end{cases} \tag{6.1}$$

where $\sigma^f(\mathbf{x}, t)$ is the stress tensor of a viscous incompressible fluid, and $\sigma^e(\mathbf{x}, t)$ is the stress tensor that describes the elasticity of the immersed structure. The fluid stress tensor is defined as

$$\sigma^f(\mathbf{x}, t) = -P\mathbb{I} + \mu \left[\nabla \mathbf{u} + (\nabla \mathbf{u})^T\right] \tag{6.2}$$

in which $P = P(\mathbf{x}, t)$ is the pressure and $\mathbf{u} = \mathbf{u}(\mathbf{x}, t)$ is the Eulerian fluid velocity field. In order to describe the elasticity of the structure with respect to the Lagrangian material

coordinate system, it is convenient to use the first Piola-Kirchhoff elastic stress tensor $\mathcal{P}^e(\mathbf{s},t)$, which is defined as

$$\int_{\partial V} \mathcal{P}^e(\mathbf{s},t)\mathbf{N}dA(\mathbf{s}) = \int_{\partial\chi(V,t)} \sigma^f(\mathbf{x},t)\mathbf{n}da(\mathbf{x}) \tag{6.3}$$

for any smooth region $V \subset U$, in which $\mathbf{N} = \mathbf{N}(\mathbf{s})$ is the outward unit normal along ∂V and $\mathbf{n} = \mathbf{n}(\mathbf{x},t)$ is the outward normal along $\partial\chi(V,t)$. The hyperelastic constitutive models can be characterized by a strain-energy functional $W^e = W^e(\mathbb{F})$, in which $\mathbb{F} = \mathbb{F}(\mathbf{s},t) = \nabla_{\mathbf{s}}\chi(\mathbf{s},t) = \frac{\partial\chi(\mathbf{s},t)}{\partial\mathbf{s}}$ is the deformation gradient associated with the mapping $\chi : (U,t) \to \Omega$. For such constitutive laws, $\mathcal{P}^e(\mathbf{s},t) = \frac{\partial W^e}{\partial\mathbb{F}}(\mathbf{s},t)$.

The weak form of the equations of motion for the coupled fluid-structure system are

$$\rho\left(\frac{\partial\mathbf{u}}{\partial t}(\mathbf{x},t) + \mathbf{u}(\mathbf{x},t)\cdot\nabla\mathbf{u}(\mathbf{x},t)\right) = -\nabla P(\mathbf{x},t) + \mu\nabla^2\mathbf{u}(\mathbf{x},t) + \mathbf{f}(\mathbf{x},t), \tag{6.4}$$

$$\nabla\cdot\mathbf{u}(\mathbf{x},t) = 0, \tag{6.5}$$

$$\mathbf{f}(\mathbf{x},t) = \int_U \mathbf{F}(\mathbf{s},t)\delta(\mathbf{x}-\chi(\mathbf{s},t))d\mathbf{s}, \tag{6.6}$$

$$\begin{aligned}\int_U \mathbf{F}(\mathbf{s},t)\cdot\mathbf{V}(\mathbf{s})d\mathbf{s} &= \int_U \mathcal{P}^e(\mathbf{s},t)\cdot\nabla_{\mathbf{s}}\mathbf{V}(\mathbf{s})d\mathbf{s}\\ &- \int_{\partial U} \mathcal{P}^e(\mathbf{s},t)\mathbf{N}(\mathbf{s})\cdot\nabla_{\mathbf{s}}\mathbf{V}(\mathbf{s})dA(\mathbf{s}),\ \forall\mathbf{V}(\mathbf{s}),\end{aligned} \tag{6.7}$$

$$\frac{\partial\chi(\mathbf{s},t)}{\partial t} = \int_\Omega u(\mathbf{x},t)\delta(\mathbf{x}-\chi(\mathbf{s},t))d\mathbf{x}, \tag{6.8}$$

In the equations of motion, (6.4) and (6.5) are the incompressible Navier–Stokes equations, which are written in terms of the Eulerian velocity field $\mathbf{u}(\mathbf{x},t) = (u(x,t), v(x,t), w(x,t))$ and the Eulerian pressure field $P(\mathbf{x},t)$, along with a Eulerian elastic force density $\mathbf{f}(\mathbf{x},t)$ applied by the structure to the fluid, which is determined by a time-independent functional of the Lagrangian configuration of the immersed structure.

(6.6) and (6.7) are Lagrangian–Eulerian interaction equations that use integral transformations with three-dimensional Dirac delta function kernels $\delta(\mathbf{x}) = \delta(x)\delta(y)\delta(z)$, to couple the Lagrangian and Eulerian descriptions. Specifically, (6.6) converts the Lagrangian elastic force density $\mathbf{F}$ into the equivalent Eulerian elastic force density $\mathbf{f}$. Notice that $\mathbf{F}$ and $\mathbf{f}$ have totally different characters: $\mathbf{F}(\mathbf{s},t)$ is the Lagrangian elastic force density (i.e., the force density with respect to the curvilinear coordinate system so that $\mathbf{F}(\mathbf{s},t)d\mathbf{s}$ has units of force), whereas $\mathbf{f}(\mathbf{x},t)$ is the Eulerian elastic force density (i.e., the force density with respect to the physical coordinate system so that $\mathbf{f}(\mathbf{x},t)d\mathbf{x}$ has units of force). Nonetheless, $\mathbf{F}$ and $\mathbf{f}$ are equivalent as densities [99]. Notice that a unified body force density $\mathbf{F}(\mathbf{s},t)$ is used to take into account the effects of both the internal and transmission elastic force densities and $\mathbf{V}(\mathbf{s})$ is an arbitrary Lagrangian test function that is not assumed to vanish on ∂U.

The velocity of the structure is determined for the Eulerian fluid velocity field $\mathbf{u}(\mathbf{x},t)$ via the integral transform equation (6.8), which is equivalent to

$$\frac{\partial \chi}{\partial t}(\mathbf{s},t) = \mathbf{u}(\chi(\mathbf{s},t),t) \tag{6.9}$$

with the no slip condition on the structure walls and no penetration of a viscous incompressible fluid.

6.1.2 Spatial discretization

We employ a finite element (FE) discretization of the Lagrangian equations and a uniform, staggered-grid finite difference discretization of the Eulerian equations. For further details on these spatial discretization, see Griffith [43, 44, 45]. The time stepping scheme used is similar to that of Griffith [45]. However, in the present work we employ a second-order Adams–Bashforth scheme for the convective terms when solving the incompressible Navier–Stokes equations.

Briefly, let $u_{i+\frac{1}{2},j,k}$, $v_{i,j+\frac{1}{2},k}$ and $w_{i,j,k+\frac{1}{2}}$ denote staggered-grid approximations to the components of the Eulerian velocity field that are defined at positions $\mathbf{x}_{i+\frac{1}{2},j,k}$, $\mathbf{x}_{i,j+\frac{1}{2},k}$ and $\mathbf{x}_{i,j,k+\frac{1}{2}}$, respectively. Let $P_{i,j,k}$ denote the cell-centered approximation pressure at position $\mathbf{x}_{i,j,k}$. The position and Lagrangian elastic force density at node (l,m) of the Lagrangian curvilinear mesh are denoted as $\mathbf{x}_{l,m}$ and $\mathbf{F}_{l,m}$. Let ∇_h, $\nabla_h \cdot$ and ∇_h^2 denote standard second-order accurate finite-difference approximations to the gradient, divergence, and Laplace operators, respectively, in which h is the Cartesian grid spacing.

Let $\tau_h = \bigcup_e U^e$ be a triangulation of U composed of elements U^e . We denote the time-dependent physical positions of the nodes of the Lagrangian mesh by $\chi_l(t)_{l=1}^M$. Using the Lagrangian basis functions, we define an approximation to $\chi(\mathbf{s},t)$ by

$$\chi_h(\mathbf{s},t) = \sum_{l=1}^{M} \chi_l(t)\phi_l(\mathbf{s}), \tag{6.10}$$

where $\phi_l(s)$ denotes the Lagrangian basis functions. An approximation to the deformation gradient is given by

$$\mathbb{F}_h(\mathbf{s},t) = \frac{\partial \chi_h(\mathbf{s},t)}{\partial \mathbf{s}} = \sum_{l=1}^{M} \chi_l(t) \frac{\partial \phi_l(\mathbf{s})}{\partial \mathbf{s}}. \tag{6.11}$$

Using $\mathbb{F}_h(\mathbf{s},t)$, we compute directly $\mathcal{P}_h^e(\mathbf{s},t)$ and $\tau_h(\mathbf{s},t)$ to approximate the first Piola-Kirchhoff stress tensor and the Lagrangian transmission force density, respectively. We approximate the Lagrangian force densities $\mathbf{F}(\mathbf{s},t)$ by

$$\mathbb{F}_h(\mathbf{s},t) = \sum_{l=1}^{M} \mathbf{F}_l(t)\phi_l(\mathbf{s}). \tag{6.12}$$

where the nodal values $\mathbf{F}_l(t)_{l=1}^M$ must be determined from $\mathcal{P}_h(\mathbf{s},t)$.

To compute an approximation to $\mathbf{f} = (f_x, f_y, f_z)$ on the Cartesian grid, we construct for each element $U^e \in \tau_h$ a Gaussian quadrature rule with N^e quadrature points $\mathbf{s}_Q^e \in U^e$ and weights $w_Q^e, Q = 1, ..., N^e$. We then compute f_x, f_y and f_z on the edges of the Cartesian grid cells via

$$({f_x}^{n+\frac{1}{2}})_{i+\frac{1}{2},j,k} = \sum_{U^e \in \tau_h} \sum_{Q=1}^{N^e} F_x(\mathbf{s}_Q^e, t)\delta_h\left(x_{i+\frac{1}{2},j,k} - \chi(\mathbf{s}_Q^e, t)\right) w_Q^e, \tag{6.13}$$

$$({f_y}^{n+\frac{1}{2}})_{i,j+\frac{1}{2},k} = \sum_{U^e \in \tau_h} \sum_{Q=1}^{N^e} F_y(\mathbf{s}_Q^e, t)\delta_h\left(x, j_{i+\frac{1}{2},k} - \chi(\mathbf{s}_Q^e, t)\right) w_Q^e, \tag{6.14}$$

$$({f_z}^{n+\frac{1}{2}})_{i,j,k+\frac{1}{2}} = \sum_{U^e \in \tau_h} \sum_{Q=1}^{N^e} F_z(\mathbf{s}_Q^e, t)\delta_h\left(x, j, k_{i+\frac{1}{2}} - \chi(\mathbf{s}_Q^e, t)\right) w_Q^e, \tag{6.15}$$

where the Lagrangian force density $\mathbf{F}(\mathbf{s},t) = (F_x(\mathbf{s},t), F_y(\mathbf{s},t), F_z(\mathbf{s},t))$. We use the shorthand

$$\mathbf{f} = \mathcal{S}\mathbf{F} \tag{6.16}$$

where $\mathcal{S} = \mathcal{S}(\chi)$ is the force prolongation operator implicitly defined by (6.13), (6.14) and (6.15).

A corresponding velocity restriction operator $\mathcal{R} = \mathcal{R}(\chi)$ is used to determine the motion of the nodes of the Lagrangian mesh from the Cartesian grid velocity field via

$$\frac{d\chi}{dt} = \mathcal{R}\mathbf{u} \tag{6.17}$$

where the approximated Lagrangian vector field $\mathbf{U}(\mathbf{s},\mathbf{t}) = (U(\mathbf{s},t), V(\mathbf{s},t), W(\mathbf{s},t)) = \mathcal{R}\mathbf{u}$ is given by

$$U(\mathbf{s},t) = \sum_{i,j,k} u_{i+\frac{1}{2},j,k}\delta_h\left(x_{i+\frac{1}{2},j,k} - \chi(\mathbf{s},t)\right)h^3, \tag{6.18}$$

$$V(\mathbf{s},t) = \sum_{i,j,k} v_{i,j+\frac{1}{2},k}\delta_h\left(x_{i,j+\frac{1}{2},k} - \chi(\mathbf{s},t)\right)h^3, \tag{6.19}$$

$$W(\mathbf{s},t) = \sum_{i,j,k} w_{i,j,k+\frac{1}{2}}\delta_h\left(x_{i,j,k+\frac{1}{2}} - \chi(\mathbf{s},t)\right)h^3, \tag{6.20}$$

where $\delta_h(\mathbf{x}) = \delta_h(x)\delta_h(y)\delta_h(z)$ is the four-point delta function of Peskin [99].

Notice that the constructed $\mathbf{S}$ and $\mathbf{R}$ are adjoint operators which ensures the semi-discrete scheme conserves energy during Lagrangian–Eulerian interaction.

6.1.3 Temporal discretization

Let $\mathbf{x}_n$, $\mathbf{u}^n$ and $p^{n-\frac{1}{2}}$ denote the approximations to the values of $\mathbf{x}$ and $\mathbf{u}$ at time t^n, and to the value of p at time $t^{n-\frac{1}{2}}$, respectively. First, we determine a preliminary approximation to the deformed structure configuration at time t^{n+1} via

$$\frac{\widetilde{\chi}^{n+1} - \chi^n}{\Delta t} = \mathbf{R}^n\mathbf{u}^n, \tag{6.21}$$

where $\mathbf{R} = \mathbf{R}(\chi^n)$, and an approximation to χ at time $t^{n+\frac{1}{2}}$ is defined as

$$\chi^{n+\frac{1}{2}} = \frac{\widetilde{\chi}^{n+1} + \chi^n}{2}. \tag{6.22}$$

we next solve

$$\rho\left(\frac{\mathbf{u}^{n+1} - \mathbf{u}^n}{\Delta t} + \mathbf{A}^{n+\frac{1}{2}}\right) = -\nabla_h P^{n+\frac{1}{2}} + \mu\nabla_h^2\frac{\mathbf{u}^{n+1} + \mathbf{u}^n}{2} + \mathbf{f}^{n+\frac{1}{2}}, \tag{6.23}$$

$$\nabla_h \cdot \mathbf{u}^{n+1} = 0, \tag{6.24}$$

$$\mathbf{f}^{n+\frac{1}{2}} = \mathbf{S}(\chi^{n+\frac{1}{2}})\mathbf{F}(\chi^{n+\frac{1}{2}}), \tag{6.25}$$

$$\frac{\chi^{n+1} - \chi^n}{\Delta t} = \mathcal{R}(\chi^{n+\frac{1}{2}})\frac{\mathbf{u}^{n+1} + \mathbf{u}^n}{2}, \tag{6.26}$$

for χ^{n+1}, $\mathbf{u}^{n+1}$, and $P^{n+\frac{1}{2}}$, where $\mathbf{A}^{n+\frac{1}{2}} = \frac{3}{2}\mathbf{u}^n \cdot \nabla_h\mathbf{u}^n - \frac{1}{2}\mathbf{u}^{n-1} \cdot \nabla_h\mathbf{u}^{n-1}$ is computed via a piecewise parabolic method (PPM) approximation to the nonlinear advection term [26, 45].

Since time step-lagged values of $\mathbf{u}$ and P are used by the time step, we can not use that scheme for the initial time step. In order to have an initial value for the pressure, $P = 0$ is assumed to be an initial guess for $P^{n+\frac{1}{2}}$. So during the initial time, we first solve

$$\rho\left(\frac{\widetilde{\mathbf{u}}^{n+1}-\mathbf{u}^n}{\Delta t}+\mathbf{A}^n\right)=-\nabla_h\widetilde{P}^{n+\frac{1}{2}}+\mu\nabla_h^2\frac{\widetilde{\mathbf{u}}^{n+1}+\mathbf{u}^n}{2}+\mathbf{f}^n, \tag{6.27}$$

$$\nabla_h\cdot\widetilde{\mathbf{u}}^{n+1}=0, \tag{6.28}$$

$$\mathbf{f}^n=\mathbf{S}(\chi^n)\mathbf{F}(\chi^n), \tag{6.29}$$

$$\frac{\widetilde{\chi}^{n+1}-\chi^n}{\Delta t}=\mathcal{R}(\chi^n)\mathbf{u}^n, \tag{6.30}$$

for $\widetilde{\chi}^{n+1}$, $\widetilde{\mathbf{u}}^{n+1}$, $\widetilde{P}^{n+\frac{1}{2}}$, where $\mathbf{A}^n=\mathbf{u}^n\cdot\nabla_h\mathbf{u}^n$. Then we set

$$\chi^{n+1}=\frac{\widetilde{\chi}^{n+1}+\chi^n}{2}, \tag{6.31}$$

and finally solve (6.23)-(6.26) for χ^{n+1}, $\mathbf{u}^{n+1}$, $P^{n+\frac{1}{2}}$, except that we use $\mathbf{A}^{n+\frac{1}{2}}=\mathbf{u}^{n+\frac{1}{2}}\cdot\nabla_h\mathbf{u}^{n+\frac{1}{2}}$ with $\mathbf{u}^{n+\frac{1}{2}}=\frac{1}{2}\left(\widetilde{\mathbf{u}}^{n+1}+\mathbf{u}^n\right)$.

Note that, because in this chapter we consider a constricted channel with rigid wall, the Piola-Kirchhoff elastic stress tensor $\mathcal{P}$ is thus not used. Instead, a feedback force, of the form

$$\mathbf{F}(\mathbf{s},t)=\kappa(\mathbf{s},\chi(\mathbf{s},t)), \tag{6.32}$$

is used in order to force the wall not to move. $\kappa>0$ is a penalty parameter. Note that as $\kappa\to\infty$, $\chi(\mathbf{x},t)\to\mathbf{s}$.

6.2 Numerical results

In the simulations[1], the immersed boundary method is applied to describe steady pressure-driven flow through a constricted channel. A geometrical model of the channel structure is generated using the SolidWorks CAD software, and the resulting CAD structure is converted into a mesh with tetrahedron cells. The constricted channel has a total length $L_z=22.5$cm with radius $r_x=1.25$cm at the inlet and outlet. The constricted portion is of length $L_c=2.5$cm

[1]The simulations described herein employ the freely available IBAMR code (`http://ibamr.googlecode.com`), an adaptive and distributed-memory parallel implementation of the IB method that provides software infrastructure for developing fluid–structure interaction models that use the IB method. IBAMR leverages functionality provided by other freely available software libraries, including SAMRAI (`http://computation.llnl.gov/casc/SAMRAI`) [52, 53], PETSc (`http://www.mcs.anl.gov/petsc`) [7, 6] and hypre (`http://www.llnl.gov/CASC/hypre`) [35].

with cross section area 0.79cm^2. The unconstricted upstream portion has length $L_u = 5$cm and the unconstricted downstream portion has length $L_d = 15$cm. The channel walls are rigid and have a thickness of 0.1cm. The structure is immersed in a rectangular 5.4cm×5.4cm×22.5cm fluid box shown in Fig. 6.1[2].

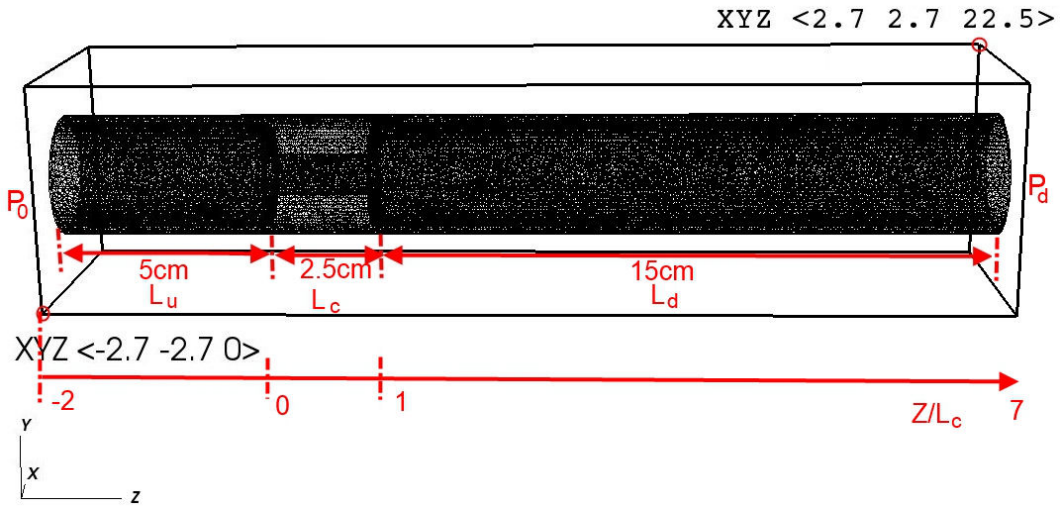

Figure 6.1: Illustration of the structure immersed in a 5.4cm×5.4cm×22.5cm rectangular fluid box for which two corner points coordinates are given [cm]. The streamwise direction corresponds to the Z direction. The lengths of the unconstricted upstream portion L_u, constriction portion L_c and unconstricted downstream portion L_d are indicated. The upstream pressure P_0 and downstream pressure P_d are indicated as well. Note, that the streamwise direction is normalized as Z/L_c.

In the current simulations, we initialize the discretization of the fluid box with an $N \times N \times N$ Cartesian grid for $N = 128$. The penalty parameter κ is set to $\kappa = 10^6$, which is large enough to fix the structure for the physical and numerical parameters considered. A pressure gradient is prescribed between the inlet ($Z/L_c = -2$) and outlet ($Z/L_c = 7$) of the interior part of the flow channel, *i.e.* $P_0 - P_d$, whereas zero pressure boundary conditions are employed along the remainder of the fluid domain boundary. The fluid is air with density $\rho = 1.2$kg/m^3 and dynamic viscosity $\mu = 1.8 \times 10^{-5}$Pa·s as indicated in Table 4.1. Several upstream pressures are considered ($P_0 = 10$Pa, 35Pa or 100Pa), whereas the downstream pressure is fixed to $P_d = 0$Pa. Imposed upstream pressures P_0 and corresponding approximated volume flow rates Q and Reynolds numbers[3] Re are listed in Table 6.1. Concretely, as summarized in Table 6.2, simulations for different cross section shapes are performed for $P_0 = 35$Pa, whereas the upstream pressure is varied for a channel with circular cross section shape. The total simulation time for each geometrical configuration and upstream pressure P_0 is indicated in Table 6.2 as well. A front view of structures with different cross section shapes (circular, elliptical, rectangular, circular sector and asymmetric) rounded inlet and outlet with radius

[2]To avoid numerical errors all sharp corners are rounded with a radius of 0.5mm, such as *e.g.* at the inlet and outlet of the constriction.

[3]As before, the Reynolds number is based on the hydraulic diameter of the constricted area.

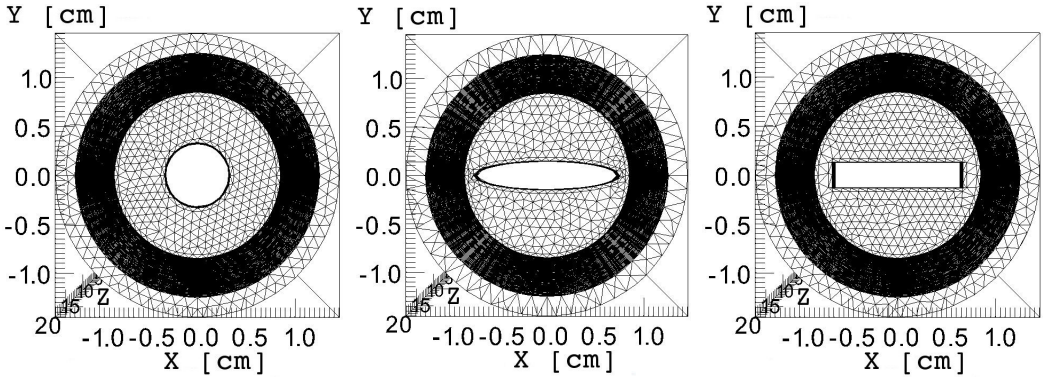

(a) circle (b) ellipse (c) rectangle

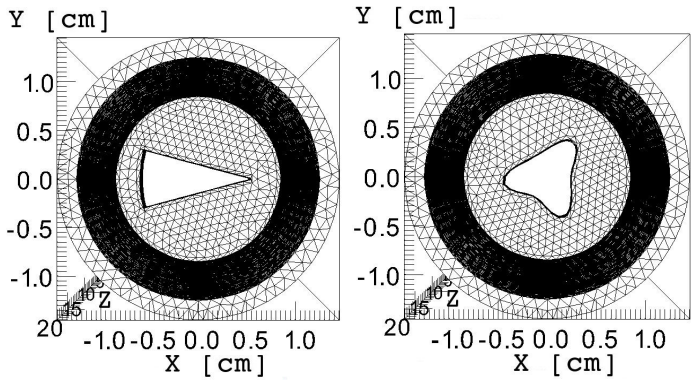

(d) circular sector (e) asymmetric

Figure 6.2: Front view of the channel structure mesh for different constriction cross section shapes. Geometrical characteristics of the circular, elliptical, rectangular, circular and asymmetrical section cross section shape are shown Table 6.3. The asymmetrical shape is obtained using the general polar equation (2.14) with the parameters listed in Table 6.4. The shaded part coincides with the structure mesh of the rigid wall and the blank space in the center denotes the constricted channel. Note that the angle of the circular sector yields 30^o.

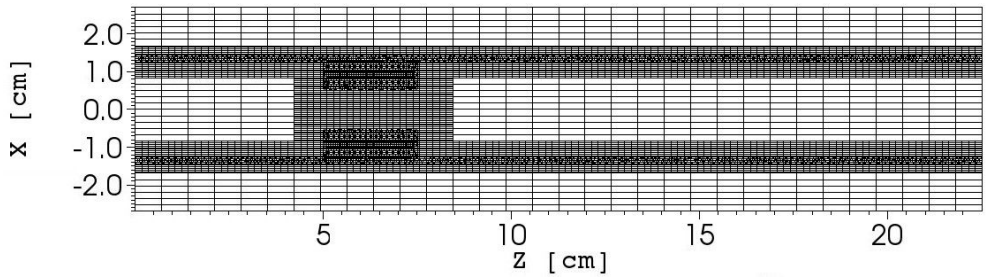

Figure 6.3: Example of fluid and structure mesh along the streamwise direction for $Y = 0$ in the case of a circular constriction. Self-adjustment of the fluid mesh near the structure walls and within the constricted channel portion is illustrated.

0.5mm[4] is illustrated in Fig. 6.2. The corresponding geometrical parameters (hydraulic diameter D, total width along the X-direction w and maximum height along the Y-direction h) are listed in Table 6.3. Fig. 6.3 illustrates the self-adjustment property of the fluid mesh so that the fluid mesh is more dense along the walls of the structure as well as within the constricted channel portion. The size of the fluid mesh within the constriction is $\Delta X = \Delta Y = 0.42$mm and $\Delta Z = 1.76$mm. Fig. 6.4 shows an example (at t=40ms) of the imposed uniform pressure profile at the entrance $Z/L_c = -2$ and the corresponding pressure distribution along the X-axis and the Y-axis for a channel with circular constriction.

Table 6.1: Overview of imposed upstream pressure P_0 and corresponding approximated volume flow rate Q and Reynolds number Re for a channel with circular constriction.

	Upstream pressure, P_0 [Pa]		
	10	35	100
Q [l/min]	16	30	53
Re	2000	3700	7800

Table 6.2: Overview of the total simulation time T_s [ms] for different geometrical configurations and imposed inlet pressures P_0 [ms].

P_0 [Pa]	Total simulation time, T_s [ms]				
	circle	asymmetric	circular sector	ellipse	rectangle
10	90ms	-	-	-	-
35	43ms	50ms	50ms	50ms	50ms
100	40ms	-	-	-	-

Table 6.3: Overview of geometrical parameters of different constriction shapes: hydraulic diameter D, total width along the X-direction w and maximum height along the Y-direction h. Constrictions have constant area A_c and constant length L_c.

[mm]	circle	asymmetric	circular sector	ellipse	rectangle
D	10	8.5	7.2	6.7	6.6
w	10	11.4	17.3	22.4	19.8
h	10	12.1	9.0	4.5	4.0

$A_c = 0.79\text{cm}^2$, $L_c = 2.5$cm

[4]The reason of roundness is due to the limitation of code in the finite element version of immersed boundary method.

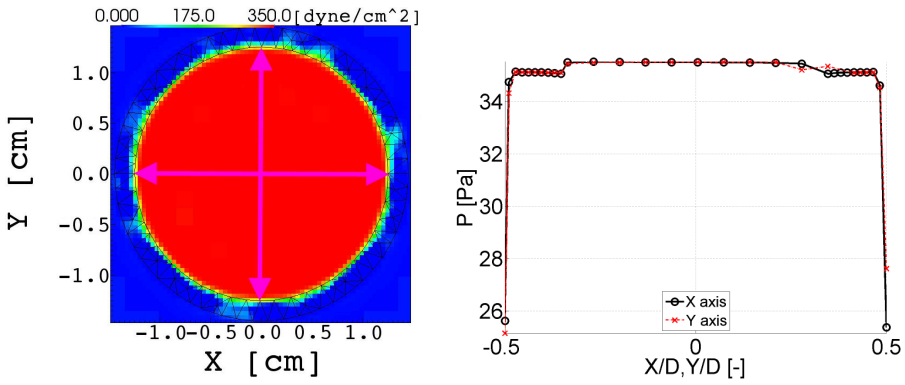

(a) (b)

Figure 6.4: Example of the imposed pressure profile $P_0 = 35$Pa at the inlet $Z/L_c = -2$ for a channel with circular constriction at t=40ms: a) pressure profile in (X,Y)-plane. Note that the pressure unit is dyne/cm^2 with 10dyne/cm^2 = 1Pa . and b) pressure distribution [Pa] along the center of the X-axis and the Y-axis along the lines (magenta) depicted in (a).

Table 6.4: Overview of general polar equation parameters (2.14) to generate the asymmetrical constriction shape.

shape	m	n_1	n_2	n_3	$g(\theta)$	a	b
asymmetrical	3	2	8	4	3.68×10^{-3}	1	1

Fig. 6.5 illustrates the temporal evolution of simulated flow quantities, pressure and velocity, for a channel with circular sector cross section shape at positions corresponding to the maximum velocity at the transverse (X,Y) position associated with the maximum velocity in the analytical model assuming viscous developed flow through the constricted channel as outlined in chapter 2. The transverse (X,Y) position is taken within transverse planes located at the following streamwise Z positions: immediately upstream from ($Z/L_c = -0.4$), in the middle of ($Z/L_c = 0.5$), immediately downstream from ($Z/L_c = 1.04$) and further downstream from ($Z/L_c = 1.4$) of the constricted channel portion. It is seen that both the pressure and velocity converges and reaches a relatively steady state for $t \geq 20$ms. In this example, the flow properties fluctuate less for quantities sampled upstream from ($Z/L_c = -0.4$) or within ($Z/L_c = 0.5$) the constriction compared to quantities sampled downstream from ($Z/L_c = 1.04$ and $Z/L_c = 1.4$) the constriction. Fluctuations downstream from the constriction are likely due to the imprint of complex flow phenomena such as jet formation and recirculation vortices. Jet formation is occurring as seen from Fig. 6.6 and Fig. 6.7 illustrating the instantaneous spatial evolution of the flow field at times $t \geq 20$ms for all assessed cross section shapes in the streamwise (plane XZ and plane YZ) and transverse (plane XY at $Z/L_c = 0.5$) direction. The influence of boundary layer development on the velocity distribution within and downstream of the constricted channel is observed to be important regardless the cross section shape as

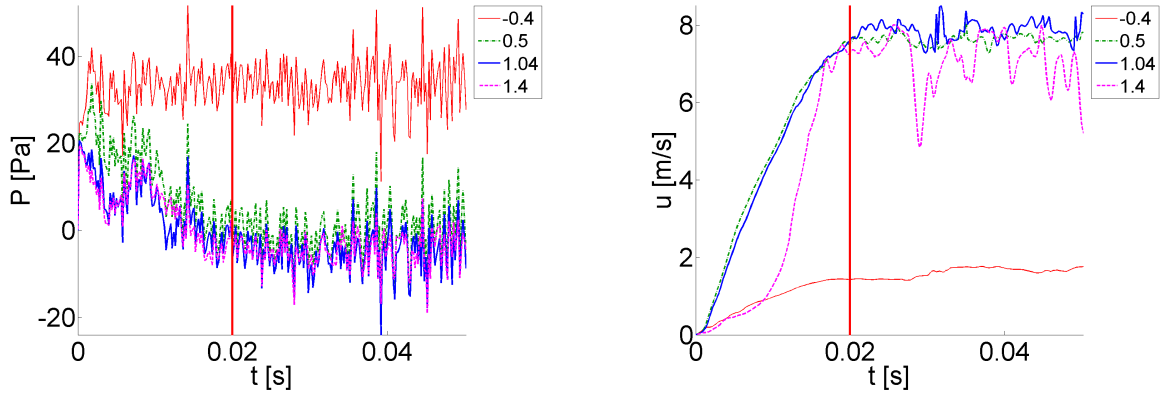

(a) $P(t, Z/L_c)$ (b) $u(t, Z/L_c)$

Figure 6.5: Illustration of simulated flow quantities as a function of time t for a channel with circular sector cross section shape and upstream pressure $P_0 = 35$Pa at the transverse (X,Y) position associated with the maximum velocity in the analytical model assuming viscous developed flow through the constricted channel as outlined in Chap. 2. The transverse (X,Y) position is taken at the following streamwise Z positions, immediately upstream from ($Z/L_c = -0.4$), in the middle of ($Z/L_c = 0.5$), immediately downstream from ($Z/L_c = 1.04$) and further downstream from ($Z/L_c = 1.4$) the constricted channel portion: a) pressure $P(t)$ and b) velocity $u(t)$. Note that the flow converges for $t \geq 20$ms (vertical red line).

seen from the evolution of the velocity field within the constriction. At the constriction outlet, the velocity magnitude distribution for the circular sector clearly illustrates reduced velocity within the sharp corner of the constricted portion. It is also observed that as a result of the symmetry break of the velocity profile, the jet downstream of the constriction reattaches to the wall portion nearest to the circular portion of the constriction, whereas for example in the case of the asymmetrical shape, jet reattachment occurs further downstream of the constriction due to jet spreading. Note that in general jet reattachment does not occur within 3cm downstream from the constriction, which corresponds to at least 3 times the hydraulic diameter. An asymmetrical velocity distribution, such as observed for the circular sector, was also found for purely viscous flow as outlined in chapter 2. Nevertheless, the modeled velocity distribution was continuously decreasing away from the position of maximum velocity, which is not the case for the simulated instantaneous flow field due to its time dependence. Complex phenomena such as flow recirculation and vortex formation can indeed be observed in the instantaneous velocity field immediately downstream of the constriction outlet as shown in Fig. 6.8 and Fig. 6.9 (Plane XZ and plane YZ). Obviously, recirculation and jet spreading are not accounted for when using the simplified 'quasi-three-dimensional' (quasi-3D) flow model presented in chapter 4, so that it is of interest to compare simulated and modeled flow quantities in order to determine the relevance of the proposed 'quasi-three-dimensional' flow model. In the following, we focus on the streamwise pressure and velocity distribution.

Fig. 6.10, Fig. 6.11 and Fig. 6.12 illustrate simulated (IB) and modeled (mod) streamwise

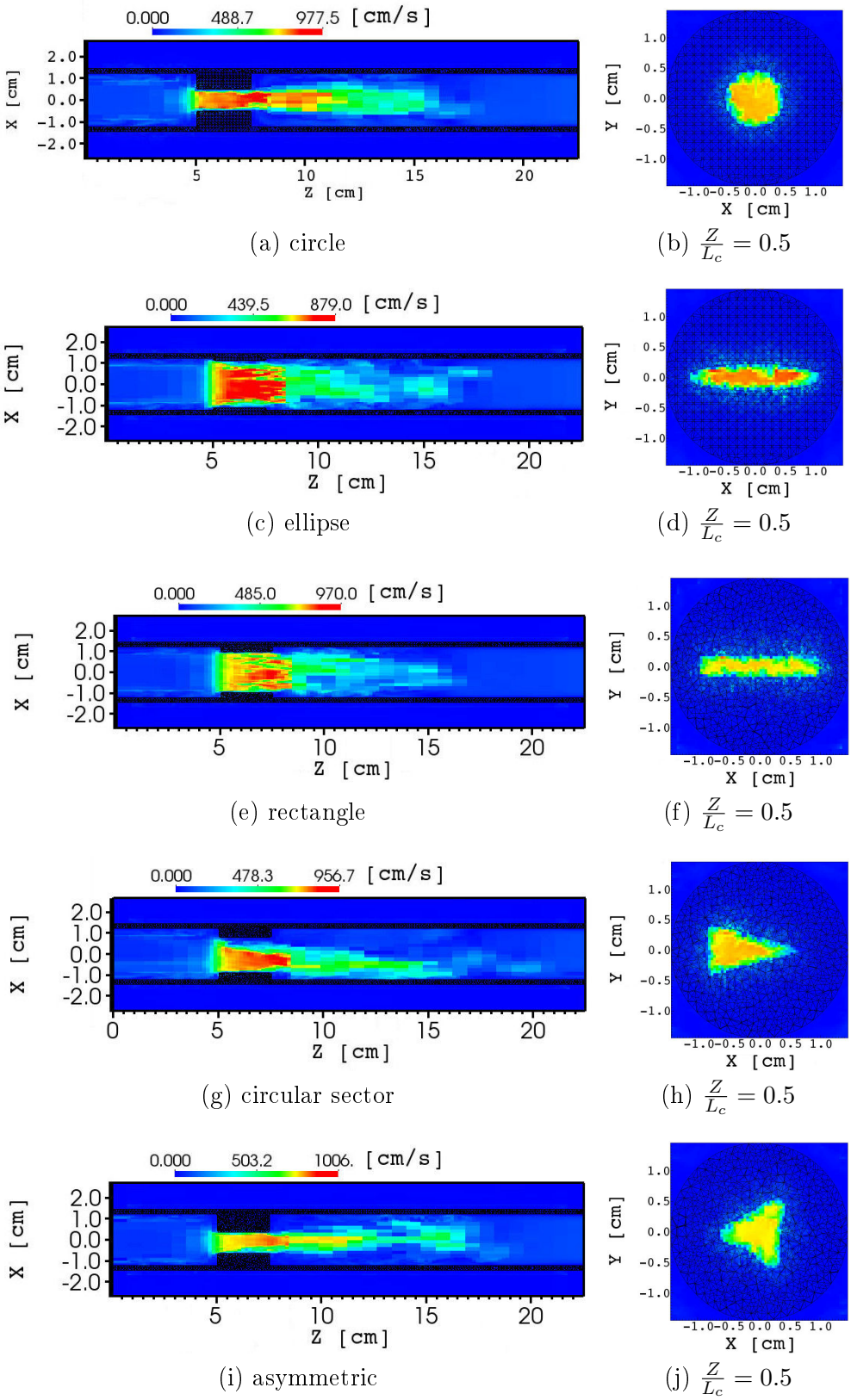

(a) circle (b) $\frac{Z}{L_c} = 0.5$

(c) ellipse (d) $\frac{Z}{L_c} = 0.5$

(e) rectangle (f) $\frac{Z}{L_c} = 0.5$

(g) circular sector (h) $\frac{Z}{L_c} = 0.5$

(i) asymmetric (j) $\frac{Z}{L_c} = 0.5$

Figure 6.6: Illustration of the magnitude of the instantaneous spatial velocity field for $P_0 = 35$Pa: a) streamwise XZ plane and b) transverse XY plane within the constriction at streamwise position $Z/L_c = 0.5$. Profiles are sampled at time $t = 43$ms for the circular shape and at time $t = 50$ms for the other shapes. Note that the unit of the velocity is [cm/s] and 1cm/s= 0.01m/s. The velocity along the streamwise YZ plane is illustrated in Fig. 6.7.

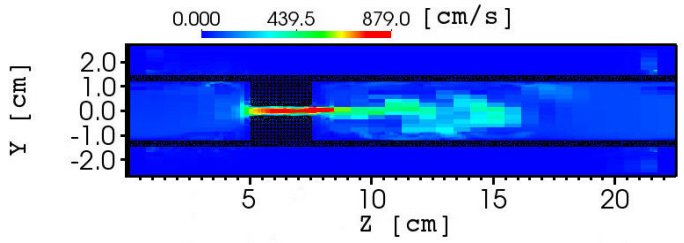

(a) ellipse

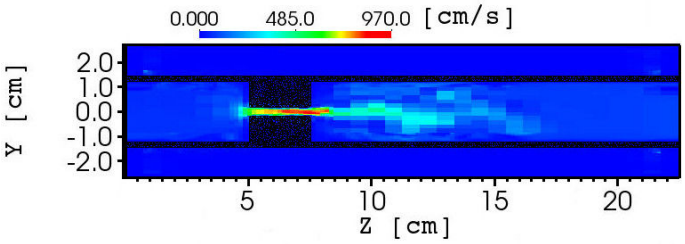

(b) rectangle

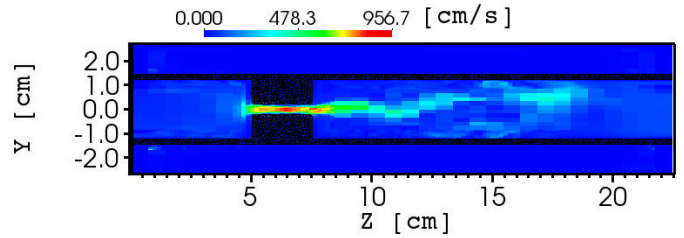

(c) circular sector

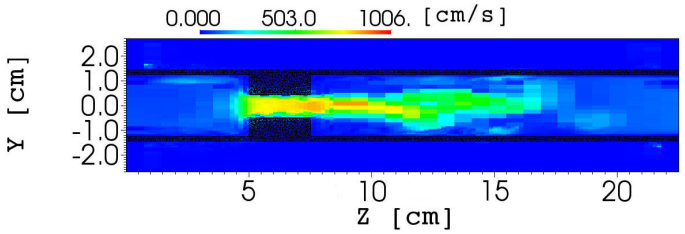

(d) asymmetric

Figure 6.7: Illustration of the magnitude of the instantaneous (t = 50ms) spatial velocity field for P_0 = 35Pa along the streamwise YZ plane. The magnitude of the instantaneous velocity distribution along the streamwise XZ plane and the transverse XY plane is illustrated in Fig. 6.6.

pressure and velocity distributions for $P_0 = 35$Pa. Distributions are shown for a circular, elliptical, rectangular and circular sector cross section shape. The modeled pressure distribution shown in Fig. 6.10 results from the quasi-three-dimensional model outlined in chapter 4. For the IB method, the streamwise pressure distribution in Fig. 6.10 and the velocity distribution in Fig. 6.12 are obtained by sampling instantaneous values for each streamwise Z position at

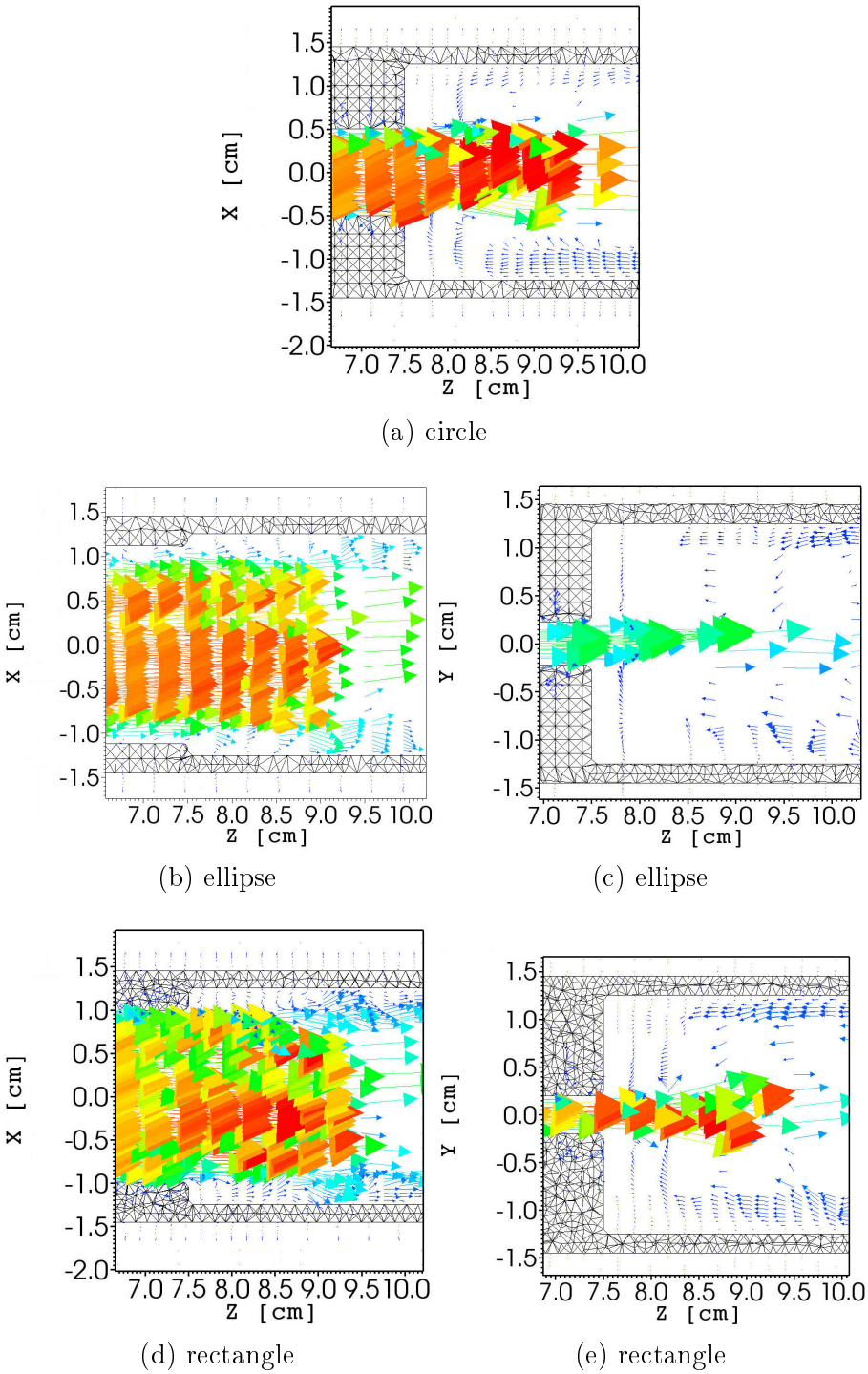

(a) circle

(b) ellipse

(c) ellipse

(d) rectangle

(e) rectangle

Figure 6.8: Illustration of the instantaneous velocity vector field for $P_0 = 35$Pa downstream from the constricted portion with circular ($t = 43$ms), elliptical ($t = 50$ms) and rectangular ($t = 50$ms) cross section shape.

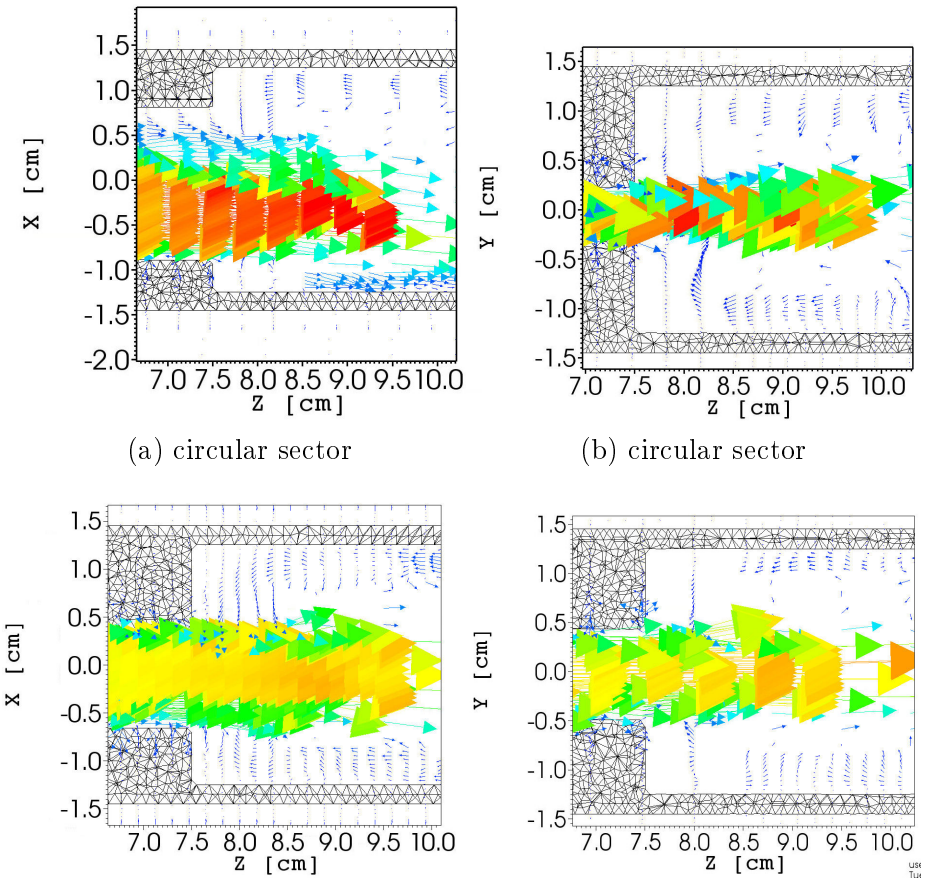

(a) circular sector (b) circular sector

(c) asymmetric (d) asymmetric

Figure 6.9: Illustration of the instantaneous velocity vector field for $P_0 = 35$Pa downstream from the constricted portion with circular sector ($t = 50$ms) and asymmetrical ($t = 50$ms) cross section shape.

the transverse (X,Y) position associated with the maximum velocity in the analytical model assuming viscous developed flow through the constricted channel as outlined in chapter 2. Fig. 6.11 illustrates the modeled (mod) and simulated (IB) local streamwise bulk velocity obtained as the transverse mean velocity[5]. Fig. 6.12 illustrates the velocity distribution obtained from sampling the velocity, for each streamwise Z position, at the transverse (X,Y) position associated with the maximum velocity in the analytical model assuming viscous developed flow through the constricted channel as outlined in chapter 2. The modeled values are sampled at the same transfers (X,Y) position whereas the transverse velocity profile is obtained from the volume flow rate Q_{mod} resulting from the quasi-three-dimensional flow model to compute the velocity distribution along the constricted portion assuming developed viscous flow as outlined

[5]The modeled mean velocity is obtained as $\bar{u}(Z) \approx Q_{mod}/A(Z)$ with Q_{mod} the volume flow rate resulting from the quasi-three-dimensional model described in chapter 4 and $A(Z)$ the streamwise varying channel area. Alternatively, a one-dimensional velocity distribution could be obtained from the modeled streamwise pressure distribution as $\bar{u}(Z) \approx \sqrt{2\Delta P(Z)/\rho}$ using the local pressure difference $\Delta P(Z) \approx P_0 - P(Z)$ resulting from the quasi-three-dimensional model.

in chapter 2.

Fig. 6.10 shows that within the constriction both the quasi-three-dimensional model and the simulated pressure distribution[6] are decreasing and result in negative pressures[7]. In general, the quasi-three-dimensional model provides a good approximation of the simulated pressure within the constriction since an overall difference of 5% between simulated and modeled pressure distribution is found. This motivates the use of the quasi-three-dimensional flow model to compute the fluid forces on the wall within the constriction while accounting for the cross section shape as was done in the stability analysis to derive phonation quantities as presented in chapter 4. On the other hand, it is seen that the quasi-three-dimensional model is incapable to account for jet reattachment downstream from the constriction. Consequently, the simplified quasi-three-dimensional model is not able to capture the pressure distribution downstream from the constriction. This is a major drawback of the proposed quasi-three-dimensional flow model[8] and as a consequence the quasi-three-dimensional model underestimates the pressure difference immediately downstream from the constriction with 20% or more.

The main findings of comparing the modeled and simulated streamwise pressure distribution holds also when comparing the modeled and simulated mean streamwise velocity as seen from Fig. 6.11. Indeed, within the constriction, the modeled mean velocities overestimate the simulated values with maximum 30% and minimum 15%, whereas immediately downstream from the constriction the error increases since no reattachment is accounted for in the quasi-three-dimensional flow model. Comparing modeled and simulated streamwise velocities at the position of maximum velocity seems a less fair comparison even within the constriction, since from Fig. 6.12 is seen that modeled values overestimate simulated values with 50% up to 60%. The overestimation of the maximum velocity could be expected since developed viscous flow is assumed in the combination of the flow models (the quasi-three-dimensional flow model to estimate the volume flow rate, which is then used to compute the transverse velocity field assuming developed viscous flow). As before, the simplified model does not account for jet spreading and flow recirculation so that downstream from the constriction, the proposed quasi-three-dimensional model fails.

Modeled[9], simulated and measured transverse profiles along the X-dimension are illustrated in Fig. 6.13 using the transverse velocity measurements immediately downstream from the constriction outlet for $Q = 35\text{l/min}$ presented in chapter 5. The simulated profiles at the

[6] A comparison could also be made between the modeled streamwise pressure distribution and the mean streamwise pressure distribution of the simulated flow field.

[7] Note that for the quasi-three-dimensional model the rounded corners at the outlet of the constriction result in the negative pressure values since as extensively shown in chapter 4 a sharp outlet results in a positive pressure distribution.

[8] Note that this could be partly corrected for by implementing an *ad-hoc* jet model, *e.g.* by forcing jet reattachment at $Z/L_c \approx 3$ as observed from the simulated data, but some thoughts should be given to the sense of such a correction prior to adding it to the model.

[9] Here again, the velocity profile is estimated by applying the quasi-three-dimensional model to estimate the volume flow rate and then using this volume flow rate to predict the transverse velocity profile for developed viscous flow within the constriction.

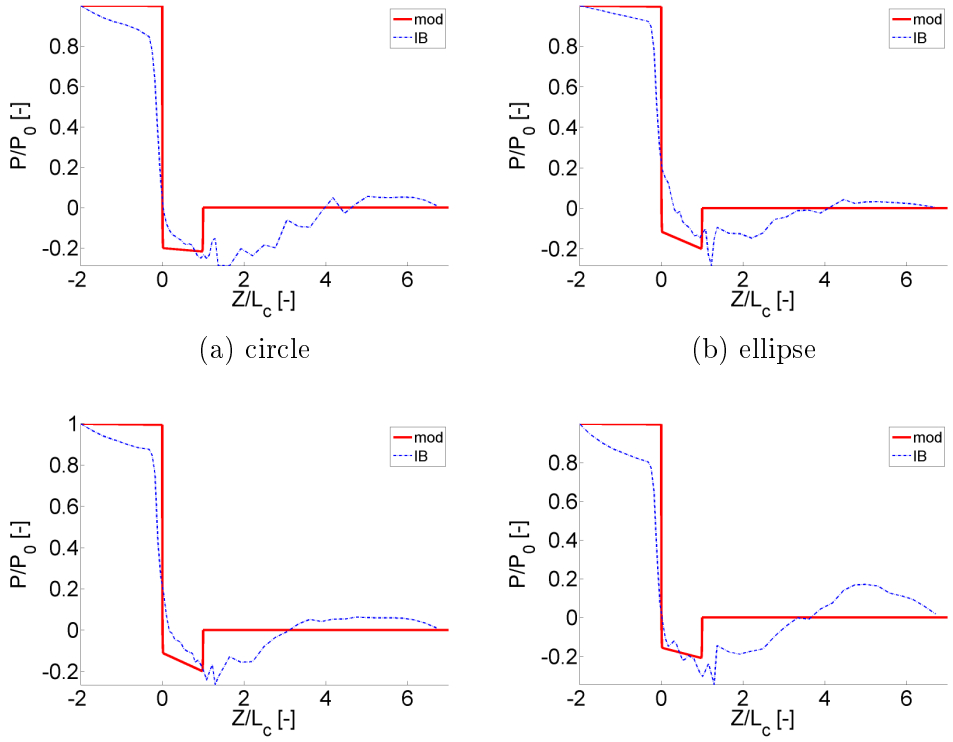

(a) circle (b) ellipse

(c) rectangle (d) circular sector

Figure 6.10: Streamwise pressure distributions obtained using the quasi-three-dimensional model (mod) described in chapter 4 and the instantaneous simulated pressure distribution using the immersed boundary method (IB). For the IB method, values are taken at the transverse (X,Y) position associated with the maximum velocity in the analytical model assuming viscous developed flow through the constricted channel as outlined in chapter 2. Instantaneous simulated values are assessed at time $t = 43$ms for the circular constriction shape and at time $t = 50$ms for the other constriction shapes.

inlet ($Z/L_c = 0$), middle ($Z/L_c = 0.5$) and outlet ($Z/L_c = 1$) of the constriction are shown. Boundary layer development along the constricted portion is observed for the simulated flow profiles so that for $Z/L_c \geq 0.5$, the simulated, measured and modeled profiles matches near the walls and so that the simulated center velocity provides a better approximation of the measured center velocity as Z/L_c increases. Since developed flow is assumed[10], the modeled maximum velocity overestimates the measured and the simulated transverse velocity at the center with 40% as was also observed from Fig. 6.12. Simulated and measured center velocities provide a good match to within 5% and 10% depending on the cross section shape.

Fig. 6.13 depicted simulated instantaneous profiles at the constriction outlet whereas the

[10]Note that the constriction length provides only 1% of the length required to obtain developed flow in a uniform channel. It could be argued that despite the severe overestimation, the result is better than expected due to the presence of the constriction which favors boundary layer development.

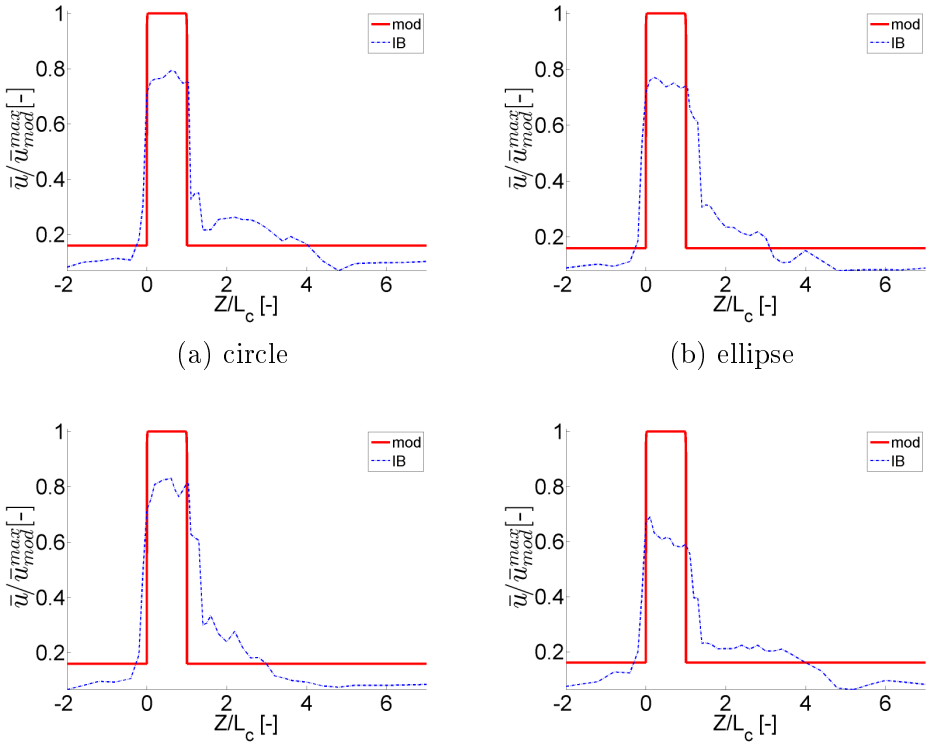

(a) circle (b) ellipse

(c) rectangle (d) circular sector

Figure 6.11: Modeled (mod) and simulated (IB) streamwise mean or local bulk velocity distributions are normalized by the maximum modeled local bulk velocity $\bar{u}_{mod}^{max}$. Modeled velocity values correspond to the local bulk velocity $Q_{mod}/A(Z)$ with Q_{mod} the volume flow rate resulting from the quasi-three-dimensional model described in chapter 4 and $A(Z)$ the streamwise varying channel area. For the IB method, the shown values correspond to the transverse mean value at each streamwise Z position. Instantaneous simulated values are assessed at time $t = 43$ms for the circular constriction shape and at time $t = 50$ms for the other constriction shapes.

shown measured profiles are gathered immediately downstream from the constriction and represent mean velocities. In order to estimate the impact of the streamwise position and the variation between instantaneous and mean flow profiles Fig. 6.14 shows the transverse profiles at the constriction outlet ($Z/L_c = 1$) and immediately downstream from the constriction outlet ($Z/L_c = 1.04$ or 1mm downstream from the constriction) as well as several instantaneous and the corresponding mean velocity profile for $t \geq 20$ms in order to make sure that the flow simulation is converged (see Fig. 6.5). It is seen that both conditions do not alter the velocity magnitude significantly. Indeed, the difference is smaller than 5% in the center and smaller than 10% within the boundary layer, illustrating that the flow is easier to be disturbed in the boundary layer than along the center core.

Fig. 6.15 presents mean and standard variation of pressure values at different streamwise

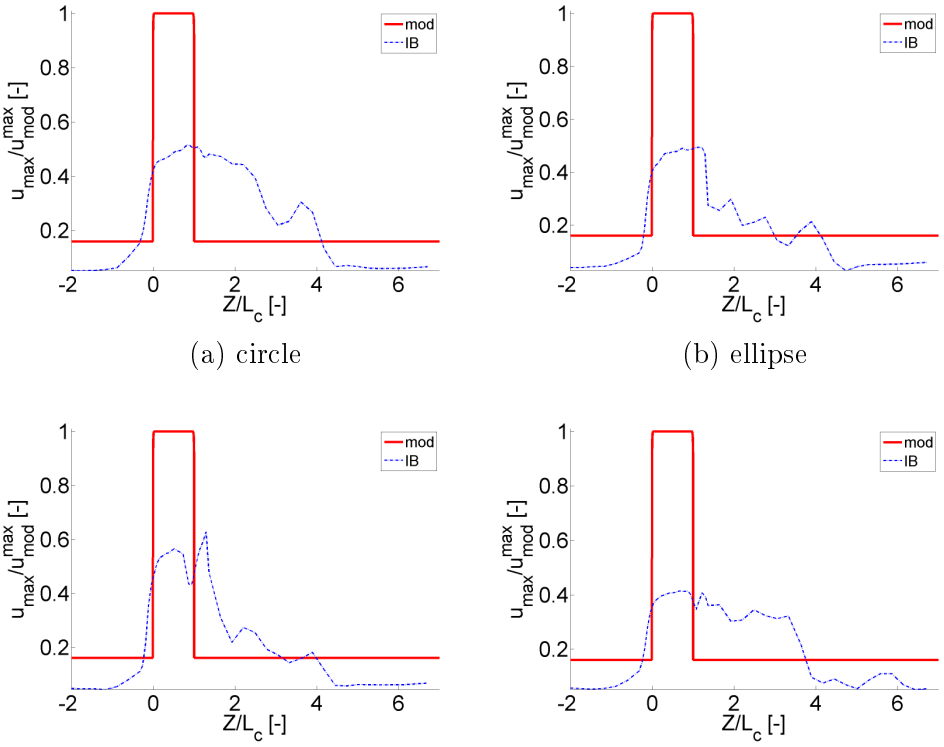

(a) circle (b) ellipse

(c) rectangle (d) circular sector

Figure 6.12: Modeled (mod) and simulated (IB) streamwise velocity distributions are normalized by the maximum modeled velocity u^{max}_{mod}. Simulated and modeled values are sampled at the transverse (X,Y) position associated with the maximum velocity in the analytical model for viscous developed flow through a constricted channel as outlined in chapter 2. for a volume rate obtained from the quasi-three-dimensional model described in chapter 4. Instantaneous simulated values are assessed at time $t = 43$ms for the circular constriction shape and at time $t = 50$ms for the other constriction shapes.

positions, immediately upstream from ($Z/L_c = -0.4$), in the middle of ($Z/L_c = 0.5$), immediately downstream from ($Z/L_c = 1.04$) and further downstream from ($Z/L_c = 1.4$). The pressure was measured for $Z/L_c = -0.4$ and $Z/L_c = 0.5$ as detailed in chapter 5. Consequently, modeled, simulated and measured mean values and their standard deviation can be compared. In general, a good match is obtained between measured and predicted values. In particular, the measured and modeled values within the constriction provide a good match since the difference is limited to about 2Pa, whereas the simulated value slightly overestimates the pressure (5Pa to 10Pa). It is further observed that the standard variation for both the simulated and measured data yields about 10Pa. Note that the standard variation for the modeled streamwise pressure yields 0Pa since no time dependence is taken into account. The modeled pressure downstream from the constriction is shown for completeness, although from the previous discussion is seen that the model can not capture downstream flow development which is shaped by complex flow phenomena such as jet spreading, jet reattachment and flow

recirculation.

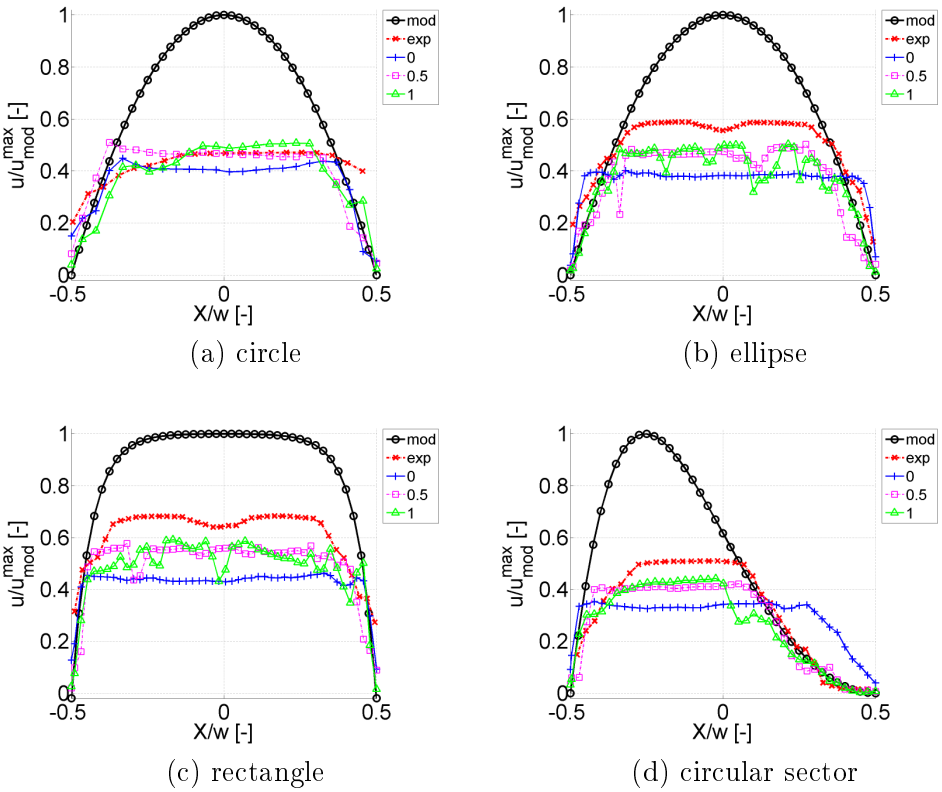

Figure 6.13: Illustration of normalized transverse velocity distributions along the X direction: modeled (mod), experimental (exp) and simulated (IB). Simulated profiles are shown for different streamwise positions within the constriction: at the inlet ($Z/L_c = 0$), in the middle ($Z/L_c = 0.5$) and at the outlet ($Z/L_c = 1$). Instantaneous simulated profiles are assessed at time $t = 43$ms for the circular constriction shape and at time $t = 50$ms for the other shapes. The X coordinate is normalized by the the width of the constricted portion w along the X dimension.

Fig. 6.16 further illustrates the simulated and measured time signal of the velocity immediately downstream from the constriction for a circular and elliptical constriction and $P_0 = 35$Pa. It is observed that for $t > 20$ms, as the flow simulation converges, the simulated and measured flow velocity matches well with respect to their magnitude as well as with respect to the observed quasi-periodic behavior of the signal representing the flow dynamics[11]. The measured velocity signal for the elliptical cross section shows in addition irregular variations, which are likely due to the onset of turbulence, so that the laminar flow (IB) simulation is not able to reproduce flow features related to the dissipation of those turbulent structures and the consequent generation of turbulent flow.

The previous discussion dealt with the influence of the cross section shape on the flow

[11] It is of interest to further quantify the flow dynamics of the measured and simulated velocity field.

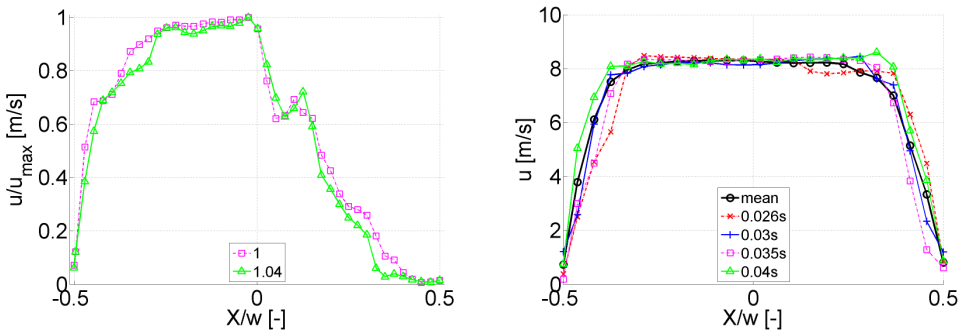

Figure 6.14: (a) Simulated transverse velocity profile along the X direction (t = 50ms) at the constriction outlet (Z/L_c =1) and downstream from the constriction (Z/L_c = 1.04) for a constriction with circular section shape. (b) Several instantaneous (t = 26ms, t = 30ms, t = 35ms and t = 40ms) and mean transverse velocity profiles immediately downstream (Z/L_c = 1.04) from a circular constriction are shown. The mean value is obtained for $t \geq$ 20ms. The X coordinate is normalized by the the width of the constricted portion w along the X dimension.

field for a single upstream pressure P_0 = 35Pa. In the following, we consider the impact of varying the upstream pressure P_0 for a single cross section shape, *i.e.* a circular cross section shape. Fig. 6.17 illustrates the simulated velocity as a function of time for P_0 = 10Pa and P_0 = 100Pa at different downstream positions (immediately upstream from ($Z/L_c = -0.4$), in the middle of (Z/L_c = 0.5), immediately downstream from (Z/L_c = 1.04) and further downstream from ($Z/L_c = 1.4$) the constriction). The flow simulation is seen to converge for $t >$ 50ms for P_0 = 10Pa and for $t >$ 15ms for P_0 = 100Pa. As expected the velocity variation within and downstream from the constriction is smaller for P_0 = 10Pa than for P_0 = 100Pa since flow structures will occur as the pressure increases. The simulated velocity field, pressure distribution and streamwise velocity profiles are further shown in Fig. 6.18 for P_0 = 10Pa and in Fig. 6.19 for P_0 = 100Pa. The simulated streamwise distributions are compared with the modeled distributions obtained using the quasi-three-dimensional flow model. The streamwise and transverse velocity field seems more homogenous for P_0 = 10Pa as for P_0 = 100Pa, again indicating an increase of the flow complexity as the upstream pressure and hence the Reynolds number increases. In general, observations made for the comparison of modeled and simulated streamwise pressure and velocity distributions for P_0 = 35Pa hold for P_0 = 10Pa and P_0 = 100Pa is well, so that in general the quasi-three-dimensional model provides a good approximation for the pressure distribution and mean velocity within the constriction whereas the model result in a severe overestimation ($> 50\%$) of the maximum velocity within the constriction compared to the simulated streamwise distributions. Downstream the constriction, the quasi-three-dimensional model does not capture the flow dynamics. Nevertheless, looking in more detail at the streamwise distribution illustrates that flow reattachment occurs further downstream from the constriction for P_0 = 10Pa than for P_0 = 100Pa, *i.e.* at $x/L_c \approx 5$ compared to $x/L_c \approx 3$. This corresponds to the decrease of the potential core extent of the jet

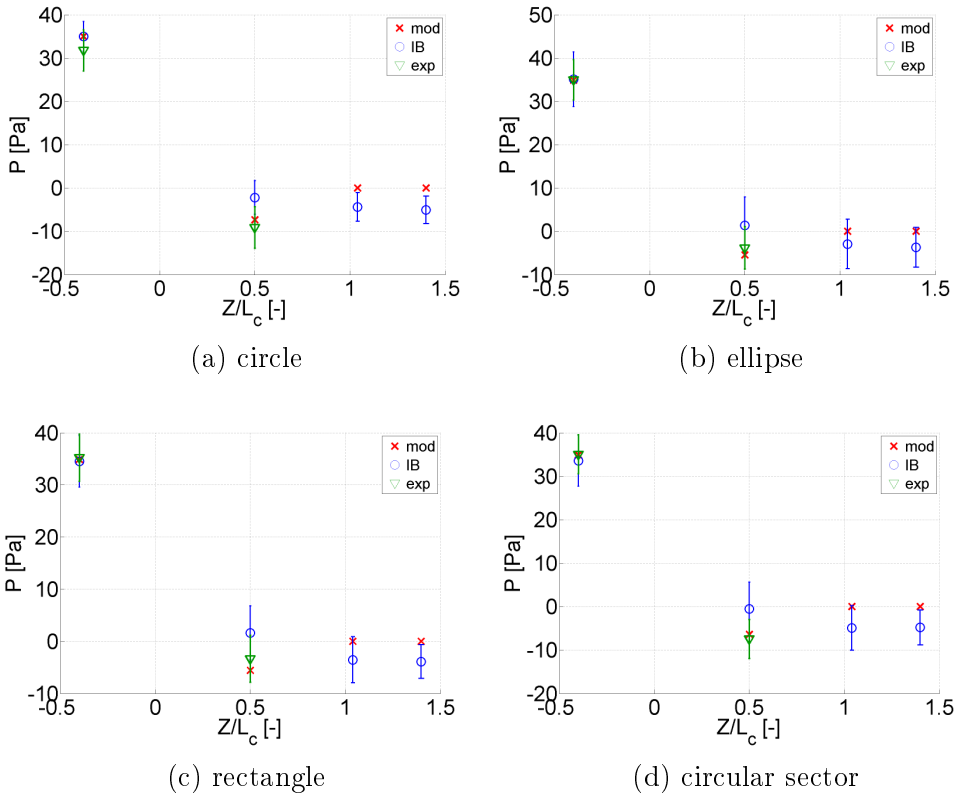

(a) circle (b) ellipse

(c) rectangle (d) circular sector

Figure 6.15: Mean pressure and associated standard variation at different streamwise positions (immediately upstream from ($Z/L_c = -0.4$), in the middle of ($Z/L_c = 0.5$), immediately downstream from ($Z/L_c = 1.04$) and further downstream from ($Z/L_c = 1.4$) the constriction): modeled (mod), simulated (IB) of measured (exp). Simulated mean values are taken for $t > 20$ms. Note that the standard deviation of the model is 0Pa.

as the upstream pressure or Reynolds number increases as was observed from the visualized flow field in chapter 5. Note that flow visualization also showed the absence of flow structures for low Reynolds numbers as expected for laminar flow, whereas coherent structures influence the flow dynamics as the upstream pressure increases.

An overview of measured (E), modeled (M) and simulated (IB) pressure values P_1 at the center of the constriction ($Z/L_c = 0.5$) and of velocity values u_{max} along the centerline of immediately downstream from the constriction ($Z/L_c = 1.04$) is shown in Fig. 6.20a and in Fig. 6.21, respectively.Mean values and their standard variation are indicated for different cross section shapes, upstream pressures P_0 and volume flow rates Q, so that the impact of the cross section shape on P_1 and u_{max} can be quantified as a function of increasing upstream pressure or Reynolds number. From Fig. 6.20a is seen that the standard variation of the simulated and measured pressure P_1 increases as the imposed upstream pressure P_0 increases for all cross section shapes in accordance with the previous findings of an increased flow complexity. A good overall match of the mean pressures and their standard deviation

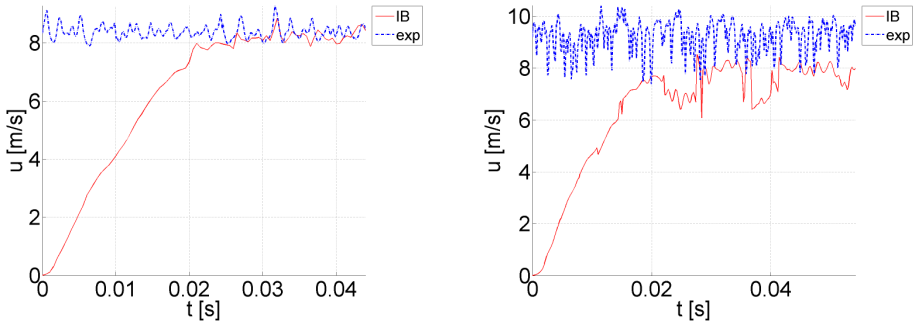

(a) circle (b) ellipse

Figure 6.16: Measured (exp) and simulated (IB) velocity signal as a function of time immediately downstream from the constriction ($Z/L_c = 1.04$) for P_0 =35Pa: a) circular constriction and b) elliptical constriction.

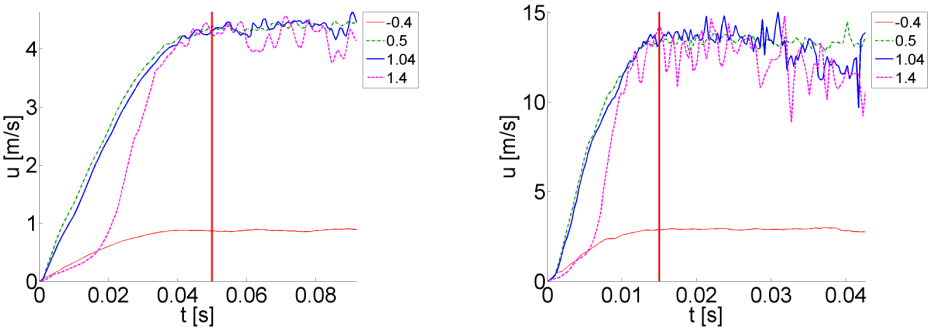

(a) P_0=10Pa (b) P_0=100Pa

Figure 6.17: Illustration of simulated (IB) velocity signal for a circular constriction at different streamwise positions (immediately upstream from ($Z/L_c = -0.4$), in the middle of ($Z/L_c = 0.5$), immediately downstream from ($Z/L_c = 1.04$) and further downstream from ($Z/L_c = 1.4$) the constriction) and for different upstream pressures: a) $P_0 = 10$Pa and b) $P_0 = 100$Pa.

is observed for $P_0 \leq 60$Pa (corresponding to $Re > 4000$) between modeled, simulated and measured values. As the pressure increases, the model underestimates the impact of the cross section shape on the pressure values as seen from the limited range of predicted values compared to the measured values, stressing again the limitations of the quasi-three-dimensional flow model to capture more complex flow phenomena. The same observation holds with respect to the prediction of the centerline velocity u_{max} downstream from the constriction shown in Fig. 6.21. The magnitude as well as the range associated with varying the cross section shape of simulated, measured and modeled values exhibit the same tendency for $Q < 40$l/min. For higher volume flow rates, the modeled values overestimate measured values in agreement with previous findings. It is seen that the standard variation of u_{max} can be neglected. Moreover, simulated values of u_{max} match the experimental tendency as illustrated in Fig. 6.22.

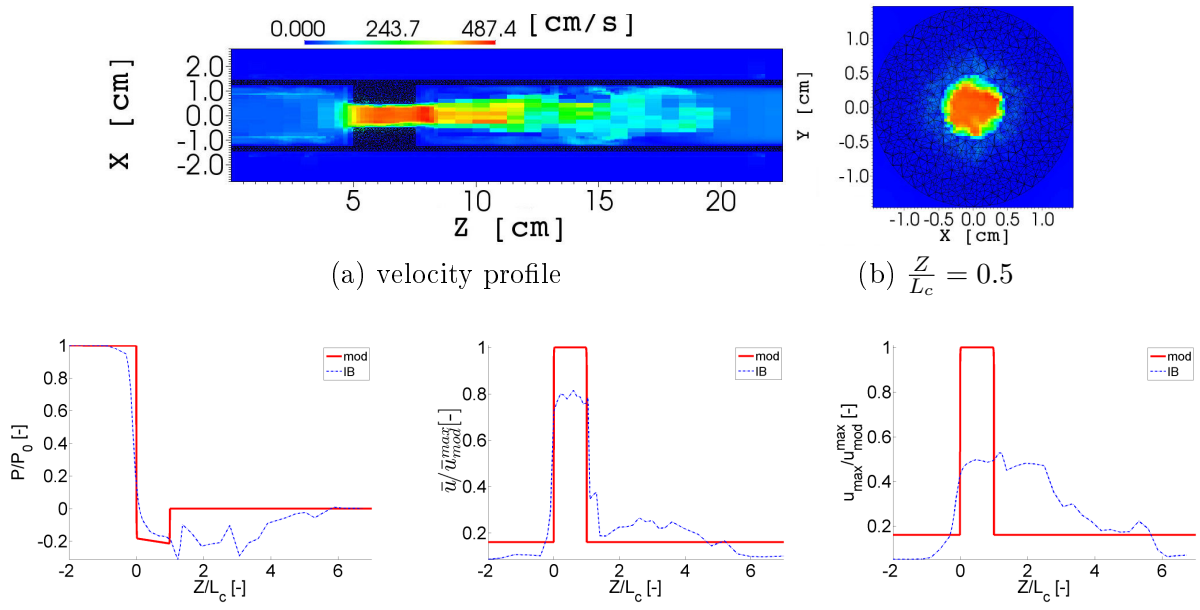

(a) velocity profile (b) $\frac{Z}{L_c} = 0.5$

(c) pressure (d) mean velocity (e) maximum velocity

Figure 6.18: Illustration of flow field for a channel with circular constriction for upstream pressure $P_0 = 10$Pa. Simulated (IB) quantities are obtained at time $t = 90$ms: a) instantaneous simulated (IB) streamwise velocity magnitude, b) instantaneous simulated (IB) transverse velocity magnitude at the middle of the constriction ($Z/L_c = 0.5$), c) normalized modeled (mod) and simulated (IB) streamwise pressure distribution, d) normalized modeled (mod) and simulated (IB) mean streamwise velocity distribution and e) normalized modeled (mod) and simulated (IB) streamwise velocity distribution along the centerline of the constriction.

In order to further quantify the impact of the cross section shape on the pressure P_1 the range of the mean P_1 values, *i.e.* $|(P_1^{max} - P_1^{min})|$, is quantified for the experimental and simulated flow field and normalized with respect to the range observed for the quasi-three-dimensional model as $|(P_1^{max} - P_1^{min})/(P_{1,mod}^{max} - P_{1,mod}^{min})|$. Consequently, a value smaller than 1 indicates that the range is smaller than the range estimated for the quasi-three-dimensional model whereas a value greater than 1 indicates a range which is larger than the one predicted from the quasi-three-dimensional model. The quantity is illustrated in Fig. 6.23 as a function of the upstream pressure P_0. Consequently, it is seen that for all upstream pressures the quasi-three-dimensional model underestimates the impact of the cross section shape on the range of the mean pressure P_1 within the constriction and the underestimation becomes more prominent as the pressure increases. It is interesting to note that a minimum is found around $P_0 = 30$, corresponding to $2800 < Re < 4200$ and hence the transition regime, for which the modeled range corresponds best to the experimental range. Moreover, it is seen that the simulated values provide an overestimation of the range of pressure values P_1 due to varying the cross section shape.

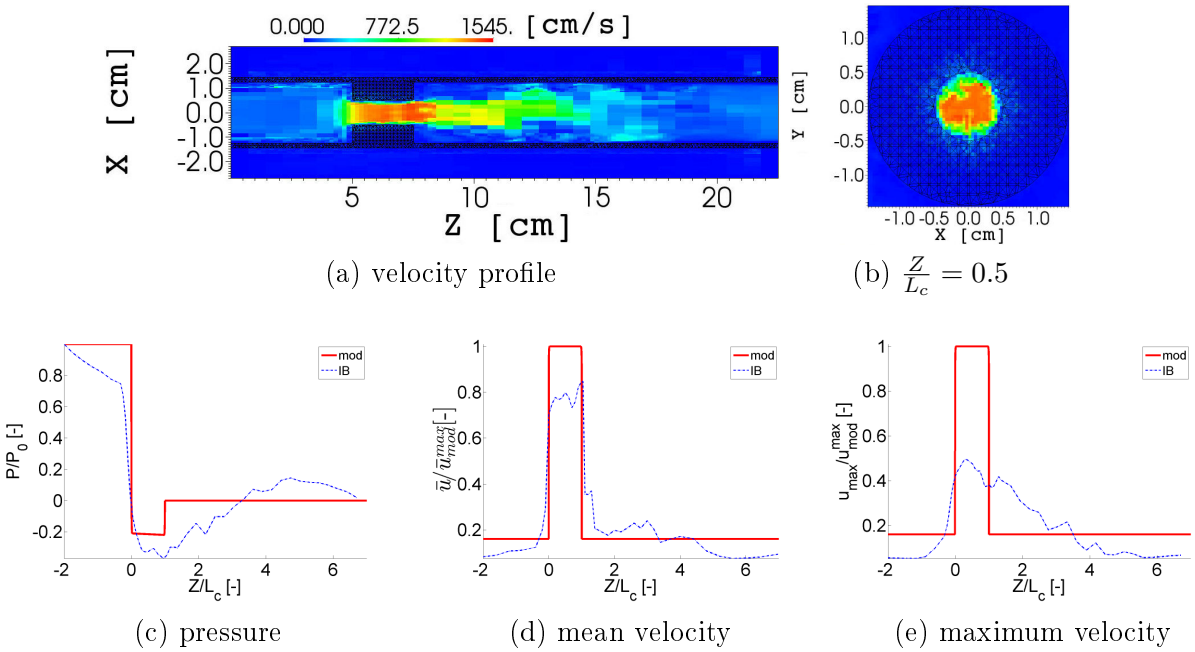

(a) velocity profile (b) $\frac{Z}{L_c} = 0.5$

(c) pressure (d) mean velocity (e) maximum velocity

Figure 6.19: Illustration of flow field for a channel with circular constriction for upstream pressure $P_0 = 100$Pa. Simulated (IB) quantities are obtained at time $t = 40$ms: a) instantaneous simulated (IB) streamwise velocity magnitude, b) instantaneous simulated (IB) transverse velocity magnitude at the middle of the constriction ($Z/L_c = 0.5$), c) normalized modeled (mod) and simulated (IB) streamwise pressure distribution, d) normalized modeled (mod) and simulated (IB) mean streamwise velocity distribution and e) normalized modeled (mod) and simulated (IB) streamwise velocity distribution along the centerline of the constriction.

6.3 Summary

In the current chapter, the immersed boundary (IB) method is applied to flow through a rigid constricted channel for a wide range of Reynolds numbers and different cross section shapes of the constriction. Simulated flow quantities are compared with the quasi-three-dimensional model outcome and with experimental values in order to estimate the relevance of the proposed simplified quasi-three-dimensional flow model and in order to validate the flow model used in the IB method before applying the method to simulate fluid-structure interaction problems. In general, it is seen that the quasi-three-dimensional flow model can be used to approximate the flow within the constriction, but does not capture flow phenomena downstream from the constriction, whereas the IB method is able to capture three-dimensional flow structures as well as jet development downstream from the constriction. Nevertheless, both models fail to capture fully the impact of the cross section shape compared to experimental values. Nevertheless, it is concluded that the IB model provides an accurate flow solution for upstream pressures $P_0 < 60$Pa corresponding to Reynolds numbers $Re < 4000$ so that fluid-structure interactions up to this Reynolds number can be assessed. Further research is required to investigate the flow dynamics. In addition, it is of interest to extent the flow models (both

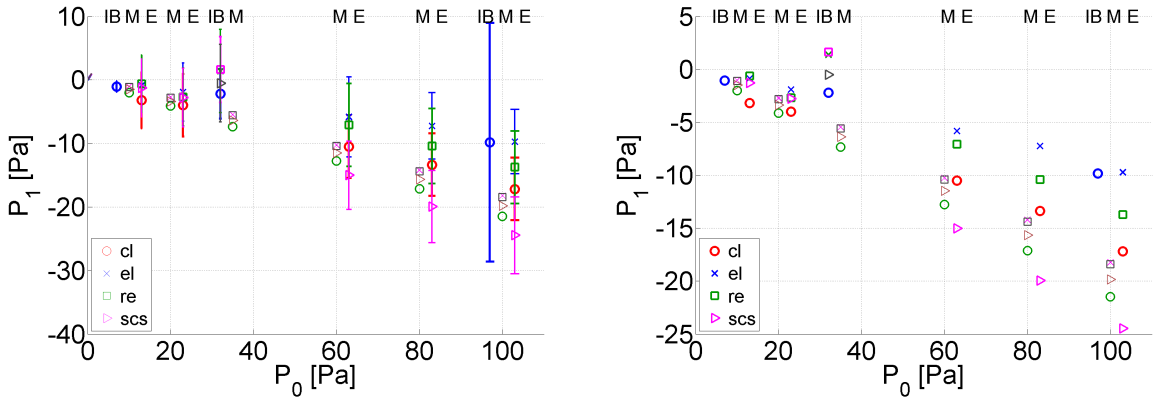

(a) (b)

Figure 6.20: Overview of pressure values at the center of the constriction ($Z/L_c = 0.5$) for a circular (∘ cl), elliptical (× el), rectangular (□ re) and circular sector (▷ scs) cross section shape as a function of the imposed upstream pressure P_0. Modeled (M), experimental (E) and simulated (IB) values are indicated. For clarity experimental and simulated values are shifted with +3Pa and −3Pa, respectively. a) mean and standard variation and b) mean values. Experimental results for upstream length L_u=2cm and downstream length L_d=15cm are indicated (see chapter 5). The standard variation of modeled values yields 0Pa.

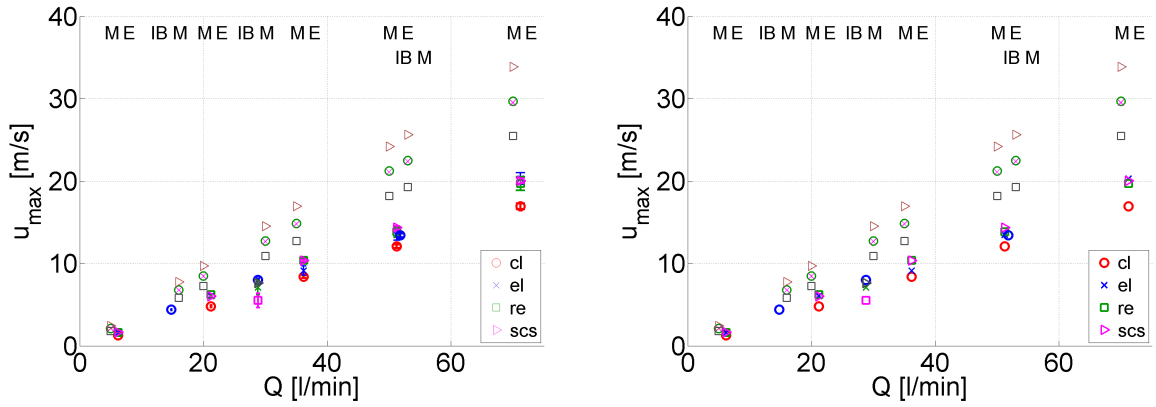

(a) (b)

Figure 6.21: Overview of velocity values sampled along the centerline immediately downstream from the constriction ($Z/L_c = 1.04$) for a circular (∘ cl), elliptical (× el), rectangular (□ re) and circular sector (▷ scs) cross section shape as a function of the measured and predicted volume flow rate Q. Modeled (M), experimental (E) and simulated (IB) values are indicated. For clarity experimental and simulated values are shifted with +1.2l/min and −1.2l/min, respectively. a) mean and standard variation and b) mean values. Experimental results for upstream length L_u=2cm and downstream length L_d=15cm are indicated (see chapter 5). The standard variation of modeled values yields 0Pa.

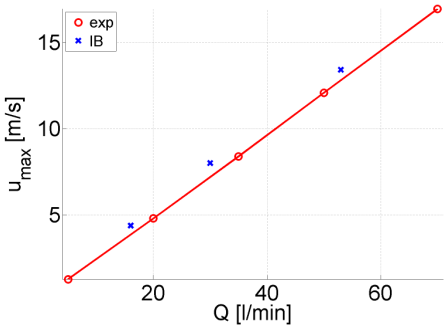

Figure 6.22: Illustration of the maximum velocity u_{max} for a circular constriction along the centerline immediately downstream from the constriction (Z/L_c=1.04) for experiment (exp) and IB method (IB).

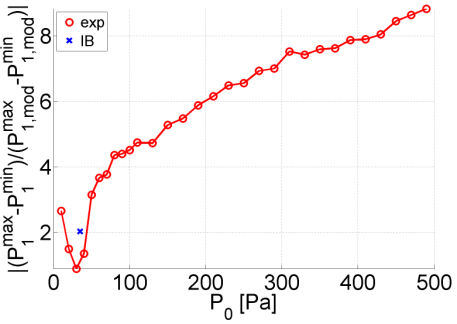

Figure 6.23: Illustration of ratio $|(P_1^{max} - P_1^{min})/(P_{1,mod}^{max} - P_{1,mod}^{min})|$ between different cross section shapes for experiment (exp) and IB method (IB). Experimental results is obtained when pressure is the initial condition for L_u=2cm and L_d=15cm. P_1^{max} and P_1^{min} denotes the maximum and minimum mean pressure for experimental and simulated result.

the quasi-three-dimensional as well as the IB flow model) to include a simple turbulence model. Finally, it need to be commented that the simulated and quasi-three-dimensional model outcome is compared to quantities measured on a constricted channel with sharp edges instead of rounded edges applied to the numerical structure. Consequently, it would be interesting to perform an additional experiment for a constricted channel for which the geometry matches the numerical structure.

Chapter 7

Conclusion and perspectives

Simple flow models have a long and successful tradition with respect to the qualitative prediction of complex biological circulation phenomena in terms of meaningful physiological parameters at a low computational cost. In addition, the last decades complex flow simulation techniques are applied to those biological circulation phenomena in order to overcome the assumptions inherent to simplified flow models so as to provide quantitatively accurate predictions at a large computational cost. A good example of a physiologically important variable which is either neglected in simple flow models or for which incorporating all its details in a computational model is firstly a huge task and secondly increases the computational cost significantly is presented by the cross section shape of a stenosis related to a biological circulation system. Besides the cross section shape, attention is given to upstream flow conditions since a stenosis might involve blood flow as well as air flow so that flow conditions vary significantly. Therefore, in this thesis we sought to describe the influence of the cross section shape for pressure-driven laminar flow at a low computational cost and taking into account the possible need to analyze the model in terms of its parameter space such as Reynolds number or a geometrical parameter. As a result, a simplified quasi-three-dimensional flow model is proposed in combination with a parametrized description of an arbitrary cross section shape. Such a model provides the sought balance between simplicity and complexity and adds a three-dimensional aspect to a simple flow model, which is uncommon since it is more natural to rely on two-dimensional boundary layer theory in case it is sought to improve the flow model. The proposed flow model relies on fully developed flow solutions and can therefore be seen at the extension of classical quasi-one-dimensional flow models. The relevance as well as the limitations of the proposed flow model with respect to constricted channel flow is shown in several ways. Firstly, it is shown that the impact of the cross section shape on the pressure distribution within the constriction can not be neglected when the flow is not completely dominated by viscosity. In the latest case, the classical quasi-one-dimensional flow model provides as good results with a minimum of computations. Secondly, it is shown that the application of the quasi-three-dimensional flow model to phonation allows indeed a mathematical analysis in terms of the parameter space and moreover affects predicted values, again compared to the quasi-one-dimensional model, of relevant physiological parameters in case the flow is affected and hence when the flow is not fully dominated by viscosity. Thirdly, pressure measurements within the constriction show that although the quantitative accuracy is poor, the quasi-three-dimensional flow model does improve predicted values compared to the quasi-one-dimensional model as well as to a boundary layer solution for axisymmetrical or two-dimensional flows (except for the lowest Reynolds numbers). The same way, transverse

velocity profiles show that the predicted profiles by the quasi-three-dimensional flow model, although not accurate, do provide some main characteristics of the velocity profile such as the asymmetrical development of the boundary layers in the case of asymmetrical geometries. On the other hand, it is shown that the proposed flow model can not capture the complexity of the flow dynamics related to the variation of upstream flow conditions. At the same time, although a prediction obtained from the numerical simulation with a more complex flow model would certainly be more accurate, it can be questioned that it would capture the impact of the upstream flow conditions in a reasonable amount of time. Fourthly, the model outcome is compared to the outcome of the numerical simulation of a laminar incompressible three-dimensional flow model. It is seen that predictions obtained from the model are suitable to predict the order of magnitude of flow quantities within the constriction whereas predictions downstream from the constriction are useless. The simulated flow field on the other hand is shown to capture some of the flow dynamics at a high computational cost.

Several research perspectives can be formulated.

In the current work, it was aimed to show the influence of the cross section shape and of upstream flow conditions. As such both were varied extensively, in order to provide an overview of their impact on the flow dynamics. Several observations related to the complexity of the flow can be an individual research topic. In particular, the stability of the flow patterns and the transition mechanism from laminar to turbulent flow needs to be addressed.

In the current work, the flow model is assessed for steady flow. Obviously, the analysis needs to be extended to unsteady flow. In addition, the model can be improved in several ways. Given the observed flow regimes, it is of interest to extent the flow model with a simple turbulence model. For the same reason, implementation of a simple flow model in the numerical model is of interest. Finally, the balance between accuracy and computational cost would probably improve when a flow model is proposed which does not rely on fully developed flow but on boundary layer development.

The numerical simulation with the immersed boundary method needs to be extended to represent the full fluid-structure interaction in order to be able to model phonation.

Finally, it is of interest to obtain experimental data using a smooth converging transition from the upstream channel to the minimum constriction for all cross section shapes and not only for the circular cross section.

Bibliography

[1] A.M.R. Agur, A.F. Dalley, and J.C.B. Grant. *Grant's atlas of anatomy*. 13th. Wolters Kluwer Health, 2012, p. 871.

[2] L.C. Andrews. *Special functions for engineers and applied mathematicians*. Macmillan New York, 1985, p. 357.

[3] D.N. Arnold, D. Boffi, R.S. Falk, and L. Gastaldi. "Finite element approximation on quadrilateral meshes". In: *Communications in numerical methods in engineering* 17.11 (2001), pp. 805–812.

[4] S. Ashforth-Frost and K. Jambunathan. "Effect of nozzle geometry and semi-confinement on the potential core of a turbulent axisymmetric free jet". In: *International communications in heat and mass transfer* 23.2 (1996), pp. 155–162.

[5] J. Awrejcewicz. "Dynamics of the human vocal cords". In: *Teoretyczna I Stosowana* 29 (1991), pp. 557–577.

[6] S. Balay, J. Brown, K. Buschelman, V. Eijkhout, W. Gropp, D. Kaushik, M. Knepley, L.C. McInnes, B. Smith, and H. Zhang. "PETSc Users Manual Revision 3.0.0". In: (2008).

[7] S. Balay, W.D. Gropp, L.C. McInnes, and B.F. Smith. "Efficient management of parallelism in object-oriented numerical software libraries". In: *Modern software tools for scientific computing*. Springer, 1997, pp. 163–202.

[8] A. Barney, C.H. Shadle, and P.O.A.L. Davies. "Fluid flow in a dynamic mechanical model of the vocal folds and tract. I. Measurements and theory". In: *Journal of the Acoustical Society of America* 105.1 (1999), pp. 444–455.

[9] G.K. Batchelor. *An Introduction to Fluid Dynamics*. Cambridge Mathematical Library. Cambridge University Press, 2000, p. 615.

[10] J.M. Bauer. "Harnessing the swarm communications policy in an era of ubiquitous networks and disruptive technologies". In: *Communications & stratégies* 54 (2004).

[11] R. Berker. *Integration des équations du mouvement d'un fluide visqueux incompressible: Handbuch der Physik, Bd VIII/2, Encyclopedia of Physics*. Springer-Verlag, 1963, p. 384.

[12] R. Blevins. *Applied Fluid Dynamics Handbook*. Malabar: Krieger publishing company, 1992, p. 570.

[13] M. Brouns, S.T. Jayaraju, C. Lacor, J. De Mey, M. Noppen, W. Vincken, and S. Verbanck. "Tracheal stenosis: a flow dynamics study". In: *Journal of Applied Physiology* 102.3 (2007), pp. 1178–1184.

[14] F. Calamante, P.J. Yim, and J.R. Cebral. "Estimation of bolus dispersion effects in perfusion MRI using image-based computational fluid dynamics". In: *Neuroimage* 19.2 (2003), pp. 341–353.

[15] C. Cancelli and T.J. Pedley. "Separated-flow model for collapsible-tube oscillations". In: *Journal of Fluid Mechanics* 157 (1985), pp. 375–404.

[16] C.A.A.H. Carbonel and A.C.N. Galeao. "A stabilized finite element model for the hydrothermodynamical simulation of the Rio de Janeiro coastal ocean". In: *Communications in numerical methods in engineering* 23.6 (2007), pp. 521–534.

[17] M.A. Castro and J.R. Putman C.M.and Cebral. "Computational fluid dynamics modeling of intracranial aneurysms: effects of parent artery segmentation on intra-aneurysmal hemodynamics". In: *American Journal of Neuroradiology* 27.8 (2006), pp. 1703–1709.

[18] H. Chen, Y. Su, and B.D. Shizgal. "A direct spectral collocation Poisson solver in polar and cylindrical coordinates". In: *Journal of Computational Physics* 160.2 (2000), pp. 453–469.

[19] G. Chiandussi, G. Bugeda, and E. Oñate. "A simple method for automatic update of finite element meshes". In: *Communications in Numerical Methods in Engineering* 16.1 (2000), pp. 1–19.

[20] F. Chouly and P.Y. Lagrée. "Comparison of computations of asymptotic flow models in a constricted channel". In: *Applied Mathematical Modelling* 36.12 (2012), pp. 6061–6071.

[21] J. Cisonni, K. Nozaki, A. Van Hirtum, X. Grandchamp, and S. Wada. "Numerical simulation of the influence of the orifice aperture on the flow around a teeth-shaped obstacle". In: *Fluid Dynamics Research* 45.2 (2013), p. 025505.

[22] J. Cisonni, K. Nozaki, A. Van Hirtum, and S. Wada. "A parameterized geometric model of the oral tract for aeroacoustic simulation of the fricatives". In: *International Journal of Information and Electronics Engineering* 1.3 (2011), pp. 223–228.

[23] J. Cisonni, A. Van Hirtum, X.Y. Luo, and X. Pelorson. "Experimental validation of quasi-one-dimensional and two-dimensional glottal flow models". In: *Medical and Biological Engineering and Computing* 48.9 (2010), pp. 903–910.

[24] J. Cisonni, A. Van Hirtum, X. Pelorson, and J. Lucero. "The influence of geometrical and mechanical input parameters on theoretical models of phonation". In: *Acta Acustica united with Acustica* 97.2 (2011), pp. 291–302.

[25] J. Cisonni, A. Van Hirtum, X. Pelorson, and J. Willems. "Theoretical simulation and experimental validation of inverse quasi one-dimensional steady and unsteady glottal flow models". In: *Journal of the Acoustical Society of America* 124 (2008), pp. 535–545.

[26] P. Colella and P.R. Woodward. "The piecewise parabolic method (PPM) for gas-dynamical simulations". In: *Journal of computational physics* 54.1 (1984), pp. 174–201.

[27] N. Curle. *The laminar boundary layer equations*. Oxford mathematical monographs. Clarendon Press, 1962, p. 162.

[28] R. Daniloff, G. Schuckers, and L. Feth. *The physiology of speech and hearing*. Prentice-Hall, 1980, p. 453.

[29] C.W. David. "The Laplacian in Spherical Polar Coordinates". In: *Chemistry Education Materials* (2007), p. 34.

[30] M. Deverge, X. Pelorson, C. Vilain, P.Y. Lagree, F. Chentouf, J. Willems, and A. Hirschberg. "Influence of collision on the flow through in-vitro rigid models of the vocal folds". In: *Journal of the Acoustical Society of America* 114.6 (2003), pp. 3354–3362.

[31] M. Döellinger, D.A. Berry, and G.S. Berke. "A Quantitative Study of the Medial surface dynamics of an in vivo canine vocal fold during phonation". In: *Journal of the Acoustical Society of America* 117 (2005), p. 3174.

[32] R. Eberhart and J. Kennedy. "A new optimizer using particle swarm theory". In: *Micro Machine and Human Science, 1995. MHS'95., Proceedings of the Sixth International Symposium on*. IEEE. 1995, pp. 39–43.

[33] R.C. Eberhart and Y.H. Shi. "Particle swarm optimization: developments, applications and resources". In: *Evolutionary Computation, 2001. Proceedings of the 2001 Congress on*. Vol. 1. IEEE. 2001, pp. 81–86.

[34] H. Eisen, W. Heinrichs, and K. Witsch. "Spectral collocation methods and polar coordinate singularities". In: *Journal of Computational Physics* 96.2 (1991), pp. 241–257.

[35] R.D. Falgout and U.M. Yang. "hypre: A library of high performance preconditioners". In: *Computational Science—ICCS 2002*. Springer, 2002, pp. 632–641.

[36] Y. Fan, L.K. Cheung, M.M. Chong, H.D. Chua, K.W. Chow, and C.H. Liu. "Computational Fluid Dynamics Analysis on the Upper Airways of Obstructive Sleep Apnea Using Patient- Specific Models". In: *IAENG International Journal of Computer Science* 38.4 (2011), pp. 401–408.

[37] G. Fant. *Acoustic theory of speech production*. Mouton & Co., 1960, p. 323.

[38] M. Fleischer. "Foundations of swarm intelligence: From principles to practice". In: *arXiv preprint nlin/0502003* (2005).

[39] J. Gielis. "A generic geometric transformation that unifies a wide range of natural and abstract shapes". In: *American Journal of Botany* 90.3 (2003), pp. 333–338.

[40] X. Grandchamp. "Modélisation physique des écoulements turbulents appliquée aux voies aériennes supérieures chez l'humain". THESE. Nov. 2009.

[41] X. Grandchamp, Y. Fujiso, B. Wu, and A. Van Hirtum. "Steady laminar axisymmetrical nozzle flow at moderate Reynolds numbers: modeling and experiment". In: *Journal of Fluids Engineering* 134.1, 011203 (2012), p. 011203.

[42] X. Grandchamp, A. Van Hirtum, and X. Pelorson. "Hot film/wire calibration for low to moderate flow velocities". In: *Measurement Science and Technology* 21.11 (2010), p. 115402.

[43] B.E. Griffith. "An accurate and efficient method for the incompressible Navier–Stokes equations using the projection method as a preconditioner". In: *Journal of Computational Physics* 228.20 (2009), pp. 7565–7595.

[44] B.E. Griffith. "Immersed boundary model of aortic heart valve dynamics with physiological driving and loading conditions". In: *International Journal for Numerical Methods in Biomedical Engineering* 28.3 (2012), pp. 317–345.

[45] B.E. Griffith. "On the volume conservation of the immersed boundary method". In: *Communications in Computational Physics* 12.2 (2012), p. 401.

[46] B.E. Griffith and X.Y. Luo. "Hybrid finite difference/finite element of the immersed boundary method (submitted)". 2013.

[47] B.E. Griffith, X.Y. Luo, D.M. McQueen, and C.S. Peskin. "Simulating the fluid dynamics of natural and prosthetic heart valves using the immersed boundary method". In: *International Journal of Applied Mechanics* 1.01 (2009), pp. 137–177.

[48] E.J. Gutmark and F.F. Grinstein. "Flow control with noncircular jets". In: *Annual Review of Fluid Mechanics* 31.1 (1999), pp. 239–272.

[49] M. Haslam and M. Zamir. "Pulsatile Flow in Tubes of Elliptic Cross Sections". In: *Annals of Biomedical Engineering* 26 (5 1998). 10.1114/1.106, pp. 780–787.

[50] A.F. Heenan, E. Matida, A. Pollard, and W.H. Finlay. "Experimental measurements and computational modeling of the flow field in an idealized human oropharynx". In: *Experiments in Fluids* 35.1 (2003), pp. 70–84.

[51] E.B. Holmberg, R.E. Hillman, and J.S. Perkell. "Glottal airflow and transglottal air pressure measurements for male and female speakers in soft, normal, and loud voice". In: *Journal of the Acoustical Society of America* 84 (1988), p. 511.

[52] R.D. Hornung and S.R. Kohn. "Managing application complexity in the SAMRAI object-oriented framework". In: *Concurrency and Computation: Practice and Experience* 14.5 (2002), pp. 347–368.

[53] R.D. Hornung, A.M. Wissink, and S.R. Kohn. "Managing complex data and geometry in parallel structured AMR applications". In: *Engineering with Computers* 22.3-4 (2006), pp. 181–195.

[54] C. Hsu and R. Dillon. "A 3D motile rod-shaped monotrichous bacterial model". In: *Bulletin of mathematical biology* 71.5 (2009), pp. 1228–1263.

[55] W. Huang and D.M. Sloan. "Pole condition for singular problems: the pseudospectral approximation". In: *Journal of Computational Physics* 107.2 (1993), pp. 254–261.

[56] K. Ishizaka and J.L. Flanagan. "Synthesis of voiced sounds from a two-mass model of the vocal cords". In: *Bell System Technical Journal* 51.6 (1972), pp. 1233–1268.

[57] S.T. Jayaraju, M. Brouns, S. Verbanck, and C. Lacor. "Fluid flow and particle deposition analysis in a realistic extrathoracic airway model using unstructured grids". In: *Journal of aerosol science* 38.5 (2007), pp. 494–508.

[58] S.J. Jeong, W.S. Kim, and S.J. Sung. "Numerical investigation on the flow characteristics and aerodynamic force of the upper airway of patient with obstructive sleep apnea using computational fluid dynamics". In: *Medical engineering & physics* 29.6 (2007), pp. 637–651.

[59] H.H. Jin, J.R. Fan, M.J. Zeng, and K.F. Cen. "Large eddy simulation of inhaled particle deposition within the human upper respiratory tract". In: *Journal of aerosol Science* 38.3 (2007), pp. 257–268.

[60] M.R. Kaazempur-Mofrad, M. Bathe, H. Karcher, H.F. Younis, H.C. Seong, E.B. Shim, R.C. Chan, D.P. Hinton, A.G. Isasi, A. Upadhyaya, M.J. Powers, L.G. Griffiths, and R.D. Kamm. "Role of simulation in understanding biological systems". In: *Computers & structures* 81.8 (2003), pp. 715–726.

[61] G. Kanevce and S. Oka. "Correcting hot-wire readings for influence of fluid temperature variations". In: *DISA information* (1973), pp. 21–24.

[62] A. Karageorghis. "Conforming spectral methods for Poisson problems in cuboidal domains". In: *Journal of Scientific Computing* 9.3 (1994), pp. 341–350.

[63] L.L. Koenig, W.E. Mencl, and J.C. Lucero. "Multidimensional analyses of voicing offsets and onsets in female speakers". In: *Journal of the Acoustical Society of America* 118 (2005), p. 2535.

[64] R. Laje, T. Gardner, and G.B. Mindlin. "Continuous model for vocal fold oscillations to study the effect of feedback". In: *Physical Review E* 64.5 (2001), p. 056201.

[65] K.H. Lee, S.W. Baek, and K.W. Kim. "Inverse radiation analysis using repulsive particle swarm optimization algorithm". In: *International Journal of Heat and Mass Transfer* 51.11 (2008), pp. 2772–2783.

[66] J. Lekner. "Viscous flow through pipes of various cross-sections". In: *European Journal of Physics* 28.3 (2007), p. 521.

[67] S. Liu Z, X.G. Xu, F.F.J. Lim, X.Y. Luo, A. Hirtum, and N.A. Hill. "Modeling and Simulation of Human Upper Airway". In: *6th World Congress of Biomechanics (WCB 2010). August 1-6, 2010 Singapore*. Springer. 2010, pp. 686–689.

[68] Y. Liu, R.M.C. So, and C.H. Zhang. "Modeling the bifurcating flow in an asymmetric human lung airway". In: *Journal of Biomechanics* 36.7 (2003), pp. 951–959.

[69] R. Löhner, J. Cebral, O. Soto, P. Yim, and J.E. Burgess. "Applications of patient-specific CFD in medicine and life sciences". In: *International journal for numerical methods in fluids* 43.6-7 (2003), pp. 637–650.

[70] S. Lorthois, P.Y. Lagrée, J.P. Marc-Vergnes, and F. Cassot. "Maximal wall shear stress in arterial stenoses: application to the internal carotid arteries". In: *Journal of biomechanical engineering* 122.6 (2000), pp. 661–666.

[71] N.J.C. Lous, G.C.J. Hofmans, R.N.J. Veldhuis, and A. Hirschberg. "A Symmetrical Two-Mass Vocal-Fold Model Coupled to Vocal Tract and Trachea, with Application to Prosthesis Design". In: *Acta Acustica united with Acustica* 84.6 (1998), pp. 1135–1150.

[72] J.C. Lucero. "The minimum lung pressure to sustain vocal fold oscillation". In: *Journal of the Acoustical Society of America* 98 (1995), p. 779.

[73] J.C. Lucero, C. Louremco, N. Hermant, A. Van Hirtum, and X. Pelorson. "Effect of source-tract acoustical coupling on the oscillation onset of the vocal folds". In: *Journal of the Acoustical Society of America* 132.1 (May 2012), pp. 403–411.

[74] J.C. Lucero, A. Van Hirtum, N. Ruty, J. Cisonni, and X. Pelorson. "Validation of theoretical models of phonation threshold pressure with data from a vocal fold mechanical replica". In: *Journal of the Acoustical Society of America* 125 (2009), pp. 632–635.

[75] H. Luo, R. Mittal, X. Zheng, S.A. Bielamowicz, R.J. Walsh, and J.K. Hahn. "An immersed-boundary method for flow-structure interaction in biological systems with application to phonation". In: *Journal of computational physics* 227.22 (2008), pp. 9303–9332.

[76] X.Y. Luo. "Steady and unsteady flows in collapsible channels". In: *Advances in Biomechanics* (2001), pp. 192–199.

[77] X.Y. Luo, B.E. Griffith, X.S. Ma, M. Yin, T.J. Wang, C.L. Liang, P.N. Watton, and G.M. Bernacca. "Effect of bending rigidity in a dynamic model of a polyurethane prosthetic mitral valve". In: *Biomechanics and modeling in mechanobiology* 11.6 (2012), pp. 815–827.

[78] X.Y. Luo, J.S. Hinton, T.T. Liew, and K.K. Tan. "LES modelling of flow in a simple airway model". In: *Medical Engineering & Physics* 26.5 (2004), pp. 403–413.

[79] B.S. Ma and K.R. Lutchen. "An anatomically based hybrid computational model of the human lung and its application to low frequency oscillatory mechanics". In: *Annals of biomedical engineering* 34.11 (2006), pp. 1691–1704.

[80] X.S. Ma, H. Gao, B.E. Griffith, C. Berry, and X.Y. Luo. "Image-based fluid–structure interaction model of the human mitral valve". In: *Computers & Fluids* 71.0 (2013), pp. 417–425.

[81] H.M. Macdonald. "On the torsional strength of a hollow shaft". In: *Cambridge Philosophical Society* 8 (1893), pp. 62–68.

[82] T. Matsushima and P.S. Marcus. "A Spectral Method for Polar Coordinates". In: *Journal of Computational Physics* 120.2 (1995), pp. 365–374.

[83] D.M. McQueen and C.S. Peskin. "A three-dimensional computer model of the human heart for studying cardiac fluid dynamics". In: *ACM SIGGRAPH Computer Graphics* 34.1 (2000), pp. 56–60.

[84] M. Mihaescu, S. Murugappan, M. Kalra, S. Khosla, and E. Gutmark. "Large Eddy Simulation and Reynolds-Averaged Navier–Stokes modeling of flow in a realistic pharyngeal airway model: An investigation of obstructive sleep apnea". In: *Journal of biomechanics* 41.10 (2008), pp. 2279–2288.

[85] L.A. Miller and C.S. Peskin. "A computational fluid dynamics ofclap and fling'in the smallest insects". In: *Journal of Experimental Biology* 208.2 (2005), pp. 195–212.

[86] L.M. Milne-Thomson. *Theoretical Hydrodynamics 4th.* Dover Publications, 1962, p. 660.

[87] S. Mishra. "Repulsive particle swarm method on some difficult test problems of global optimization". In: *Available at SSRN 928538* (2006), p. 9.

[88] S. Mishra. "Some new test functions for global optimization and performance of repulsive particle swarm method". In: *Available at SSRN 926132* (2006).

[89] R. Moreno, F. Nicoud, L. Veunac, and H. Rousseau. "Non-linear-transformation-field to build moving meshes for patient specific blood flow simulations". In: *European Conference on Computational Fluid Dynamics, ECCOMAS CFD*. TU Delft The Netherlands. 2006.

[90] G. Mylavarapu, S. Murugappan, M. Mihaescu, M. Kalra, S. Khosla, and E. Gutmark. "Validation of computational fluid dynamics methodology used for human upper airway flow simulations". In: *Journal of Biomechanics* 42.10 (2009), pp. 1553–1559.

[91] S.S. Narayanan, A.A. Alwan, and K. Haker. "An articulatory study of fricative consonants using magnetic resonance imaging". In: *Journal of the Acoustical Society of America* 98 (1995), p. 1325.

[92] P. Nithiarasu, O. Hassan, K. Morgan, N.P. Weatherill, C. Fielder, H. Whittet, P. Ebden, and K.R. Lewis. "Steady flow through a realistic human upper airway geometry". In: *International journal for numerical methods in fluids* 57.5 (2008), pp. 631–651.

[93] P. Nithiarasu, C.B. Liu, and N. Massarotti. "Laminar and turbulent flow calculations through a model human upper airway using unstructured meshes". In: *Communications in Numerical Methods in Engineering* 23.12 (2007), pp. 1057–1069.

[94] E. Ozcan and C.K. Mohan. "Particle swarm optimization: surfing the waves". In: *Evolutionary Computation, 1999. CEC 99. Proceedings of the 1999 Congress on*. Vol. 3. IEEE. 1999, p. 5.

[95] T. Papanastasiou, G. Georgiou, and A.N. Alexandrou. *Viscous fluid flow*. CRC, 2000.

[96] K.E. Parsopoulos and M.N. Vrahatis. "Particle swarm optimization method in multiobjective problems". In: *Proceedings of the 2002 ACM symposium on Applied computing*. ACM. 2002, pp. 603–607.

[97] T.J. Pedley and X.Y. Luo. "Modelling flow and oscillations in collapsible tubes". In: *Theoretical and computational fluid dynamics* 10.1 (1998), pp. 277–294.

[98] X. Pelorson, A. Hirschberg, R. Van Hasselt, A. Wijnands, and Y. Auregan. "Theoretical and experimental study of quasisteady-flow separation within the glottis during phonation. Application to a modified two-mass model". In: *Journal of the Acoustical Society of America* 96.6 (1994), pp. 3416–3431.

[99] C.S. Peskin. "The immersed boundary method". In: *Acta numerica* 11.0 (2002), pp. 479–517.

[100] C.S. Peskin and D.M. McQueen. "Fluid dynamics of the heart and its valves". In: *American Physical Society* (1997), p. 309.

[101] N.A.V. Piercy, M.S. Hooper, and H.F. Winny. "Viscous flow through pipes with cores". In: *Philosophical Magazine Series 7* 15.99 (1933), pp. 647–676.

[102] I. Rahman, A.K. Das, R.B. Mankar, and B.D. Kulkarni. "Evaluation of repulsive particle swarm method for phase equilibrium and phase stability problems". In: *Fluid Phase Equilibria* 282.2 (2009), pp. 65–67.

[103] C. Renotte, V. Bouffioux, and F. Wilquem. "Numerical 3D analysis of oscillatory flow in the time-varying laryngeal channel". In: *Journal of Biomechanics* 33.12 (2000), pp. 1637–1644.

[104] N. Ruty, X. Pelorson, A. Van Hirtum, I. Lopez, and A. Hirschberg. "An in-vitro setup to test the relevance and the accuracy of low-order vocal folds models". In: *Journal of the Acoustical Society of America* 121.1 (2007), pp. 479–490.

[105] H. Schlichting and K. Gersten. *Boundary Layer Theory*. 7th. Berlin: Springer, 2000, p. 817.

[106] R.K. Shah and A.L. London. *Laminar flow forced convection in ducts : a source book for compact heat exchanger analytical data*. New York: Academic Press, 1978.

[107] A.H. Shapiro. "Steady flow in collapsible tubes". In: *Journal of Biomechanical Engineering* 99 (1977), p. 126.

[108] J. Shen. "A new fast Chebyshev–Fourier algorithm for Poisson-type equations in polar geometries". In: *Applied Numerical Mathematics* 33.1 (2000), pp. 183–190.

[109] P. Šidlof, O. Doaré, O. Cadot, and A. Chaigne. "Measurement of flow separation in a human vocal folds model". In: *Experiments in fluids* 51.1 (2011), pp. 123–136.

[110] K. Stevens. *Acoustic Phonetics*. London: MIT Press, 1998.

[111] P.S. Stewart, M. Heil, S.L. Waters, and O.E. Jensen. "Sloshing and slamming oscillations in a collapsible channel flow". In: *Journal of Fluid Mechanics* 662 (2010), p. 288.

[112] B.H. Story and I.R. Titze. "Voice simulation with a body-cover model of the vocal folds". In: *Journal of the Acoustical Society of America* 97 (1995), p. 1249.

[113] Y. Su. "Collocation spectral methods in the solution of poisson equation". PhD thesis. University of British Columbia, 1998.

[114] S.J. Sung, S.J. Jeong, Y.S. Yu, C.J. Hwang, and E.K. Pae. "Customized three-dimensional computational fluid dynamics simulation of the upper airway of obstructive sleep apnea". In: *The Angle Orthodontist* 76.5 (2006), pp. 791–799.

[115] G. Tabor, D. Tame, F. Pierron, P.G. Young, A. Watkinson, and J. Thompson. "Patient-specific arterial flow simulation with additional geometric elements". In: *European Conference on Computational Fluid Dynamics. The Netherlands*. Citeseer. 2006, pp. 1–12.

[116] C.A. Taylor, T.J.R. Hughes, and C.K. Zarins. "Finite element modeling of blood flow in arteries". In: *Computer methods in applied mechanics and engineering* 158.1 (1998), pp. 155–196.

[117] I.R. Titze. "The physics of small-amplitude oscillation of the vocal folds". In: *Journal of the Acoustical Society of America* 83 (1988), p. 1536.

[118] R. Torii, M. Oshima, T. Kobayashi, K. Takagi, and T.E. Tezduyar. "Computer modeling of cardiovascular fluid–structure interactions with the deforming-spatial-domain/stabilized space–time formulation". In: *Computer Methods in Applied Mechanics and Engineering* 195.13 (2006), pp. 1885–1895.

[119] L.N. Trefethen. *Spectral methods in MATLAB*. Vol. 10. Siam, 2000.

[120] A. Van Hirtum, J. Cisonni, and X. Pelorson. "On quasi-steady laminar flow separation in the upper airways". In: *Commun. Numer. Meth. Engng.* 25 (2009), pp. 447–461.

[121] A. Van Hirtum, J. Cisonni, N. Ruty, X. Pelorson, I. Lopez, and F. Van Uittert. "Experimental validation of some issues in lip and vocal folds physical models". In: *Acta Acustica united with Acustica* 93.2 (2007), pp. 314–323.

[122] A. Van Hirtum, X. Grandchamp, X. Pelorson, K. Nozaki, and S. Shimojo. "LES and in-vitro experimental validation of flow around a teeth-shaped obstacle". In: *International Journal of Applied Mechanics* 2.2 (2010), pp. 265–279.

[123] I.E. Vignon-Clementel, C. Alberto Figueroa, K.E. Jansen, and C.A. Taylor. "Outflow boundary conditions for three-dimensional finite element modeling of blood flow and pressure in arteries". In: *Computer methods in applied mechanics and engineering* 195.29 (2006), pp. 3776–3796.

[124] W.A. Wall and T. Rabczuk. "Fluid–structure interaction in lower airways of CT-based lung geometries". In: *International Journal for Numerical Methods in Fluids* 57.5 (2008), pp. 653–675.

[125] F.M. White. *Fluid mechanics 4ed.* McGraw-Hill, Singapore, 2002.

[126] F.M. White. *Viscous Fluid Flow.* 2nd. New York: McGraw-Hill, 1991.

[127] B. Wu, A. Van Hirtum, and X.Y. Luo. "Pressure driven steady flow in constricted channels of different cross section shapes". In: *International Journal of Applied Mechanics* 5.1 (2013), pp. 1–18.

[128] C. Xu, S.H. Sin, J.M. McDonough, J.K. Udupa, A. Guez, R. Arens, and D.M. Wootton. "Computational fluid dynamics modeling of the upper airway of children with obstructive sleep apnea syndrome in steady flow". In: *Journal of biomechanics* 39.11 (2006), pp. 2043–2054.

[129] X. Yang, R.H. Dillon, and L.J. Fauci. "An integrative computational model of multiciliary beating". In: *Bulletin of mathematical biology* 70.4 (2008), pp. 1192–1215.

[130] G. Yu, Z. Zhang, and R. Lessmann. "Fluid flow and particle diffusion in the human upper respiratory system". In: *Aerosol science and technology* 28.2 (1998), pp. 146–158.

[131] E. Yumoto, Y. Kadota, and T. Mori. "Vocal fold vibration viewed from the tracheal side in living human beings". In: *Otolaryngology - Head and Neck Surgery* 115.4 (1996), pp. 329 –334.

[132] L.T. Zhang, G.J. Wagner, and W.K. Liu. "Modelling and simulation of fluid structure interaction by meshfree and FEM". In: *Communications in numerical methods in engineering* 19.8 (2003), pp. 615–621.

Appendix A

Derivation of fully developed laminar viscous flow

A.1 Basic equation

For fully developed pressure-driven flow through a uniform channel with arbitrary but constant cross section shape, and under the assumptions of laminar, incompressible, parallel and steady viscous flow, the streamwise component of the momentum equation expressed in Cartesian coordinates (x, y, z) reduces to the following Poisson equation [9, 126]

$$\frac{1}{\mu}\frac{\partial P}{\partial x} = \left(\frac{\partial^2 u}{\partial y^2} + \frac{\partial^2 u}{\partial z^2}\right). \tag{A.1}$$

with driving pressure gradient dP/dx, velocity $u(y, z)$ and dynamic viscosity μ. The spanwise and transverse components of the momentum equation become,

$$\frac{\partial P}{\partial y} = 0, \quad \frac{\partial P}{\partial z} = 0, \tag{A.2}$$

and the continuity equation yields

$$\frac{\partial u}{\partial x} = 0. \tag{A.3}$$

In cylindrical coordinates (r, θ, x), and under the same assumptions, the Poisson equation (A.1) becomes

$$\frac{1}{\mu}\frac{dP}{dx} = \frac{1}{r}\frac{\partial}{\partial r}\left(r\frac{\partial u}{\partial r}\right) + \frac{1}{r^2}\frac{\partial^2 u}{\partial \theta^2}. \tag{A.4}$$

while the spanwise and transverse components of the momentum equation become,

$$\frac{\partial P}{\partial r} = 0, \quad \frac{\partial P}{\partial \theta} = 0. \tag{A.5}$$

A.2 Circle

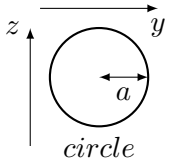

In cylindrical coordinates where the pipe radius is indicated by a and the length scale becomes $r^* = \frac{r}{a}$, the general equation can be rewritten as

$$u^* = -\frac{1}{4} r^{*2} + C_1 \ln r^* + C_2, \tag{A.6}$$

where the Laplace operator reduces to

$$\nabla^2 = \frac{1}{r}\frac{\partial}{\partial r}\left(r\frac{\partial}{\partial r}\right) + \frac{1}{r^2}\frac{\partial^2}{\partial \theta^2} + \frac{\partial^2}{\partial x^2} = \frac{1}{r}\frac{d}{dr}\left(r\frac{d}{dr}\right).$$

Since the velocity cannot be infinite at the centerline, on physical grounds, we reject the logarithm term and set $C_1 = 0$. The no slip condition $u^* = 0$ is satisfied by setting $C_2 = \frac{1}{4}$. The pipe solution is thus

$$u(r) = \frac{1}{4\mu}\left(-\frac{dP}{dx}\right)(a^2 - r^2). \tag{A.7}$$

The velocity distribution in fully developed laminar pipe flow is then a paraboloid of revolution about the centerline. The total volume flow rate Q is of interest, as defined for any duct by $\Phi = \int_A u dA$ where the element of area is $2\pi r dr$ for this pipe case. The integration is simple and yields

$$\Phi = \frac{\pi a^4}{8\mu}\left(-\frac{dP}{dx}\right). \tag{A.8}$$

From this the bulk velocity defined as $\bar{u} = \Phi/A$ gives

$$\bar{u} = \frac{a^2}{8\mu}\left(-\frac{dP}{dx}\right) = \frac{1}{2}u_{max}, \tag{A.9}$$

and the wall shear stress is given as

$$\tau_w = \mu \left(-\frac{du}{dr} \right)_w = \frac{a}{2} \left(-\frac{dP}{dx} \right) = \frac{4\mu\bar{u}}{a}. \tag{A.10}$$

A.3 Ellipse

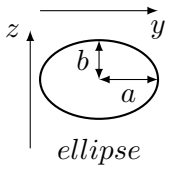

Elliptical cross section with axes (a, b) and the area $A = \pi ab$ defined as

$$\frac{y^2}{a^2} + \frac{z^2}{b^2} \leq 1,$$

and the solution of (A.1) is sought subject to the no slip boundary condition $u = 0$. We postulate the velocity profile to be the form

$$u(y, z) = A_c \left(1 - \frac{y^2}{a^2} - \frac{z^2}{b^2} \right). \tag{A.11}$$

Since it automatically satisfies the boundary condition for a elliptical cross section and determine A_c by substituting for u in (A.1) gives $A_c = \frac{1}{2\mu} \frac{a^2 b^2}{a^2 + b^2}$. Because the assumed form of u satisfies both the Poisson equation and the boundary condition, it's the correct and only solution possible[1]. So

$$u(y, z) = \frac{1}{2\mu} \left(-\frac{dP}{dx} \right) \frac{a^2 b^2}{a^2 + b^2} \left(1 - \frac{y^2}{a^2} - \frac{z^2}{b^2} \right). \tag{A.12}$$

Imposing $\frac{\partial u}{\partial y} = \frac{\partial u}{\partial z} = 0$ the maximum velocity is given as

$$u_{max}(y = z = 0) = \frac{1}{2\mu} \left(-\frac{dP}{dx} \right) \frac{a^2 b^2}{a^2 + b^2}. \tag{A.13}$$

Using the transformation $y = ar\cos\theta$, $z = br\sin\theta$ with the limits $r \in [0, 1]$, $\theta \in [0, 2\pi]$ the volume flow rate is given as

[1] The proof of uniqueness solution is followed at section A.3.1

$$\Phi = \int_A u dy dz = \frac{\pi}{4\mu}\left(-\frac{dP}{dx}\right)\frac{a^3 b^3}{a^2+b^2}, \tag{A.14}$$

From here it follows

$$\bar{u} = \frac{1}{4\mu}\left(-\frac{dP}{dx}\right)\frac{a^2 b^2}{a^2+b^2}. \tag{A.15}$$

For the wall shear stress, we need transform to an elliptical cylinder coordinate system with $y + iz = d\cosh(\xi + i\eta)$ and

$$\begin{aligned} y &= d\cosh\xi \cdot \cos\eta, \\ z &= d\sinh\xi \cdot \sin\eta, \end{aligned} \tag{A.16}$$

where $d = \sqrt{a^2 - b^2}$. The ellipse now be represented by $\xi = \xi_0 = \frac{1}{2}\log\frac{a+b}{a-b}$. Now we can convert (A.12) in Cartesian coordinates to (ξ, η) coordinate system via equations (A.16)

$$u(y,z) = \frac{d^2}{8\mu}\left(-\frac{dP}{dx}\right)\left(\cosh 2\xi_0 - \cosh 2\xi - \cos 2\eta + \frac{\cosh 2\xi \cos 2\eta}{\cosh 2\xi_0}\right). \tag{A.17}$$

Consider the different geometry of the elliptical cylinder coordinate system, the elemental arc length in the (ξ, η) directions are given as

$$\begin{aligned} d_{s_\eta} &= \left[\frac{\partial y}{\partial \eta}^2 + \frac{\partial z}{\partial \eta}^2\right]^{\frac{1}{2}} d\eta = \delta d\eta, \\ d_{s_\xi} &= \left[\frac{\partial y}{\partial \xi}^2 + \frac{\partial z}{\partial \xi}^2\right]^{\frac{1}{2}} d\xi = \delta d\xi, \end{aligned} \tag{A.18}$$

respectively, where $\delta = d[\cosh^2\xi - \cos^2\eta]^{\frac{1}{2}}$. As we know the wall shear stress is given as

$$\tau_{w_0}(\eta) = -\mu\left(\frac{\partial u}{\partial n}\right)_{\partial D}, \tag{A.19}$$

where ∂D represents the boundary of the region D and n is an outward normal from the boundary. We have $dn = \delta d\xi$ so that the wall shear stress can be written as

$$\tau_{w_0}(\eta) = -\frac{\mu}{\delta}\left(\frac{\partial u}{\partial \xi}\right)_{\xi=\xi_0}. \tag{A.20}$$

Substituting the (A.17) into (A.20) the wall shear stress is found that

$$\tau_{w_0}(\eta) = \frac{d}{4\sqrt{\cosh^2\xi_0 - \cos^2\eta}}\left(-\frac{dP}{dx}\right)(\sinh 2\xi_0 - \tanh 2\xi_0 \cos 2\eta)\,, \tag{A.21}$$

The expression of wall shear stress can be converting back to Cartesian coordinate by using equations (A.16), the wall shear stress then becomes

$$\tau_{w_0}(y_1, z_1) = \left(-\frac{dP}{dx}\right)\frac{a^2b^2}{a^2+b^2}\sqrt{\frac{y^2}{a^4}+\frac{z^2}{b^4}}. \tag{A.22}$$

Here the set of (y_1, z_1) correspond to those which define the elliptical boundary.

A.3.1 Proof of the uniqueness of solution

Suppose that there exist two solutions u_1 and u_2 that satisfies (A.1) and the prescribed boundary condition, i.e.,

$$\begin{aligned} \nabla^2 u_1 &= \frac{1}{\mu}\frac{dP}{dx}, \\ u_1 &= 0, \quad on \text{ boundary} \end{aligned} \tag{A.23}$$

and

$$\begin{aligned} \nabla^2 u_2 &= \frac{1}{\mu}\frac{dP}{dx}, \\ u_2 &= 0. \quad on \text{ boundary} \end{aligned} \tag{A.24}$$

From these we know that the function $u = u_1 - u_2$ satisfies

$$\begin{aligned} \nabla^2 u &= 0, \\ u &= 0. \; on \text{ boundary} \end{aligned} \tag{A.25}$$

Using the identity

$$\int_s u(\nabla u \cdot n)ds = \int_A (\nabla u \cdot \nabla u)dA + \int_A u\nabla^2 u dA, \tag{A.26}$$

with s means on the boundary. Substitutes this in u and gives $\int_A (\nabla u \cdot \nabla u) dA = 0$ which implies that $\nabla u = 0$, thus $u = const.$ But since $u = 0$ on the boundary we have $u_1 \equiv u_2$ everywhere which yields the desired result.

A.4 Rectangle

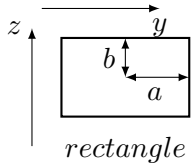

The rectangular cross section with axes (a, b) and the area $A = 4ab$ defined with $|y| \leq a$, $|z| \leq b$. Taking into account the symmetry with respect to the planes $y = 0$, $z = 0$, the flow can studied only in the first quadrant. The boundary condition can be rewritten as follows

$$\begin{cases} \frac{\partial u}{\partial y} = 0, & y = 0, \\ u = 0, & y = a \\ \frac{\partial u}{\partial z} = 0, & z = 0, \\ u = 0, & z = b. \end{cases} \tag{A.27}$$

(A.1) can be transformed into Laplace equation by setting

$$u(y, z) = u_1(y, z) + \frac{1}{2\mu} \frac{dP}{dx}(z^2 - b^2). \tag{A.28}$$

The second term in the right hand side of (A.28) is just the Poiseuille flow profile between two infinite plates at $z = \pm b$. Substitutes (A.28) into (A.1) and (A.27) it gives

$$\frac{\partial^2 u_1}{\partial y^2} + \frac{\partial^2 u_1}{\partial z^2} = 0, \tag{A.29}$$

subjected to

$$\begin{cases} \frac{\partial u_1}{\partial y} = 0, & y = 0, \\ u_1 = \frac{1}{2\mu} \frac{dP}{dx}(b^2 - z^2), & y = a, \\ \frac{\partial u_1}{\partial z} = 0, & z = 0, \\ u_1 = 0, & z = b. \end{cases} \tag{A.30}$$

The above problem can be solved using separation of variables setting $u_1(y, z) = u_y \cdot u_z$. (A.29) gives

$$\begin{aligned} u_y'' - \lambda u_y = 0, \\ u_z'' + \lambda u_z = 0. \end{aligned} \tag{A.31}$$

Solutions of (A.31) then can be got

$$\begin{aligned} u_{y,k} = c_k e^{\frac{(2k-1)\pi}{2b}y} + d_k e^{-\frac{(2k-1)\pi}{2b}y}, \\ u_{z,k} = A\cos\left(\frac{(2k-1)\pi}{2b}z\right). \end{aligned} \tag{A.32}$$

Then the special solution of (A.29) is

$$u_{1k}(y,z) = \left(c_k e^{\frac{(2k-1)\pi}{2b}y} + d_k e^{-\frac{(2k-1)\pi}{2b}y}\right) \cdot \cos\left(\frac{(2k-1)\pi}{2b}z\right). \tag{A.33}$$

So the general solution of (A.29) is

$$u_{1k}(y,z) = \sum_{k=1}^{\infty}\left(c_k e^{\frac{(2k-1)\pi}{2b}y} + d_k e^{-\frac{(2k-1)\pi}{2b}y}\right) \cdot \cos\left(\frac{(2k-1)\pi}{2b}z\right). \tag{A.34}$$

Using other two boundary conditions

$$\begin{cases} \frac{\partial u_y}{\partial y} = 0, \quad y = 0, \\ u_y = \frac{1}{2\mu}\frac{dP}{dx}(b^2 - z^2)/u_z, \quad y = a, \end{cases} \tag{A.35}$$

which gives

$$\begin{cases} c_k = d_k, \\ \sum\limits_{k=1}^{\infty} 2c_k \cosh\left(\frac{(2k-1)\pi}{2b}a\right) \cdot \cos\left(\frac{(2k-1)\pi}{2b}z\right) = \frac{1}{2\mu}\frac{dP}{dx}(b^2 - z^2). \end{cases} \tag{A.36}$$

The pivotal point in the analysis is the determination of the C_k. Because $\cos\left(\frac{(2k-1)\pi}{2b}z\right)$ forms a complete orthogonal set, as a first approach it is natural to consider the methods of Fourier series. By multiply other item $\cos\left(\frac{(2m-1)\pi}{2b}z\right)$ in orthogonal set and integral with the limits $[-b, b]$, we get

$$c_k = \frac{8b^2}{\mu}\left(-\frac{dP}{dx}\right)\frac{(-1)^k}{(2k-1)^3\pi^3}\frac{1}{\cosh\left(\frac{(2k-1)\pi}{2b}a\right)}. \tag{A.37}$$

Then general (A.29) becomes

$$u_1(y,z) = \sum_{k=1}^{\infty}\frac{16b^2}{\mu}\left(-\frac{dP}{dx}\right)\frac{(-1)^k}{(2k-1)^3\pi^3}\frac{\cosh\left(\frac{(2k-1)\pi}{2b}y\right)}{\cosh\left(\frac{(2k-1)\pi}{2b}a\right)}\cdot\cos\left(\frac{(2k-1)\pi}{2b}z\right). \tag{A.38}$$

Finally, with the substituting (A.38) let $i = 2k-1$, there is obtained that

$$u(y,z) = \frac{1}{2\mu}\left(-\frac{dP}{dx}\right)\left[b^2 - z^2 - \frac{32b^2}{\pi^3}\sum_{i=1,3,\ldots}^{\infty}(-1)^{(i-1)/2}\frac{\cosh(\frac{i\pi y}{2b})}{\cosh(\frac{i\pi a}{2b})}\frac{\cos(\frac{i\pi z}{2b})}{i^3}\right]. \tag{A.39}$$

The other same results can be also obtained

$$u(y,z) = \frac{16a^2}{\mu\pi^3}\left(-\frac{dP}{dx}\right)\sum_{i=1,3,\ldots}^{\infty}(-1)^{(i-1)/2}\left[1 - \frac{\cosh(\frac{i\pi z}{2a})}{\cosh(\frac{i\pi b}{2a})}\right]\frac{\cos(\frac{i\pi y}{2a})}{i^3}. \tag{A.40}$$

The volume flow rate defined as $\Phi = \int_A u(y,z)dA$ gives

$$\Phi = \frac{4a^3}{3\mu}\left(-\frac{dP}{dx}\right)\left[b - \frac{192a}{\pi^5}\sum_{i=1,3,\ldots}^{\infty}\frac{\tanh(i\pi b/2a)}{i^5}\right]. \tag{A.41}$$

From this it follows that the velocity

$$\bar{u} = \frac{a^2}{3\mu}\left(-\frac{dP}{dx}\right)\left[1 - \frac{192a}{\pi^5 b}\sum_{i=1,3,\ldots}^{\infty}\frac{\tanh(i\pi b/2a)}{i^5}\right], \tag{A.42}$$

$$u_{max}(y=z=0) = \frac{16a^2}{\mu\pi^3}\left(-\frac{dP}{dx}\right)\sum_{i=1,3,\ldots}^{\infty}\frac{(-1)^{(i-1)/2}}{i^3}\left[1 - \frac{1}{\cosh(\frac{i\pi b}{2a})}\right], \tag{A.43}$$

and the wall shear stress are

$$\tau(z, y = \pm a) = -\frac{8a}{\pi^2}\left(-\frac{dP}{dx}\right)\sum_{i=1,3,\ldots}^{\infty}\frac{(-1)^{(i-1)/2}}{i^2}\left[1 - \frac{\cosh(\frac{i\pi z}{2a})}{\cosh(\frac{i\pi b}{2a})}\right], \tag{A.44}$$

$$\tau(y, z = \pm b) = -\frac{8a}{\pi^2}\left(-\frac{dP}{dx}\right)\sum_{i=1,3,\ldots}^{\infty}(-1)^{(i-1)/2}\left[\tanh(\frac{i\pi b}{2a})\right]\frac{\cos(\frac{i\pi y}{2a})}{i^2}. \tag{A.45}$$

A.5 Equilateral triangle

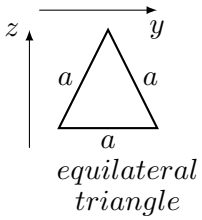

equilateral triangle

Equilateral triangle cross section with axes a and the area $A = \frac{\sqrt{3}a^2}{4}$ defined with the following three boundaries

$$\begin{aligned} 2z - \sqrt{3}a &= 0, \\ \sqrt{3}y - z &= 0, \\ \sqrt{3}y + z &= 0. \end{aligned} \tag{A.46}$$

Since the velocity profile $u(y, z)$ is zero on the boundaries, the following solution form for (A.1) is prompted,

$$u(y, z) = A_c\left(\sqrt{3}y - z\right)\left(\sqrt{3}y + z\right)\left(2z - \sqrt{3}a\right), \tag{A.47}$$

where A_c is a constant to be determined. It turns out that the solution of (A.1) is satisfied provided that $A_c = \frac{1}{4\sqrt{3}a\mu}\left(-\frac{dP}{dx}\right)$. Thus, the velocity profile is given by

$$u(y, z) = \frac{1}{4\sqrt{3}}\left(-\frac{dP}{dx}\right)\frac{1}{a\mu}\left(\sqrt{3}y - z\right)\left(\sqrt{3}y + z\right)\left(2z - \sqrt{3}a\right). \tag{A.48}$$

The proof of uniqueness solution is already described in section A.3.1. Since the assumed from of u satisfies both the Poisson equation and the boundary condition, it is the correct and only solution possible. Then the volume flow rate defined by $\Phi = \int_A u(y, z)dA$ gives

$$\Phi = \int_0^{\frac{\sqrt{3}a}{2}} dz \int_{-\frac{\sqrt{3}z}{3}}^{\frac{\sqrt{3}z}{3}} u(y,z)dy = \frac{\sqrt{3}a^4}{320\mu}\left(-\frac{dP}{dx}\right). \tag{A.49}$$

From this it follows that the velocity

$$\bar{u} = \frac{a^2}{80\mu}\left(-\frac{dP}{dx}\right), \tag{A.50}$$

$$u_{max}\left(y=0, z=\frac{\sqrt{3}a}{3}\right) = \frac{a^2}{36\mu}\left(-\frac{dP}{dx}\right), \tag{A.51}$$

and the wall shear stress are

$$\tau_w(z=\frac{\sqrt{3}a}{2}) = \frac{\sqrt{3}}{2a}\left(-\frac{dP}{dx}\right)\left(\frac{a^2}{4}-y^2\right), \tag{A.52}$$

$$\tau_w(y=\frac{\sqrt{3}z}{3}) = \frac{1}{a}\left(-\frac{dP}{dx}\right)z\left(\frac{\sqrt{3}a}{2}-z\right). \tag{A.53}$$

A.6 Circular sector

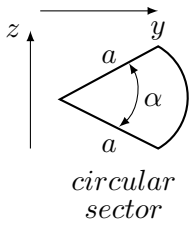

circular sector

For circular sector it is convenient to analysis by considering the Poisson equation (A.4) in cylindrical coordinates. In approaching the task of solving this equation perhaps the most reasonable beginning is to reduce it to Laplace equation, which is the most familiar and perhaps best understood of any partial differential equation. Thus there is introduced a reduced velocity u^*

$$u = u^* + \frac{r^2}{4\mu}\frac{dP}{dx}. \tag{A.54}$$

After substituting in (A.4) one finds that u must satisfy Laplace equation

$$\frac{\partial^2 u^*}{\partial r^2} + \frac{1}{r}\frac{\partial u^*}{\partial r} + \frac{1}{r^2}\frac{\partial^2 u^*}{\partial^2 \theta} = 0. \tag{A.55}$$

Using the separation of variables method of the form $u^* = R(r) \cdot \Phi(\theta)$ gives

$$\frac{\partial^2 \Phi(\theta)}{\partial \theta^2} + k\Phi(\theta) = 0, \tag{A.56}$$

$$\frac{r^2}{R(r)}\frac{\partial^2 R(r)}{\partial r^2} + \frac{r}{R(r)}\frac{\partial R(r)}{\partial r} = k. \tag{A.57}$$

For (A.56) the solution is obtained as follows

$$\Phi_n(\theta) = A_n \cos\sqrt{k}\theta. \tag{A.58}$$

For (A.57) let $t = \ln r$ which gives

$$\frac{d^2 R}{dt^2} - kR = 0. \tag{A.59}$$

Thus the general solution for $R(r)$ is

$$R_n(r) = C_n e^{\sqrt{k}t} + D_n e^{-\sqrt{k}t} = C_n r^{\sqrt{k}} + D_n r^{-\sqrt{k}}. \tag{A.60}$$

Therefore the general solution of u^*

$$u^* = A_0 + \sum_{n=1}^{\infty} \left(A_n r^{\sqrt{k}} + B_n r^{-\sqrt{k}} \right) \cos(\sqrt{k}\theta). \tag{A.61}$$

If one utilizes the fact that velocity is infinite at $r = 0$ then $B_n = 0$. The remaining constants are determined by imposing the condition that $u = 0$ on all boundaries. To satisfy this requirement at $r = 0$ it is necessary that $A_0 = 0$. Thus

$$u^* = \sum_{n=1}^{\infty} A_n r^{\sqrt{k}} \cos(\sqrt{k}\theta), \tag{A.62}$$

Substitutes the resulting expression for u^* into (A.54), there is obtained

$$u = \frac{r^2}{4\mu}\frac{dP}{dx} + \sum_n A_n r^k \cos(k\theta). \tag{A.63}$$

When one applies (A.63) on the oblique sides $\theta = \pm\frac{\alpha}{2}$

$$0 = \frac{r^2}{4\mu}\frac{dP}{dx} + \sum_n A_n r^k \cos\left(\frac{k\theta}{2}\right). \tag{A.64}$$

This may be satisfied by taking $\cos\left(\frac{k\alpha}{2}\right) = 0$, from which it follows that $k = \frac{(2n-1)\pi}{\alpha}, n = 1, 2, ..., \infty$. And in order to cancel the term $\frac{r^2}{4\mu}\frac{dP}{dx}$ it is necessary to take $k = 2$ and

$$A_{k=2} = \frac{1}{4\cos(\alpha)}\left(-\frac{1}{\mu}\frac{dP}{dx}\right), \tag{A.65}$$

with these the velocity solution (A.63) becomes

$$u/\left(-\frac{1}{4\mu}\frac{dP}{dx}\right) = r^2\left(\frac{\cos(2\theta)}{\cos(\alpha)} - 1\right) + \sum_{n=1}^{\infty} A_n r^{\frac{(2n-1)\pi}{\alpha}} \cos\left(\frac{(2n-1)\pi\theta}{\alpha}\right). \tag{A.66}$$

The set of constants A_n, still remains to be found, and for this there is available the condition that $u = 0$ ar $r = a$. The introduction of this into (A.66) and the setting of $u = 0$ leads to

$$\left(1 - \frac{\cos(2\theta)}{\cos(\alpha)}\right) = \sum_{n=1}^{\infty} C_n \cos\left(\frac{(2n-1)\pi\theta}{\alpha}\right), \tag{A.67}$$

where the C_n, are the dimensionless counterparts of the constants A_n, that is

$$C_n = A_n a^{\frac{(2n-1)\pi}{\alpha}-2}. \tag{A.68}$$

Consider the orthogonality of function $\cos\left(\frac{(2n-1)\pi\theta}{\alpha}\right)$ and integral with the limits $[-\frac{\alpha}{2}, \frac{\alpha}{2}]$ we have

$$C_n = (-1)^{(i+1)/2}\frac{16\alpha^2}{\pi^3}\frac{1}{i(i+\frac{2\alpha}{\pi})(i-\frac{2\alpha}{\pi})},\ i = 1, 3, ..., \infty. \tag{A.69}$$

Finally, with the substituting (A.68) and (A.69) we get

$$u(r,\theta)=\frac{1}{4\mu}\left(\frac{dP}{dx}\right)\left[r^2\left(1-\frac{\cos 2\theta}{\cos\alpha}\right)-\frac{16a^2\alpha^2}{\pi^3}\sum_{i=1,3,\ldots}^{\infty}(-1)^{\frac{i+1}{2}}\left(\frac{r}{a}\right)^{\frac{i\pi}{\alpha}}\frac{\cos\left(i\pi\theta/\alpha\right)}{i(i+2\alpha/\pi)(i-2\alpha/\pi)}\right]. \tag{A.70}$$

It is convenient to calculate the volume flow rate Φ which passes through the cross section $\Phi=\int_A urdrd\theta$ so that

$$\Phi=\frac{a^4}{4\mu}\left(-\frac{dP}{dx}\right)\left[\frac{\tan\alpha-\alpha}{4}-\frac{32\alpha^4}{\pi^5}\sum_{i=1,3,\ldots}^{\infty}\frac{1}{i^2(i+2\alpha/\pi)^2(i-2\alpha/\pi)}\right]. \tag{A.71}$$

From this it follows that the mean velocity with the area $A=\frac{\alpha a^2}{2}$ is

$$\bar{u}=\frac{\Phi}{A}=\frac{a^2}{2\mu\alpha}\left(-\frac{dP}{dx}\right)\left[\frac{\tan\alpha-\alpha}{4}-\frac{32\alpha^4}{\pi^5}\sum_{i=1,3,\ldots}^{\infty}\frac{1}{i^2(i+2\alpha/\pi)^2(i-2\alpha/\pi)}\right], \tag{A.72}$$

and the wall shear stress are

$$\tau\left(\theta=\pm\frac{\alpha}{2}\right)=\frac{1}{4}\left(-\frac{dP}{dx}\right)\left[r^2\left(1+2\tan\alpha\right)+\frac{16a^2\alpha}{\pi^2}\sum_{i=1,3,\ldots}^{\infty}\left(\frac{r}{a}\right)^{\frac{i\pi}{\alpha}}\frac{1}{(i+2\alpha/\pi)(i-2\alpha/\pi)}\right] \tag{A.73}$$

$$\tau(r=a)=\frac{a}{2}\left(-\frac{dP}{dx}\right)\left[1-\frac{\cos 2\theta}{\cos\alpha}-\frac{8\alpha}{\pi^2}\sum_{i=1,3,\ldots}^{\infty}-i^{\frac{i+1}{2}}\frac{\cos\left(i\pi\theta/\alpha\right)}{(i+2\alpha/\pi)(i-2\alpha/\pi)}\right] \tag{A.74}$$

A.7 Concentric annulus

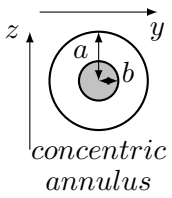

Consider the general (A.1) for concentric annulus we have

$$u = \frac{r^2}{4\mu}\frac{dP}{dx} + C_1 \ln r + C_2. \tag{A.75}$$

Impose the boundary conditions the solution in concentric annulus is thus

$$u = \frac{1}{4\mu}\left(-\frac{dP}{dx}\right)\left[a^2 - r^2 + (a^2 - b^2)\frac{\ln(a/r)}{\ln(b/a)}\right]. \tag{A.76}$$

The volume flow rate Φ then gives

$$\Phi = \frac{\pi}{8\mu}\left(-\frac{dP}{dx}\right)\left[a^4 - b^4 - \frac{(a^2 - b^2)^2}{\ln(a/b)}\right]. \tag{A.77}$$

From this it follows that the mean velocity with the area $A = \pi(a^2 - b^2)$ is

$$\bar{u} = \frac{1}{8\mu}\left(-\frac{dP}{dx}\right)\left[a^2 + b^2 - \frac{(a^2 - b^2)}{\ln(a/b)}\right], \tag{A.78}$$

and the wall shear stress are

$$\tau(r = b) = -\frac{1}{4}\left(-\frac{dP}{dx}\right)\left[2b + \frac{(a^2 - b^2)}{b\ln(b/a)}\right], \tag{A.79}$$

$$\tau(r = a) = \frac{1}{4}\left(-\frac{dP}{dx}\right)\left[2a + \frac{(a^2 - b^2)}{a\ln(b/a)}\right]. \tag{A.80}$$

A.8 Eccentric annulus

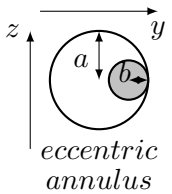

For eccentric annulus the general equation (A.1) may be arranged as

$$\nabla^2\left(\Psi + \frac{1}{4\mu}\frac{dP}{dx}(y^2 + z^2)\right) = \frac{1}{\mu}\frac{\partial P}{\partial x}, \tag{A.81}$$

where Ψ is a plane harmonic function $\nabla^2\Psi = 0$. The boundary $u = 0$ leads to $\Psi = -\frac{1}{4\mu}\frac{dP}{dx}(y^2 + z^2) + d$, where d is an arbitrary constant which will not be the same for the two bounding circles. Let the y-axis contain the centers of pipe and core, of radii a and b respectively, and distant c apart.

Using complex-variable technique, exact solutions can be obtained if the cross section can mapped conformal onto a region where Laplace equation has a known solution. The present case of an eccentric annulus can be mapped by the transformation

$$W = y + iz = M \tan \frac{1}{2}\zeta,\ \zeta = \xi + \eta, \tag{A.82}$$

onto a concentric annulus, where the solution is known, (A.76). The inner and outer boundaries are described by $\eta = \beta$ and α, respectively. In the new (ξ, η) coordinate system, it is necessary to solve

$$\left(\frac{\partial^2\Psi}{\partial\xi^2} + \frac{\partial^2\Psi}{\partial\eta^2}\right) = 0. \tag{A.83}$$

Since $W = M\frac{\sin\xi + i\sinh\eta}{\cosh\eta + \cos\xi}$, so that

$$\begin{gathered} y = M\frac{\sin\xi}{\cosh\eta + \cos\xi},\quad z = M\frac{\sinh\eta}{\cosh\eta + \cos\xi}, \\ M = \sqrt{\frac{(c^2 - (a+b)^2)\,(c^2 - (a-b)^2)}{4c^2}}, \end{gathered} \tag{A.84}$$

In this system the outer and inner cylinders are $\eta = \alpha$ and $\eta = \beta$ respectively, where α and β are constants given by $\sinh\alpha = M/a$, $\sinh\beta = M/b$. Referred to the Cartesian coordinate system (x, y, z), the axes of the cylinders are the lines $(M\coth\alpha, 0)$ and $(M\coth\beta, 0)$ respectively. Thus the distance between their centers is $c = M(\coth\alpha - \coth\beta)$. Then the (A.82) subject to $\Psi = \Psi_1 \cdot (-\frac{dP}{dx})\frac{1}{\mu}$ with

$$\Psi_1 = \frac{M^2}{4\mu}\left(\frac{2\cosh\eta}{\cosh\eta + \cos\xi} - 1\right) + d,\ \eta = \alpha, \beta. \tag{A.85}$$

Using the Fourier expansion

$$\frac{\cosh\eta}{\cosh\eta + \cos\xi} = \coth\eta \cdot \left(1 + 2\sum_{n=1}^{\infty}(-1)^n e^{-n\eta}\cos n\xi\right). \tag{A.86}$$

(A.85) may be rewritten as

$$\Psi_1 = \frac{M^2}{2\mu}\coth\eta\sum_{n=1}^{\infty}(-1)^n e^{-n\eta}\cos n\xi + const, \eta = \alpha, \beta. \tag{A.87}$$

Assume

$$\Psi_1 = \sum_{n=1}^{\infty}(-1)^n\left(A_n e^{-n\eta} + B_n e^{n\eta}\right)\cos n\xi. \tag{A.88}$$

Using the orthogonality property we have

$$\begin{aligned} A_n &= M^2\frac{\coth\alpha e^{-2n\alpha} - \coth\beta e^{-2n\beta}}{e^{-2n\alpha} - e^{-2n\beta}}, \\ B_n &= M^2\frac{\coth\alpha - \coth\beta}{e^{-2n\alpha} - e^{-2n\beta}}. \end{aligned} \tag{A.89}$$

Therefore

$$\Psi_1 = M^2\sum_{n=1}^{\infty}(-1)^n\frac{e^{-n\beta}\coth\beta\sinh\left(n(\eta-\alpha)\right) - e^{-n\alpha}\coth\alpha\sinh\left(n(\eta-\beta)\right)}{\sinh\left(n(\beta-\alpha)\right)}\cos\left(n\xi\right), \tag{A.90}$$

where α, β are the values of η on the outer and inner boundaries respectively, which satisfies $\left(\frac{\partial^2\Psi_1}{\partial\xi^2} + \frac{\partial^2\Psi_1}{\partial\eta^2}\right) = 0$ and makes $\Psi_1 = -\frac{1}{4\mu}\frac{dP}{dx}(y^2+z^2)+d$ constant when $\eta = \alpha$ or β. Inspection of (A.81) shows that

$$u = \frac{M^2}{\mu}\left(-\frac{dP}{dx}\right)\left[\frac{\Psi_1}{M^2} + A\eta + B - \frac{\cosh\eta - \cos\xi}{4(\cosh\eta + \cos\xi)}\right], \tag{A.91}$$

where A and B are constants, will satisfy (A.81), since the first three terms within the brackets form a plane harmonic function in the ζ-plane which transforms into a plane harmonic function in the W-plane. On the boundaries Ψ is readily shown to be given by

$$\Psi_1 = \frac{M^2}{2}\left(\frac{\cosh\eta}{\cosh\eta + \cos\xi} - \coth\eta\right), \tag{A.92}$$

so that on the boundaries

$$u = \frac{M^2}{\mu}\left(-\frac{dP}{dx}\right)\left(A\eta + B - \frac{1}{2}\coth\eta + \frac{1}{4}\right), \tag{A.93}$$

and substituting α, β in turn for η, yields two equations for A and B, which together gives

$$\begin{aligned} A &= \frac{\coth\alpha - \coth\beta}{2(\alpha-\beta)}, \\ B &= \frac{\beta(1-2\coth\alpha) - \alpha(1-2\coth\beta)}{4(\alpha-\beta)}, \end{aligned} \tag{A.94}$$

and (A.91) is then completely determined.

The volume flow rate evaluated by $\Phi = 2\int_0^\pi \int_\alpha^\beta u \cdot |\frac{dW}{d\zeta}| d\xi d\eta$ is obtained

$$\Phi = \frac{\pi}{8\mu}\left(-\frac{dP}{dx}\right)\left[a^4 - b^4 - \frac{4c^2M^2}{\beta-\alpha} - 8c^2M^2\sum_{n=1}^{\infty}\frac{ne^{-n(\beta+\alpha)}}{\sinh(n\beta - n\alpha)}\right], \tag{A.95}$$

where

$$\begin{aligned} M = \left(F^2 - a^2\right)^{1/2}, \quad F &= \frac{a^2 - b^2 + c^2}{2c}, \\ \alpha = \frac{1}{2}\ln\frac{F+M}{F-M}, \quad \beta &= \frac{1}{2}\ln\frac{F-c+M}{F-c-M}, \end{aligned}$$

$\eta = \alpha$ and $\eta = \beta$ being the outer bounding circle and inner bounding circle, respectively.

From this it follows that the mean velocity with area $A = \pi(a^2 - b^2)$ is

$$\bar{u} = \frac{1}{8\mu}\left(-\frac{dP}{dx}\right)\left[\frac{a^4 - b^4 - \frac{4c^2M^2}{\beta-\alpha} - 8c^2M^2\sum\limits_{n=1}^{\infty}\frac{ne^{-n(\beta+\alpha)}}{\sinh(n\beta-n\alpha)}}{a^2-b^2}\right], \tag{A.96}$$

and the wall shear stress are

$$\tau_1 = \sum_{n=1}^{\infty}(-1)^n n\frac{e^{-n\beta}\coth\beta\cosh(n(\eta-\alpha)) - e^{-n\alpha}\coth\alpha\cosh(n(\eta-\beta))}{\sinh(n(\beta-\alpha))}\cos(n\xi), \tag{A.97}$$

$$\tau = \frac{M^2}{\mu}\left(-\frac{dP}{dx}\right)\left[\tau_1 + \frac{\coth\alpha - \coth\beta}{2(\alpha-\beta)} - \frac{\sinh\eta\cos\xi}{2(\cosh\eta+\cos\xi)^2}\right], \tag{A.98}$$

substituting the boundary $\eta = \alpha$ and $\eta = \beta$ the wall shear stress at radius $r = a$ and $r = b$ are obtained.

A.9 Half moon

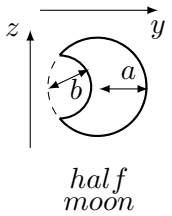

half moon

Recall the basic equation in cylindrical coordinates.

$$\frac{dP}{dx} = \mu\left(\frac{\partial^2 u}{\partial r^2} + \frac{1}{r}\frac{\partial u}{\partial r} + \frac{1}{r^2}\frac{\partial^2 u}{\partial \theta^2}\right). \tag{A.99}$$

If (A.99) can be solved subject to the no-slip condition that u is zero on all duct boundaries, then all flow quantities of interest can be determined. Consider the two boundary conditions $(y-a)^2 + z^2 = a^2$ in inner circle and $y^2 + z^2 = b^2$ of outer circle and the corresponding equations in polar coordinate give $r = 2a\cos\theta$ and $r = b$, respectively. The domain is thus $\theta \in [-\arccos(\frac{b}{2a}),\ \arccos(\frac{b}{2a})]$. Normally we can postulate the solution to be the form

$$u(r,\theta) = B(r-b)\left(2a\cos\theta - r\right), \tag{A.100}$$

$$u(r,\theta) = B(r-b)\left(\frac{2a\cos\theta}{r} - 1\right), \tag{A.101}$$

$$u(r,\theta) = B(r^2-b^2)\left(2a\cos\theta - r\right), \tag{A.102}$$

$$u(r,\theta) = B(r^2-b^2)\left(\frac{2a\cos\theta}{r} - 1\right). \tag{A.103}$$

For (A.100) to (A.102) it can be validated that $\nabla u \neq const$ so that are not correct solution. Consider the (A.103) it gives $\nabla u = B = \frac{1}{\mu}(-\frac{dP}{dx})$. Since the uniqueness solution of such problem already been done in section (A.3.1), it's the correct and only solution possible. Thus, we obtain that

$$u = \frac{1}{4\mu}\left(-\frac{dP}{dx}\right)\left(r^2-b^2\right)\left(\frac{2a\cos\theta}{r} - 1\right), \tag{A.104}$$

when $\frac{\partial u}{\partial r} = \frac{\partial u}{\partial \theta} = 0$ which gives $\theta = 0$ and $r^3 - ar^2 - ab^2 = 0$, then the maximum velocity is got from the root of cubic equations. Obviously, the position of maximum velocity depend on the radius ratio b/a. The volume flow rate defined by $\Phi = \int_{-\theta_1}^{\theta_1}\int_b^{2a\cos\theta} u dr d\theta$, $\theta_1 = \arccos\left(\frac{b}{2a}\right)$ gives

$$\Phi = \frac{1}{4\mu}\left(-\frac{dP}{dx}\right)\left[(2a^3b + \frac{21}{12}ab^3)\sin\theta_1 + (a^4 - \frac{b^4}{2} - 2a^2b^2)\theta_1\right], \tag{A.105}$$

From this it follows that the mean velocity can be obtained by $\bar{u} = \frac{\Phi}{A}$ with $A = a^2\left(\pi - \theta_2 + \frac{1}{2}\sin(2\theta_2)\right) - \frac{1}{2}b^2(\pi - \theta_2 - \sin\theta_2)$ while $\theta_2 = 2\arcsin\left(\frac{b}{2a}\right)$. And the wall shear stress are

$$\tau(r = b) = -\frac{1}{4}\left(-\frac{dP}{dx}\right)(4a\cos\theta - 2b), \tag{A.106}$$

$$\tau(r = 2a\cos\theta) = \frac{1}{4}\left(-\frac{dP}{dx}\right)(\frac{b^2}{2a\cos\theta} - 2a\cos\theta), \tag{A.107}$$

where $-\theta_1 \leq \theta \leq \theta_1$.

A.10 Limacon

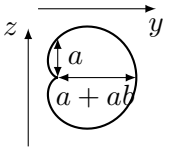

limacon
$(b \leq 1)$

Limacon cross section with axes a, constant b and the area $A = \pi a^2(1 + 2b^2)$ defined by the following equations

$$\begin{aligned} y &= a(\cos\theta + b\cos 2\theta), \\ z &= a(\sin\theta + b\sin 2\theta), \end{aligned} \tag{A.108}$$

with the corresponding polar coordinate is $r = a(1 + 2b\cos\theta)$. Consider the equation (A.1) which may be arranged as

$$\nabla^2\left(\Psi + \frac{1}{4\mu}\frac{dP}{dx}(y^2 + z^2)\right) = \frac{1}{\mu}\frac{dP}{dx}, \tag{A.109}$$

where Ψ is a plane harmonic function $\nabla^2\Psi = 0$. As $u = 0$ on the solid boundaries, so

$$\Psi = -\frac{1}{4\mu}\frac{dP}{dx}(y^2+z^2)+d, \tag{A.110}$$

where d is an arbitrary constant.

Using the following map, we can map a circle $(\xi^2+\eta^2)\leq 1$ to the case of Limacon

$$y = a(\xi + b(\xi^2-\eta^2)), \tag{A.111}$$
$$z = a(\eta + 2b\xi\eta). \tag{A.112}$$

In the new (ξ,η) coordinate system it is necessary to solve $(\frac{\partial^2\Psi}{\partial\xi^2}+\frac{\partial^2\Psi}{\partial\eta^2})=0$. From the boundary (A.110), inspection of (A.109) shows that

$$u = \frac{a^2}{4\mu}\left(-\frac{dP}{dx}\right)\left[B_1\xi + B_2\eta + B_3\xi\eta + B_4 - (\xi^2+\eta^2) - 2b\xi(\xi^2+\eta^2) - b^2(\xi^4+\eta^4) - 2b^2\xi^2\eta^2\right], \tag{A.113}$$

where B_1, B_2, B_3 and B_4 are constants. Using the boundary $(\xi^2+\eta^2)=1$, we have $B_1=2b$, $B_2=0$, $B_3=0$ and $B_4=1+b^2$. Thus, the velocity profile is

$$u(y,z) = \frac{a^2}{4\mu}\left(-\frac{dP}{dx}\right)\left[1 + 2b\xi + b^2 - (\xi^2+\eta^2) - 2b\xi(\xi^2+\eta^2) - b^2(\xi^4+\eta^4) - 2b^2\xi^2\eta^2\right]. \tag{A.114}$$

Impose $\frac{\partial u}{\partial\xi}=\frac{\partial u}{\partial\eta}=0$ which gives $\eta=0$ and $2b^2\xi^3+3b\xi^2+\xi-b=0$, then the maximum velocity can be obtained from the root of cubic equations. Obviously, the position of maximum velocity depend on the constant b. The volume flow rate defined by $\Phi=\int_{-1}^{1}\int_{-\sqrt{1-\eta^2}}^{\sqrt{1-\eta^2}} u(\xi,\eta)|\frac{\partial(y,z)}{\partial(\xi,\eta)}|d\xi d\eta$ gives

$$\Phi = \frac{\pi}{8\mu}\left(-\frac{dP}{dx}\right)a^4\left(1+4b^2-2b^4\right), \tag{A.115}$$

where $|\frac{\partial(y,z)}{\partial(\xi,\eta)}| = a^2(1+2b\xi)^2+4a^2b^2\eta^2$. From this it follows that the velocity

$$\bar{u} = \frac{a^2}{8\mu}\left(-\frac{dP}{dx}\right)\left(\frac{1+4b^2-2b^4}{1+2b^2}\right), \tag{A.116}$$

and the wall shear stress is

$$\tau = \frac{a^2}{2}(-\frac{dP}{dx})(1 + 2b\cos\theta + 2b^2)\cos\theta,\ 0 \leq \theta \leq 2\pi. \tag{A.117}$$

Appendix B

Estimation of parameters for an arbitrary shape

B.1 Method

In the previous chapter 2 the proposed parametrization of an arbitrary cross section shape following the "superformula"

$$r(\theta) = g(\theta)\left[\left|\frac{\cos(\frac{m\theta}{4})}{a}\right|^{n_2} + \left|\frac{\sin(\frac{m\theta}{4})}{b}\right|^{n_3}\right]^{-1/n_1} = g(\theta).f(\theta), \quad m > 0, \tag{B.1}$$

describes almost any closed curve base on the deformed circle, $f(\theta)$ and another function, $g(\theta)$ and their parameters. This function $g(\theta)$ can be considered as a modifier factor of the function $f(\theta)$. For a scientific purpose, the parameters need to be estimated from empirical data which are considered in this chapter.

Let the n true points be $z_i = (x_i, y_i),\ i = 1, 2, ..., n$, of which the corresponding observed values are $z_i^{'} = (x_i^{'}, y_i^{'})$, possibly with errors of measurement and displacement of unknown origin by (c_x, c_y). Let $(\tilde{c}_x, \tilde{c}_y)$ be the approximate or assumed values of (c_x, c_y). Let us denote by $\tilde{z}_i = (\tilde{x}_i, \tilde{y}_i) = (x_i^{'} - \tilde{c}_x, y_i^{'} - \tilde{c}_y)$ so that we obtain $\tilde{r}_i = \sqrt{\tilde{x}_i^2 + \tilde{y}_i^2}$ and $\tilde{\theta}_i = \tan^{-1}(\tilde{y}_i/\tilde{x}_i)$. On the other hand, we obtain $\hat{r}_i = g(\tilde{\theta}) \cdot f(\tilde{\theta}_i, \tilde{a}, \tilde{b}, \tilde{m}, \tilde{n}_1, \tilde{n}_2, \tilde{n}_3)$. The deviation of assumed values of parameters from their true values gives rise to $d_i = |\tilde{r} - \hat{r}|$ and consequently $S = \sum_{i=1}^{n} d_i^2 \geq 0$. Only if the assumed values of parameters are the true values, S can be zero, but the smaller it is, the closer are the assumed values of the parameters from their true values (assuming empirical uniqueness of the parameters to a given set of data). Thus we have to find the values of the parameters in $f(\cdot)$ and $g(\cdot)$ such that S is minimum.

In many methods of global optimization the Particle Swarm method of global optimization is a very important and effective method [32, 94, 33, 96, 10, 38]. The Particle Swarm method of global optimization mimics the behavior of a swarm of birds or other animals searching for food. Each individual of the swarm is considered as a particle in a multidimensional space which has a position and a velocity. The particles remember the best position they seen and communicate to each other to adjust their positions and velocities. Among the Particle

Swarm method, the Repulsive Particle Swarm method (RPSM) of optimization is particularly effective in finding out the global optimum in complex search spaces though may be slower for certain problems [87, 88, 65, 102]. In Repulsive Particle Swarm method the future velocity $\mathbf{u}_{i+1}$ of a particle at position $\mathbf{x}_i$ with a recent velocity $\mathbf{u}_i$ is calculated by

$$\mathbf{u}_{i+1} = \alpha\mathbf{u}_i + a\xi_1\left(\hat{\mathbf{x}}_i - \mathbf{x}_i\right) + b\xi_2\alpha\left(\hat{\mathbf{x}}_{bi} - \mathbf{x}_i\right) + c\xi_3\alpha\mathbf{z}, \tag{B.2}$$

where,

- ξ_1, ξ_2, ξ_3 are random numbers $\in [0, 1]$. a, b, c are constants. α is inertia weight $\in [0.01, 0.7]$.
- $\hat{\mathbf{x}}$ is best position of a particle. $\hat{\mathbf{x}}_{bi}$ is best position of a randomly chosen other particle from within he swarm. $\mathbf{z}$ is a random velocity vector.

The future $\mathbf{x}_{i+1}$ is thus defined as $\mathbf{x}_{i+1} = \mathbf{x}_i + \mathbf{u}_{i+1}$. Occasionally, when the process is caught in a local optimum, some perturbation of $\mathbf{u}$ may be needed.

B.2 Result

Fig.B.1 illustrates the figures generated by true and estimated parameters using 360 particles shown in Table. B.1. It is seen that the estimation is good coincidence with the true values.

Table B.1: True and estimated parameters of "superformula" function by Repulsive Particle Swarm method when $g(\theta) = 1$. 360 Particles is used.

shape	m	n_1	n_2	n_3	a	b	S
true	3	4	2	7	1	1	0.0
estimated	2.9853	4.4548	2.7747	5.6781	1.004	1.001	8.4543e-5

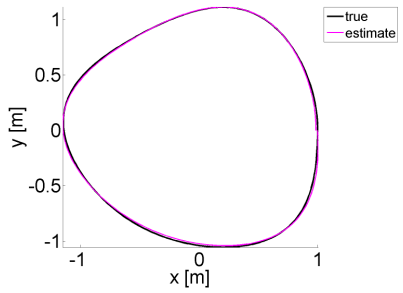

Figure B.1: Illustration of figures generated with true and estimated parameters.

Appendix C

Modeling

C.1 Quasi-1D model

The quasi-1D model, which takes into account the kinetic losses and the viscosity for two-dimensional flow, can be formulated as follows

$$\bar{u}\frac{d\bar{u}}{dx} + \frac{1}{\rho}\frac{dP}{dx} = \nu\frac{\partial^2 u}{\partial y^2}, \tag{C.1}$$

where $\bar{u}(x)$ denotes the local bulk velocity.

C.2 Thwaites method

The equations of Thwaites' method for 2D and axisymmetrical flow solving steady integral momentum equation [126, 105] are summarized in the system below

$$\begin{aligned} \delta_1(x) &= \int_0^\infty r^k(x)\left(1 - \frac{u(x,y)}{U_e(x)}\right)dy, \\ \delta_2(x) &= \int_0^\infty r^k(x)\frac{u(x,y)}{U_e(x)}\left(1 - \frac{u(x,y)}{U_e(x)}\right)dy, \\ \text{flow index } k &= \begin{cases} 0 & \text{2D flow} \\ 1 & \text{axisymmetrical flow} \end{cases} \end{aligned} \tag{C.2}$$

where $r(x)$ is the radial function of the streamwise position x. Using the quasi-similarity assumptions [126], the laminar boundary-layer momentum thickness can be represented as a function of downstream distance x with Thwaites equation

$$\begin{aligned} \delta_2^2(x) &= \frac{0.45\nu}{r^{2k}(x)U_e^6(x)}\int_0^x r^{2k}(x)U_e^5(x)dx + \frac{\delta_2^2(0)r^{2k}(0)U_e^6(0)}{r^{2k}xU_e^6(x)}, \\ \text{flow index } k &= \begin{cases} 0 & \text{2D flow} \\ 1 & \text{axisymmetrical flow} \end{cases} \end{aligned} \tag{C.3}$$

where $U_e(0)$ and $\delta_2(0)$ are the flow velocity and momentum thickness at the inlet $x = 0$. The skin friction parameter

$$S(\lambda) = \frac{\delta_2}{U_e(x)} \frac{\partial U_e}{\partial y}, \tag{C.4}$$

becomes zero at the flow separation and depends on the Thwaites parameter λ

$$\lambda = \frac{\delta_2}{\nu} \frac{\partial U_e(x)}{\partial x}. \tag{C.5}$$

In addition, a shape parameter $H(\lambda)$ is introduced characterizing the boundary layer

$$H(\lambda) = \frac{\delta_1}{\delta_2}. \tag{C.6}$$

The skin friction parameter $S(\lambda)$ and shape parameter $H(\lambda)$ are derived from experimental data described by modified universal Thwaites functions [12, 27]

$$\begin{aligned} S(\lambda) &= 0.22 + 1.402\lambda + \frac{0.018\lambda}{0.107 + \lambda} \quad -0.1 \le \lambda \le 0, \\ H(\lambda) &= 2.088 + \frac{0.0731\lambda}{0.14 + \lambda}, \\ S(\lambda) &= 0.22 + 1.57\lambda - 1.8\lambda^2 \qquad 0 \le \lambda \le 0.1, \\ H(\lambda) &= 2.61 - 3.75\lambda + 5.24\lambda^2. \end{aligned} \tag{C.7}$$

This system can be discretized spatially, with the step Δx and discretisation index i in the x direction. The values of variable $U_e(i\Delta x)$, $\delta_1(i\Delta x)$, $\delta_2(i\Delta x)$ and $\lambda(i\Delta x)$ are denoted $U_{e,i}$, $\delta_{1,i}$, $\delta_{2,i}$ and λ_i respectively. Then the system can be rewritten as

$$\begin{cases} \delta_{2,i}^2 = \frac{0.45\nu}{r_i^{2k} U_{e,i}^6} \Delta x \sum_{j=1}^{i} r_j^{2k} U_{e,j}^5 + \frac{\delta_2^2(0) r^{2k}(0) U_e^6(0)}{r_i^{2k} U_{e,i}^6}, \\ \lambda_i = \frac{\delta_{2,i}}{\nu} \frac{U_{e,i} - U_{e,i-1}}{\Delta x}, \\ \delta_{1,i} = \delta_{2,i} H(\lambda_i), \\ U_{e,i} = \frac{Q}{A(\delta_{1,i})}, \\ \tau_{s,i} = \frac{\rho \nu U_{e,i}}{\delta_{2,i}} S(\lambda_i), \end{cases} \tag{C.8}$$

where the area $A(\delta_{1,i})$ based on the displacement thickness $\delta_{1,i}$ is defined respectively as

$$A(\delta_{1,i}) = \begin{cases} l(h_i - 2\delta_{1,i}), & \text{k=0} \\ \pi(r_i - \delta_{1,i})^2, & \text{k=1} \end{cases} \tag{C.9}$$

The code use the volume flow rate Q and discretised contraction geometry A_i as the input parameters. The limit conditions at entrance are

$$\begin{cases} \delta_2^0 = \delta_1^0 = 0, \\ \lambda^0 = 0, \\ U_{e,i}^0 = \frac{Q}{A_i}, \\ \tau_{s,i}^0 = 0. \end{cases} \tag{C.10}$$

Once the initial conditions are known, the calculation is performed in the following steps

- The velocity $U_{e,i}^0$ in the flow entrance is deduced in (C.10).
- After each step of the computational domain, the following steps are repeated until convergence

  a. The velocity $U_{e,i}^0$ is calculated according to the precedent values as

  $$U_{e,i} = \frac{Q}{A(\delta_{1,i-1})}. \tag{C.11}$$

  b. Knowing the value $U_{e,i}$, we can calculate $\delta_{2,i}$ with the first equation of (C.8)

  $$\delta_{2,i} = \sqrt{\frac{0.45\nu}{r_i^{2k} U_{e,i}^6} \Delta x \sum_{j=1}^{i} r_j^{2k} U_{e,j}^5 + \frac{\delta_2^2(0) r^{2k}(0) U_e^6(0)}{r_i^{2k} U_{e,i}^6}}. \tag{C.12}$$

  c. Then λ_i is determined by the second relation of (C.8) and new $\delta_{1,i}$ is obtained by $\delta_{1,i} = \delta_{2,i} H(\lambda_i)$.

  d. With new values obtained, the velocity $U_{e,i}$ is recalculated by

  $$U_{e,i} = \frac{Q}{A(\delta_{1,i})}. \tag{C.13}$$

- Finally, the process is reiterated until it converges (the criterion of convergence is determined by the user) and the wall shear stress $\tau_{s,i}$ can be calculated by the last equation of (C.8).

Appendix D

Detailed constriction geometries

D.1 Sharp edged

The detailed geometries for the sharp edged constrictions used for the experiments presented in chapter 5 is illustrated in Fig. D.1.

D.2 Round edged

The details of three-dimensional printed geometries with rounded edges adapted from the numerical grid presented in Chap 6 is illustrated in Fig. D.2.

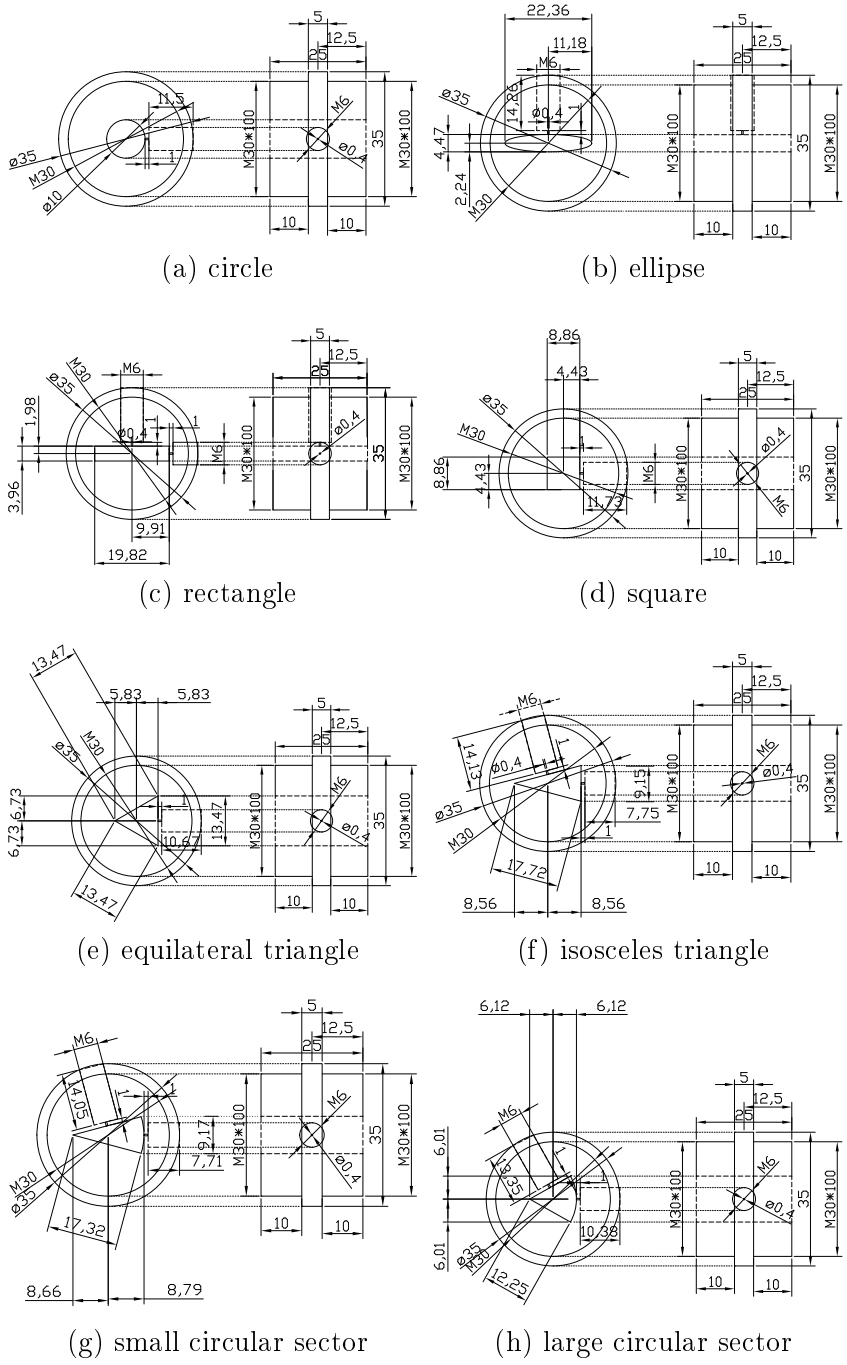

(a) circle (b) ellipse

(c) rectangle (d) square

(e) equilateral triangle (f) isosceles triangle

(g) small circular sector (h) large circular sector

Figure D.1: Detailed geometries for the sharp edged constrictions used for the experiments presented in chapter 5.

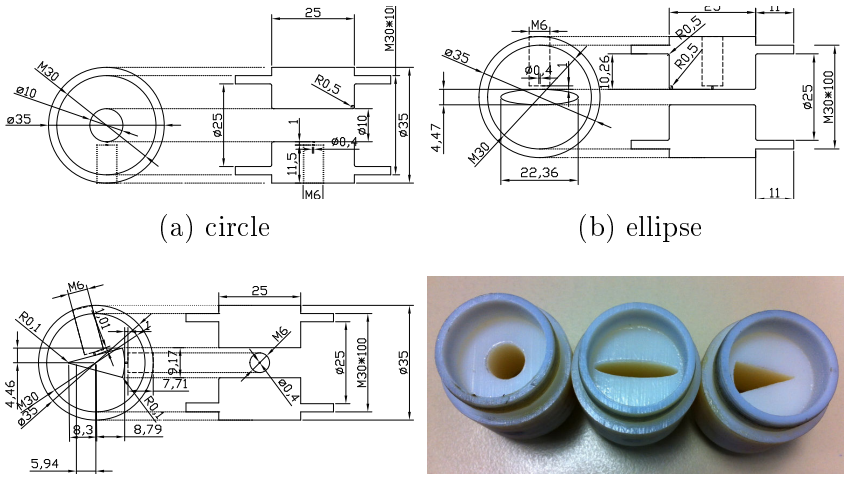

(a) circle (b) ellipse

(c) small circular sector (d) photograph

Figure D.2: Three-dimensional printed geometries with rounded edges adapted (screwthread is added) from the numerical grid presented in chapter 6.

Appendix E

Measurement instruments

During experiments, senors are used to measure physical quantities: pressure, velocity, etc. These sensors deliver a variable voltage with the digital acquisition system (PCI-MIO, NI, Labview NI). Converting these voltages into the physical quantities requires calibration.

E.1 Calibration of pressure sensors and visualization images

E.1.1 Electronic manometer

The electronic gauge (Ashcroft-XLdP) is used to calibrate the piezoelectric pressure transducers (see next section). Its calibration is done using a water manometer. The two gauges are connected to a point of constant pressure, the value is changed by means of a pressure regulator which allows fine adjustment. This arrangement is shown schematically in Fig. E.1a.

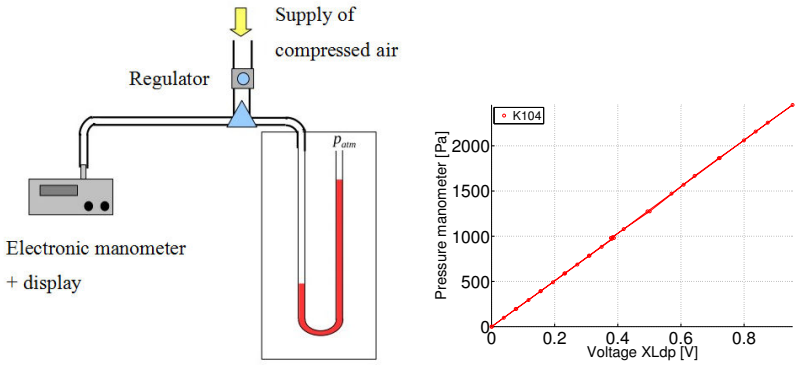

(a) (b)

Figure E.1: (a) The calibration device Electronic manometer. (b) The voltage delivered by pressure manometer Ashcroft-XLdP depending on the pressure read from the water manometer. It is shown that the slope of the line obtained by linear regression on all measurement points.

Two different water manometers were used: the first is a little limited to a pressure of 100mm H_2O model, and the second has a larger liquid column up to 300mm H_2O. Use both

helped us to ensure that we found the same pressure (with an accuracy of about 0.5mm H_2O or 5 Pa). The calibration is illustrated in Fig. E.1b.

E.1.2 Piezoelectric pressure transducers

Piezoelectric pressure transducers are used to measure the pressure at various points in the model. The Kulite XCS-093 models need to be calibrated before use. The calibration procedure is quite similar to the electronic manometer, while it is connected to the transducer at a point of sampled pressure. On each sensor, a dozen tension / pressure points covering a range of 0 to 3000 Pa are measured. Then a linear regression is applied as done for the electronic manometer (Fig. E.1b). The response of both sensors is linear (correlation of 0.99 between the points and the right) to for example gain 2587 Pa/V for the Kulite XCS-093 model.

E.1.3 Smoke visualization: image calibration

In the experiment of smoke visualization in order to remain the same region of observation and redress the position of cross section shape calibration using a grid square pattern with 1cm side shown in Fig. E.2 is performed before film the first time of every new component.

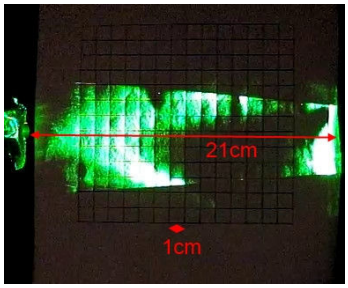

Figure E.2: Calibration using a grid square pattern with 1cm side.

E.2 Single hot film anemometry

Constant temperature anemometer IFA-300 TSI is used. In our study a single hot film anemometer called model 1201-20 TSI shown in Fig. E.3 is used for one-dimensional flow measurements. The diameter and the length of sensing area are 50.8μm and 1.02mm respectively. More features of the hot film are detailed in Table. E.1. The probe is mounted on an positioning system and connected to the TFA-300.

The entire system of constant temperature anemometer is depicted in Fig. E.4. Briefly the main function of constant temperature anemometer is to maintain the temperature of the probe and thus keep its resistance R_{op} constant. Any variation of the flow will induce a change

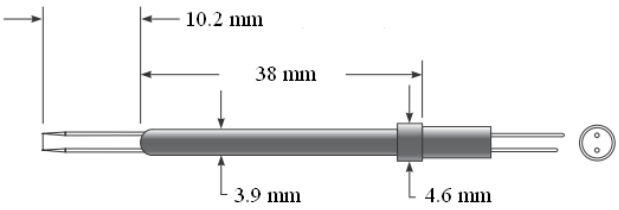

Figure E.3: Hot film model 1201-20 TSI (`http://www.tsi.com/uploadedFiles/Product_Information/Literature/Catalogs/Hotwire_Catalog_2980465.pdf`).

Table E.1: Features of hot film model 1201-20 TSI (`http://www.tsi.com/uploadedFiles/Product_Information/Literature/Catalogs/Hotwire_Catalog_2980465.pdf`).

Material	Maximum sustained ambient temperature	Maximum sensor operating temperature	Temperature coefficient of resistance	Distance between supports
Platinum	300 °C	425 °C	0.0024 $°C^{-1}$	1.65mm

in the resistance R_{op} and then cause a small voltage change e_b at amplifier input. Finally, the current out from the differential amplifier changes the bridge voltage E_B at output. Once the temperature becomes stable, the flow velocity can be indirectly measured from the resulting tension.

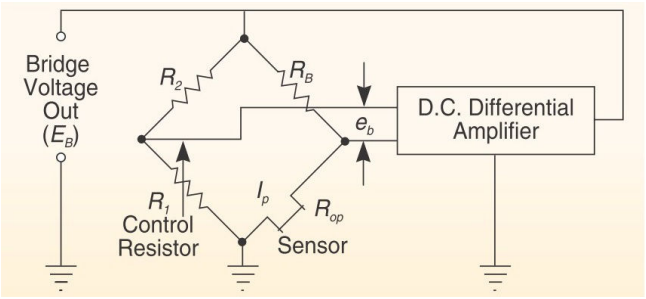

Figure E.4: Schema of constant temperature anemometer, where E_B: bridge voltage output, e_b: small voltage change at amplifier input, I_P: current through sensor, R_{op}: resistance of sensor at operating temperature, R_1, R_2, R_B: bridge resistor (`http://www.tsi.com/uploadedFiles/Product_Information/Literature/Catalogs/Hotwire_Catalog_2980465.pdf`).

Calibration is an important step for the accuracy of the measurements. The instrument for the calibration of hot film is illustrated in Fig. E.5. The compressed air flow measured by a flow meter. The flow goes through a tube which consists of a diverging portion, a 2m uniform PVC tube with diameter 10cm and a converging portion with diameter 2.14cm at outlet. More details can be found in Ref. [42].

The hot film is positioned at the center of converging portion at 1mm distance from the nozzle exit. The displacement is controlled by a user-defined matrix implemented in LabView

7 (National Instruments). The speed signal is recorded by hot film with frequency 10kHz for 10s at every position. Volume flow rate is acquired with sampling frequency 100Hz. In order to avoid any flow disturbances and temperature variation the whole setup except for the air compressor is arranged in a confined room with an air conditioning system. To account for the drift in room temperature T_a based on the reference ambient temperature, $T_{a,r} = 21.1^oC$, the measured output bridge voltages E_{meas} are corrected to E_{cor} using the approach adopted by Kanevce [61], where T_f denotes the airflow temperature:

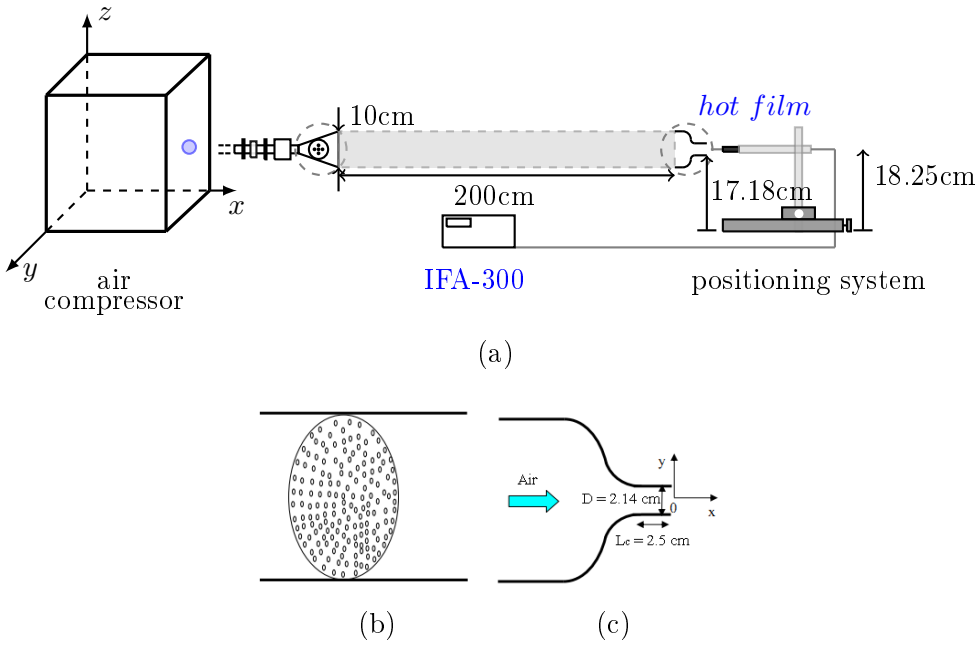

Figure E.5: a) Overview the setup of calibration for hot film. b) cross sectional view of the tube arranged in the diverging portion. c) cross sectional view of the converging tube.

$$E_{cor} = E_{meas} \left(\frac{T_f - T_{a,r}}{T_f - T_a} \right)^{1/2} \tag{E.1}$$

The voltages are plotting with a fifth order polynomial curve fit. The calibration procedure is outlined in Ref. [42]. Results are shown in Fig. E.6, which include the ideal velocity (+) by considering the exit centerline velocity to be equal to the bulk velocity [40, 61], the calibration velocity (x) and the fitting velocity (o). The main calibration error is due to the experimental error on the measured volume flow rates ($< 2\%$ of its recording).

An illustration of the home-made one-dimensional positioning system used to position the hot film sensor to obtain transverse and longitudinal velocity profiles is given in Fig. E.7. The position is determined by means of a step motor so that the precision is determined by the number of steps (200 steps) in a rotation. The precision based on the step motor is 0.01mm. The accuracy was validated up to 0.1mm due to the limitation of the used measurement instrument.

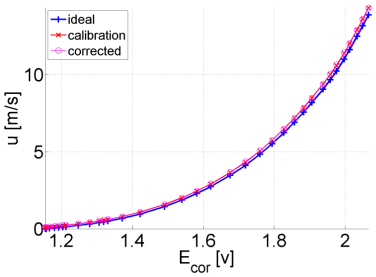

Figure E.6: Single hot film calibration.

Figure E.7: Illustration of the home-made one-dimensional positioning system used to measure transverse and longitudinal velocity profiles.

Appendix F

Velocity profiles and flow visualization

F.1 Measured longitudinal profiles

Measured longitudinal profiles are presented in Fig. F.1, Fig. F.2, Fig. F.3 and Fig. F.4.

F.2 Transverse profiles

F.2.1 Measured transverse profiles

Measured transverse profiles are presented in Fig. F.5 and Fig. F.6

F.2.2 Modeled and measured transverse profiles

In the previous chapter 5 the comparison of modeled and measured transverse profiles along the 'major' and 'minor' axis of constriction was presented only for rectangular shape, in the current section the comparison of constrictions with other shapes are shown in F.7∽F.14.

In general, for both the 'major' and 'minor' axis, it is observed that the modeled and measured transverse profiles matches well within the boundary layer. However, since the modeled profile is fully developed, it tends to overestimate the velocity for the core flow enveloped by the boundary layers. Given that the simplified model does not accounts for complex flow dynamics, which based on the presented experimental results suggested to contribute to the flow development – such as vortex generation, vortex interaction or turbulence – at first sight the comparison is surprisingly good.

The estimated error between modeled and experimental velocities defined by (5.5), is illustrated in Fig. F.15. The error vary from 33% to 85% and from 12% to 57% of the bulk velocity at the center of 'major' and 'minor' axis respectively. It is seen that the error tendency depends on the cross section shape and the volume flow rate and The variation of the error with the volume flow rate is more pronounced fore velocity profiles along the 'major' axis than for the 'minor' axis. The precision is mainly depend on the unaccounted complex phenomena in model and the undeveloped flow due to the limit of the length of the upstream pipe and

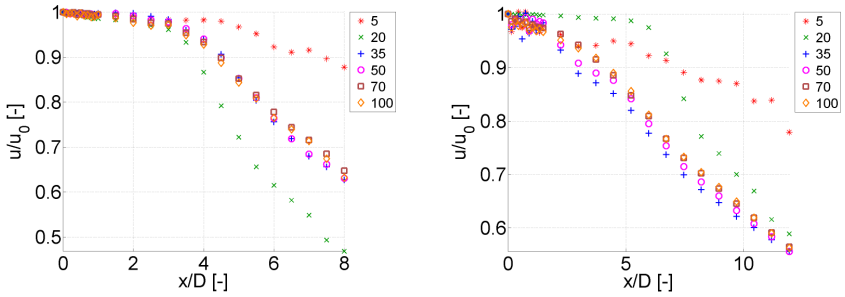

(a) circle (b) ellipse

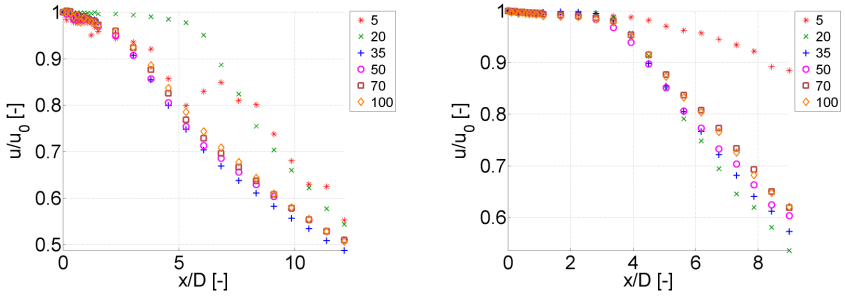

(c) rectangle (d) square

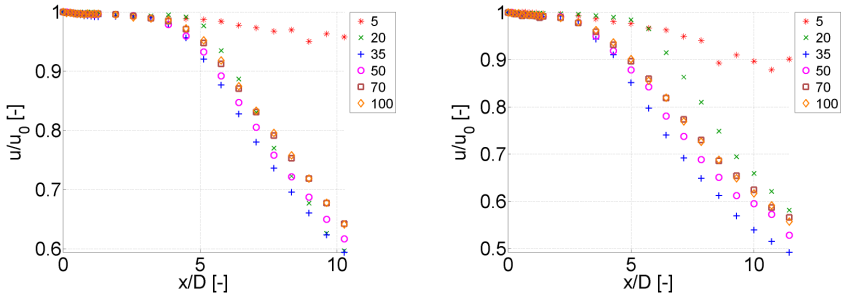

(e) equilateral triangle (f) isosceles triangle

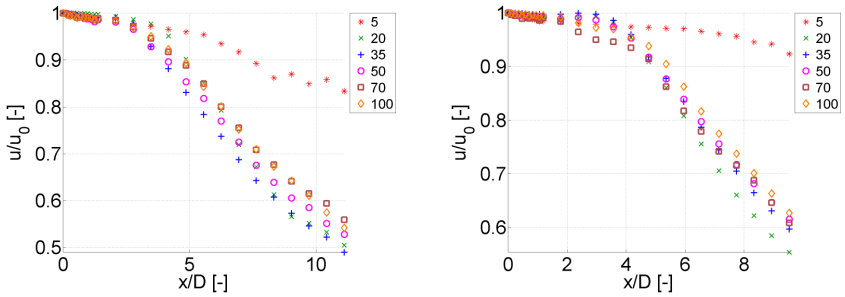

(g) small circular section (h) large circular section

Figure F.1: Measured near field normalized longitudinal mean velocity profiles u/u_0 along the centerline of the jet for cross section shapes shown in Fig. 5.1 as a function of volume flow rate Q (5, 20, 35, 50, 70 or 100l/min) for sharp edges at the constriction inlet (label C of Table 5.4). u_0 denotes the initial velocity of the jet along the centerline.

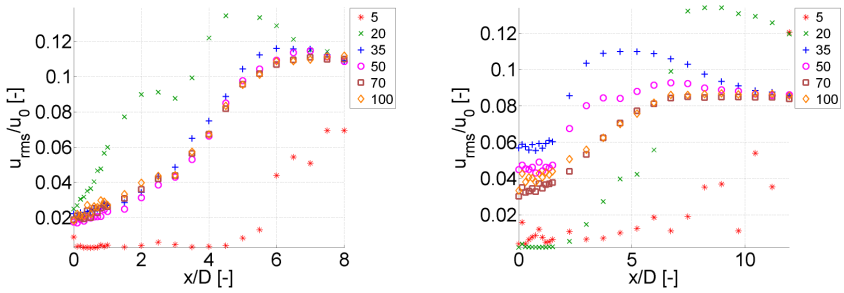

(a) circle (b) ellipse

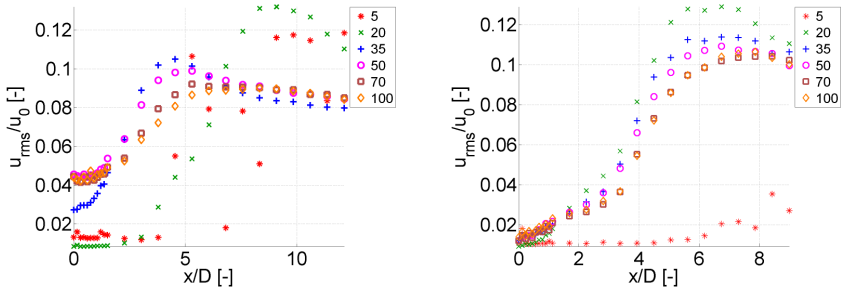

(c) rectangle (d) square

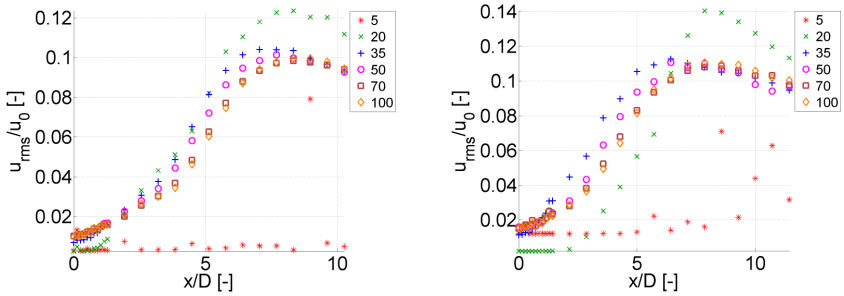

(e) equilateral triangle (f) isosceles triangle

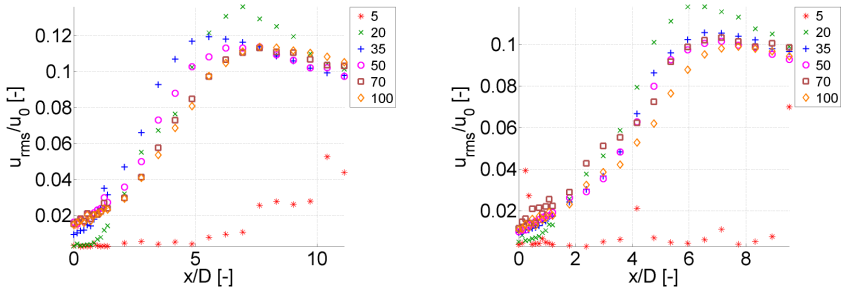

(g) small circular section (h) large circular section

Figure F.2: Measured near field normalized longitudinal root mean square velocity profiles u_{rms}/u_0 along the centerline of the jet for cross section shapes shown in Fig. 5.1 as a function of volume flow rate Q (5, 20, 35, 50, 70 or 100l/min) for sharp edges at the constriction inlet (label C of Table 5.4). u_0 denotes the initial velocity of the jet along the centerline.

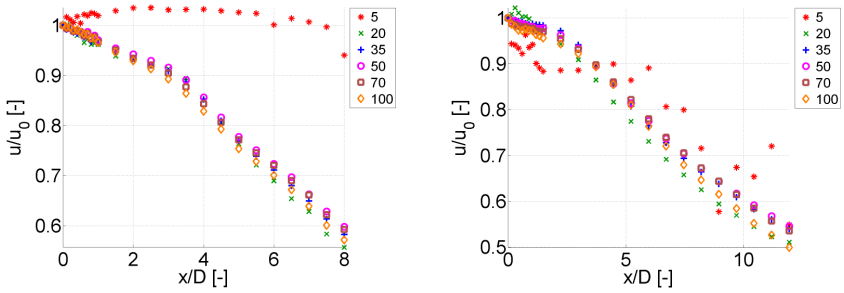

(a) circle (b) ellipse

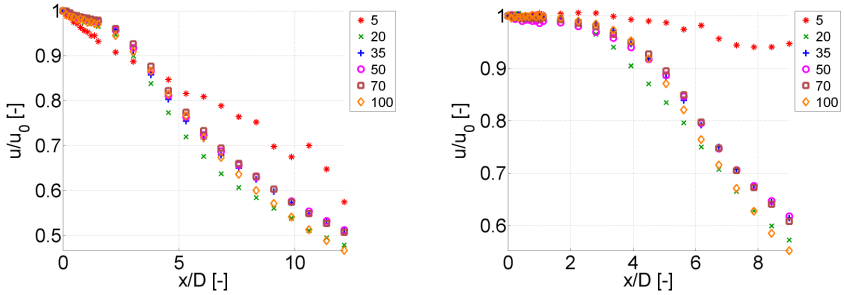

(c) rectangle (d) square

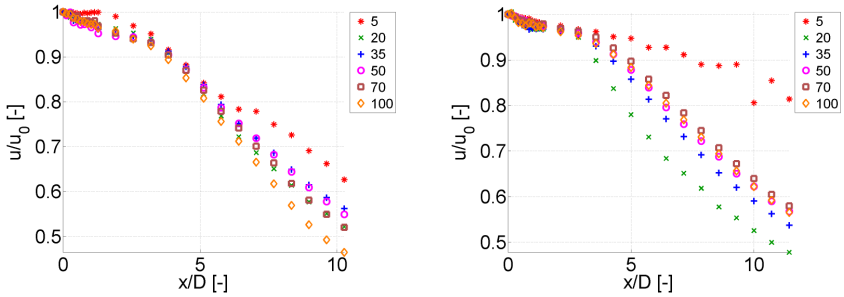

(e) equilateral triangle (f) isosceles triangle

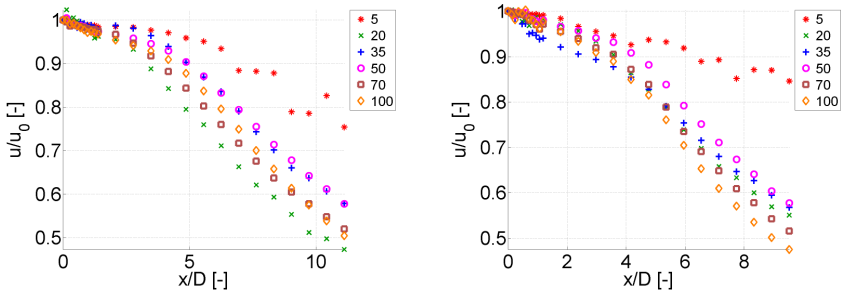

(g) small circular section (h) large circular section

Figure F.3: Measured near field normalized longitudinal mean velocity profiles u/u_0 along the centerline of the jet for cross section shapes shown in Fig. 5.1 as a function of volume flow rate Q (5, 20, 35, 50, 70 or 100l/min) for a single grid placed immediately upstream from the constriction inlet (label D of Table 5.4). u_0 denotes the initial velocity of the jet along the centerline.

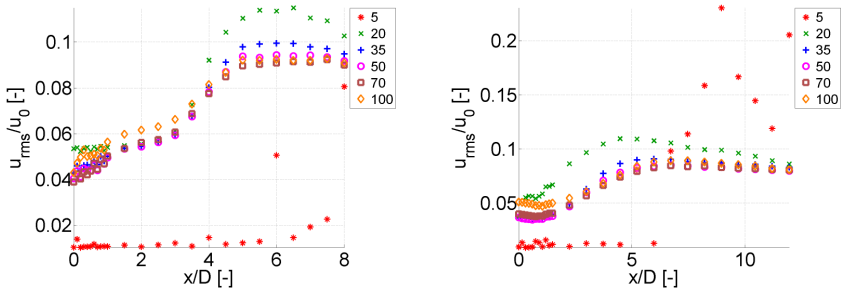

(a) circle (b) ellipse

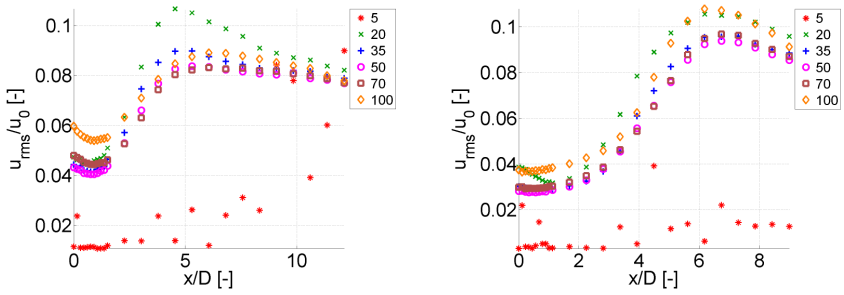

(c) rectangle (d) square

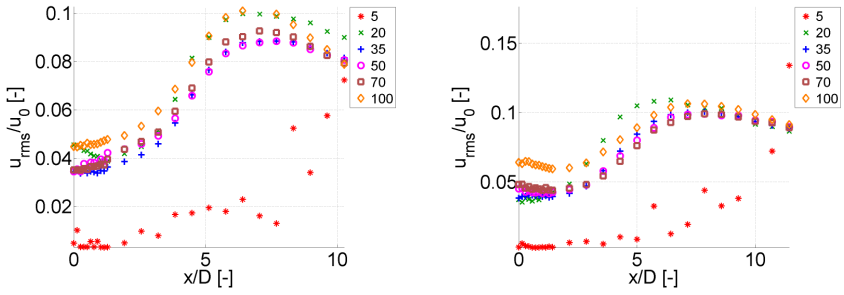

(e) equilateral triangle (f) isosceles triangle

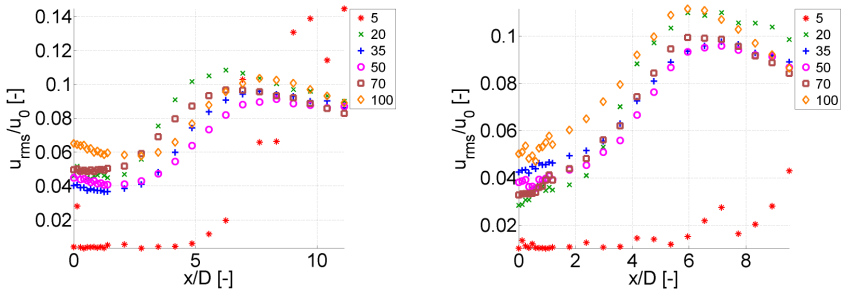

(g) small circular section (h) large circular section

Figure F.4: Measured near field normalized longitudinal root mean square velocity profiles u_{rms}/u_0 along the centerline of the jet for cross section shapes shown in Fig. 5.1 as a function of volume flow rate Q (5, 20, 35, 50, 70 or 100l/min) for a single grid placed immediately upstream from the constriction inlet (label D of Table 5.4). u_0 denotes the initial velocity of the jet along the centerline.

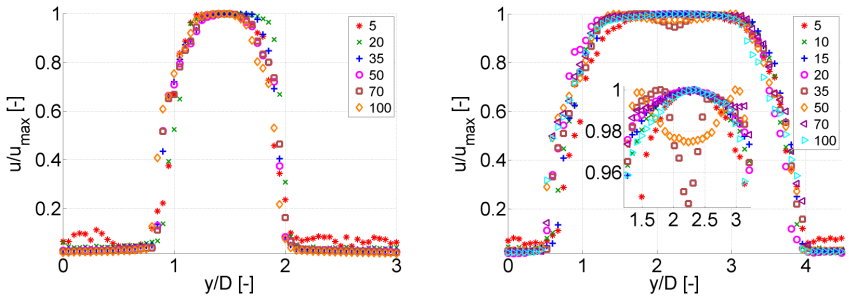

(a) circle

(b) ellipse

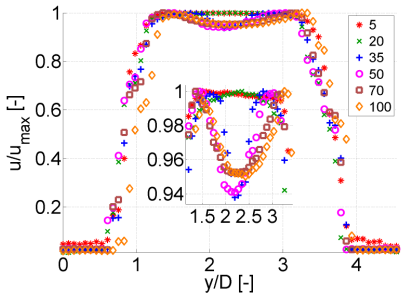

(c) rectangle

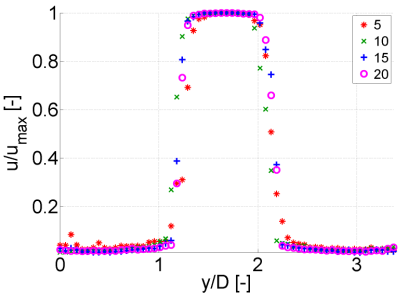

(d) square

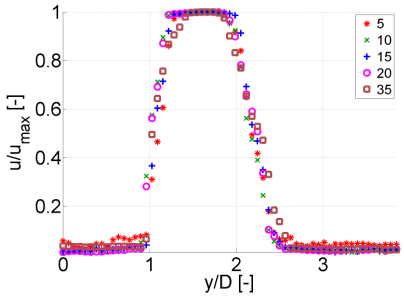

(e) equilateral triangle

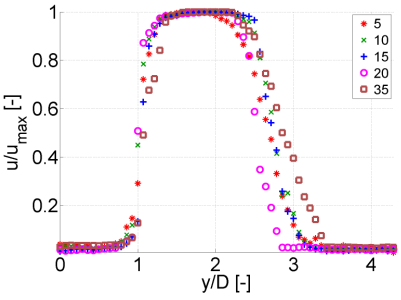

(f) isosceles triangle

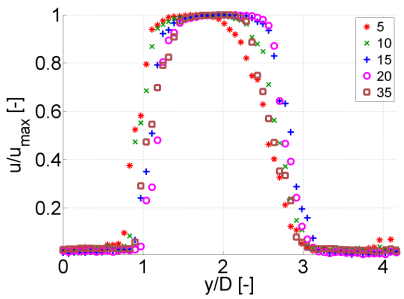

(g) small circular section

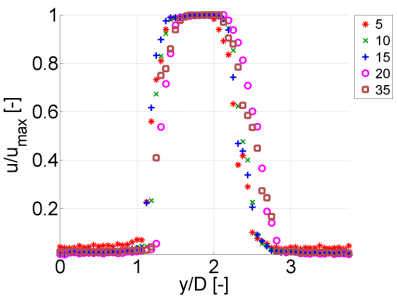

(h) large circular section

Figure F.5: Measured normalized transverse mean velocity profiles u/u_{max} at the exit of the constriction for cross section shapes shapes shown in Fig. 5.1 as a function of volume flow rate Q (5, 20, 35, 50, 70 or 100l/min) for sharp edges at the constriction inlet (label C of Table 5.4). u_{max} denotes the maximum velocity of each volume flow rate for each cross section shape. The measure direction is indicated by full arrow shown in Fig. 5.3a and is along the major axis.

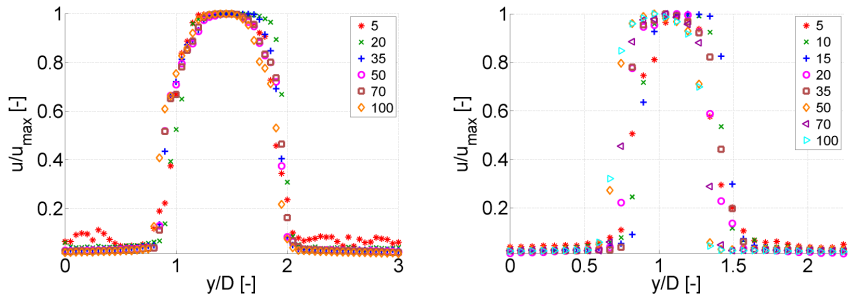

(a) circle

(b) ellipse

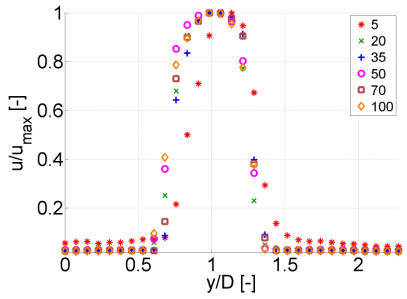

(c) rectangle

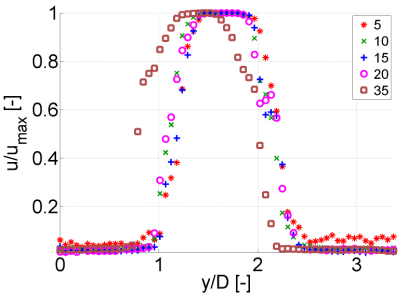

(d) square

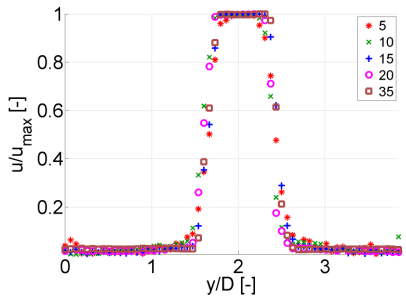

(e) equilateral triangle

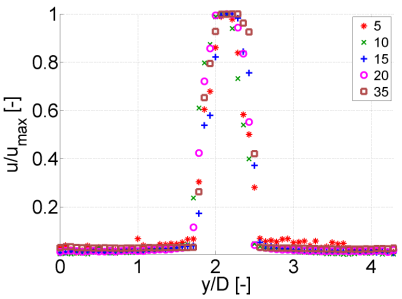

(f) isosceles triangle

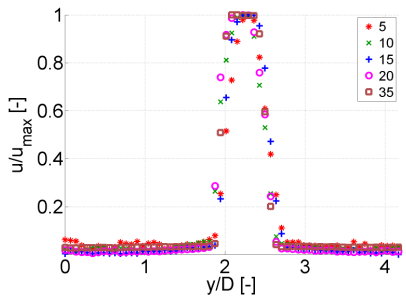

(g) small circular section

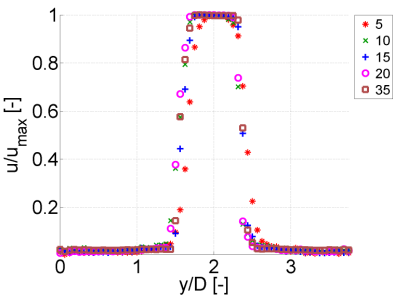

(h) large circular section

Figure F.6: Measured normalized transverse mean velocity profiles u/u_{max} at the exit of the constriction for cross section shapes shapes shown in Fig. 5.1 as a function of volume flow rate Q (5, 20, 35, 50, 70 or 100l/min) for sharp edges at the constriction inlet (label C of Table 5.4). u_{max} denotes the maximum velocity of each volume flow rate for each cross section shape. The measure direction is indicated by dashed arrow shown in Fig. 5.3a. Note that for a square it denotes the diagonal direction and not the minor axis.

constricted portion. Anyway, the discrepancy between modeled and experimental values is quantified.

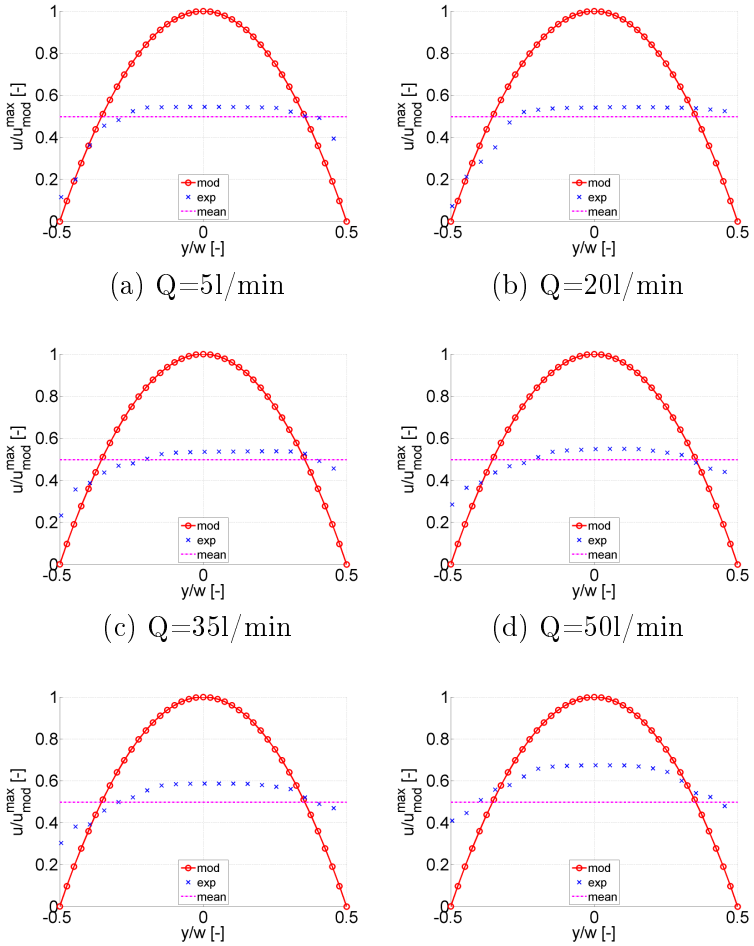

(a) Q=5l/min (b) Q=20l/min

(c) Q=35l/min (d) Q=50l/min

(e) Q=70l/min (f) Q=100l/min

Figure F.7: Comparison of modeled and experimental assessed velocities normalized by the maximum modeled velocity u_{mod}^{max} at the exit of constriction for major axis of circular shape. Volume flow rate are assessed for 5, 20, 35, 50, 70 and 100l/min. Velocity estimated from transverse profiles using spatial step $\Delta y = 0.5$mm is labeled "exp". The modeled results is denoted as "mod" and $\bar{u}$ is the bulk velocity. The width of the constricted portion along major axis is labeled 'w'.

F.3 Flow visualization

Table F.1: Ratio $\delta_{exp}/\delta_{mod} = u_{exp}^{max}/u_{mod}^{max}$ resulting from the threshold criterion illustrated in Fig. 5.29 for a threshold value of 100% for transverse profiles along the 'major' and 'minor' axis of all assessed cross sections. The uncertainty due to the spatial discretization (spatial step) is indicated. Bold volume flow rates indicate an overall change of tendency.

	D [mm]	Q [l/min]								position error [%]	tendency
		5	10	15	20	35	**50**	**70**	100		
		major axis									
cl	10	54	-	-	54	54	55	59	67	2.5	→↗
sq	8.9	62	62	61	60	-	-	-	-	3	↘
lcs	8.4	63	62	61	60	59	-	-	-	2	↘
tr	7.8	62	60	58	58	56	-	-	-	2	↘
scs	7.2	61	60	57	57	57	-	-	-	1.5	↘
ntr	7.0	60	59	58	46	45	-	-	-	1.5	↘
el	6.7	72	70	68	67	65	64	67	82	1	↘↗
re	6.6	81	-	-	77	75	75	79	100	1.5	↘↗
		minor axis									
sq	8.9	64	63	62	60	-	-	-	-	2	↘
lcs	8.4	73	73	71	70	69	-	-	-	2	↘
tr	7.8	71	71	69	68	66	-	-	-	2	↘
scs	7.2	94	94	92	92	96	-	-	-	3	↘↗
ntr	7.0	97	93	97	75	75	-	-	-	3	↘↗↘
el	6.7	72	70	68	66	63	65	69	80	5.5	↘↗
re	6.6	83	-	-	79	74	72	77	91	6.5	↘↗

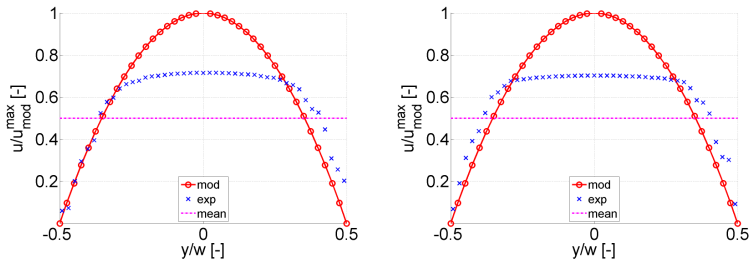

(a) Q=5l/min (b) Q=10l/min

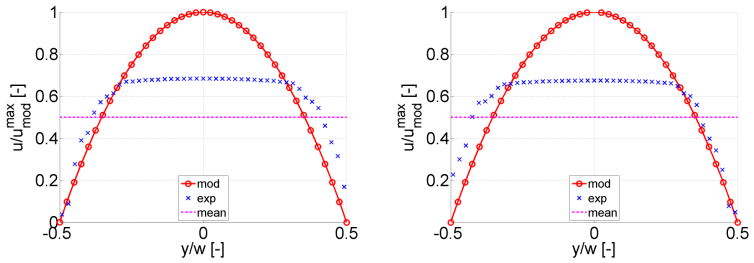

(c) Q=15l/min (d) Q=20l/min

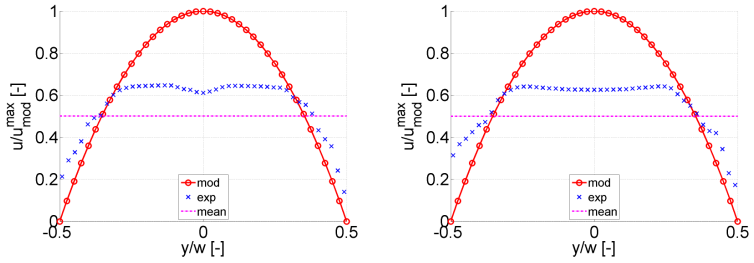

(e) Q=35l/min (f) Q=50l/min

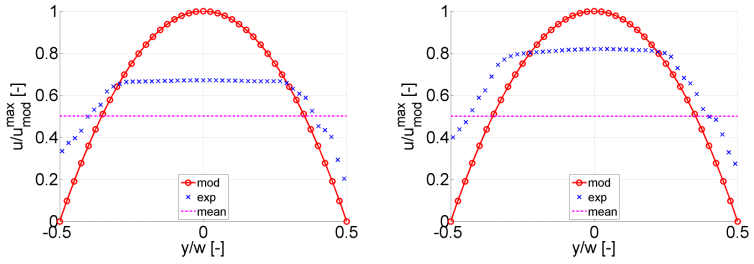

(g) Q=70l/min (h) Q=100l/min

Figure F.8: Comparison of modeled and experimental assessed velocities normalized by the maximum modeled velocity u_{mod}^{max} at the exit of constriction for major axis of elliptic shape. Volume flow rate are assessed for 5, 10, 15, 20, 35, 50, 70 and 100l/min. Velocity estimated from transverse profiles using spatial step $\Delta y = 0.5$mm is labeled "exp". The modeled results is denoted as "mod" and $\bar{u}$ is the bulk velocity. The width of the constricted portion along major axis is labeled 'w'.

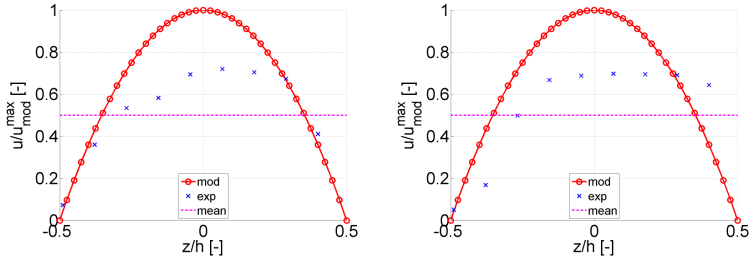

(a) Q=5l/min

(b) Q=10l/min

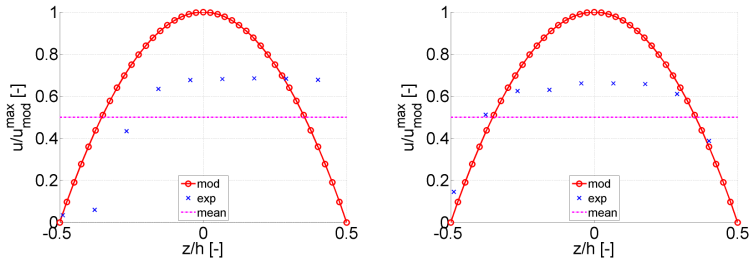

(c) Q=15l/min

(d) Q=20l/min

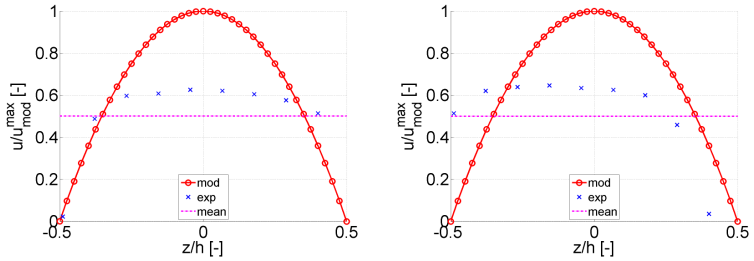

(e) Q=35l/min

(f) Q=50l/min

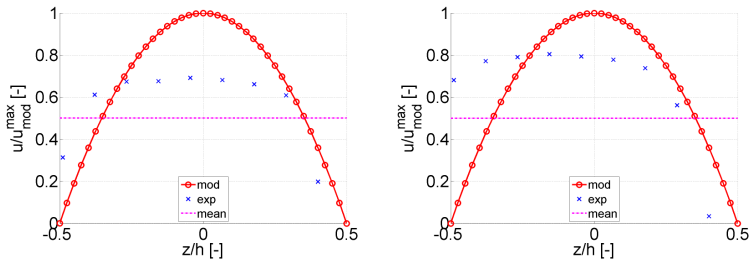

(g) Q=70l/min

(h) Q=100l/min

Figure F.9: Comparison of modeled and experimental assessed velocities normalized by the maximum modeled velocity u_{mod}^{max} at the exit of constriction for minor axis of elliptic shape. Volume flow rate are assessed for 5, 10, 15, 20, 35, 50, 70 and 100l/min. Velocity estimated from transverse profiles using spatial step $\Delta y = 0.5$mm is labeled "exp". The modeled results is denoted as "mod" and $\bar{u}$ is the bulk velocity. The height of the constricted portion along minor axis is labeled 'h'.

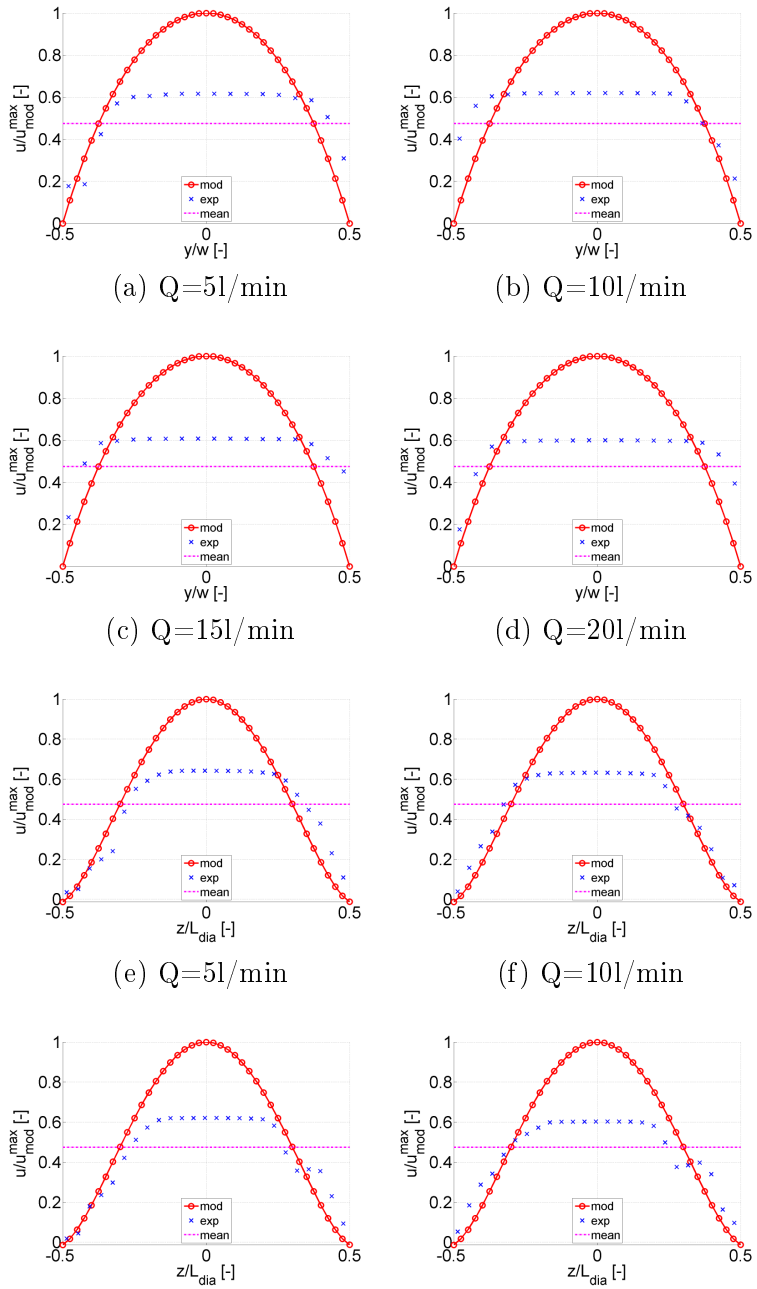

(a) Q=5l/min (b) Q=10l/min

(c) Q=15l/min (d) Q=20l/min

(e) Q=5l/min (f) Q=10l/min

(g) Q=15l/min (h) Q=20l/min

Figure F.10: Comparison of modeled and experimental assessed velocities normalized by the maximum modeled velocity u_{mod}^{max} at the exit of constriction for: (a-d) major axis and (e-h) diagonal axis of square shape. Volume flow rate are assessed for 5, 10, 15 and 20l/min. Velocity estimated from transverse profiles using spatial step $\Delta y = 0.5$mm is labeled "exp". The modeled results is denoted as "mod" and $\bar{u}$ is the bulk velocity. The width and diagonal length of the constricted portion along major and minor axis is labeled 'w' and 'L_{dia}'.

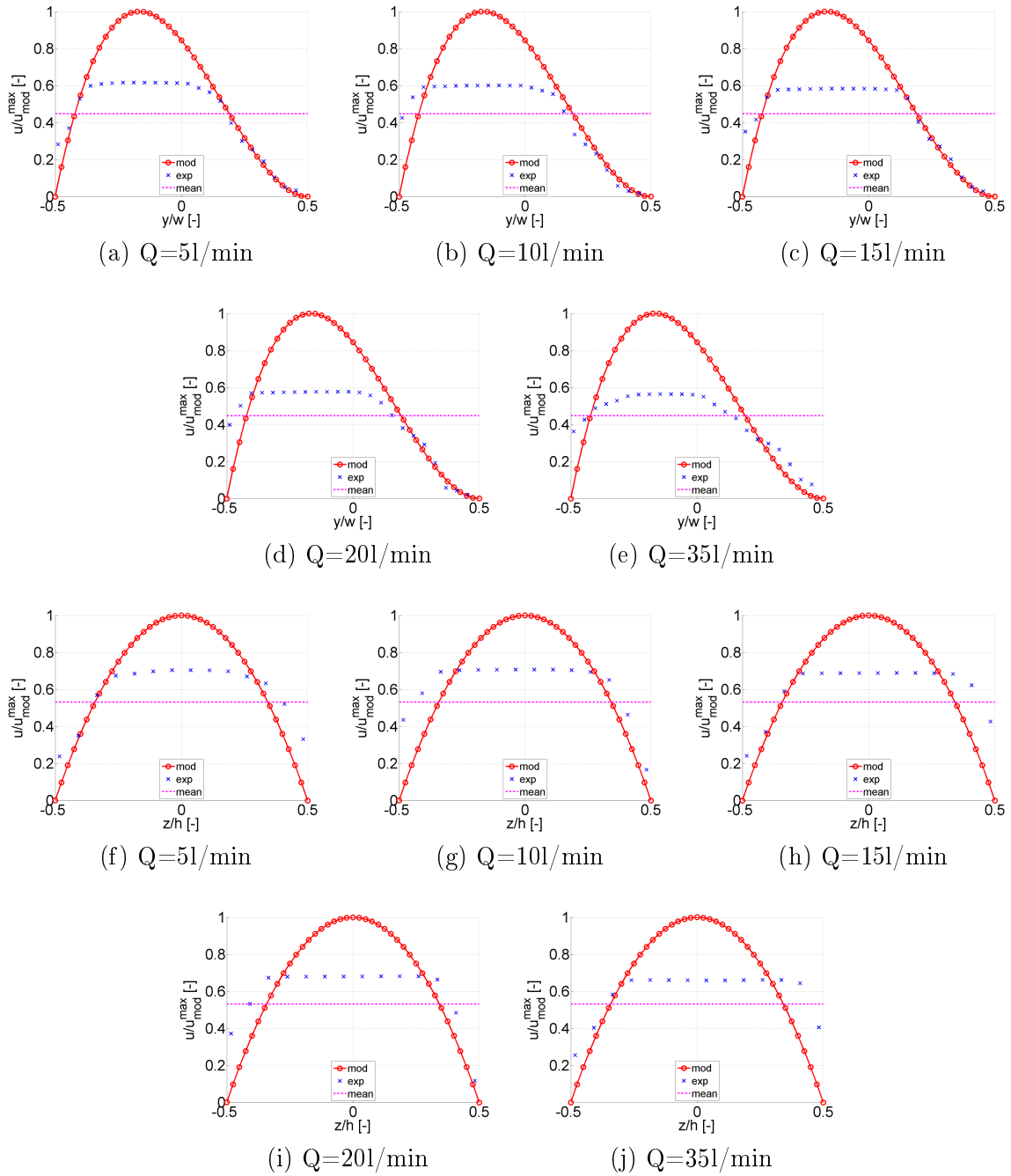

(a) Q=5l/min (b) Q=10l/min (c) Q=15l/min

(d) Q=20l/min (e) Q=35l/min

(f) Q=5l/min (g) Q=10l/min (h) Q=15l/min

(i) Q=20l/min (j) Q=35l/min

Figure F.11: Comparison of modeled and experimental assessed velocities normalized by the maximum modeled velocity u_{mod}^{max} at the exit of constriction for: (a-e) major axis and (f-j) minor axis of equilateral triangle. Volume flow rate are assessed for 5, 10, 15, 20 and 35l/min. Velocity estimated from transverse profiles using spatial step $\Delta y = 0.5$mm is labeled "exp". The modeled results is denoted as "mod" and $\bar{u}$ is the bulk velocity. The width and height of the constricted portion along major and minor axis is labeled 'w' and 'h'.

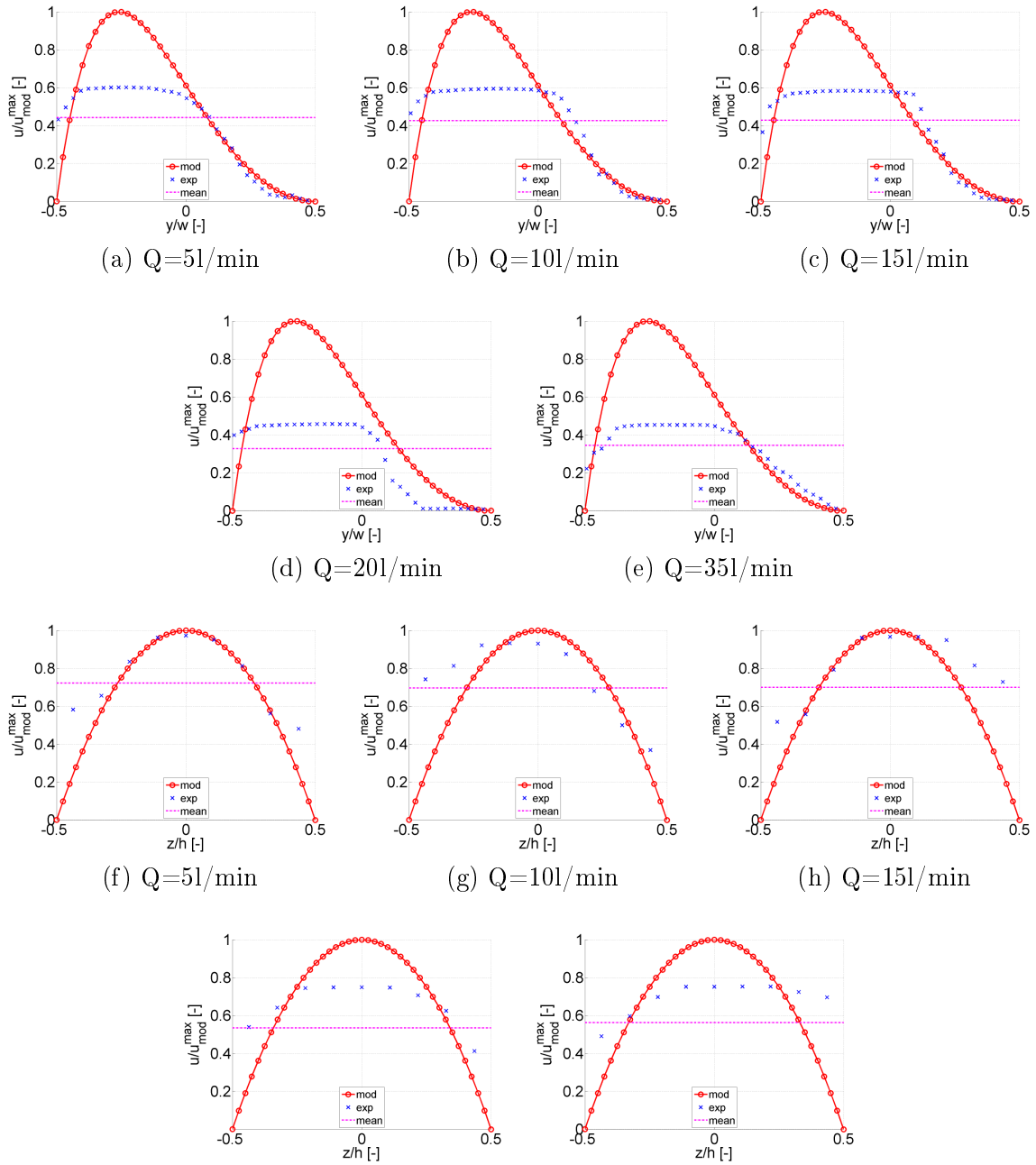

(a) Q=5l/min (b) Q=10l/min (c) Q=15l/min

(d) Q=20l/min (e) Q=35l/min

(f) Q=5l/min (g) Q=10l/min (h) Q=15l/min

(i) Q=20l/min (j) Q=35l/min

Figure F.12: Comparison of modeled and experimental assessed velocities normalized by the maximum modeled velocity u_{mod}^{max} at the exit of constriction for: (a-e) major axis and (f-j) minor axis of isosceles triangle. Volume flow rate are assessed for 5, 10, 15, 20 and 35l/min. Velocity estimated from transverse profiles using spatial step $\Delta y = 0.5$mm is labeled "exp". The modeled results is denoted as "mod" and $\bar{u}$ is the bulk velocity. The width and height of the constricted portion along major and minor axis is labeled 'w' and 'h'.

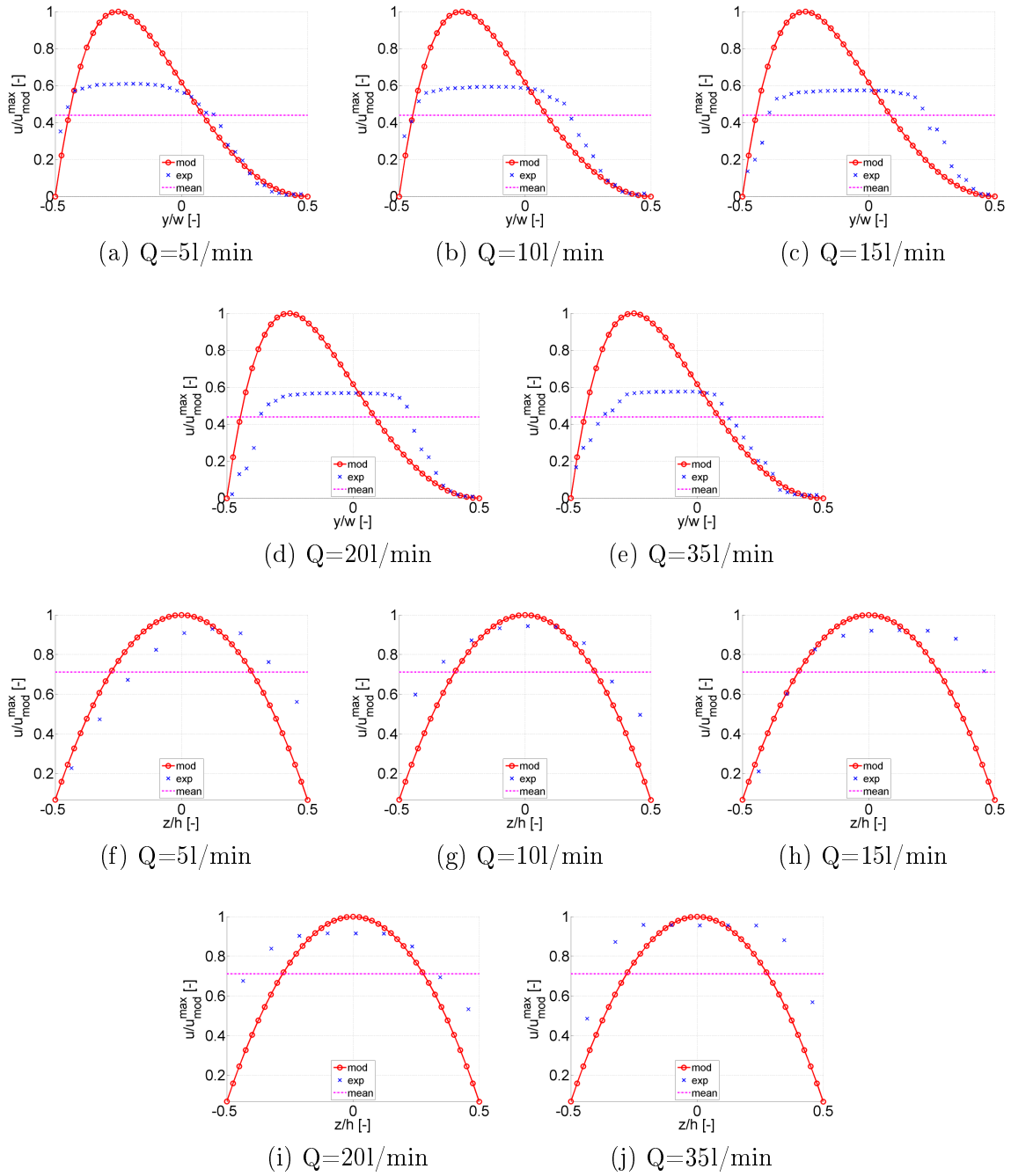

(a) Q=5l/min (b) Q=10l/min (c) Q=15l/min

(d) Q=20l/min (e) Q=35l/min

(f) Q=5l/min (g) Q=10l/min (h) Q=15l/min

(i) Q=20l/min (j) Q=35l/min

Figure F.13: Comparison of modeled and experimental assessed velocities normalized by the maximum modeled velocity u_{mod}^{max} at the exit of constriction for: (a-e) major axis and (f-j) minor axis of small circular sector. Volume flow rate are assessed for 5, 10, 15, 20 and 35l/min. Velocity estimated from transverse profiles using spatial step $\Delta y = 0.5$mm is labeled "exp". The modeled results is denoted as "mod" and $\bar{u}$ is the bulk velocity. The width and height of the constricted portion along major and minor axis is labeled 'w' and 'h'.

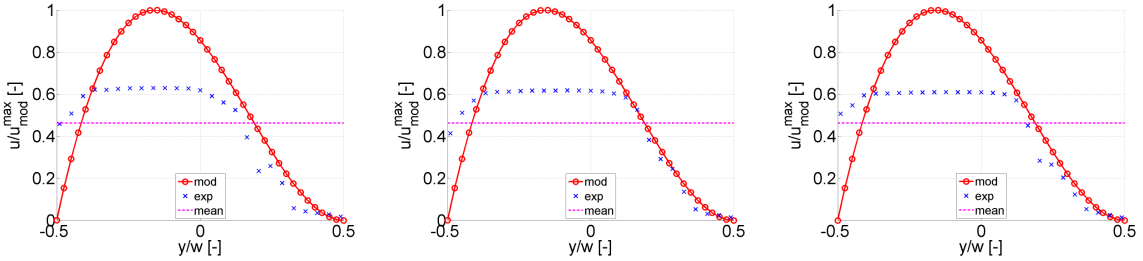

(a) Q=5l/min (b) Q=10l/min (c) Q=15l/min

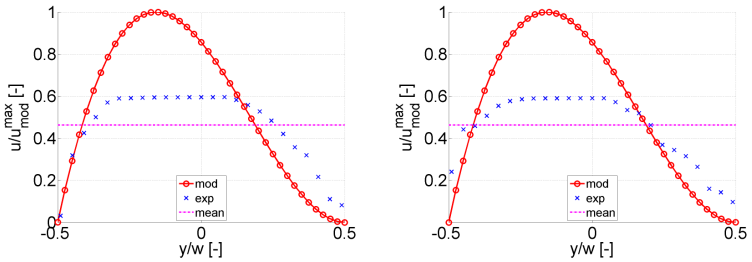

(d) Q=20l/min (e) Q=35l/min

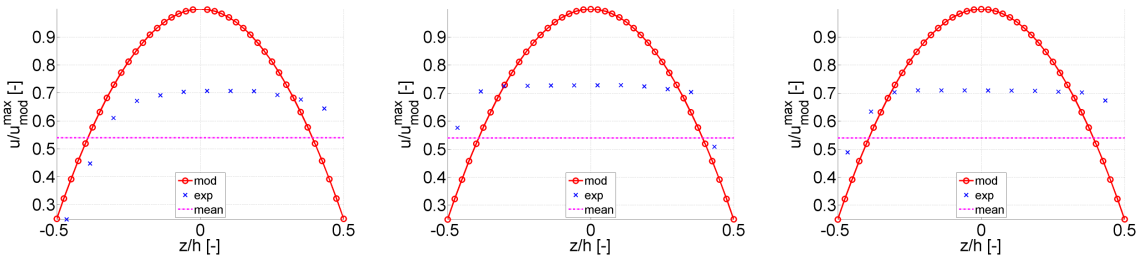

(f) Q=5l/min (g) Q=10l/min (h) Q=15l/min

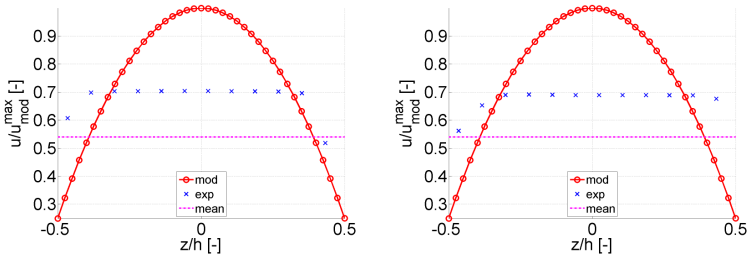

(i) Q=20l/min (j) Q=35l/min

Figure F.14: Comparison of modeled and experimental assessed velocities normalized by the maximum modeled velocity u_{mod}^{max} at the exit of constriction for: (a-e) major axis and (f-j) minor axis of large circular sector. Volume flow rate are assessed for 5, 10, 15, 20 and 35l/min. Velocity estimated from transverse profiles using spatial step $\Delta y = 0.5$mm is labeled "exp". The modeled results is denoted as "mod" and $\bar{u}$ is the bulk velocity. The width and height of the constricted portion along major and minor axis is labeled 'w' and 'h'.

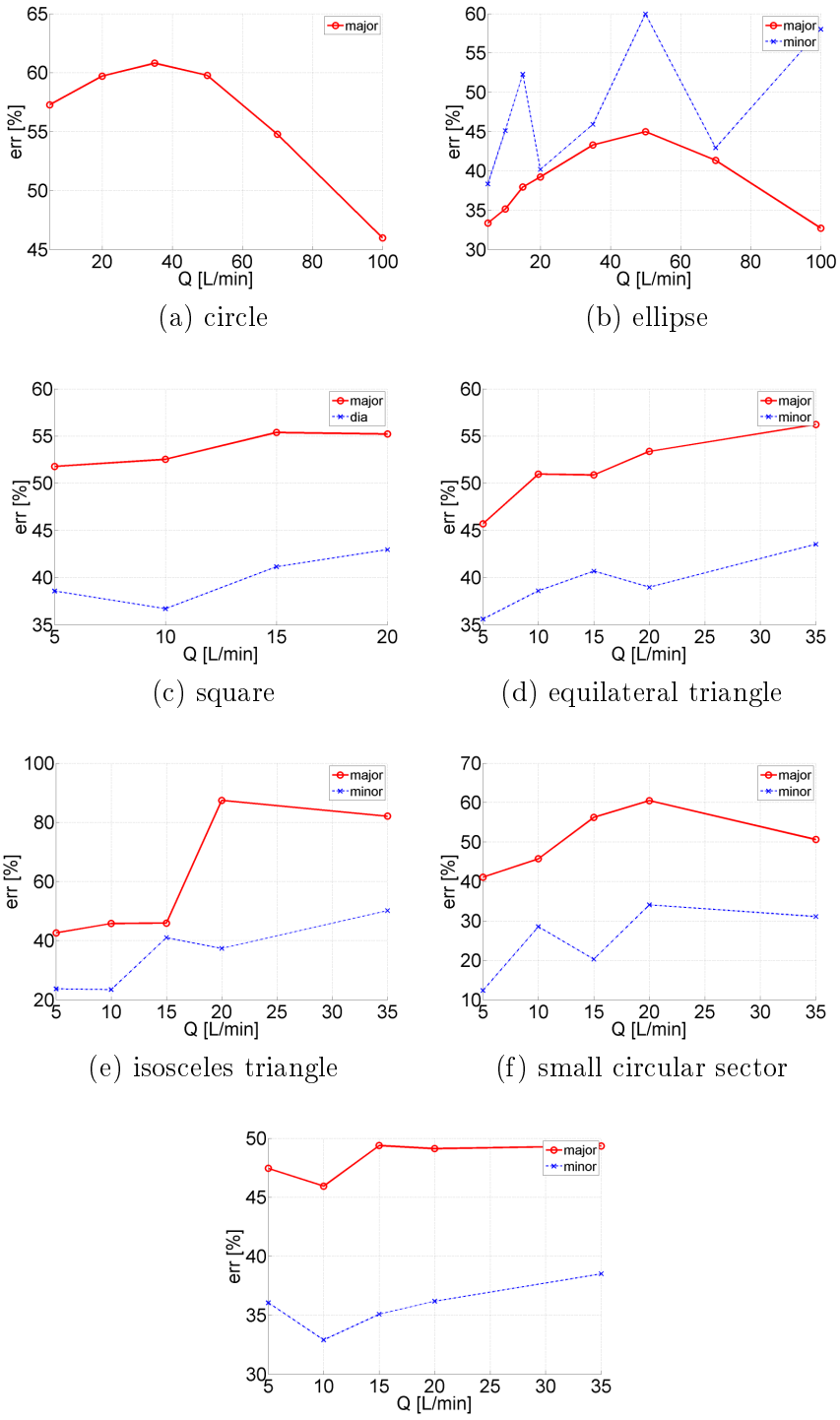

(a) circle (b) ellipse

(c) square (d) equilateral triangle

(e) isosceles triangle (f) small circular sector

(g) large circular sector

Figure F.15: Illustration of the estimated error between modeled and experimental velocities for shapes except rectangular shape. The error along the center of major axis is labeled as "major" and so is the "minor" for minor axis. Notice that the measured in diagonal axis of square is labeled as "dia".

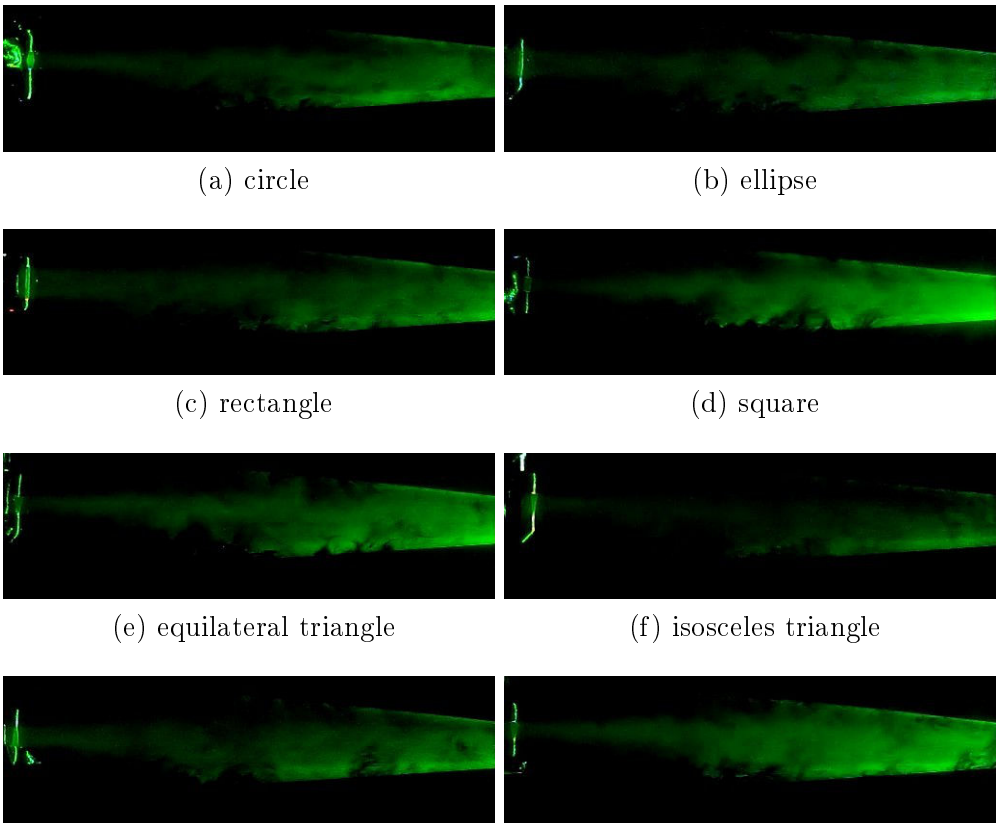

(a) circle (b) ellipse

(c) rectangle (d) square

(e) equilateral triangle (f) isosceles triangle

(g) small circular section (h) large circular section

Figure F.16: Illustration of the visualization at major axis for all cross section shapes when volume flow rate equal to 50l/min.

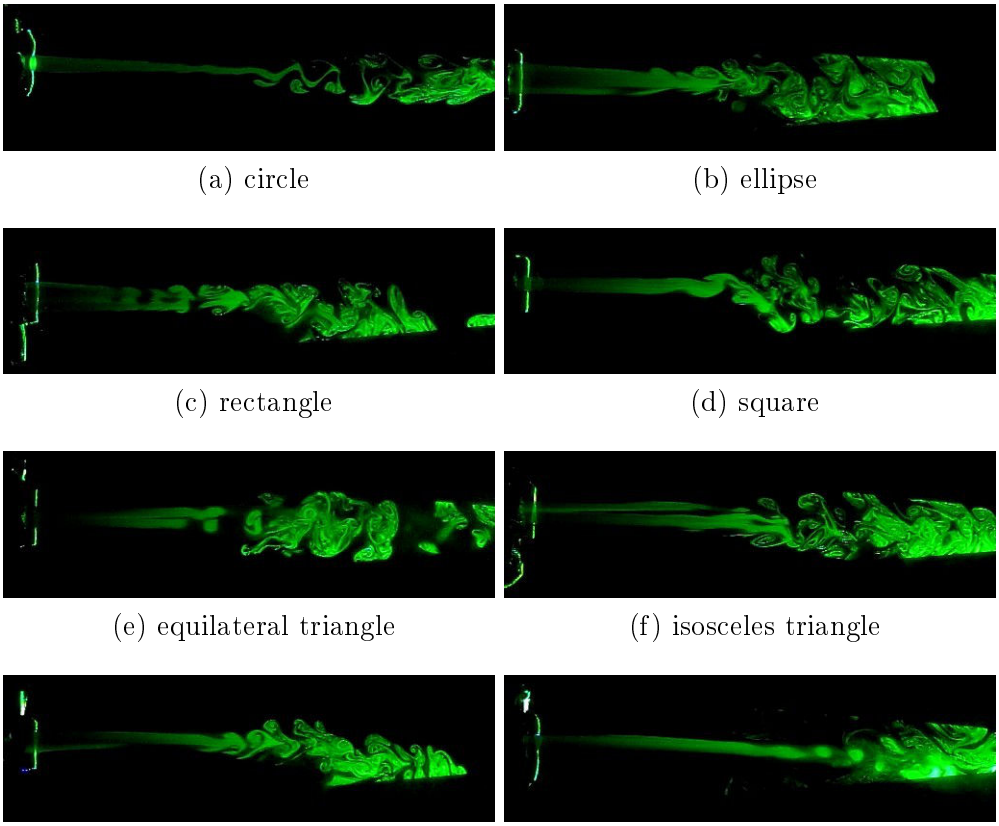

(a) circle (b) ellipse

(c) rectangle (d) square

(e) equilateral triangle (f) isosceles triangle

(g) small circular section (h) large circular section

Figure F.17: Illustration of the visualization of centerline flow profile at major axis for all cross section shapes with one grid plate placed at the inlet of the constricted portion when volume flow rate equal to 5l/min.

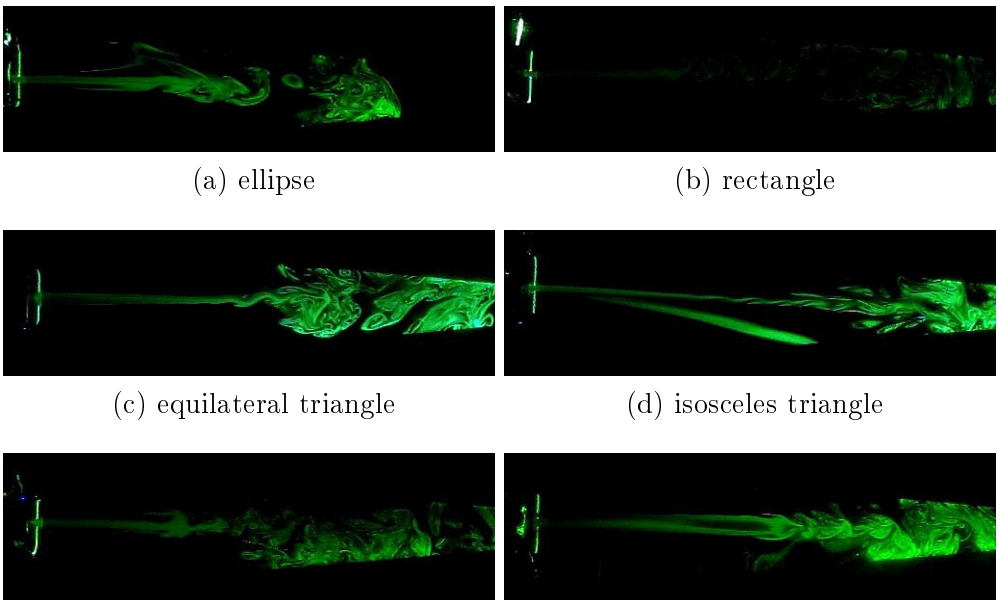

(a) ellipse (b) rectangle

(c) equilateral triangle (d) isosceles triangle

(e) small circular section (f) large circular section

Figure F.18: Illustration of the visualization of centerline flow profile at minor axis for all cross section shapes with one grid plate placed at the inlet of the constricted portion when volume flow rate equal to 5l/min.

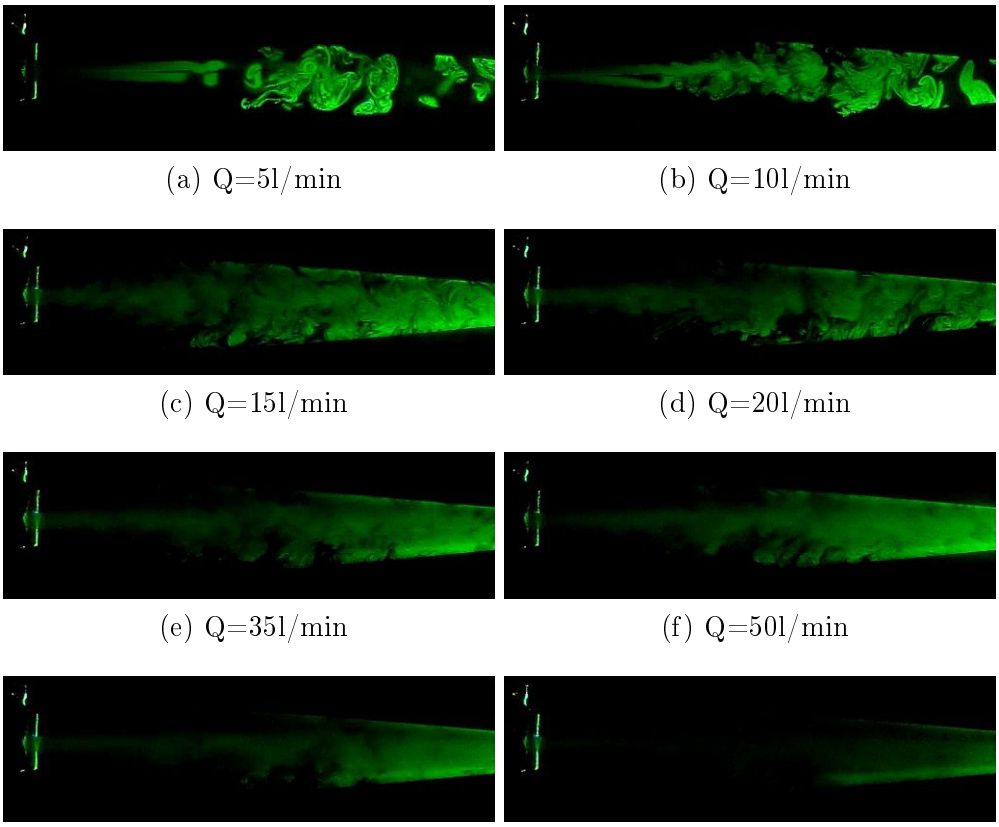

(a) Q=5l/min (b) Q=10l/min

(c) Q=15l/min (d) Q=20l/min

(e) Q=35l/min (f) Q=50l/min

(g) Q=70l/min (h) Q=100l/min

Figure F.19: Visualization of the flow profiles along the centerline of major axis of equilateral triangle at a distance from 0cm to 21cm of the exit. One grid plate is placed at the inlet of the constricted portion. Volume flow rate equal to 5, 10,15, 20, 35, 50, 70 and 100l/min are experimentally assessed.

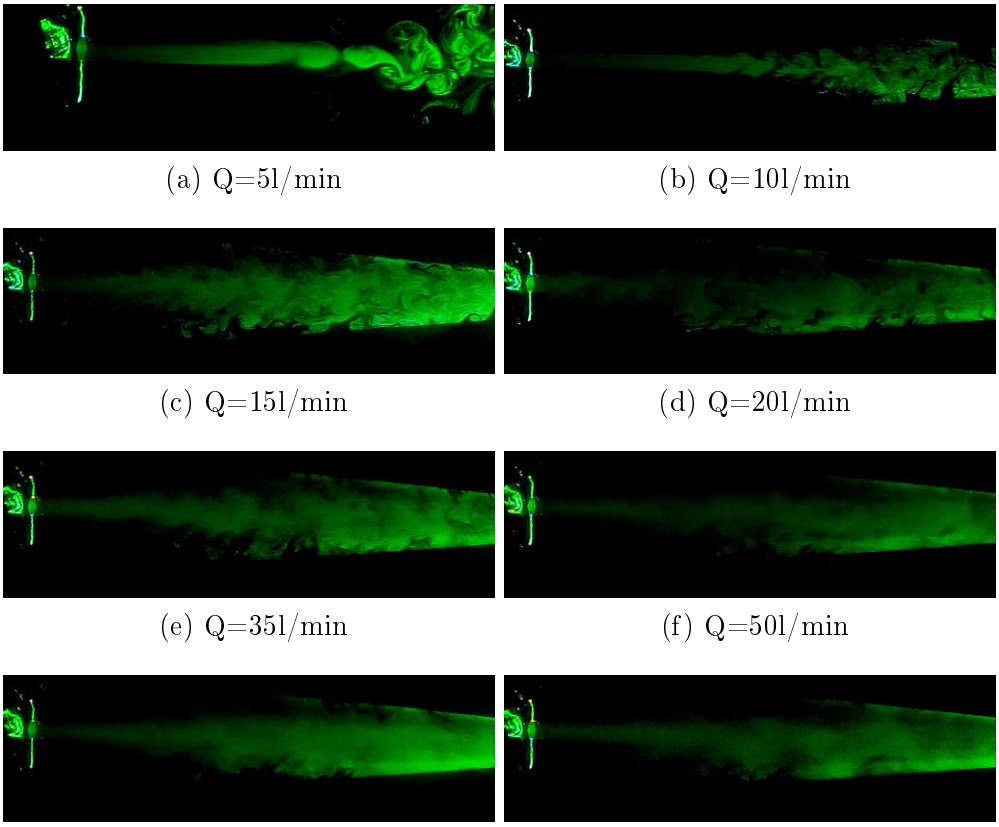

(a) Q=5l/min (b) Q=10l/min

(c) Q=15l/min (d) Q=20l/min

(e) Q=35l/min (f) Q=50l/min

(g) Q=70l/min (h) Q=100l/min

Figure F.20: Visualization of the flow profiles along the centerline of major axis of circular shape at a distance from 0cm to 21cm of the exit. Volume flow rate equal to 5, 10,15, 20, 35, 50, 70 and 100l/min are experimentally assessed.

Appendix G

Unsteady flow

G.1 Modeling

In the previous work the main work is focus on the influence of the cross section shape on steady flow, in the current the unsteady flow is assessed by extend the flow model described in chapter 4. Experimental data are presented in order to assess the influence of cross section shape for unsteady flow. The model outcome is validated.

Consider the streamwise area variation consists of a uniform constriction, with fixed length $L = 25\text{mm}$ and varying cross section shape, which is inserted in a uniform tube of internal diameter 25mm as schematically depicted in Fig. G.1. As the abrupt expansion is characterized by a sharp trailing edge, the streamwise position of flow separation x_s is at the constriction end ($x_s = x_3$). The pressure downstream from the flow separation point is assumed to be zero so that $P_d = 0$ and the model outcome remains constant for $x \geq x_s$. Consequently, imposing the upstream pressure P_0 is equivalent to imposing the driving pressure gradient $P_0 - P_d$.

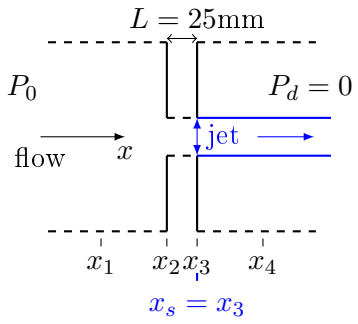

Figure G.1: Flow through an abrupt expansion.

For a given fluid and under assumption of a laminar and incompressible flow the streamwise momentum equation of the governing Navier-Stokes equations is simplified using additional assumptions. With driving pressure gradient dP/dx, bulk velocity $\overline{u}$, cross section area A, volume flow rate Q, velocity $u(x, y, z)$, kinematic viscosity ν ($1.5 \times 10^{-5}\text{m}^2/\text{s}$ for air) and density ρ ($1.2\text{kg}/\text{m}^3$ for air), applying conservation of volume flow rate $\frac{dQ}{dx} = 0$, the following simplified flow model accounts for both viscosity and flow inertia and depends therefore on both shape and area of cross section:

$$\frac{d\overline{u}}{dt} - \frac{Q^2}{A^3}\frac{dA}{dx} = -\frac{1}{\rho}\frac{dP}{dx} + \nu\left(\frac{\partial^2 u}{\partial y^2} + \frac{\partial^2 u}{\partial z^2}\right) \tag{G.1}$$

Making a 2D assumption allows to drop the first term within brackets resulting in the quasi-one dimensional flow model, which is further labeled Bernoulli-Poiseuille flow (BP) [25]. The first term at the left hand side accounts for flow unsteadiness. Note that in the current work, unsteadiness is due to varying the upstream flow conditions, *i.e.* $P_0(t)$, whereas the cross section area is time independent. Thus

$$P(x,t) = P_0(t) - \rho\int_0^x \frac{d\overline{u}}{dt}dx - \frac{\rho Q^2}{2}\left(\frac{1}{A^2(x)} - \frac{1}{A_0^2}\right) + \mu\int_0^x \left(\frac{\partial^2 u}{\partial y^2} + \frac{\partial^2 u}{\partial z^2}\right)dx \tag{G.2}$$

The bulk Reynolds number $Re = \frac{QD}{\nu A}$ and Strouhal number $Sr = \frac{f_0 DA}{Q}$ are defined using volume flow rate Q, hydraulic diameter D and characteristic frequency f_0. The experimental setup is described in Fig. 5.9b for $L_d = 0$cm. unsteady flow is assessed for $Q = 5$, 20 and 150l/min with driving frequency $f_0 = 500$Hz.

G.2 Results

Measured pressures $P_0(t)$ and $P_1(t)$ in case of a circular and elliptic cross section shape are illustrated in Fig. G.2. The unsteady oscillatory flow $P_0(t)$ with period $T = 1/f_0$ illustrates flow for $Sr \approx 1$ and $Sr < 1$. It is seen that the mean pressure value within the constriction varies as function of the cross section shape, *e.g.* the ratio observed for the elliptic section is greater than the one observed for the circular cross section. In addition, the amplitude of the pressure in the constriction around its mean value, $P_1(t) - \overline{P_1}(t)$, observed for the elliptic section is greater than the one observed for the circular cross section. Moreover, a phase difference between the upstream pressure P_0 and constriction pressure P_1 is observed, which is seen to depend on both Reynolds number and cross section shape as summarized in Table G.1. As for the unsteady flow, further research is needed to fully determine the flow dynamics.

Table G.1: Normalized phase difference of $P_0(t)$ and $P_1(t)$.

Q[l/min]	$\frac{t}{T}[-]$					
	cl	re	el	sq	tr	ntr
5	0.08	0	0.02	0.98	0.98	0.02
20	0.10	0.02	0.02	0.98	0.98	0.04
150	0.04	0.02	0.94	0.90	0.94	0.92

Fig. G.3 illustrates the scaled upstream pressure (P_0=1000Pa at time t=0s) and corresponding model outcome while accounting for the cross section. The influence of the unsteady

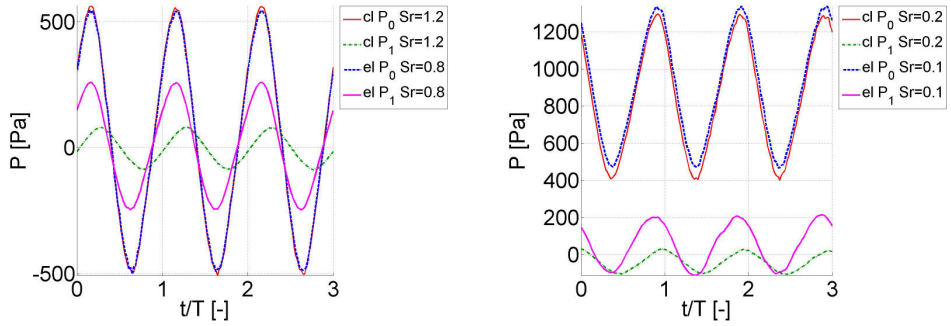

(a) $Q = 20\text{l/min}$, $Re \approx 2000$ (b) $Q = 150\text{l/min}$, $Re \approx 1.4 \times 10^4$

Figure G.2: Measured pressures P_0 and P_1 for a circular (cl) and elliptic (el) cross section.

term is apparent.

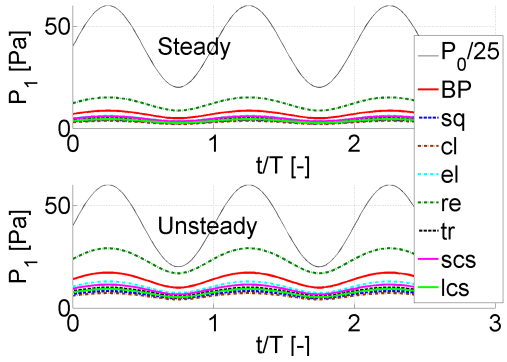

Figure G.3: Experimental values of P_1 for steady and unsteady flow.

G.3 Conclusion

The influence of the cross section shape on unsteady flow through a constricted channel is shown for modeled outcome and validated on experimental data.

Appendix H

Résumé de Français

Introduction

Des écoulements dans des canaux – commande par la pression – sont associés à des flux physiologiques pour lesquelles portions de canaux rétrécis se produisent naturellement ou sont dus à une pathologie. Des exemples bien connus sont le flux d'air à travers des voies respiratoires (asthme, production de la parole humaine, l'apnée obstructive du sommeil) et le flux sanguin à travers une sténose.

Par conséquent, des efforts sont faits pour modéliser ces écoulements afin de comprendre les mécanismes en jeu et de développer des outils d'aide pour les soins de santé. En raison de la complexité de l'appareil respiratoire humain et le système cardio-vasculaire, la plupart des études simplifient fortement la physiologie afin d'arriver à une configuration en fonction d'un nombre limité de paramètres physiologiques et physiques significatives. Une telle simplification améliore la compréhension des phénomènes physiques en cours et facilite la validation expérimentale de la précision des modèles.

En général, les simplifications du modèle d'écoulement à travers des parties du système respiratoire ou cardiovasculaire sont fondées sur une analyse non dimensionnelle des équations de Navier -Stokes tout en tenant compte des valeurs typiques de caractéristiques physiologiques, géométriques et écoulement. A partir de ces observations pertinentes des nombres non - dimensionnelles sont obtenus (nombre de Mach Ma, nombre de Reynolds Re, nombre de Strouhal Sr et le rapport largeur - hauteur du canal Ar) qui permettent de simplifier le modèle d'écoulement. Par exemple, le débit glottique lors de la phonation peut-être considérée incompressible, laminaire non visqueux, quasi - stationnaire et bi-dimensionel. L'hypothèse d'un débit glottique bi-dimensionelle implique une glotte pour laquelle la forme de section transversale est rectangulaire dont la hauteur $h(x)$ varie le long de la direction principale de l'écoulement x, alors que la glotte largeur w est fixé. Des modèles théoriques d'écoulement fondées sur ces hypothèses se traduisent par une description de l'écoulement quasi - unidimensionnel pour la comptabilisation des pertes cinétiques ainsi que les pertes visqueuses. Par conséquent, des modèles de flux quasi - unidimensionnel (1D) ou bi-dimensionnel (2D) se sont avérées extrêmement utiles pour comprendre la physique sous-jacente et sont appliqués à reproduire et prédire les phénomènes en cours en utilisant peu de ressources informatiques tout en permettant la validation expérimentale sur les répliques avec différents degrés de complexité.

Donc, le but du travail actuel est d'évaluer l'impact potentiel d'un modèle simplifie 'quasi-tridimensionnel' - avec un faible coût de calcul et qui prend en compte les pertes cinétiques, la viscosité ainsi que la forme de la section transversale - sur l'écoulement. L'issue du modèle d'écoulement proposes est considéré en ce qui concerne le résultat du modèle d'écoulement quasi-unidimensionnelle et bi-dimensionnelle, un modèle d'écoulement en trois dimensions, ainsi que des données de flux expérimentaux. Le modèle proposé avec un faible coût de calcul, est appliqué à la phonation, les systèmes de circulation biologiques et équations physiques.

Méthodologie

Tout d'abord, nous considérons des solutions quasi-analytiques pour l'écoulement visqueux développé laminaire alimente par la pression pour des canaux uniformes de différent, mais constante forme de section. Dans un premier temps, une solution quasi-analytique pour un nombre limité de formes de section transversale est considéré. Ensuite, une solution générale pour une forme arbitraire en coupe transversale est proposé, et la solution est comparée à une solution numérique obtenue en utilisant une approche pseudo-spectral.

Deuxièmement, nous exploitons la paramétrisation proposée d'une forme de section transversale arbitraire en utilisant les coordonnées tendues après l'équation de "Superformula". Nous nous concentrons sur des solutions pour les équations physiques en cas de deux dimensions (2D), ainsi que trois dimensions (3D). Solutions pour les équations de Laplace, Helmholtz et l'équation d'onde sont formulées et les résultats numériques sont présentés.

Troisièmement, étant donné que l'écoulement commandé par la pression dans les canaux rétrécis est une question importante pour les flux physiologiques pour des conditions normale ainsi que pathologiques, d'abord, nous considérons des canaux resserrées. Nous proposons un modèle simplifie 'quasi - tridimensionnel' (quasi-3D) qui prend en compte des pertes cinétiques, la viscosité ainsi que la forme de la section transversale. L'influence de la forme de la section transversale sur la distribution de pression dans le canal est examine. La distribution de la pression permettra de déterminer les forces exercées par l'écoulement sur les parois enveloppantes. C'est donc une quantité importante pour des applications biologiques. Le résultat de la 'quasi- tridimensionnel' modèle d'écoulement est comparée à l'issue d'un 'quasi-unidimensionnel' modèle de flux dont les détails de la forme de la section transversale sont négligés. Sténose biologique se produit pour différents fluides, dans lequel nous considérons la circulation sanguine et le flux d'air, car ces liquides se produisent dans des systèmes circulatoires importantes, *i.e.* le système cardio-vasculaire et le système respiratoire. Nous appliquons le modèle d'écoulement quasi - tridimensionnel proposé à un modèle physique de la phonation humaine, *i.e.* cordes vocales auto-oscillation pendant la production du son voisé. Nous discutons de l'impact potentiel du modèle d'écoulement en tenant compte de la forme de la section transversale de la pression minimum nécessaire pour maintenir la phonation.

Quatrièmement, on cherche à évaluer l'impact de la forme de la section transversale sur les propriétés d'écoulement expérimentalement ainsi qu'a valider le modelé quasi-3D sur des

données expérimentales. Le champ d'écoulement est quantifiée par échantillonnage spatio-temporelle de la pression et de champ de vitesse. Afin de caractériser complètement le champ d'écoulement, les conditions d'écoulement en amont sont modifiés. Un aperçu spatiale du champ d'écoulement est présentée en utilisant une visualisation de l'écoulement.

Enfin, 'Immersed Boundary Methode' est utilise pour simuler l'écoulement pour des canaux avec une forme de section différents. Les résultats numériques sont présentés et les quantités de flux simulés sont comparés aux quantités modélisées obtenues en utilisant le modèle 'quasi-tridimensionnel' et les quantités de flux mesurées.

Résultats

Tout d'abord, considérons un canal uniforme qui est entièrement définie par son section (forme et surface) et dont la forme peut être exprimé analytiquement en utilisant un ou deux paramètres géométriques (a, b). Concrètement, les formes suivants sont évalués: cercle (cl), rectangle (re), ellipse (el), anneau excentrique (ea), anneau concentrique (ca), half moon (hm), secteur circulaire (cs), triangle équilatéral (tr) et limacon (lm). Les formes de section transversale et les paramètres géométriques associés sont illustrés dans la Fig. H.1.

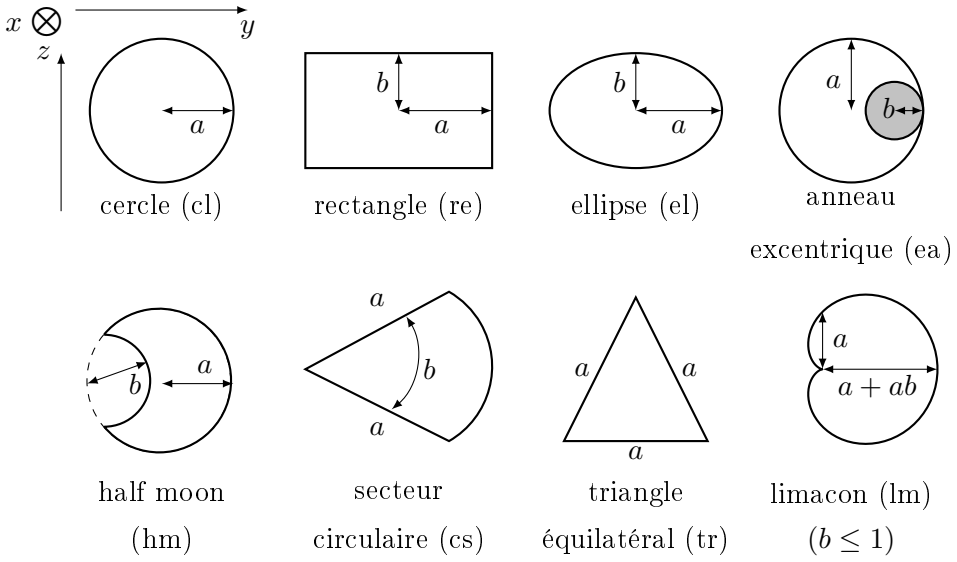

Figure H.1: Formes de section transversale avec leur paramètres (a, b) dans le plan (y, z). Notez que pour un secteur circulaire, b indique un angle. x désigne le sens de l'écoulement, y la largeur et z la hauteur.

Afin d'évaluer l'impact de la forme de la section transversale, deux jeu de paramètres α sont choisis, le jeu de paramètres par défaut (α_1) et le jeu de paramètres non-défaut (α_2), résultant en $u_{max}/u^{cl}_{max} \approx 1$ et $u_{max}/u^{cl}_{max} \ll 1$, respectivement. Par défaut le jeu de paramètres (α_1) est défini comme : $a_{re} = 1a_{cl}$, $a_{el} = 1.2a_{cl}$, $b_{ea} = 0.2a_{ea}$, $b_{cs} = \pi/3$, $b_{hm} = 0.2a_{hm}$ and

$b_{lm} = 0.2$. Le jeu de paramètres non-défaut (α_2) correspond a : $a_{re} = 10a_{cl}$, $a_{el} = 10a_{cl}$, $b_{ea} = 0.6a_{ea}$, $b_{cs} = \pi/6$, $b_{hm} = 0.6a_{hm}$ and $b_{lm} = 0.6$. Ceci permets de considéré trois jeu de paramétrés pour un forme de section donne avec un mémé surface $A = 79\text{mm}^2$:

- jeu de paramètres par défaut (α_1),
- jeu de paramètres non-défaut (α_2),
- largeur fixe w, *i.e.* $y_{tot} = w$.

La distribution de vitesse résultant $u(y/a_{cl}, z/a_{cl})$ pour un canal uniforme avec surface $A = 79$ mm^2 et le gradient de pression $dP/dx = 75$Pa est en outre illustrée dans la Fig. H.2 pour le jeu de paramètres par défaut (α_1) et à la Fig. H.3 pour le jeu de paramètres non-défaut (α_2) et pour la condition avec largeur ixe ($y_{tot} = w$).

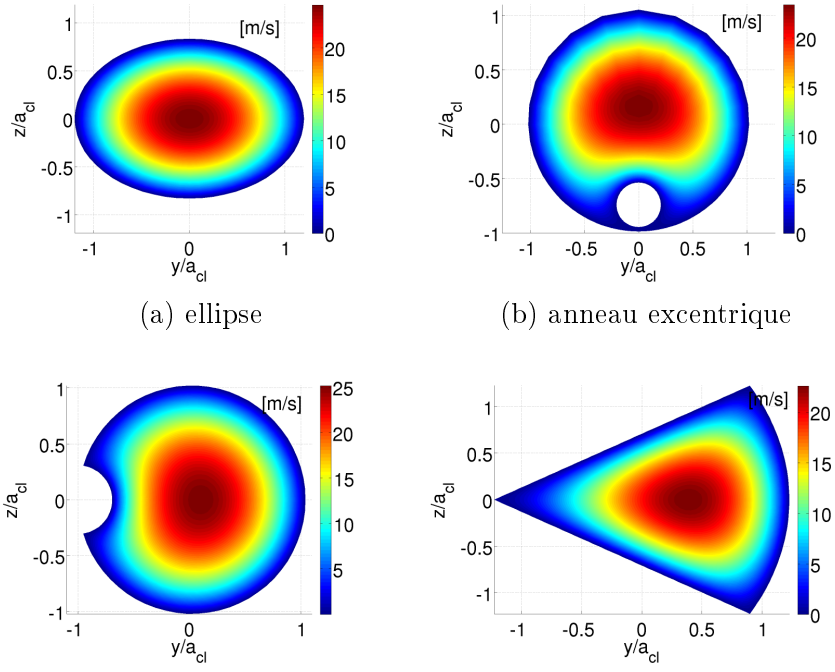

(a) ellipse (b) anneau excentrique

(c) half moon (d) secteur circulaire

Figure H.2: Distributions de vitesse $u(y/a_{cl}, z/a_{cl})$ pour A $= 79\text{mm}^2$ et $dP/dx = 75\text{Pa/m}$ pour le jeu de paramètres par défaut (α_1) correspondant $a_{cl} = 5$mm.

Dans la Fig. H.2, obtenue en utilisant le jeu de paramètres par défaut (α_1), on voit que la vitesse maximale pour toutes les formes de section transversale varie entre les valeurs observées pour un cercle et un triangle équilatérale. A noter que la vitesse est réduite avec 20%. Fig. H.3

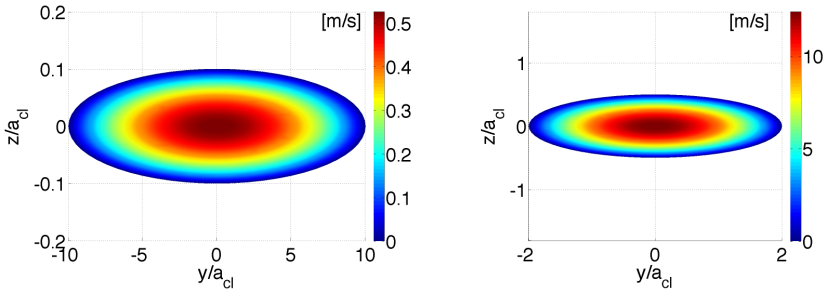

(a) ellipse

(b) ellipse

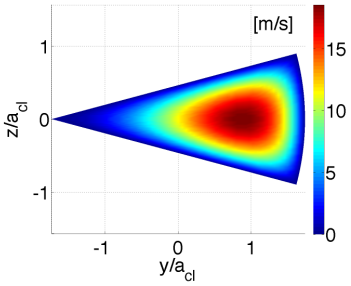

(c) secteur circulaire

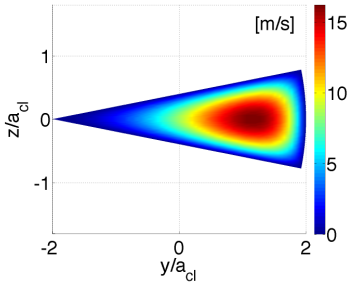

(d) secteur circulaire

Figure H.3: Distribution de vitesse $u(y/a_{cl}, z/a_{cl})$ pour A = 79mm^2 et $dP/dx = 75$Pa/m. A gauche) le jeu de paramètres par défaut (α_2) et à droite) largeur fixe (w) avec $w = 4 \times a_{cl}$ et $a_{cl} = 5$mm.

illustre le jeu de paramètres non-défaut (α_2) ainsi qu'une largeur fixe (w). La réduction de vitesse est plus importante et varie entre 20% à 98% dépendant la forme.

Ensuite, pour les formes de section arbitraires, Fig. H.4 illustre l'erreur maximale E_{max} en fonction de la nombre de discrétisation radiale N pour les formes tout en utilisant la méthode pseudo-spectrale. L'erreur estimée devient constante lorsque le nombre radial $N > 40$ et $E_{max} < 10\%$. Pour les formes avec des frontières lisses, une haute précision ($E_{max} < 1\%$) peut être obtenue pour un nombre radiale inférieure a 40 ($N < 40$), tandis que $E_{max} < 4\%$ pour $N \geq 73$ lorsque les formes ne sont pas lisses. Quoi qu'il en soit, la tendance est que l'erreur estimée E_{max} diminue lors que N augmente. Ce qui montre la convergence de la solution numérique.

L'estimation de l'erreur maximale en fonction de la nombre de troncature N de la somme est illustrée sur la Fig. H.5. On voit que pour toutes les formes évalués une bonne précision est atteint pour l'erreur général ainsi que l'erreur maximal ($E_{RMS} < 0,5\%$ et $E_{max} < 0,03\%$) pour $N > 6$. Table H.1 illustre la comparaison des erreurs E_{max}. Une bonne précision est obtenu pour toutes les formes de section évalue.

Deuxièmement, laissez $f^H(x, y) = x + 3y + \cos(x + 2y)$ soit la condition limite pour le problème de Dirichlet de l'équation de Helmholtz. Fig. H.6a illustre l'erreur relative en fonction

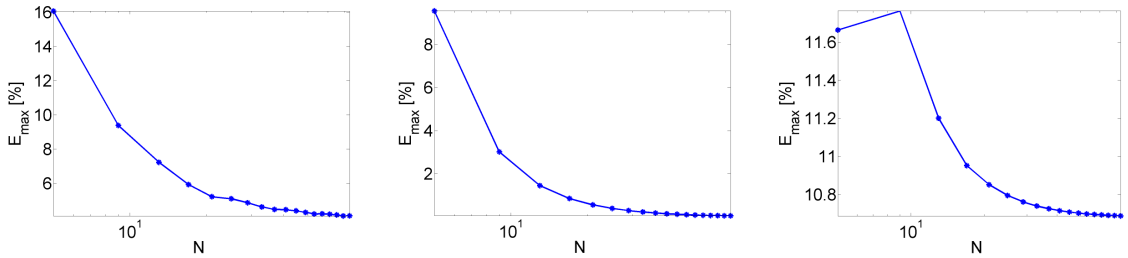

(a) rectangle (b) ellipse (c) triangle équilatéral

Figure H.4: Illustration de l'erreur maximale estimée E_{max} avec la fonction de radiale nombre N lorsque $M = 72$.

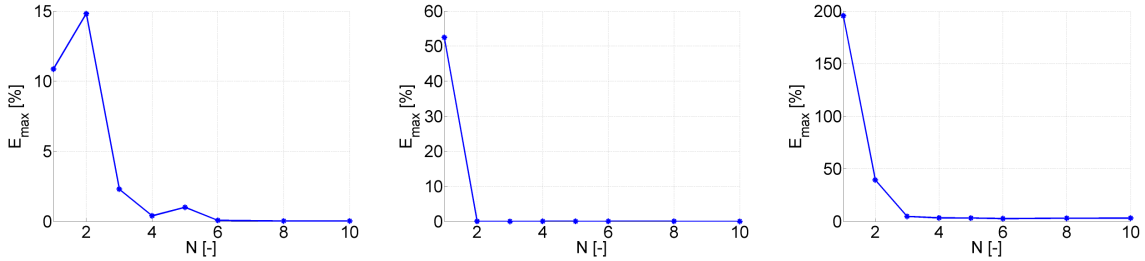

(a) rectangle (b) ellipse (c) triangle équilatéral

Figure H.5: Illustration de l'estimation de l'erreur maximale E_{max} en fonction de la nombre de troncature N de la somme.

Table H.1: Comparaison de l'erreur E_{max} à l'approche générale de pseudo-spectrale analytique et numérique.

approche	circle	rectangle	ellipse	triangle équilatéral
présent [%] ($N > 6$)	0	0.393	1.44e-14	0.479
numérique [%] ($N > 40$)	0.046	0.046	4.09	10.69

du nombre tronqué de somme N. De Fig. H.6a et Fig. H.6b on voit qu'un bonne ($err_H < 2\%$) estimation de l'état initial peut être observée pour la solution de développement de Fourier à l'ordre $N = 7$ et le modèle et les valeurs limites imposés correspondent bien. En outre, la solution de domaine intérieur pour $N = 7$ est représenté sur la Fig. H.6c.

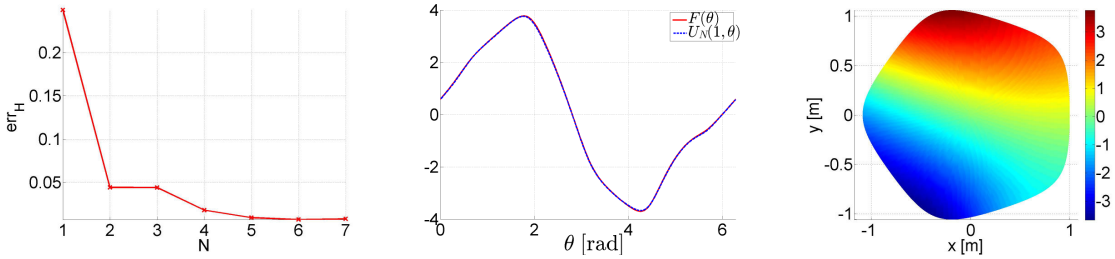

(a) erreur (b) valeur frontières (c) distribution

Figure H.6: (a) Illustration d'erreur relative de frontières en fonction du nombre tronqué de somme N pour le problème de Dirichlet de l'équation de Helmholtz. (b) Comparaison de la valeur limite entre l'état initial et la somme tronqué issu u_N^H lorsque l'ordre $N = 7$ pour l'équation de Helmholtz. (c) Distribution de la solution représentée par la somme tronquée $N = 7$.

Troisièmement, nous modélisons la distribution de pression à l'aide du modèle d'écoulement quasi - tridimensionnel proposé pour une douceur et un canal resserré brusque avec différentes formes de section transversale pour l'écoulement d'air et la circulation sanguine. Différents configurations de sténose sont considérés en faisant varier certains paramètres géométriques représentés sur la Fig. H.7: degré de sténose R_C, superficie minimale A_{min}, et l'étendue streamwise de constriction minimum L_C. L'impact possible des données de section transversale sur la répartition de la pression est évaluée pour: jeu de paramètres par défaut (α_1), jeu de paramètres non - défaut (α_2) et le jeu de paramétrés correspondant a une largeur fixe ($y_{tot} = w$).

Fig. H.8 illustre la répartition de la pression pour une extension lisse et pour une détente brusque pour les différents jeux de paramètres - jeu de paramètres par défaut (α_1), jeu de paramètres non - défaut (α_2) et largeur fixe ($y_{tot} = w$) - appliqué à chacune des formes de section transversale. Les paramètres de sténose sont définies comme surface minimal $A_{min} = 79\text{mm}^2$, $R_c = 30\%$ et $L_C/D_{cl} = 6$. La pression en amont est fixé à $P_0 = 75\text{Pa}$. La distribution de pression est modélisée en utilisant le modèle d'écoulement quasi tridimensionnel, un modèle quasi - unidimensionnel (BP) et un écoulement idéal (B) sont indiqués également.

On voit que l'influence de la forme de section sur les résultats du modèle en utilisant le jeu de paramètres par défaut défini α_1 est moins prononcée que pour le jeu de paramètre non- défaut α_2 ou pour le jeu de paramétrés correspondant a une largeur fixe $y_{tot} = w$. Les distributions de pression obtenues pour toutes les formes de section transversale à l'aide de paramètres par défaut α_1 se rapproche de la distribution d'un écoulement idéal (B) pour laquelle $\Delta P_{visc} = 0$ de sorte que l' approximation quasi - unidimensionnel (BP) se traduit par une sous-estimation grave de la chute de pression le long de la partie resserré. D'autre part, on voit que pour le jeu de paramètre non - défaut α_2 et largeur fixe $y_{tot} = w$ l'ampleur de la chute de pression varie de façon significative de sorte que, en fonction de la section transversale de forme, la modelé quasi - unidimensionnels (BP) résulte dans une surestimation, une sous-

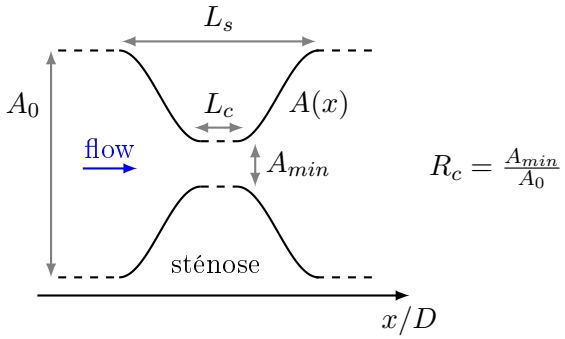

Figure H.7: Vue d'ensemble schématique d'un canal resserré, ce qui représente une sténose, orienté selon la streamwise x direction. Le degré de sténose est exprimée par rapport $R_c = A_{min}/A_0$ et son streamwise extension par L_s.

estimation ou une estimation précise de la chute de pression dans la constriction. Notez que l'imposition d'un largeur $y_{tot} = w$ résulte dans une bon accord entre l'approximation avec le modelé quasi-unidimensionnel (BP) et la distribution de la pression obtenue en utilisant le modelé quasi-3D avec une forme de section rectangulaire (re).

Ensuite, nous voulons évaluer l'impact potentiel du modèle d'écoulement quasi - tridimensionnel, qui prend en compte la forme de la section transversale, sur les résultats d'un modèle de la phonation physique en comparaison avec un (BP) écoulement quasi - unidimensionnel modèle. Les résultats simulés sont obtenu lors d'un analyse de stabilité de modelé. On s'intéresse au seuil de pression nécessaire afin de maintenir la phonation P_{on}. Les seuils obtenus sont illustrés dans la Fig. H.9a en fonction du degré de rétrécissement de $1 - A^{10}/A_0$ qui est indépendant de la section la forme et la Fig. H.9b en fonction du rapport d'aspect $Ar^{10}_{\cdot} = w/h^{10}_{\cdot}$, qui dépend de la forme de section transversale.

Pour les grands degrés de constriction (plus de 75% dans la Fig. H.9a) la forme de la section transversale peut être négligé. Pour moyennes ou petites constriction degrés (moins de 75% dans la Fig. H.9a) la pression de seuil de déclenchement de la phonation prédit P_{on} dépend de la forme de section. En effet, moins de pression est nécessaire pour maintenir l'oscillation d'un forme circulaire que pour une forme rectangulaire ou elliptique. L'écart entre les pressions estimées P_{on} pour des sections différentes augmente à mesure que le degré de constriction (Fig. H.9a) ou rapport d'aspect (Fig. H.9b) diminue. En outre, on observe que pour toute la plage des degrés d'étranglement et des rapports d'aspect teste, une géométrie rectangulaire peut être modélisée à l'aide approximation quasi- unidimensionnel (BP) d'écoulement. Les simulations de la phonation et les seuil de pressions P_{on} obtenus suggèrent que pour les grands degrés de constriction (plus de 75% dans la Fig. H.9a) le résultat du modèle dépend d'une valeur précise de la zone rétrécie A^{10} en tant que paramètre d'entrée de modèle. Ce résultat est la conséquence de la faible différence constatée dans les quantités d'écoulement prédites lorsque la viscosité domine le comportement d'écoulement et des effets relie a l'inertie deviennent moins prononcées et donc la forme de la section transversale devient plus important. Pour les degrés de constriction moyennes ou petites (moins de 75% dans la Fig. H.9a), il est nécessaire

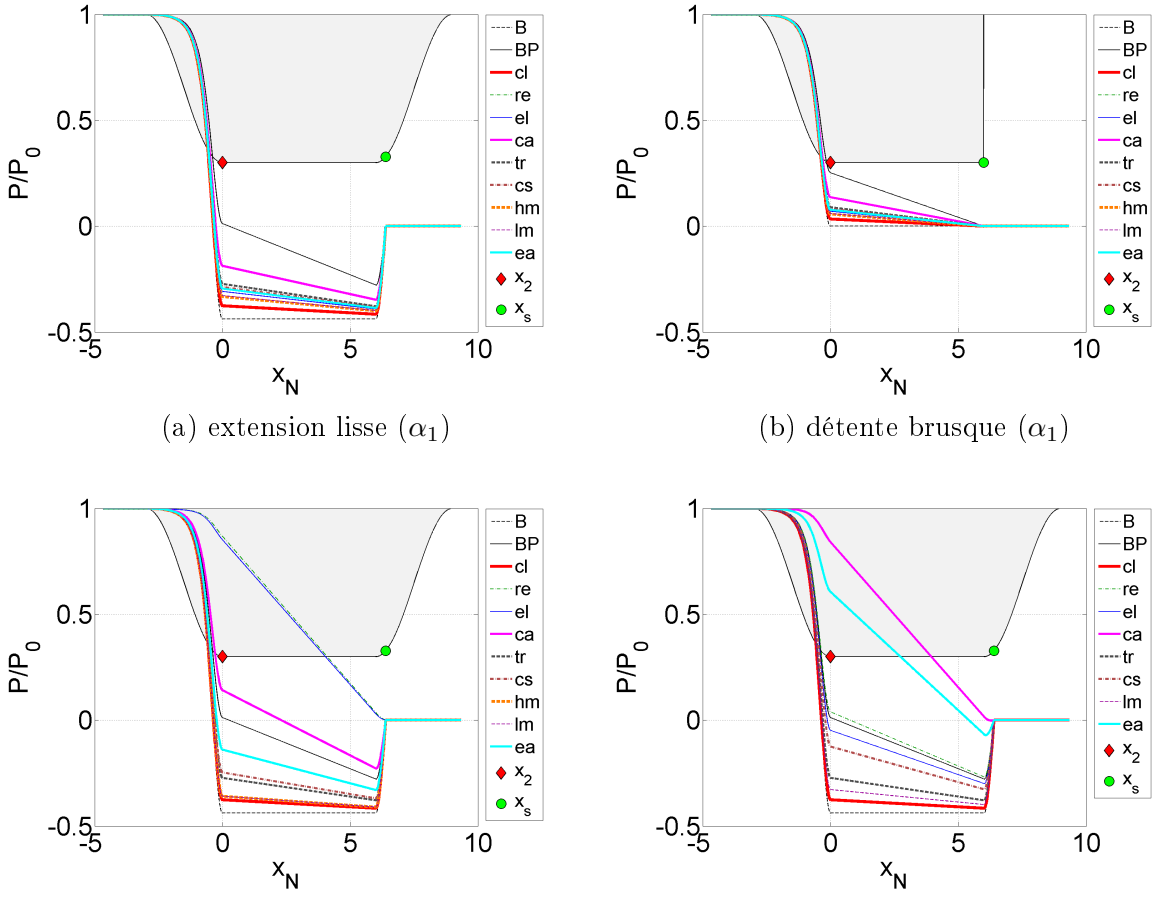

(a) extension lisse (α_1)

(b) détente brusque (α_1)

(c) extension lisse (α_2)

(d) extension lisse ($y_{tot} = w$)

Figure H.8: Illustration de la distribution de pression normalisée $P(x)/P_0$ selon le modèle quasi-tridimensionnel pour l'écoulement d'air et surface minimum $A_{min} = 79\text{mm}^2$, $P_0 = 75\text{Pa}$, $R_c = 30\%$ et $L_C/D_{cl} = 6$ pour les différentes formes de sections transversales obtenues pour a) l'expansion lisse et jeu de paramètres par défaut (α_1), b) une expansion brusque et jeu de paramètres par défaut (α_1), c) jeu de paramètres non-défaut (α_2) et d) largeur fixe ($y_{tot} = w$). La répartition de pression associé à un modèle quasi-unidimensionnel (BP) et un écoulement idéal (B) sont indiqués. La géométrie normalisée est indiquée en nuance de gris et la streamwise x direction est normalisée comme $X_N = x/D_{cl}$. Titre de référence, la constriction apparition x_2 et la position de séparation x_s sont indiquées.

de quantifier la zone rétrécie A^{10} ainsi que d'obtenir des informations sur la forme de la section transversale afin de déterminer l'impact de la forme en coupe transversale sur les pertes visqueuses dans le modèle d'écoulement. Lorsque le rapport d'aspect Ar^{10} est utilisé comme paramètre d'entrée du modèle (Fig. H.9b) des informations supplémentaires sur la forme de la section transversale est nécessaire comme un paramètre d'entrée de modèle pour tous les rapports d'aspect.

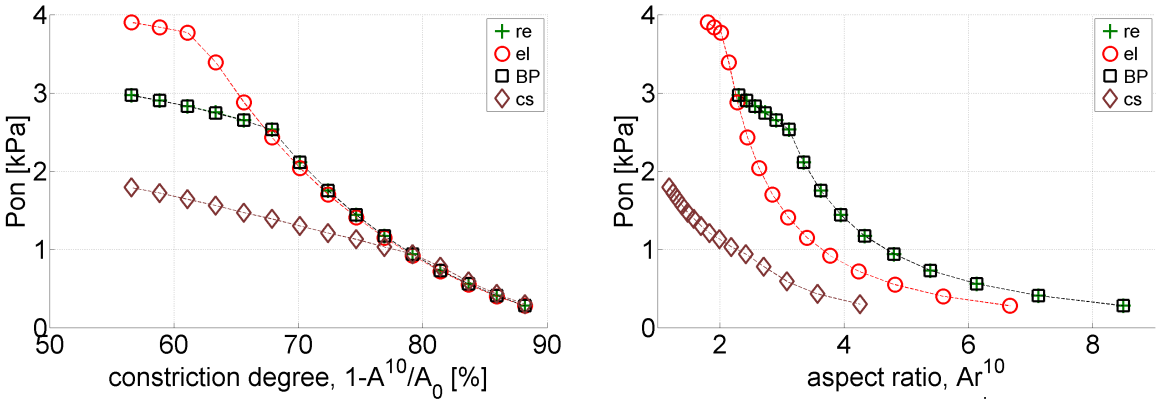

(a) $Pon(1 - A^{10}/A_0)$ (b) $Pon(Ar^{10})$

Figure H.9: (a, b) seuil de pression minimum de phonation P_{on} en fonction du degré de rétrécissement de $1 - A^{10}/A_0$ (a) et en fonction du rapport d'aspect Ar^{10}.

Quatrièmement, huit portions de canaux resserrés avec différentes formes de section transversale illustrés dans la Fig. H.10 sont considérés. Les formes de sections transversales ont surface constante $A_c = 79$ mm^2 et longueur constante $L_c = 25$mm le long de la streamwise x direction. Chaque constriction peut être vissé à un canal en amont et en aval avec le filetage le long des parois externes de façon à obtenir une partie de canal rétrécie. Un aperçu des configurations évaluées pour chacune des formes de constriction de la Fig. H.10 est donnée dans le tableau H.2.

Dans un premier temps, nous quantifier et évaluer l'impact de la forme de la section sur les valeurs de pression mesurées dans la constriction. Des pressions sont mesurées pour différentes conditions. Afin de quantifier l'influence de l'impact global de la forme de la section transversale sur la pression mesurée dans le rétrécissement on mesure les valeurs de la pression relative pour toute la gamme des débits considérés $\Delta(P_1/P_0)$ et les valeurs particulières de la pression amont P_0 ou nombre de Reynolds Re.

De l'observation de l'impact global de la section sur la pression moyenne dans l'étranglement, il se trouve que les deux mesures $\Delta P_1/P_0$ ou $\Delta(P_1/P_0)$ resultent dans les mêmes tendances qui sont resume à partir des observations suivantes:

- observations lorsqu'on différé soit la forme de la section (de l'impact de la forme de la section transversale) soit le conditionnement de flux (impact des flux conditionné):
  - l'ordre de grandeur de l'impact s'élève à 10% jusqu'à 30% de la pression amont. Ce résultat illustre le fait que, au moins pour la gamme de P_0 ou Re utilisée, les détails de la forme de la section ou les détails de l'installation de débit sont tout aussi importants.
  - en général, l'effet est plus grande en présence d'un canal en aval de l'étranglement

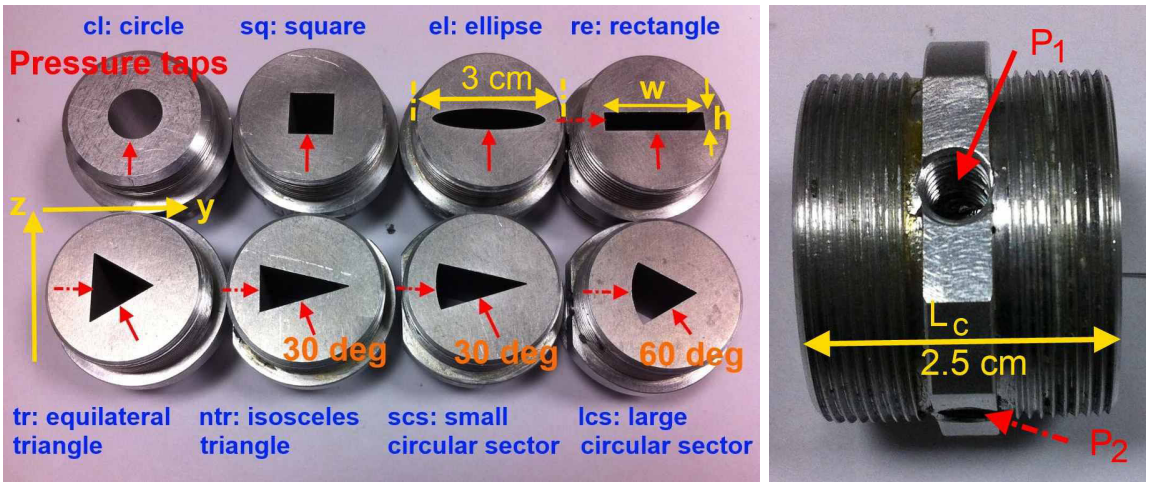

(a) vue de transversale (b) vue de streamwise

Figure H.10: Illustration de formes de section uniforme expérimentalement évaluées et la position des prises de pression P_1 (plein flèche) et P_2 (flèche pointillée): a) vue de face des formes de section transversale le long de la plan (y, z). A titre d'exemple, la largeur totale w et la hauteur h est indiqué pour la forme de section transversale rectangulaire. b) vue par fractions de la partie rétrécie de longueur L_C. Filetage est présente au niveau des bords extérieurs de la partie de canal rétrécie. Les positions des prises de pression est souligné.

(confiné à jet à la sortie de la constriction) qu'en absence d'un tel canal en aval (à jet libre à la sortie de la constriction).

- observation due a la variation de la section transversale de forme (l'impact de la forme de section):
  - l'impact des formes de section transversale réduit (de ≈25%, à ≈10%) quand on conditionne le développement de flux amont (L_u augmente) ou quand on utilise un élément de mélange de fluide (OGP).
  - l'augmentation de la pression en amont ou le nombre de Reynolds n'augmente pas de manière significative l'influence de la forme de la section transversale. Cela donne à penser que, en raison de la dissipation de la turbulence et le développement, le champ d'écoulement perd de l'identité ou empreinte de la géométrie au moyen des structures d'écoulement caractérisant la forme de la section transversale. Visualisation de l'écoulement et de l'analyse de la vitesse d'écoulement peuvent éventuellement offrir une confirmation de ce point.
- observations lorsque on varie le débit conditionné (impact des flux conditionné):
  - l'impact de l'écoulement conditionné dans la présence d'un canal en amont (jet confiné) est moins sensible à une augmentation du nombre de Reynolds que, en l'absence d'un canal en amont (à jet libre dont l'impact réduit de plus de la moitié de

Table H.2: Vue d'ensemble des conditions expérimentales évaluées pour les formes de constriction de la Fig. H.10 indiquant le flux conditionné occasion. Au cas où aucun écoulement conditionné est mentionné bords tranchants d'entrée sont évalués. Les quantités de flux mesurées sont indiquées: prises de pression, transversale et profils de vitesse longitudinales en utilisant anémométrie à film chaud (HF) et les flux de visualisation (FV).

Label	L_u	L_d	**Pression**[1]	**Champ d'écoulement**[2,3]	**Commentaire**	
	Conditions entrée: arêtes vives (Fig. 5.9) → développement écoulement					toutes les formes
A	2cm	0cm	P_0, $P_1(P_2)$		jet libre	
		15cm	P_0, $P_1(P_2)$, P_3		jet confiné	
B	35cm	0cm	P_0, $P_1(P_2)$		jet libre	
		15cm	P_0, $P_1(P_2)$, P_3		jet confiné	
C	1m	0cm	P_0, $P_1(P_2)$	HF, FV	jet libre	
		15cm	P_0, $P_1(P_2)$, P_3		jet confiné	
	Conditions entrée: élément de mélange (Fig. 5.10) → écoulement de mélange					
D	35cm (ogp)	0cm	P_0, $P_1(P_2)$	HF	jet libre	
		15cm	P_0, $P_1(P_2)$, P_3		jet confiné	
E	35cm (tgph)	0cm	P_0, $P_1(P_2)$	HF	jet libre	forme circulaire
		15cm	P_0, $P_1(P_2)$, P_3		jet confiné	
F	35cm (tgps)	0cm	P_0, $P_1(P_2)$	HF	jet libre	
		15cm	P_0, $P_1(P_2)$, P_3		jet confiné	
	Conditions d'entrée: pas de bords tranchants (Fig. 5.8) → développement écoulement					
G	35cm (cone)	0cm	P_0, $P_1(P_2)$	HF	jet libre	
		15cm	P_0, $P_1(P_2)$, P_3		jet confiné	
H	1m (d1cm)			HF	jet libre	

(1) Flux régulier pour $0 < Q \leq 200$l/min ou $Re \leq 25000$.
(2) Flux régulier pour $0 < Q \leq 100$l/min ou $Re \leq 15000$.
(3) Pour l'anemometrie avec film-chaud on utilise un canql en amont avec un longueur de 1m.

sa grandeur que Re est accru), de sorte que le canal en amont a un effet de mémoire des conditions d'écoulement en amont, même pour des nombres de Reynolds bien au-dessus du régime de transition. Notez que on ne trouve pas un tel effet de mémoire prononcée (ou empreinte de débit) à la forme de la section transversale.

Ensuite, les profils de vitesse mesurés et les champs d'écoulement visualisées sont présentés en mettant l'accent sur l'influence de la forme de la section transversale et le conditionnement de flux. Par conséquent, les profils mesurés sont représentés en fonction de la forme de la section transversale et en fonction de l'écoulement conditionné appliquée plutôt que comme une fonction de la vitesse d'écoulement volumique appliqué afin d'évaluer leur impact sur les propriétés d'écoulement. Afin de quantifier l'effet de la forme de la section transversale sur l'étendue de cône potentiel, la vitesse longitudinale est évaluée dans le champ proche en aval de l'étranglement étant donné les variations de la structure de l'écoulement en raison soit de la forme de la section transversale ou les conditions d'écoulement en amont. L'impact

de la forme de la section sur le champ proche est évident pour tous les débits de volume évalués par rapport à la vitesse initiale u_0, dans la mesure du cône potentiel par rapport à son déclin initial. La vitesse initiale à la sortie de l'étranglement, par exemple, est considéré de faire varier jusqu'à 20%. Comme pour les mesures de pression, les profils de vitesse mesurés suggèrent que le comportement de l'écoulement est formé par les arêtes vives et la présence de structures d'écoulement. En effet, la tendance à la baisse de la vitesse dans le cône potentiel suggère le foracage du jet dû aux arêtes vives à l'entrée du rétrécissement.

Ensuite, l'influence de l'état d'écoulement en amont évaluée sur les mesures de profils de vitesse longitudinales proche de la sortie est exploré. En comparant les profils de vitesse en présence de l'élément de mélange (grille unique à l'entrée de constriction) avec les profils de vitesse en l'absence d'un tel élément de mélange (des arêtes vives à l'entrée de constriction) illustre l'impact sévère de l'élément de mélange sur la mise au point d'écoulement de champ proche pour tous les débits. La présence de l'élément de grille de mélange unique diminuera la zone à l'entrée de constriction avec $\approx 50\%$ de la zone de constriction. Il est évident que, en conséquence la vitesse augmente en présence de l'élément de mélange par rapport à la vitesse obtenue en l'absence de l'élément de mélange pour le même débit volumique. Par conséquent, en plus d'affecter le champ proche en raison de l'augmentation du débit de mélange, l'effet de l'élément de mélange est de nature à réduire le nombre de Reynolds pour laquelle la transition à un écoulement turbulent se produit. Une première confirmation de cet effet est fourni par le minimum du cône potentiel associée à la transition régime étendue qui réduit de $Q \approx$35l/min à $Q \approx$20l/min lors d'un élément de mélange est utilisé. En outre, l'augmentation du débit de mélange augmente la décroissance de la vitesse observée dans l'étendue de cône potentiel en raison de l'interaction accrue de la vitesse et de la ligne centrale du fluide enveloppant. Cela suggère aussi que le motif d'écoulement est moins stable en présence d'un élément de mélange qui à son tour à nouveau justifié la diminution des nombres de Reynolds associés au régime de transition. Néanmoins, bien que le motif d'écoulement est soutenu à être moins stable, la présence de l'élément de mélange ne semble homogénéiser le comportement de l'écoulement de telle sorte que, en particulier les profils de vitesses mesurés pour la section transversale circulaire et rectangulaire ne sont plus en accord avec les tendances observées pour d'autres formes de section transversale.

En outre, plus de conditions sont testes pour la constriction circulaire afin d'évaluer l'influence de l'état d'écoulement en plus de profondeur. On constate que l'état d'écoulement en amont détermine le comportement de l'écoulement, ainsi que sa stabilité et donc les nombres de Reynolds de la transition lorsqu'on examine l'écoulement immédiatement en aval de la sortie de la constriction. Le taux de décroissance du jet en aval de la sortie est moins influencée par l'état de la circulation en amont et 'oublie' la condition d'écoulement en amont. Comme tel, il peut être remarqué que le début de décroissance observée pour les deux conditions de référence correspond. De plus, l'influence de la forme de la section transversale sur les profils de vitesse transversale mesurée est évaluée. On voit que, à la fois pour l'axe 'majeure' et 'mineur' du jet initiale à la sortie de la constriction occupée par la couche limite (par rapport à la partie centrale plane) dépend de la forme de la section transversale. Évidemment, cela dépend de la vitesse d'écoulement aussi bien que l'augmentation du débit car ceci aug-

mentera le nombre de Reynolds exprimant une contribution visqueuse réduite a l'écoulement. Des structures d'écoulement d'une grande diversité (y compris l'inversement de l'axe) sont observés lors de l'examen des deux planes de visualisation du jet en sortie des constrictions avec des formes différents.

Enfin, une comparaison des quantités de flux mesurés et modélisés est évaluée afin de commenter sur l'exactitude et les limites du modèle simplifié quasi - tridimensionnel proposé. Étant donné que le modèle d'écoulement quasi tridimensionnel est présenté comme une amélioration d'un modèle d'écoulement quasi- unidimensionnel (BP). Il semble juste de décider qu'une prédiction réussie est obtenu sous la forme du modèle d'écoulement quasi-tridimensionnel fournit une prédiction plus précise par rapport aux données mesurées obtenues que par le modèle d'écoulement quasi- unidimensionnel. En outre, dans le précédent, il a été soutenu que par rapport aux solutions de la couche limite classiques, le modèle d'écoulement quasi - tridimensionnel proposé a l'avantage offrant un moyen (cruel) de rendre compte de la forme de section transversale. Néanmoins, nous nous intéressons à l'évaluation des résultats d'une solution de couche limite sur le modèle d'écoulement quasi - tridimensionnel proposé. Dans la suite, une solution de couche limite est obtenue pour deux dimensions (2D) et écoulement de révolution (Axi) par l'application de la méthode Thwaites (Th). Par conséquent, des mesures de pression, à l'intérieur de la constriction partie de canal P_1, pour le rectangle et la forme circulaire de la section transversale sont comparés à des résultats de la quasi- tridimensionnel (mod), quasi-unidimensionnel (BP) et de la couche limite solution (ThAxi pour circulaire et Th2D pour rectangulaire). Pour les autres formes évalués de section transversale, les pressions mesurées au sein de la constriction P_1 sont comparés aux résultats de la quasi - tridimensionnel (mod) et quasi - unidimensionnel (BP) modèle. Concrètement, les pressions mesurées obtenues sont comparées à des valeurs modélisées de la Fig. H.11.

Étant donné que le rétrécissement est uniforme, toutes les valeurs modélisées résultent dans une prédiction positive de la pression à l'intérieur de la constriction. En outre, le rapport P_1/P_0 diminue si on augmente P_0. Par conséquent, aucune de modèle de flux appliqué est capable de prédire avec précision les pressions négatives mesurées dans le rétrécissement ou l'extrémale observée pour les pressions mesurées au sein du régime de transition $2000 < Re < 4000$. Les deux phénomènes résultent de phénomènes d'écoulement plus complexes alors comptabilisés dans les modèles de flux appliquées et elles sont déclenchées probablement par les bords tranchants à l'entrée de l'étranglement. La précision du modèle quasi - tridimensionnel par rapport à des données mesurées se résume comme $< 5\%$ pour $P_0 > 300$Pa et de $<5\%$ jusqu'à $< 20\%$ pour $P_0 < 300$Pa selon la forme de la section transversale. Observations mentionnées sont en général en faveur de modèle d'écoulement quasi - tridimensionnel, il est donc conclu que le modèle quasi - tridimensionnel proposé est évalué positif, tandis que les pauvres précision lorsqu'ils sont confrontés à des phénomènes de flux complexes est gardé à l'esprit.

En outre, les mesures de profil de vitesse transversale moyenne à la sortie de l'étranglement en l'absence d'un tuyau en aval, offrent (en plus des mesures de pression au sein de la constriction) une occasion pour examiner avec plus de précision la pertinence et les limites du modèle quasi - tridimensionnel proposé et donc l'approche qui consiste a exploite en partie une écoulement pleinement développé. En effet, le débit volumique mesuré Q permet d'estimer

la distribution de vitesse en supposant un écoulement visqueux pleinement développé. Une comparaison est faite entre les profils transversaux modélisées et mesurées le long de l'axe 'majeur' et 'mineur'. En général, à la fois pour l'axe 'majeur' et 'mineur', on constate que les profils transversaux modélisées et mesurées correspondent bien à l'intérieur de la couche limite. Toutefois, étant donné le profil modélisé est entièrement développé, il a tendance à surestimer la vitesse de l'écoulement de base enveloppé par les couches limites. Étant donné que le modèle simplifié ne comptes pas pour la dynamique des fluides complexes, qui joue bien sur un rôle dans les résultats expérimentaux présentés - telles que la génération de vortex, la turbulence ou l'interaction d'un vortex avec la turbulence - à première vue, la comparaison est étonnamment bonne.

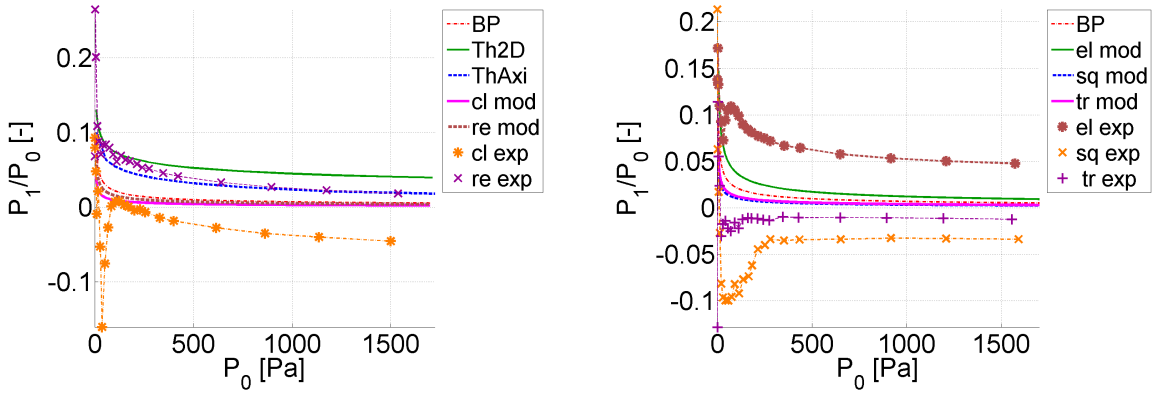

(a) cl and re

(b) sq, tr and el

Figure H.11: Pressions mesurées et modélisées normalisées au sein de la constriction P_1/P_0 en fonction de la pression amont P_0: a) la forme de la section transversale rectangulaire et circulaire et b) forme elliptique, carré et équilatéral section triangulaire. Valeurs modélisées sont obtenues à partir des résultats de la quasi-tridimensionnel (mod), quasi-unidimensionnel (BP) et une solution de la couche limite (ThAxi pour circulaire et Th2D pour rectangulaire).

Enfin, les données numériques du champ d'écoulement sont obtenues en présence d'un tuyau en aval de forme différente en coupe transversale. Fig. H.12 et Fig. H.13 illustrent les résultats simulé (IB, Immersed Boundary Method) et modélise (mod) pour la distribution de pression et la distribution de vitesse selon x pour $P_0 = 35$Pa. Les distributions sont présentés pour une forme de section circulaire, elliptique, rectangulaire et secteur circulaire. La répartition de la pression modélisée représenté sur la Fig. H.12 montre les resultats du modèle quasi-tridimensionnel. Pour la méthode IB, la répartition de la pression selon la direction principal de l'écoulement (x) sur la Fig. H.12 est obtenue en échantillonnant les valeurs instantanées pour chaque position par fractions de Z à la direction transversale (X, Y) qui corresponds a la position associée à la vitesse maximale pour un écoulement pleinement développe. Fig. H.13 illustre la vitesse streamwise modélisé (mod) et simulé (IB) obtenu comme la vitesse moyenne transversale. Les valeurs modélisées sont échantillonnées aux mêmes postions (X, Y) tandis que le profil de vitesse transversale est obtenue à partir du débit volumique Q_{mod} résultant du modèle d'écoulement quasi tridimensionnel pour calculer la

distribution de vitesse le long de l'partie rétrécie en supposant développé écoulement visqueux.

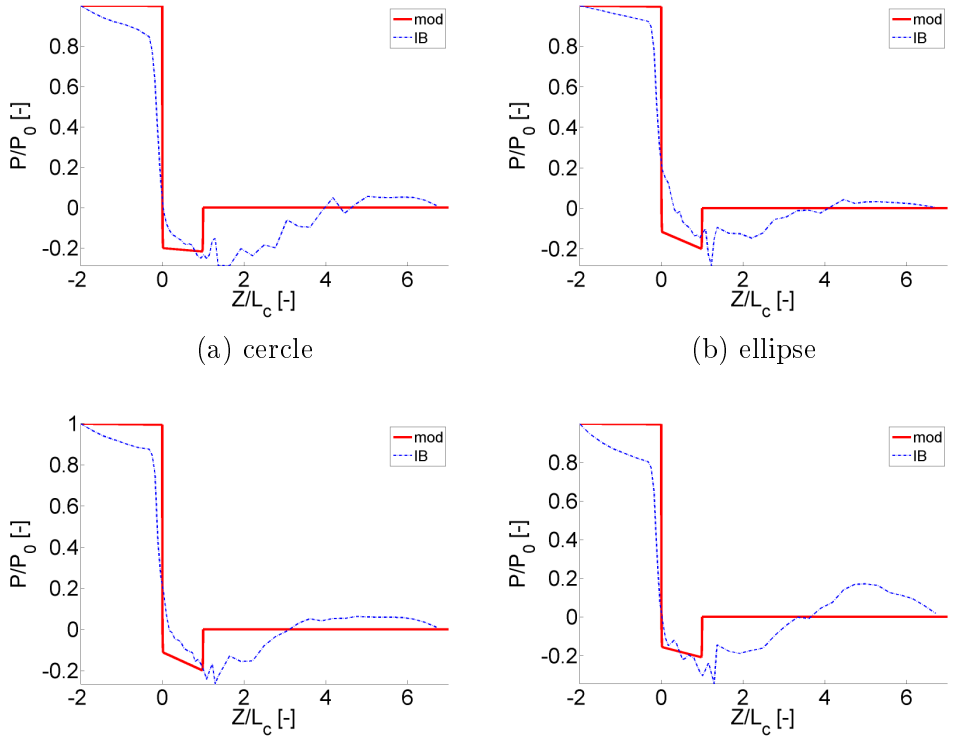

(a) cercle (b) ellipse

(c) rectangle (d) secteur circulaire

Figure H.12: Les distributions de la pression par fractions obtenues en utilisant le modèle quasi tridimensionnel (mod) et la répartition de la pression instantanée simulé en utilisant la méthode de 'Immersed Boundary' (IB). Pour la méthode IB, les valeurs sont prises à la transversale de position (X, Y) associée à la vitesse maximale dans le modèle d'analyse en supposant un écoulement visqueux développée par le canal étranglé. Valeurs simulées instantanées sont évalués au temps $t = 43$ms pour la forme circulaire de rétrécissement et au temps $t = 50$ms pour les autres formes de constriction.

Fig. H.12 montre que dans la constriction à la fois le modèle quasi - tridimensionnel et la distribution de pression simulée sont en baisse et se traduisent par des pressions négatives. En général, le modèle quasi-tridimensionnel fournit une bonne approximation pour la pression simulée au sein de l'étranglement parce qu'une différence globale de 5% entre la distribution de la pression simulé et modélisé est trouvé. Ceci motive l'utilisation du modèle d'écoulement quasi-tridimensionnel pour calculer les forces de fluide sur la paroi à l'intérieur de l'étranglement tout en tenant compte de la forme de la section transversale comme on le faisait dans l'analyse de stabilité pour calculer la pression minimum nécessaire pour entretenir la phonation. D'autre part, on voit que le modèle quasi-tridimensionnel est incapable de rendre compte de rattachement du jet en aval de l'étranglement. Par conséquent, le modèle quasi-tridimensionnel simplifié n'est pas en mesure de capter la répartition de pression en aval de l'étranglement. Ceci est un inconvénient majeur du modèle de l'écoulement

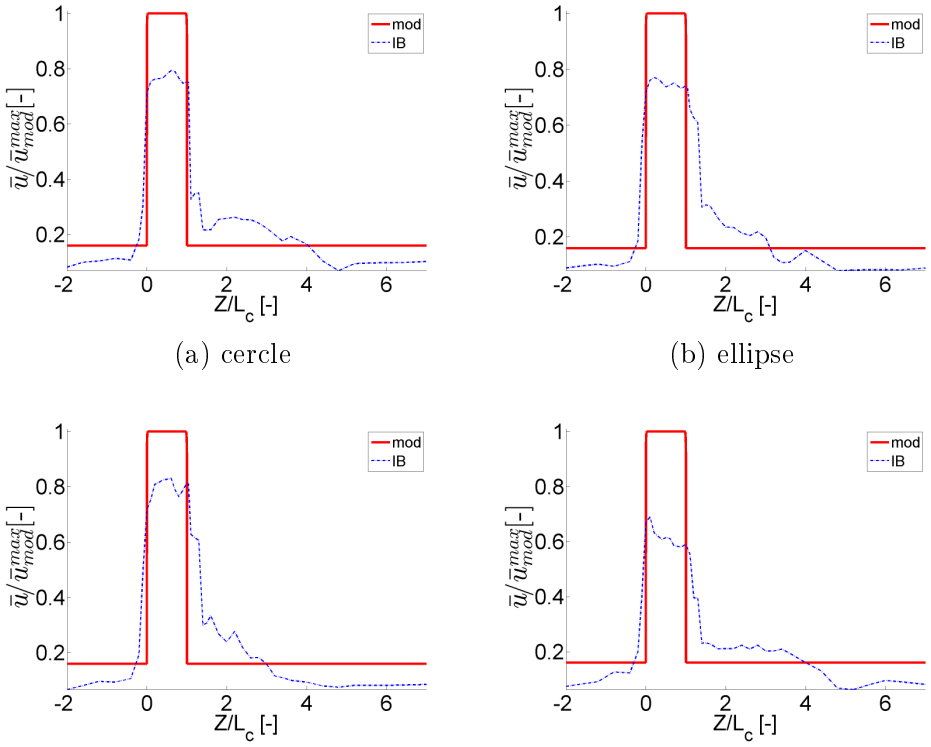

(a) cercle (b) ellipse

(c) rectangle (d) secteur circulaire

Figure H.13: Modélisé (mod) et simulé (IB) streamwise moyen ou distributions de vitesse locales sont normalisées par la vitesse local maximale modélisée $\bar{u}_{mod}^{max}$. Valeurs de vélocité modélisées correspondent à la vitesse apparente locale $Q_{mod}/A(Z)$ avec Q_{mod} le débit de volume résultant du modèle quasi-tridimensionnel et $A(Z)$ la streamwise variable la zone de canal. Pour la méthode de l'IB, les valeurs indiquées correspondent à la valeur moyenne transversale à chaque position par fractions Z. Valeurs simulées instantanées sont évalués au temps $t = 43$ms pour la forme circulaire de rétrécissement et au temps $t = 50$ms pour les autres formes de constriction.

quasi-tridimensionnel proposé et en conséquence le modèle quasi-tridimensionnel sous-estime la différence de pression immédiatement en aval de l'étranglement avec 20% ou plus.

Les principaux résultats de la comparaison de la répartition de la pression dans la direction principal de l'écoulement modélisé et simulé détient également lorsque l'on compare la vitesse moyenne streamwise modélisé et simulé comme on le voit sur la Fig. H.13. En effet, dans le rétrécissement, les vitesses moyennes modélisées surestiment les valeurs simulées avec un maximum de 30% et minimum 15%, alors que, immédiatement en aval de l'étranglement l'erreur augmente parce au'on prends pas en compte le rattachement de l'écoulement dans le modèle d'écoulement quasi - tridimensionnel.

Les profils transversaux modélisées, simulées et mesurées le long de la dimension X sont illustrés dans la Fig. H.14 en utilisant les mesures de vitesse transversales prise immédiate-

ment en aval de l'étranglement pour $Q = 35\text{l/min}$. Les profils simulés à l'entrée ($Z/L_C = 0$), moyenne ($Z/L_C = 0,5$) et de sortie ($Z/L_C = 1$) de l'étranglement sont présentés. Développement de la couche limite le long de la partie rétrécie est observée pour les profils d'écoulement simulées de sorte que pour $Z/L_C \geq 0.5$, les profils simulés, mesurés et modélisés comparé à proximité des parois est de telle sorte que la vitesse du centre simulé fournit une meilleure approximation de la vitesse au centre mesuré que les augmentations Z/L_C. Parce qu'un ecoulement développé est supposé, la vitesse maximale modélisée surestime la valeur mesurée et la vitesse transversale simulée au centre avec 40%. Vitesses au centre simulées et mesurées fournissent un bon match à moins de 5% et 10% en fonction de la forme de section transversale.

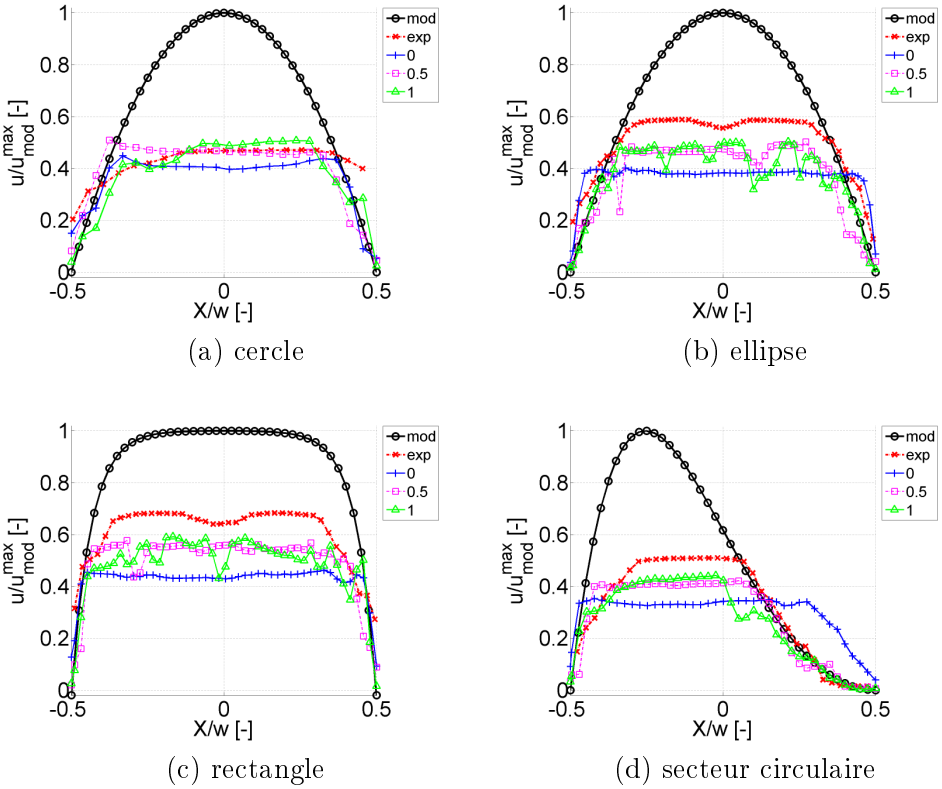

(a) cercle (b) ellipse

(c) rectangle (d) secteur circulaire

Figure H.14: Illustration de la distribution des vitesses normalisées transversales le long de la direction X: modélisées (mod), expérimentale (exp) et simulées (IB). Profils simulés sont présentés pour différentes positions de streamwise dans la constriction: à l'entrée ($Z/L_C = 0$), au milieu ($Z/L_C = 0,5$) et à la sortie ($Z/L_C = 1$). Profils simulés instantanées sont évalués au temps $t = 43\text{ms}$ pour la forme circulaire de rétrécissement et au temps $t = 50\text{ms}$ pour les autres formes. La coordonnée X est normalisée par la largeur de la partie rétrécie w le long de la dimension X.

Conclusion

Des modèles simples d'écoulement ont une longue et fructueuse tradition par rapport à la prévision qualitative des phénomènes de circulation biologique complexes en termes de paramètres physiologiques significatifs à un faible coût de calcul. En outre, les dernières décennies des techniques de simulation d'écoulement complexes sont appliqués à ces phénomènes de circulation biologiques afin de surmonter les hypothèses inhérentes aux modèles de flux simplifiés de manière à fournir des prévisions précises quantitativement à un grand coût de calcul. Un bon exemple d'une variable physiologique importante qui est soit négligé dans les modèles de flux simples ou pour lesquels incorporant tous ses détails dans un modèle de calcul est d'abord une tâche énorme et d'autre part augmente le coût de calcul significativement est la forme de la section transversale d'une sténose connexes à un système de circulation biologique. Outre la forme de section transversale, une attention particulier est accordée à l'amont des conditions d'écoulement. Des applications sont multiple et donc les conditions d'écoulement varient considérable menton si on considéré par example une sténose dans la circulation sanguine ou un flux d'air lors de la respiration.

Par conséquent, dans cette thèse, nous avons cherché à décrire l'influence de la forme de la section transversale sur un écoulement laminaire qui est commandé par la pression à un faible coût de calcul et en tenant compte de la nécessité possible d'analyser le modèle en termes d'espace de paramètres tels que le nombre de Reynolds ou un paramètre géométrique. Par conséquent, un modèle d'écoulement quasi-tridimensionnel simplifié est proposé en association avec la description d'une forme paramétrée de section transversale arbitraire. Un tel modèle permet l'équilibre recherché entre la simplicité et de la complexité et ajoute un aspect tridimensionnel dans un modèle d'écoulement simple. Un tel modelé est original car il est plus naturel de s'appuyer sur une théorie bidimensionnelle ou couche limite dans le cas où l'on cherche à améliorer le modèle d'écoulement utilise. Le modèle de flux proposée repose sur des solutions de flux entièrement développés et peut donc être considérée à l'extension d'un modèles d'écoulement quasi - unidimensionnels classique.

La pertinence ainsi que les limites du modèle de flux proposé par rapport à l'écoulement de canal resserré est représenté de plusieurs façons. Tout d'abord, il est montré que l'incidence de la forme de la section transversale sur la distribution de la pression à l'intérieur de l'étranglement ne peut pas être négligée lorsque l'écoulement n'est pas entièrement dominée par la viscosité. Dans le dernier cas, le modèle de flux de quasi - unidimensionnel classique dispose de bons résultats avec un minimum de calculs. D'autre part, il est montré que l'application du modèle d'écoulement quasi tridimensionnel de phonation permet en effet une analyse mathématique en termes de l'espace de paramètres, et affecte en outre des valeurs prédites, de nouveau par rapport au modèle quasi- unidimensionnel, des paramètres physiologique pertinente dans le cas où le débit est affectée et donc lorsque le débit n'est pas entièrement dominée par la viscosité. Troisièmement, les mesures de pression dans l'étranglement montre que, bien que la précision quantitative est faible, le modèle d'écoulement quasi - tridimensionnel améliore des valeurs prédites par rapport au modèle quasi - unidimensionnelle ainsi qu'à une solution de couche limite pour axisymétrique ou bi-dimensionelles (sauf pour les nombres de Reynolds

bas). De la même façon, les profils de vitesse transversales montrent que les profils prédits par le modèle d'écoulement quasi - tridimensionnel, mais pas précis, ne fournissent certaines caractéristiques principales du profil de vitesse tels que le développement asymétrique des couches limites dans le cas de géométries asymétriques. D'autre part, il est montré que le modèle d'écoulement proposé ne peut pas saisir la complexité de la dynamique d'écoulement liées à la variation de conditions d'écoulement en amont. Dans le même temps, même si une prédiction obtenue à partir de la simulation numérique avec un modèle d'écoulement plus complexe serait certainement plus précise, elle peut être mise en doute qu'il capture l'impact des conditions d'écoulement en amont dans un temps raisonnable. En quatrième lieu, le résultat de modèle est comparée avec les résultats de la simulation numérique d'un modèle d'écoulement laminaire incompressible tridimensionnel. On voit que les prédictions obtenues à partir du modèle sont adaptés pour prévoir l'ordre de grandeur des quantités d'écoulement à l'intérieur de l'étranglement tandis que des prédictions à partir de l'étranglement sont inutiles. Le champ d'écoulement simulé d'autre part est capable à capter une partie de la dynamique d'écoulement à un coût de calcul élevé.